In vitro studies of actin-microtubule coordination

Magdalena Preciado López

This thesis was reviewed by:

Prof.dr. Marcel E. Janson	Wageningen UR
Dr. Lukas C. Kapitein	Universiteit Utrecht
Prof.dr. Erwin J.G. Peterman	Vrije Universiteit Amsterdam
Dr. Cornelis Storm	Technische Universiteit Eindhoven
Dr. Clare M. Waterman	National Institutes of Health

The research described in this thesis was performed at the FOM Institute AMOLF, Science Park 104, 1098 XG, Amsterdam, the Netherlands. This work is part of the resarch program of the Foundation for Fundamental Research on Matter (FOM), which is financially supported by the Netherlands Organization for Scientific Research (NWO).

ISBN/EAN: 978-90-77209-89-9

A digital version of this thesis is available at www.amolf.nl/publications/theses and www.ubvu.vu.nl/dissertations. Printed copies can be requested to the library of the FOM Institute AMOLF (library@amolf.nl).

VRIJE UNIVERSITEIT

In vitro studies of actin-microtubule coordination

ACADEMISCH PROEFSCHRIFT

ter verkrijging van de graad Doctor aan
de Vrije Universiteit Amsterdam,
op gezag van de rector magnificus
prof.dr. F.A. van der Duyn Schouten,
in het openbaar te verdedigen
ten overstaan van de promotiecommissie
van de Faculteit der Exacte Wetenschappen
op maandag 9 maart 2015 om 11.45 uur
in het auditorium van de universiteit,
De Boelelaan 1105

door

Magdalena Preciado López

geboren te Mexico City, Mexico

promotor: prof.dr. G.H. Koenderink

copromotor: prof.dr. M. Dogterom

"The true biologist deals with life, with teeming boisterous life, and learns something from it, learns that the first rule of life is living."

– John Steinbeck, The Log from the Sea of Cortez

Abstract

Eukaryotic cellular life critically relies on cell division, growth and migration, all highly dynamic processes that are organized and powered by the microtubule and actin cytoskeletons. Although it is now clear that these two cytoskeletal systems must be coordinated, it remains unclear how the activity of actin-microtubule cross-linkers enables their functional co-organization in different cellular contexts. In particular, it is unknown how cross-linker mediated cytoskeletal coordination is influenced by the diversity of filamentous actin (F-actin) architectures found in cells (i.e. free, cross-linked and bundled), whose distinct mechanical properties are likely to impact the outcome of their encounters with growing microtubules.

Here, with the use of a minimal model system reconstituted from purified proteins, we elucidate how linking growing microtubule ends to F-actin structures can help direct cytoskeletal organization. To establish actin-microtubule interactions *in vitro*, we engineered a model actin-binding, microtubule plus-end tracking protein that we call TipAct. This simple cross-linking system recapitulates the *in vivo* ability of stiff actin bundles to capture and guide microtubule growth, which is highly dependent on their encounter angle and the concentration of cross-linking protein both at the microtubule tip and lattice. In a different context, the same cross-linking system conversely enables growing microtubules to globally dictate F-actin organization, as they can pull, stretch and bundle single actin filaments. To explain these effects, we developed a model of biased diffusion at microtubule tips, which recapitulates the dependency of actin-filament transport on both EB and tubulin concentration, and which also predicts that growing microtubules can potentially generate picoNewton forces through this mechanism.

We conclude that, independently of biochemical regulation, a variety of cytoskeletal organizations can arise from the interplay between physical cross-links and the mechanical properties of F-actin and microtubule structures. And finally, that cross-linkers can establish a mechanical feedback between actin and microtubule organization which is likely to be relevant in diverse biological contexts.

Contents

Chapter 1

Introduction: The eukaryotic cytoskeleton and actin-microtubule coordination

In this introductory chapter we first outline the general properties of the three eukaryotic cytoskeletal systems: actin, microtubules and intermediate filaments, and how they individually shape the cell interior. Thereafter, we focus on cytoskeletal cross-talk with a focus on actin-microtubule interactions. We highlight the mechanisms that allow cross-linking proteins and biochemical regulators to efficiently orchestrate the cytoskeletal architecture, and discuss how their activity is modulated by the basic mechanical and dynamical properties of microtubules, actin filaments and intermediate filaments. Finally, we provide an outline for this thesis.

1.1 The eukaryotic cytoskeleton

Cells, the basic unit of life, have the incredible ability to change shape, divide and move. These vital cellular functions are powered by a dynamic supramolecular assembly known as the cytoskeleton. Among others, the key roles of the cytoskeleton are: to power the drastic morphological changes required in cell division, growth and migration; to provide the cell with mechanical stability and integrity to interact with its environment; and finally, to function as an internal scaffold that organizes the cell interior, by providing tracks for the transport of molecules and vesicles.

In metazoans, the cytoskeleton is typically composed of three distinct protein polymers: microtubules (MTs), filamentous actin (F-actin), and intermediate filaments (IFs) (Fig. 1.1). Depending on cell cycle and cell type, the cytoskeleton can adopt a variety of higher-order architectures to better serve the task at hand. To this end, actin, microtubules and intermediate filaments rely on their individual mechanical properties and assembly dynamics, as well as on the activity of accessory proteins. Some of these proteins regulate the spatial organization of these systems, some their assembly dynamics, while others mediate cooperation across systems. All of these functions are equally required for proper cellular function.

In the following sections we summarize the main properties of microtubules, actin filaments and intermediate filaments; followed by a review on cytoskeletal cross-talk between F-actin and microtubules; and finally, we provide an outline for this thesis.

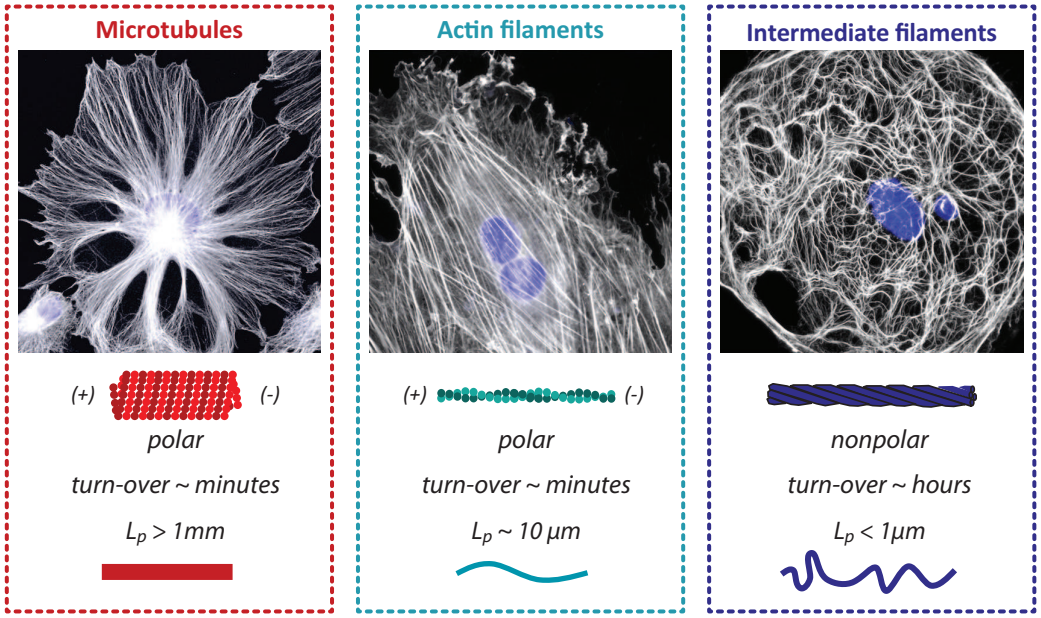

Figure 1.1: The main components of the metazoan cytoskeleton. Top, Fluorescence micrographs of CV-1 monkey fibroblastic kidney cells (left), PtK_2 rat-kangaroo epithelial kidney cells (middle), and A-10 rat myoblastic thoracic cells in 2D culture immunostained with tubulin (left) and cyto-keratin (right) antibodies, or labeled with pEGFP-βActin (middle). DAPI staining (blue) marks the nucleus. Figures taken from [1]. Bottom, polarity, turn-over dynamics and persistence length L_p of microtubules, actin filaments and intermediate filaments.

1.1.1 Microtubules

Microtubules are protein polymers that assemble through the longitudinal addition of GTP-bound $\alpha - \beta$ tubulin heterodimers (Fig. 1.2 a and b). The three main types of tubulin in eukaryotes are α, β and γ tubulin, highly-homologous $\sim$ 55 kDa GTP-binding proteins, with multiple isoforms that are cell- and tissue-specific [2, 3]. While the $\alpha - \beta$ tubulin heterodimers constitute the soluble unit for microtubule polymerization in cells, γ-tubulin is typically found in large protein assemblies that mediate microtubule nucleation [4–7].

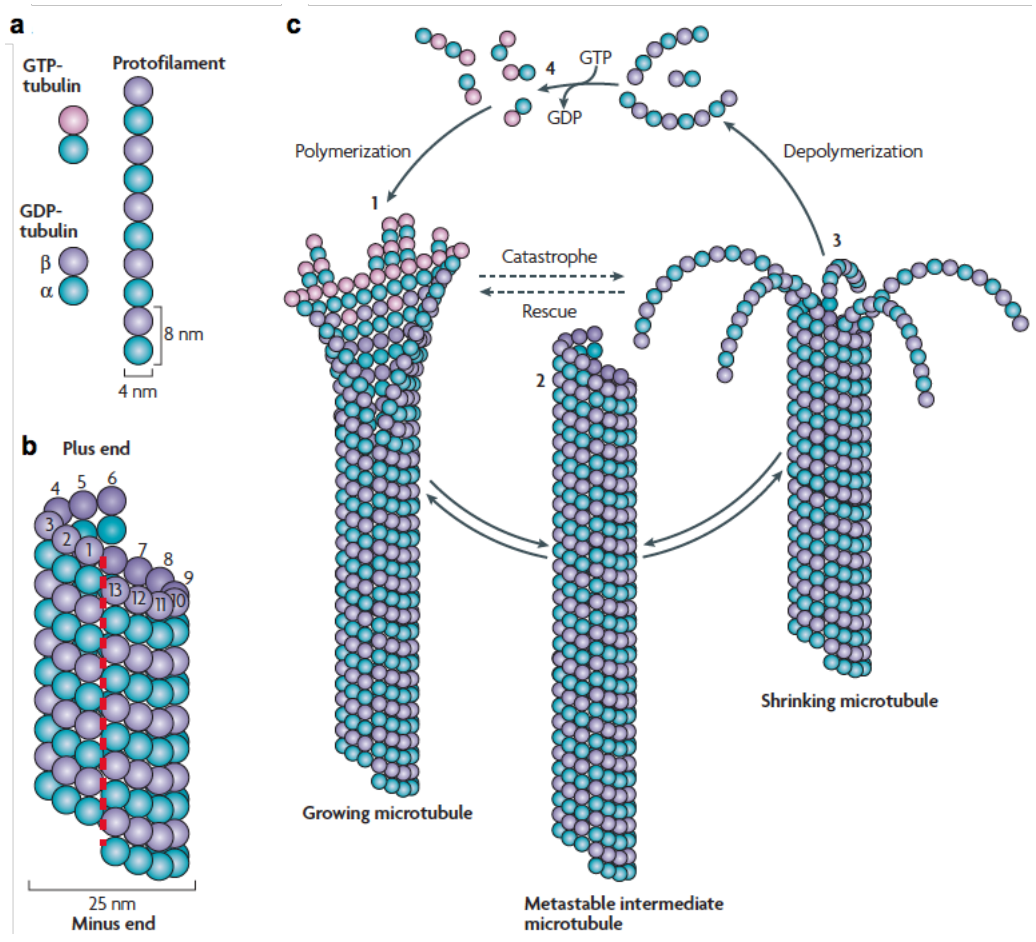

Figure 1.2: Microtubule structure and dynamic instability. (a) Microtubules polymerize from the longitudinal assembly of $\alpha - \beta$ tubulin dimers. (b) The most typical tubulin assembly in cells is a 13-protofilament hollow tube in which lateral contacts are dominated by $\alpha - \alpha$ and $\beta - \beta$ tubulins, with a discontinuity called the microtubule *seam* in which α tubulins contact β tubulins. (c) GTP hydrolysis allows microtubules to undergo dynamic instability [8], a process by which they transition between phases of growth and shrinkage, with transitions in between called catastrophes and rescues. Figure taken from [9].

In vitro, tubulin can assemble into a variety of structures [10], whose rate of polymerization depends on tubulin concentration, Mg^{2+} concentration, pH and ionic strength [11, 12]. *In vivo*, the predominant mode of tubulin assembly is a hollow cylindrical tube, with a diameter of $\sim$ 25 nm, composed of 13-protofilaments [13], (Fig. 1.2 b). In this type of microtubular architecture, commonly called *B-lattice* [14], longitudinal contacts primarily occur between α and β subunits, while lateral contacts occur between $\alpha - \alpha$ and $\beta - \beta$ subunits [15]. This organization results in all protofilaments running parallel to the long axis of the microtubule, but also in a structural discontinuity (called the microtubule *seam*) where α and β subunits contact laterally, in an *A-lattice* architecture [16]. It has been proposed that A-lattice type lateral bonds at the seam constitute the weakest structural feature in microtubules [17]. Recent *in vitro* work supports this notion, as reconstitutions of seeded microtubule polymerization with ectopic A-lattice seams revealed that these microtubules are more prone to depolymerization [18]. The fact that longitudinal contacts occur between α and β subunits results in two distinct microtubule ends, with distinct polymerization dynamics: a slowly growing *minus*-end, where the α-tubulins are exposed, and a faster growing *plus*-end where the β-tubulins are exposed [19]. This architecture renders the microtubules structurally polar, a property that is exploited by molecular motors (both plus and minus-end directed) to transport molecules, vesicles, and organelles in the cell interior.

The rate-limiting step in microtubule polymerization is nucleation [20], in which a $\sim 6-15$-mer unit first needs to form for microtubule polymerization to proceed [12, 21–24]. *In vitro*, the critical concentration for nucleation at room temperature and in the absence of co-factors ranges from $\sim 20-40$ µM [25, 26]. This is comparable to the cytosolic tubulin concentration in a variety of eukaryotic cells [27], which helps explain why spontaneous microtubule nucleation is rarely (if ever) observed. Notwithstanding, microtubules constitute $\sim$ 65% of the total tubulin content in cells [28]. This balance suggests the existence of potent microtubule nucleators. Indeed, cells have evolved a variety of microtubule organizing centers (MTOCs) whose spatial distribution and activity are tightly regulated throughout the cell cycle [29]. The elemental unit for microtubule nucleation in cells is γ-tubulin. While in monomeric form it is a poor nucleator of microtubules [6], γ-tubulin is usually found in large ($\sim 280 - 2,200$ kDa) protein assemblies (i.e. the γ-tubulin ring complex, γ-TuRC, and γ-tubulin small complex, γ-TuSC), which drive efficient microtubule nucleation [4–7]. Notably, the γ-TuRC is a ring-like structure with a diameter of $\sim$ 25 nm, which contains 13 vertically-staggered γ-TuSC units, and thus mimics the 13-protofilament architecture of microtubules [30]. The highest concentration of microtubule nucleating centers is found at the centrosome,

which serves as the primary MTOC in most cells. During interphase, the centrosome is kept in tight association with the nuclear membrane, where it drives the polymerization of radial microtubule arrays from the cell center towards the cell edge. In contrast, during mitosis the duplicated-centrosomes migrate to opposite sides of the cell to drive the polymerization of the mitotic spindle. Additionally, non-centrosomal microtubule-nucleation and/or minus-end stabilization is a common feature in cells [31]. Notable examples include microtubule branching events driven by augmin at the mitotic spindle of animal and plant cells [32–35], microtubule nucleation and minus-end stabilization at the Golgi apparatus [36–39], microtubule minus-end capture at the apical membrane of polarized epithelial cells [40–43], and microtubule minus-end stabilization by the CAMSAP/Nezha/Patronin family of proteins [44, 45].

GTP-hydrolysis is tightly coupled to the polymerization dynamics and stability of microtubules [46–48]. However, hydrolysis is not required for polymerization, as slowly-(or non-) hydrolyzable GTP-analogs (i.e. GMPCPP and GMPPNP) can also promote microtubule growth [49, 50]. GTP hydrolysis (which occurs only at the β-tubulin part of the dimer [51]), is enhanced through polymerization [52], and results in destabilization of the microtubule structure. The manner by which GTP-hydrolysis destabilizes the microtubule has been the subject of extensive work [53]. For a long time the prevailing picture was that GDP-bound dimers are curved [54, 55], whereas GTP-bound dimers are straight [56]; consequently, it was postulated that GTP-hydrolysis would introduce strain in the microtubule lattice as the GDP-bound tubulin dimers tend to curl outwards. However, recent work has revealed that GTP and GDP-bound tubulin dimers have similar curvatures [57–59], and that straightening of the GTP-bound tubulin is induced only as it incorporates into the microtubule lattice [60, 61]. These observations are consistent with electron-microscopy studies which showed that polymerizing microtubules tend to *flare* outwards [54, 62, 63]. The precise conformational changes induced by GTP hydrolysis inside the microtubule have just been recently elucidated. Contrary to the previous picture, in which hydrolysis destabilized lateral tubulin contacts (which are weaker than their longitudinal counterparts [64]), it has been shown that hydrolysis and phosphate release are accompanied by a compaction of the longitudinal dimer-dimer interface, and a rearrangement of the α-tubulin subunits [65]. The ways by which these conformational changes introduce instability to the microtubule as a whole are yet to be elucidated.

Both *in vivo* and *in vitro*, microtubules undergo cycles of fast polymerization and even faster depolymerization, with transitions in between that are commonly called *catastrophes* and *rescues* (Fig. 1.2 c). This property of microtubule growth has been

termed *dynamic instability*, and it allows microtubules to quickly remodel in order to explore the cell interior efficiently [8]. The parameters of dynamic instability are tightly regulated across cell types [66], during the cell cycle [67], and even between distinct regions in the cell [68]. In mitotic and meiotic spindles, microtubule turnover takes place in the order of tens of seconds [67, 69], whereas in interphase microtubules turn over takes place in the order of minutes [70]. These differences result from regulated changes in the balance between dimer and polymer concentration through the activity of tubulin-sequestering proteins such as stathmin [71, 72], as well as regulation of microtubule polymerases and depolymerases [73–75]. An emerging picture, worth noting, is that slight changes in microtubule dynamic properties can have huge effects on the stability of microtubule assemblies [76, 77].

The dynamic instability of microtubule growth is intimately related to the fact that the transition from GTP to GDP-bound tubulins does not occur instantaneously but with some delay after tubulin addition, resulting in what has been termed a stabilizing *GTP-cap* at the microtubule tip [48, 78]. The nature and length of the GTP-cap has been controversial. *In vitro* experiments in which microtubule catastrophes were induced by tubulin removal revealed that the GTP-cap consists of up to ~ 200 tubulin dimers [79]. In contrast, later studies with GMPCPP-tubulin-capped microtubules suggested that a GTP-cap of ~ 13 tubulin dimers is sufficient to stabilize microtubules against depolymerization [80]. *In vitro* measurements of tubulin on and off dynamics at microtubule tips revealed that even during growth-phases, microtubules can lose many layers of tubulin dimers without undergoing a catastrophe, and that the extent of polymer loss during these tip fluctuations increases with tubulin concentration [81]. This observation suggests that the length of the stabilizing cap at microtubule tips is probably longer than a couple of dimers. Recent work suggests that the GTP-cap is more likely to be an intermediate in the GTP-hydrolysis cycle, which is precisely the structure that is recognized by end-binding proteins (EBs) [82–85]. EB proteins are master regulators of microtubule dynamics and organization in cells, both intrinsically [86], but also by recruiting microtubule-associated proteins to the microtubule plus-tip [87]. *In vivo* measurements of cap-length obtained by imaging the distribution of EB proteins at microtubule tips estimate that the average GTP-cap consists of ~ 750 tubulin dimers, extending ~ 0.5 µm from the microtubule tip [88].

Microtubules are about 100- and 1000-fold stiffer than F-actin and intermediate filaments respectively (Fig. 1.1). A variety of methods have been applied to measure the bending rigidity, EI, of microtubules, such as analysis of filament thermal fluctuations and probing with optical tweezers. In the absence of microtubule-stabilizing agents, the

bending rigidity of microtubules is ~ 8 pN µm^2 [89–91]. The addition of the microtubule stabilizing agent taxol tends to soften microtubules ~ 3 pN µm^2 [89, 91], whereas polymerization with BeF^{-3} (which occupies the site of the cleaved γ-phosphate, and thus mimics the GTP·Pi intermediate [84, 89]) increases the bending rigidity to ~ 29 pN µm^2 [89]. The increased bending rigidity of BeF^{-3}-stabilized microtubules suggests that the GTP-cap could have distinct mechanical properties from the rest of the microtubule, which could play a key role in the sensitivity of microtubule growth to force [92, 93]. The bending rigidity of microtubules corresponds to a persistence length in the order of millimeters, which is larger than the average eukaryotic cell size ($\sim 5 - 15$ µm [94]). This helps explain why microtubules often seem *straighter* than actin filaments or intermediate filaments in cells, whose persistence lengths are at or below the average eukaryotic cell size (Fig. 1.1).

1.1.2 EB and the family of microtubule plus-tip interacting proteins (+TIPs)

End-binding (EB) proteins were first identified as binding partners of the C-terminus of adenomatous polyposis coli (APC), and hence their name [95]. They are ubiquitously expressed proteins with homologues in all eukaryotes. EBs are small (~ 35 kDa) dimeric proteins [96], which contain an N-terminal microtubule-binding domain (MTBD) made up of two calponin homology (CH) domains [97], a coiled-coil region which mediates dimerization, and two unstructured and negatively charged C-terminal tails that regulate their affinity for the microtubule lattice [98] (Fig. 1.3 a). Furthermore, EBs can adopt an auto-inhibited conformation through associations between the N-terminal MTBD and the C-terminal tails, which is thought to be relieved by binding to their many interacting partners in cells [99]. There are three main members of the EB family in mammals: EB1, EB2 and EB3. Both EB1 and EB3 autonomously recognize a feature of the microtubule growing end where they quickly exchange, displaying a localization pattern commonly termed the EB *comet* [86, 100] (Fig. 1.3 b). In contrast, EB2 tends to localize along the length of microtubules, with no clear preference for their growing ends [86]. Perhaps the most striking feature of EB1 and EB3 is not that they can autonomously localize at growing microtubule ends, but that, by doing so, they can enhance the dynamicity of microtubule polymerization. Both *in vivo* and *in vitro* studies have revealed that EB1 and EB3 promote faster microtubule polymerization [86, 101–104], while also induce catastrophes by accelerating the transition from GTP- to GDP-tubulin [100]. The microtubule-binding domain of EB lies at the interface between four tubulin dimers

(except at the seam), in direct contact with the exchangeable GTP-binding site of β-tubulin [84]. *In vitro* studies revealed that EB recognizes an intermediate in the GTP-hydrolysis cycle, as it strongly binds to microtubules polymerized with the slowly-hydrolyzable GTP analog GTPγS, or with GTP and BeF^{-3}, which occupies the position of the hydrolyzed γ-phosphate ion after its release [83, 89]. Contrary to previous belief [82], EB does not bind microtubules polymerized from GMPCPP with high-affinity. Given the intermediate curvature of GMPCPP-stabilized microtubule protofilaments [105], which lies between that of the straight polymer-incorporated tubulin, and the curved dimeric tubulin, it is now thought that GMPCPP rather mimics the end-most structure of microtubule tips, where GTP has not yet been hydrolyzed [53]. This is the region where the potent microtubule polymerase XMAP215 binds, whereas EB localizes slightly behind [100, 106].

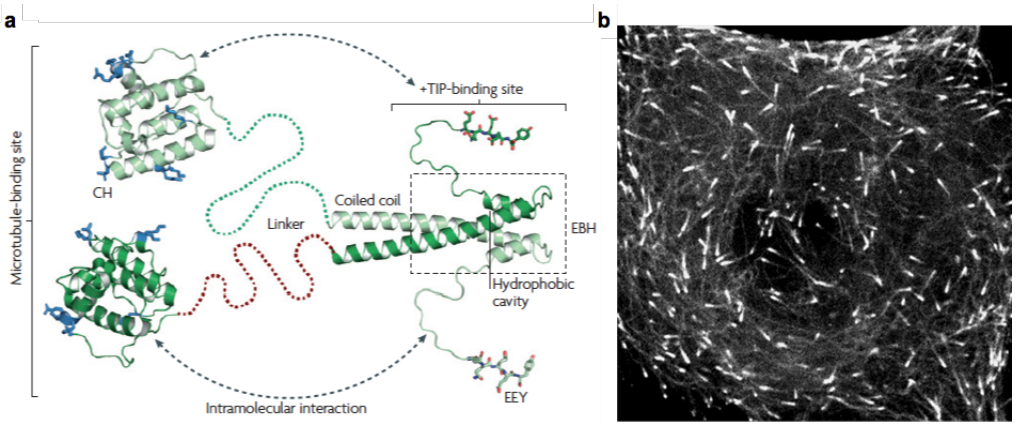

Figure 1.3: EB protein structure and localization in cells. (a) Domain architecture of EB molecules: N-terminal microtubule-binding domain (MTBD) made up of two calponin homology (CH) domains [97], unstructured linker regions, coiled-coil region which mediates dimerization, EB-homology (EBH) domain which mediates interactions with SXIP-motif containing proteins [107], unstructured and negatively-charged C-terminal tails that regulate EB's affinity for the microtubule lattice [98], and also mediate interactions with CAP-Gly-domain containing proteins. Interactions between the C-terminal tails and the MTBD mediate intramolecular inhibition [99]. (b) Fluorescence live-cell imaging micrograph showing the representative localization of mTFP1-labeled EB3 in MDCK dog epithelial kidney cells in culture. Figures taken from (a) [9] and (b) [108].

Coupled to their role as regulators of microtubule dynamics in cells, EBs recruit a large family of proteins, collectively called *plus-tip interacting proteins* (+TIPs), to the growing ends of microtubules [9, 87, 109–113] (Fig. 1.4). Typically these proteins display similar, fast on and off dynamics at microtubule tips, suggesting that their plus-end localization is regulated by EB's exchange dynamics [114–116]. The +TIP family is large, and new members are still being discovered [113]. It includes proteins which stabilize

microtubules (i.e. CLIP-170 [115, 117, 118] and sentin [119]), microtubule depolymerases (i.e. MCAK [120]), F-actin binding proteins (i.e. CLASPs [121], MACF/Shot [122–125], and APC [126, 127]), endoplasmic-reticulum-bound proteins (i.e. STIM1 [128]), regulators of F-actin polymerization (i.e. RhoGEF2 [129]), and adaptors of motor proteins (i.e. p150^{glued} [130, 131]).

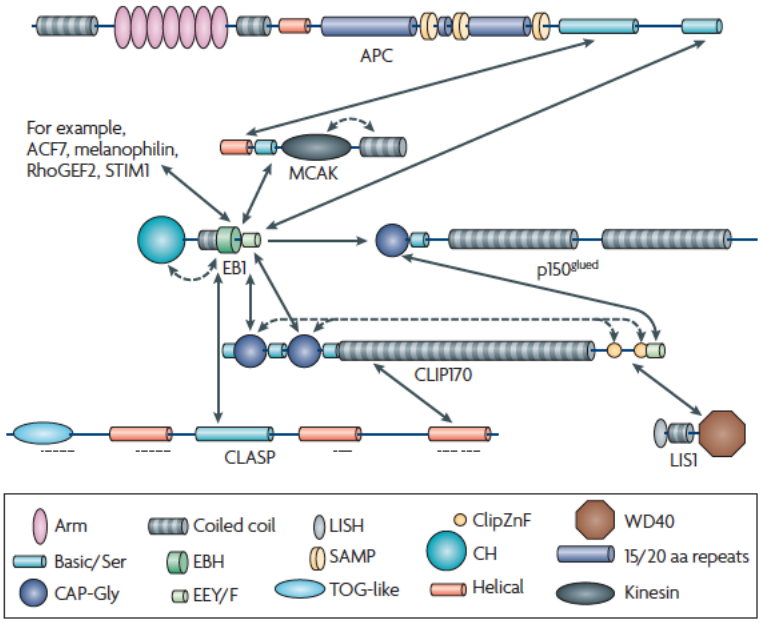

Figure 1.4: The +TIP family of proteins and their interactions. The SXIP-motif containing proteins (i.e. APC, MCAK, CLASP, ACF7, RhoGEF2, melanophilin and STIM1) interact with the EBH domain. The Cap-Gly-domain containing proteins (i.e. CLIP170, p150^{glued}) interact with EB and CLIP-170's EEY/F acidic tails. CLASPs also have TOG-like domains with which they can directly bind to the microtubule lattice. Figure taken from [9].

Broadly speaking, the +TIP family can be broken down into three subgroups (Fig. 1.4): The first two require EBs to localize at microtubule growing ends, while a third smaller group autonomously localize at microtubule tips [9, 132]. The first group, collectively called *SXIP proteins*, contain the conserved sequence SXIP, embedded within a stretch of positively-charged and serine-rich amino-acids, which has been called a microtubule tip localization signal (MtLS) [107]. This MtLS is recognized by a hydrophobic cavity (the EB homology domain, EBH, Fig. 1.3 a) at the end of the coiled-coil region of EB which only forms upon EB-dimerization [133]. Many SXIP proteins contain multiple copies of the MtLS, which serves to enhance their affinity (in the nanomolar range) for EB [134]. In contrast, serine phosphorylation in the vicinity of the MtLS has been shown to inhibit the binding of SXIP-proteins to EB [107, 127, 133, 135]. The second group of +TIPs that require EB to localize at growing microtubule ends are the *CAP-gly* family

of proteins. These proteins contain a hydrophobic cavity with the conserved sequence GKNDG, which specifically recognizes the acidic C-terminal EEY/F amino acids of EB (Fig. 1.3 a), α-tubulin, as well as the C-terminal zinc knuckle domain (ClipZnF) of CLIP-170 [104, 130, 136]. The third member of the +TIP family are the TOG-proteins, which autonomously localize at growing microtubule ends independent of EB. *In vitro* and *in vivo* studies have revealed that, unlike EBs, the TOG-family of proteins localize to the edge-most tubulin dimers at the microtubule tip [100, 106]. Notable members of this family are: XMAP125, ch-TOG, CLASPs, and their homologues in lower eukaryotes [137]. TOG proteins are typically elongated proteins which contain more than one copy of the TOG-domain arranged in series. This architecture allows them to act as potent microtubule polymerases. For example, XMAP215 simultaneously localizes at microtubule tips while recruiting tubulin dimers from solution [138, 139]. Furthermore, *in vitro* reconstitutions of microtubule polymerization with EB1 and XMAP215 have shown that these proteins act in synergy, enhancing microtubule growth speeds to near cellular levels [140]. Often, +TIPs make use of more than one domain to enhance their plus-end localization (Fig. 1.4). For instance, p150^{Glued} recognizes the EB-homology domain, but also associates with CLIP-170 through its CAP-Gly domain [9]. Similarly, SLAIN2 associates both with EB via an SXIP-motif, and with and chTOG [141], and CLASPs contain both SXIP and TOG domains [142].

The variety of EB-interacting partners thus renders the microtubule plus-tip a hub where many cellular activities are regulated [87]. Not surprisingly, many interactions between microtubules and F-actin take place at this site.

1.1.3 Filamentous actin (F-actin)

Actin filaments are double-stranded helical polymers, with a diameter of $\sim 6-8$ nm, which assemble through the longitudinal addition of globular actin (G-actin) monomers (Fig. 1.5). G-actin is a $\sim$ 42 kDa ATP-hydrolyzing protein, whose ATP-binding cleft is located at the center of the molecule. ATP (or ADP) binding at this site is also essential to stabilize the structure of the G-actin molecule in monomeric form [143, 144]. In humans there are three main G-actin isoforms, α, β and γ. α-actin is mostly present in muscle tissue, while β- and γ-actin are the main components of cytosolic F-actin networks in non-muscle cells.

As the polymer assembles, new G-actin units are incorporated with their ATP-binding pockets facing in one direction, thus endowing the actin filament with structural polarity.

It is common to term the structurally-different ends as *pointed* and *barbed* ends, also called the *minus* and *plus* ends (Fig. 1.5). This terminology arose from electron microscopy studies of F-actin decorated with the S1 fragment of myosin motors, in which the motor heads were observed to align with an arrowhead shape in the direction of the more slowly growing actin-filament end, which was thus called the pointed end [145].

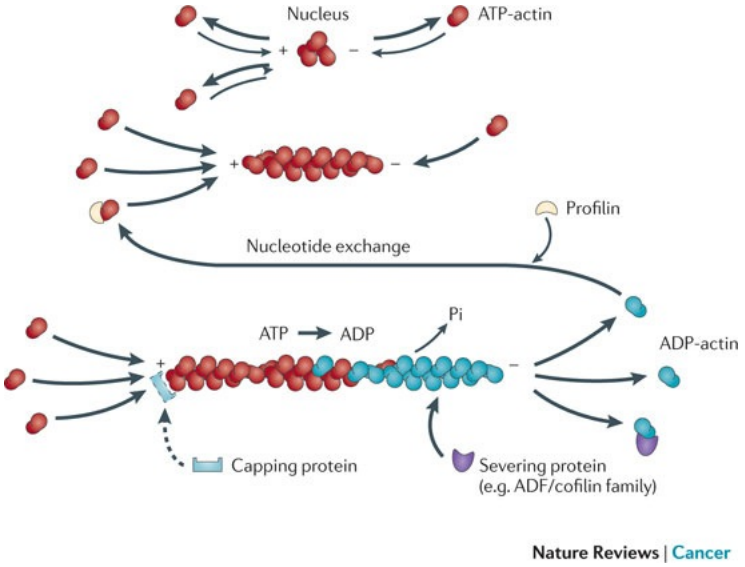

Figure 1.5: Actin filament polymerization dynamics. The rate-limiting step in F-actin assembly is the nucleation of dimers and trimers of G-actin. After this step, polymerization of GTP-bound G-actin subunits proceeds faster at the barbed end (+), than at the pointed end (−). ATP-hydrolysis and phosphate ion (Pi) release occur with a time delay, leading to a gradient of ATP to ADP-bound subunits along the filament, from barbed to pointed end. At steady-state, ADP-bound G-actins dissociate fast from the pointed end, while ATP-bound G-actins associate fast with the barbed end, leading to filament treadmilling. Accessory proteins such as profilin, capping protein, and ADF/cofilin further regulate the dynamics of actin-filament polymerization in cells. Figure taken from [146].

The rate-limiting step of F-actin assembly in the absence of cofactors is the formation of dimers and trimers of G-actin [147–149] (Fig. 1.5). After this slow nucleation step, F-actin polymerization proceeds from both pointed and barbed ends if the soluble G-actin concentration is sufficiently high. The rate of polymerization is markedly different at each end, and strongly depends on the concentration of divalent cations in solution [150, 151], as well as the ionic strength of the buffer [152]. In favorable conditions for F-actin polymerization *in vitro* (i.e. 50 mM KCl, 1 mM $MgCl_2$, 1 mM EGTA, 50 µM $CaCl_2$, 0.2 mM ATP, 0.5 mM DTT and 10 mM Imidazole, at 22°C [153]), it was found that the critical ATP-G-actin concentration for assembly at the pointed end ($C_{c-} = 0.6$ µM), is five-fold higher than that at the barbed end ($C_{c+} = 0.12$ µM). Thus, at steady-state, and

as a direct result of the different on- and off-rates of G-actin at barbed and pointed ends, actin filaments undergo a phenomenon called *treadmilling*, in which subunit addition at the barbed end is compensated by subunit loss at the pointed end (Fig. 1.5). This results in a flux of G-actin units along the polymer, even though the filament length remains constant [154, 155]. Concomitantly, barbed-end polymerization, pointed-end depolymerization, and their modulation by accessory proteins (i.e. profilin, capping protein, and cofilin, Fig. 1.5) [156, 157], are the main drivers of F-actin homeostasis in cells [158].

Similar to GTP-hydrolysis in microtubules, ATP-hydrolysis is intimately related to the polymerization dynamics of actin filaments. During filament elongation, incorporation of ATP-bound G-actin is quickly followed by ATP-hydrolysis [151], while phosphate (Pi) release proceeds more slowly. This results in the formation of a stabilizing ADP·Pi cap at the barbed end of the growing filaments [159, 160] (Fig. 1.5). Phosphate release is accompanied by destabilization of intermolecular bonds along the filament, as well as a reduction in filament bending rigidity [161, 162]. Subject of much debate, it has been recently demonstrated that phosphate release is a random process along the filament that proceeds with a half-time of ~ 100 s [163]. Besides destabilizing the filament, ATP-hydrolysis also has profound effects on the association of actin-binding proteins (ABPs). For instance, the F-actin nucleator Arp2/3 [164] preferentially mediates branching from newly-polymerized F-actin regions [165], whereas the F-actin severing enzyme cofilin preferentially acts on ADP-containing portions of actin filaments [166].

In non-muscle cells, the cytoplasmic G-actin concentration is typically in the range of $\sim 50 - 100$ µM [167]. This high monomeric pool is maintained through the activity of filament severing [156] and capping proteins [158], as well as G-actin sequestering proteins, such as profilin and thymosin-β4 [168, 169]. Both profilin and thymosin-β4 inhibit spontaneous F-actin nucleation, while profilin also participates in nucleotide exchange [170] (Fig. 1.5), and barbed-end F-actin polymerization either directly [171, 172], or through association with profilin-binding F-actin polymerases, such as the formin family of proteins [173].

Actin filaments are softer than microtubules, but stiffer than intermediate filaments (Fig. 1.1). A variety of methods have been applied to measure the bending rigidity of actin filaments, such as analysis of thermal fluctuations [162, 174, 175], and direct mechanical probing with optical tweezers [176]. Most of these studies were performed with phalloidin-stabilized actin filaments, converging on a bending rigidity in the order of ~ 0.07 pN µm^2, while in the absence of phalloidin the bending rigidity is approximately

two-fold lower ~ 0.04 pN µm^2 [162]. Such bending rigidities correspond to actin filament persistence lengths in the order of $10 - 20$ µm at room temperature (Fig. 1.1). *In vitro* reconstitutions of spontaneous F-actin polymerization in the absence of cofactors have revealed that at steady state the distribution of filament lengths is exponential, in the range of $1 - 20$ µm, depending on the initial G-actin concentration [177, 178]. Thus, at least *in vitro*, actin filaments can be comparable to, or longer than, their persistence length, and as such are considered to be semi-flexible polymers. However, in cells actin filaments are generally much shorter. For instance, in fission yeast, the average filament length in Arp2/3-nucleated cortical patches is in the order of $50-100$ nm [179, 180], while in endothelial cells the average filament length is in the order of $0.5 - 3$ µm [181]. This is the result of the many accessory proteins (i.e. severing, capping, branching proteins) that participate in F-actin length regulation *in vivo*. Thus, in cells, actin filaments are on average shorter than their persistence length. This is likely to have direct implications on their mechanical behavior, since at these length scales they behave closer to a stiff rod than to a semi-flexible polymer. In agreement with this, *in vitro* rheological studies of F-actin networks cross-linked by filamin revealed that with decreasing average filament length (by the addition of the actin-severing protein gelsolin), the networks behaved more as a collection of stiff polymers cross-linked by flexible linkers [182], in which the elasticity of the network was dominated by the compliance of the cross-linkers, rather than by the F-actin itself.

In cells, actin filaments organize into higher-order structures with the aid of several accessory proteins [183–185] (Fig. 1.6). The list of actin-binding proteins (ABPs) is large, and includes proteins that: cross-link (fimbrin, filamin), bunlde (α-actinin, fascin), cap (gelsolin, capping protein), nucleate (formin, Arp2/3), and sever (ADF/cofilin) actin filaments, among others [186]. In different combinations, ABPs help build F-actin structures that support a variety of cellular functions, such as maintaining cellular shape during mitosis and interphase; coupling the cell interior with the extra-cellular matrix; providing protrusive and retractive forces at the front and rear of the cell; as well as acting as contractile gels that regulate the mobility of membrane-bound and cytosolic components. Broadly speaking, these F-actin superstructures can be grouped into the following categories:

- Actomyosin cortex: a thin ($\sim$ 190 nm [187]) F-actin network that lines the membrane of animal cells. The cortex is primarily responsible for maintaining cellular shape both during interphase and mitosis [188–190], but is also involved in the segregation of polarity components in asymmetrical cell divisions [191, 192].

Recent work on isolated blebs of HeLa and melanoma M2 cells elucidated the proteomic content of the F-actin cortical network, revealing that it is composed of $\sim$ 170 proteins. These include actin-bundling proteins, several members of the myosin-motor family, actin-filament capping proteins, membrane-anchoring proteins, and regulators of F-actin polymerization and contractility [193].

- Lamellipodium: an actively treadmilling actin filament network located beneath the plasma membrane at the leading edge of motile and growing cells [194, 195] (Fig. 1.6). The lamellipodium is a highly dynamic structure that requires a constant flux of G-actin monomers to maintain its protrusive activity. To this end, a variety of accessory proteins are required, such as capping proteins, ADF/cofilin and gelsolin (severing proteins), and profilin (monomer-sequestering proteins), among others. The lamellipodium is composed of a branched network of short actin filaments whose fast-growing barbed ends point on average in the direction of the leading edge [196, 197]. F-actin polymerization in this region is mainly driven by branching events from existing filaments through the activity of the Arp2/3 complex [164, 198, 199], which is activated by membrane-bound WAVE/Scar and N-WASP complexes [200, 201]. Membrane-anchored F-actin polymerases such as the formins and the Ena/VASP proteins [202] contribute to the lamellipodial F-actin pool as well, by generating parallel bundles of actin filaments called filopodia and microspikes. Besides aiding in the protrusive activity of the cell, these F-actin bundles are the *seeds* for the formation of stress fibers in the lamellum. The lamellipodium thus constitutes the main driver of membrane protrusion, since it orchestrates the force-generation of individual polymerizing actin filaments (with stall forces below 1 pN [203]), into protrusive machines that collectively generate forces in the order of hundreds of nanoNewtons [204].

- Lamellum: localized immediately behind the lamellipodium, the lamellum is a $\sim 5 - 10$ µm-wide structure in which the newly polymerized F-actin from the lamellipodium is reorganized into contractile acto-myosin bundles that align parallel to the leading edge of the cell [205] (Fig. 1.6). Concomitantly, the lamellum is rich in actin bundling and cross-linking proteins such as α-actinin, filamin, and myosin II [206, 207]. While eventually some of these bundles are incorporated into the stress fiber network of cells, their primary role in this region is to generate a zone of high contractility that disassembles the incoming F-actin network polymerized in the lamellipodium [208–212], thus driving retrograde actin flow [213]. What exactly triggers the transition from a lamellipodial- to a lamellar-like F-actin network is subject of debate. It has been proposed that adhesions to the

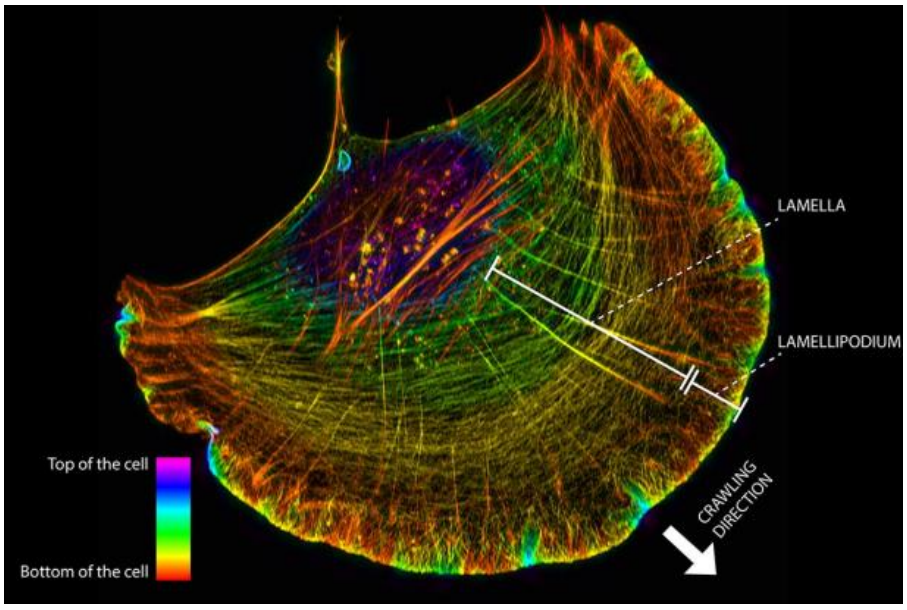

Figure 1.6: Multiplicity of F-actin structures in cells. Structured illumination microscopy image showing the diversity of actin filament structures in a crawling cell: in the lamellipodium at the leading edge of the cell, actin filaments are actively polymerized into a dense dendritic network interspersed with parallel bundles of actin filaments. These newly polymerized filaments are later on reorganized into contractile actin bundles in the lamellum. The combination of actin-filament polymerization at the lamellipodium and contractility in the lamellum drives retrograde actin flow. The contractile bundles of actin filaments created at the lamellum later on become dorsal actin arcs and actin stress fibers, which couple the cell to the extra-cellular environment. Figure taken from [220].

extra-cellular matrix might be responsible for this event, since the formation of adhesion sites co-localizes with the boundary between the two structures [195, 214]. Finally, cells with inhibited lamellipodial formation still exhibit leading-edge protrusion and migration. Thus, the individual roles of lamellipodium and lamellum in driving cell migration are not completely unraveled [215].

- Stress fibers: In the cell interior, actin filaments organize into an array of thick bundles that can at times span the whole length of the cell (Fig. 1.6). In motile cells, these bundles form through the accretion of actin filaments polymerized at the lamellipodium, and the recruitment of cross-linkers and myosin-II motors [216]. Depending on their localization and contractile properties, they can be classified into three types: Ventral stress fibers are myosin-II and α-actinin-rich anti-parallel bundles of F-actin that terminate at focal adhesion sites on each end. These bundles are under tension through myosin-contractility and are involved in focal adhesion maturation [217], and force-transduction to and from the cell exterior [218]. Dorsal stress fibers are non-contractile bundles of actin that are

anchored at a focal adhesion site on one end, and to transverse actin arcs on the other, while some are precursors of ventral stress fibers [216]. Finally, transverse arcs are contractile acto-myosin bundles localized on the dorsal surface of cells, which align parallel to the leading edge [216, 219]. Recent super-resolution live-cell microscopy studies on dorsal fiber and transverse arc dynamics revealed that myosin-powered contractility leads to actin-arc shrinkage and rearward flow [219]. This rearward flow pulls on dorsal stress fibers resulting in a flattened lamellar region [220]. In non-motile, epithelial and endothelial cells, stress fibers are also present and often terminate at cell-cell junctions [221, 222].

- Cytokinetic rings: A hallmark of dividing cells, the cytokinetic ring is a membrane-anchored contractile bundle of actin filaments, mainly polymerized by formins and cross-linked by myosin II motors, although many more key players of F-actin organization are present as well (i.e. α-actinin, septins, filamin, tropomyosin and the Arp2/3 complex [223]). The position of the cytokinetic ring defines the plane of cell division, and is tightly regulated through interactions between the actin and microtubule cytoskeletons. Although ring contraction is the main driver of cell constriction [224], actin-filament depolymerization has been shown to also contribute to this process [225].

The turnover of actin filaments is intimately related to the structures to which they belong. Studies of F-actin turnover in cells revealed that in quickly remodeling structures (i.e. lamellipodia) the actin-filament half-life is in the order of tens of seconds [226], while in more stable structures, such as stress fibers and the cytokinetic ring, the average half-life is in the order of minutes [227, 228]. The short life-times of actin filaments in actively remodeling regions in cells is the result of treadmilling combined with the activity of severing proteins such as gelsolin, which can accelerate actin-filament turnover two-fold [181].

1.1.4 Intermediate filaments (IFs)

Unlike F-actin and microtubules, intermediate filaments belong to a wide family of proteins, which in humans comprises approximately 70 different genes [229–231]. Among these, the most notable members are the cytoplasmic IFs: keratin (ubiquitous in epithelial cells), vimentin (ubiquitous in mesenchymal cells) and neurofilaments (ubiquitous in neuronal cells), and the nuclear lamins (which form a stabilizing meshwork adjacent to

the inner nuclear membrane and are present in all animal cells) [229, 232]. Intermediate filaments are expressed in most eukaryotes, with the most notable exceptions being plants and fungi. Cytoplasmic IFs are also absent from insects (with one known exception [233]), which do however express nuclear lamins.

Despite their genetic variability, the structure of intermediate-filament proteins is highly conserved. A single IF protein is an elongated molecule ($\sim$ 45 nm) which contains a central α-helical rod domain flanked on each side by non-helical head and tail domains that vary widely in length, sequence and structure [234] (Fig. 1.7). These monomers assemble in two sequential steps to form a tetramer, which is the basic soluble unit of IFs. First, two monomers assemble in an anti-parallel fashion to form a dimer, by association of the central rod domains into a coiled-coil structure [235]. This step is followed by the assembly of two dimers in a partially staggered anti-parallel fashion to form the tetramer. The tetramers are thus symmetrical, which renders intermediate filaments structurally apolar (Fig. 1.7). *In vitro* reconstitutions of vimentin polymerization have revealed that the soluble tetramers assemble into an $\sim$ 60 nm-long structure termed the unit-length filament (ULF) [235, 236]. Through end-to-end annealing, these ULFs polymerize into elongated filaments of $\sim$ 16 nm in diameter. The final step in IF assembly is a compaction event which shrinks the filaments down to a diameter between 7-11 nm [237, 238] (Fig. 1.7).

Unlike microtubules and actin-filaments, intermediate filaments in cells are rather long-lived. In general, IF depolymerization is a triggered event [239–242], such as in mitosis, where lamin phosphorylation leads to nuclear-lamina disassembly as required for nuclear-envelope breakdown [243]. Furthermore, there is evidence that IF proteins can be incorporated laterally onto existing filaments without the need for polymer disassembly [244]. Fluorescence recovery after photo-bleaching experiments have revealed that intermediate filaments have turnover times in the order of tens of minutes, while at the whole network level, the turnover times are in the order of hours [242, 244, 245] (Fig. 1.1). In cultured cells, the majority ($\sim 97 - 99\%$ [246]) of intermediate filament protein is typically found in polymerized form. However, it has been recently found that this balance strongly depends on the stiffness of the substrate on which the cells are plated [246].

Intermediate filaments are the softest of the three cytoskeletal polymers, with a persistence length of $\sim 0.5 - 1$ µm [247, 248] (Fig. 1.1). Their structural core, made up of aligned coiled-coil domains stabilized by strong hydrophobic interactions, provides IFs with remarkable mechanical properties [249]. For instance, individual IFs can be

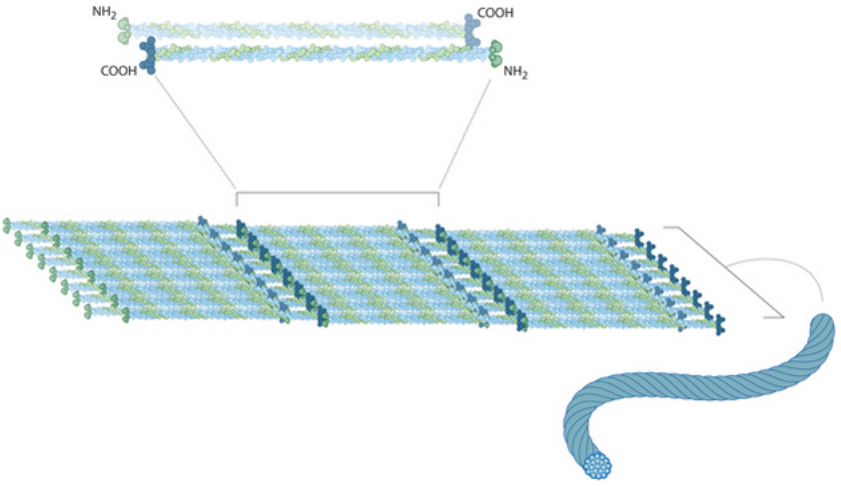

Figure 1.7: Steps in intermediate filament assembly. First, two monomers assemble into a dimer, by association of the central rod domains into a coiled-coil structure [235, 236] (not shown). Second, two dimers associate into a tetramer in a parallel staggered fashion to form a symmetrical tetramer that renders the intermediate-filament structure apolar. Third, through lateral associations the tetramers form a unit-length filament (ULF) [235, 236], which through end-to-end annealing with other ULFs polymerizes into intermediate filaments (IFs) with a ~ 16 nm diameter. The final step in IF formation is a compaction event (not shown), that shrinks the IF diameter down to $\sim 7 - 11$ nm [237, 238].

stretched up to 3.5-fold their original length without breaking [250]. Furthermore, rheological measurements on vimentin IF networks showed that IFs tend to become stiffer with increasing strain [251–253]. The mechanical resilience of intermediate filaments stems from their plasticity, as applied forces can induce partial unfolding and sliding of the individual subunits without triggering breakage or depolymerization [254].

Given their mechanical resilience, relatively slow turnover times, and the fact that IFs typically form well-connected networks of filaments and bundles that span the length of the cell [255–257] (Fig. 1.1), has led to the picture of intermediate filaments as being the mechanical integrators of cells. They are thought to provide mechanical stability against external forces, and also to integrate the much faster cytoskeletal-remodeling events carried out by microtubule and F-actin networks. Finally, as a consequence of their long life-times, IF networks can also act as scaffolds for many signaling pathways [258].

1.2 Cytoskeletal interactions

Cytoskeletal interactions between intermediate filaments, microtubules and F-actin are essential for eukaryotic cells to execute vital processes such as migration, growth, division and polarization [232, 259–262]. Historically, however, these three cytoskeletal systems have been studied independently, although the importance of their interactions has been long recognized [263, 264]. Some of the first direct evidence of microtubule-actin interactions came from *in vitro* reconstitutions with *Xenopus laevis* egg-extracts. In this studies, actin filaments were observed to consistently co-align and move with microtubules nucleated from demembranated *Xenopus* sperm cells [265, 266]. Conversely, microtubules were observed to inhibit cortical F-actin flows in *Xenopus* oocytes [267].

A chief obstacle in understanding how F-actin, microtubules and intermediate filaments affect each other's organization lies in identifying when and where in the cell they interact. This is largely due to the inherent crowdedness of the cell, the density of intermediate filament networks, the diversity of F-actin structures (i.e. stress fibers, filopodia, dendritic and cortical networks), and the complicated trajectories that growing microtubules follow (Fig. 1.1). Furthermore, in cells it is often challenging to disentangle mechanical cross-talk mediated by cross-linking proteins, from biochemical interactions mediated, for instance, by the Rho family of GTPases [268, 269]. Notwithstanding, several proteins and protein complexes capable of cross-linking all three polymer systems have been identified. Some of these form passive cross-links [270, 271]; while others mediate active connections, be it through molecular motors [272–275], actin filament nucleators [276, 277], or +TIPs [125, 278–280].

In this section we focus on interactions between actin and microtubules, and mention intermediate filament networks where it is due. We propose (inspired by a previous review [260]), that the many modes of actin-microtubule cross-talk can be narrowed down into distinct functional groups: 1) steric interactions, 2) passive cross-linking, 3) microtubule plus-end capture, 4) guidance of microtubule growth, 5) actin-filament nucleation, and 6) biochemical interactions (Fig. 1.8). We relate these modes of interaction to the basic mechanical and dynamic properties of actin and microtubule filaments, in order to understand the physical basis by which they modulate the activity of actin-microtubule cross-linkers.

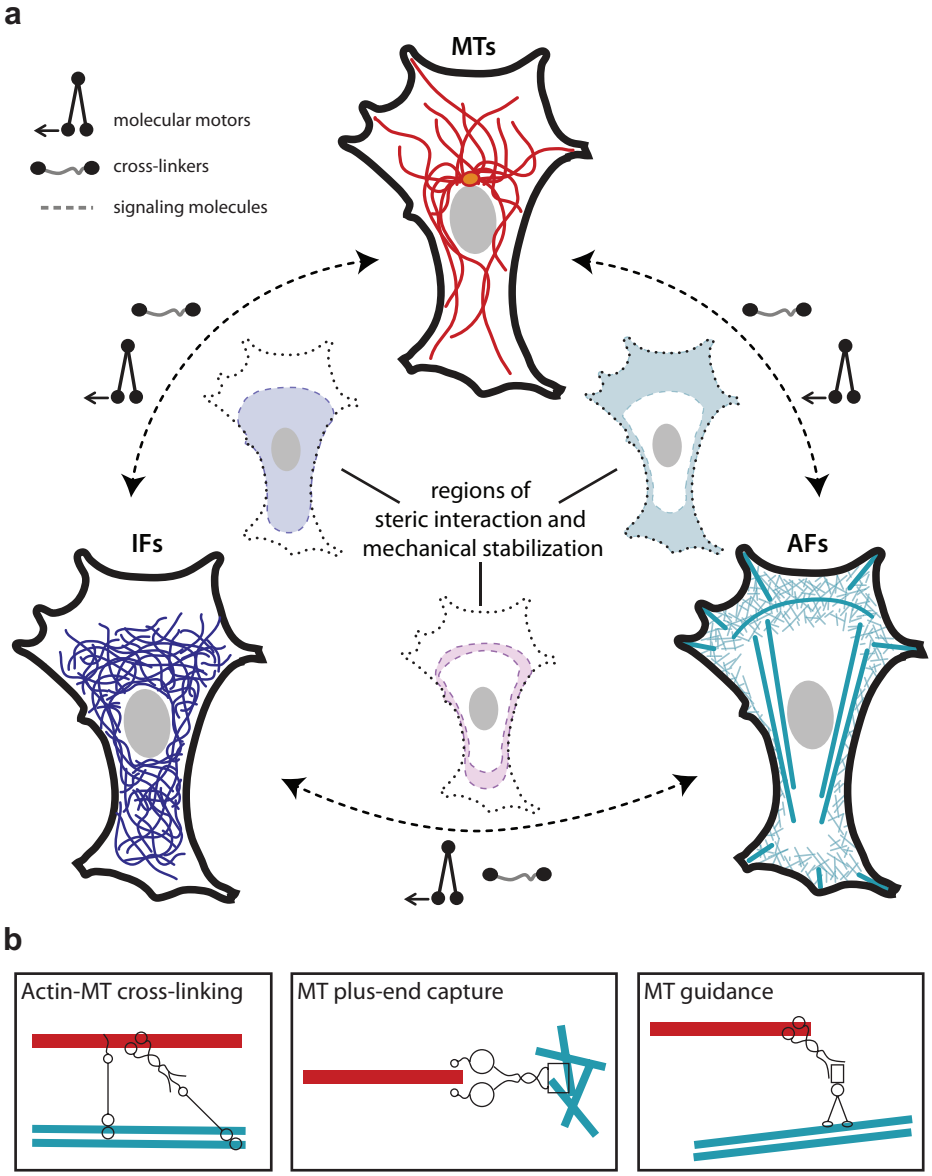

Figure 1.8: Cytoskeletal interaction modules. (a) Microtubule (MTs), actin filament (AFs) and intermediate filament (IFs) systems overlap in different regions of the cell. In these regions, steric interactions may play a key role. Furthermore, these systems can also interact through the activity of molecular motors, static cross-linkers, and biochemical signaling. (b) Different modes of cytoskeletal cross-talk between actin (cyan) and microtubules (red) that can be mediated by cross-linking proteins. Panel (a) was partially modified from [232].

1.2.1 Steric interactions and passive cross-linking

The simplest mode of cytoskeletal interaction would be where filaments, by nature of occupying space, sterically interfere with the mobility of neighboring polymers. These types of interactions, while oft-ignored, are likely to occur in regions where the cytoskeletal networks are densest (Fig. 1.8 a): at the cell interior (between IFs and microtubules), and in the cell periphery (between IFs and F-actin, and between microtubules and F-actin).

Steric interactions have a drastic impact on the organization and mechanical properties of cytoskeletal networks. A detailed picture of the mechanical reinforcement that steric interactions provide has come from *in vitro* rheological studies on composite polymer networks. For instance, the addition of a small number of microtubules to cross-linked F-actin networks promotes their non-linear stiffening [281]. This property stems from the high bending rigidity of microtubules, and it may be used by cells as a mechanism to respond to excessive deformation [281]. The addition of myosin-II molecules to these experiments revealed that contractile F-actin networks can on the one hand induce high-curvature microtubule buckling (as commonly observed in cells [282, 283]), while on the other hand mechanically reinforce the microtubules so that they can withstand higher compressive forces before breaking [284]. In a similar fashion, it has been shown that composite vimentin-actin networks have a higher stiffness than their isolated counterparts [285].

In cells, the role of steric interactions has also been probed by subjecting cells to external forces. Shearing cells by fluid flow has revealed that cells require the quick (minute time-scale) contractile response of F-actin networks in order to immobilize keratin intermediate filaments, which adjust their organization in the time-scale of hours [257, 286]. Further evidence has come from observations of F-actin-induced mobility of other cytoskeletal polymers. Both microtubules and intermediate filaments are often translocated by retrogradely-flowing and contractile F-actin networks [245, 287, 287–289]. For instance, in neuronal growth cones, translocating F-actin arcs push and compact microtubules into densely-packed bundles which are needed to stabilize the central structure of the growth cone [290, 291]. Furthermore contractile F-actin networks at the lamellum have been observed to buckle and break microtubules, a process required for proper microtubule turnover [282, 291, 292]. Conversely, during acute growth cone extension, persistent microtubule polymerization attenuates the rate of retrograde F-actin flow [293]. Similarly, intermediate-filament organization is highly dependent on the retrograde-flow transport process, as *de novo* filament formation often occurs at

the cell periphery, and these IF precursors need to be translocated to the cell interior to become incorporated into the cellular IF network [288]. Steric interactions also play a key role in plant cells, whose cytoskeletal cortical array is dominated by microtubules anchored to the plasma membrane [294]. These membrane-stabilized microtubules not only act as templates for further microtubule polymerization [295], but also guide F-actin polymerization [273, 296].

A likely example *in vivo* steric interactions, although passive cross-linkers could be also at play, involves the actin-driven inhibition of cytosolic flows required for the timely establishment of polarity in developing *Drosophila* oocytes. In this context, a cytosolic F-actin mesh nucleated by cappuccino and spire (*Drosophila* homologues of formins 1 and 2, and spire in humans, [297–299]), inhibits the mobility of microtubules driven by cytosolic flows generated via kinesin-1 vesicle transport [300]. In the absence of this F-actin mesh, microtubules are prematurely translocated to the cell cortex. Similar F-actin meshes are also used by large oocytes to orchestrate spindle-positioning and chromosome-condensation during meiosis [301, 302]. For instance, in mouse oocytes, a formin/spire-nucleated actin-mesh forms a cage around the spindle, and transports it towards the cell cortex through myosin-II pulling forces [303–306].

Thus, steric interactions on the one hand enable cells to synergistically utilize the mechanical properties of the three cytoskeletal systems to increase their mechanical stability, while on the other hand they act as a driving force for cytoskeletal turnover and organization. A chief requirement for steric interactions to play a functional role is that one of the cytoskeletal systems is mechanically reinforced in order to act as an efficient obstacle for other systems. In intermediate-filament and F-actin networks, filament cross-linking serves this purpose; while in the cortical microtubule arrays of plant cells, membrane-anchoring coupled with the high microtubule bending rigidity do the job.

The addition of passive cross-linkers further enhances the effect that steric interactions have on cytoskeletal mechanical stabilization. In this context, the plakins and spectraplakins are worth noting, as they often contain in one molecule binding sites for all three cytoskeletal polymers [307–309]. For instance, the *Drosophila* spectraplakin Shot cross-links composite bundles of F-actin and microtubules in tendon cells. Since *Drosophila* lacks cytoplasmic intermediate filaments altogether, in this context the actin and microtubule cytoskeletons are organized by Shot to provide mechanical support

and resistance against pulling forces [310]. Another well-known actin-microtubule cross-linker is the protein MAP2, which can bind to and bundle actin filaments and microtubules [311]. MAP2 is required for neuronal mechanical stability, and its actin-microtubule cross-linking ability is required for neurite initiation. This probably occurs by stabilizing the F-actin protrusive machinery via the mechanical rigidity of microtubules.

1.2.2 Microtubule plus-end capture at F-actin structures

Capture and stabilization of microtubule ends is an important requirement for cells to position the mitotic spindle and to maintain cytoskeletal organization during cell-migration and apico-basal polarization of epithelial cells [312–320]. Microtubule plus-end capture has been observed in cells through the action of minus-end directed dynein motors, as well as through +TIPs (Fig. 1.8 b). The fact that end-on forces slow-down microtubule polymerization and are potent triggers of catastrophe [92, 93], suggests that for efficient microtubule capture the proteins involved must somehow stabilize microtubules against full depolymerization, be it by promoting rescues or by inhibiting catastrophes.

The best studied example of cortical microtubule plus-end capture involves the minus-end directed motor dynein [321]. This interaction allows dynein molecules to participate in spindle positioning in small cells, by capturing and pulling on astral microtubules that span the length from the spindle poles to the cortex. The position of the spindle is a key determinant of the location of the cytokinetic ring, whose proper localization ensures the segregation of cell-fate determinants in asymmetric cell divisions [320]. The mechanisms by which dynein stabilizes microtubule ends have been elucidated through *in vitro* reconstitutions of microtubule end-on interactions with dynein molecules. These studies revealed that dynein can inhibit microtubule growth, trigger catastrophes, and exert pulling forces on shrinking microtubules, in an ATP-dependent manner [322, 323]. This requires that dynein can bind around the circumference of the microtubule, as dynein fails to stabilize microtubules against depolymerization in a gliding-assay configuration [322]. In cells, the cortical localization of dynein is dependent on a large protein complex (NuMa/LGN/Gαi), which is highly conserved across species and whose cortical distribution is tightly regulated [320, 324, 325]. The fact that the NuMa/LGN/Gαi complex binds directly to the plasma membrane (independent of F-actin), suggests that the acto-myosin cortex may rather serve to stabilize its membrane localization [326], thus allowing cortically-anchored dyneins to withstand the high forces that depolymerizing microtubules can exert ($\sim$ 70 pN [327]), without detaching.

Cortical capture of microtubule plus-ends at the leading edge of migrating cells, and in polarizing epithelia, can also occur in the absence of molecular motors. At the core of these interactions lies the +TIP APC [126, 328–332], which participates in different microtubule-binding complexes with EB1/3 and other members of the +TIP family; notably, CLASP, CLIP-170 and MACF. APC requires F-actin for its cortical recruitment [333], where it binds IQGAP [334] and formin [335]. In addition, APC also binds to the plasma membrane associated protein AMER1 [336, 337]. A variety of *in vivo* studies have revealed that APC and IQGAP act in concert to form a cortical scaffold for the recruitment of CLIP1-170 [338], CLASP [135], and MACF [339]. Although these three proteins rely on EB to track growing microtubule ends, they also have microtubule-lattice binding domains (Fig. 1.4), which are likely involved in their roles as microtubule stabilizing agents.

In vivo, CLASPs have been shown to accumulate along the microtubule lattice at the leading-edge lamellum and lamellipodium. These CLASP-associated *pioneer* microtubules [292] grow more persistently, but twice as slow, as microtubules in the cell interior [314, 315, 340]. CLASPs have also been observed to capture microtubules in the vicinity of focal adhesions (FAs), where they are anchored to the membrane by LL5β, a PIP3-binding protein [341, 342]. Microtubule capture at FAs is required for the establishment of the kinesin-dependent delivery of FA and extra-cellular matrix (ECM) degradation factors, thus ensuring cell-detachment and migration [343, 344]. *In vitro* reconstitutions of microtubule growth in the presence of the *S. pombe* CLASP homologue Cls1p, revealed that CLASPs mediate rescues in regions of the microtubule lattice where they are locally concentrated [345]. It has been postulated that CLASPs induce rescues by delivering tubulin dimers to the microtubule tip via their TOG-domains. Consistent with this, CLASPs are required for kinetochore-fiber elongation [346], and they enhance microtubule polymerization *in vitro* [347]. However, whether CLASPs can indeed recruit tubulin dimers to the microtubule tip has not yet been formally demonstrated. A second, more viable alternative could be that CLASPs, by nature of binding the microtubule lattice can somehow slow-down depolymerization, increasing the chance of microtubule rescue. The fact that CLASPs can induce microtubule bundling [348] and also stably anchor microtubule minus-ends at the Golgi-apparatus [38] supports this notion. Whether, as in the case of dynein [322], CLASPs must bind around the circumference of microtubules to effectively stop them from shrinking, is yet to be elucidated.

The role of CLIP-170 in microtubule stabilization is less clear. Some observations point at CLIP-170 being a rescue factor [349], while others suggest that CLIP-170 rather

acts as an anti-catastrophe factor [115, 350]. Electron-microscopy studies showed that CLIP-170 can induce the formation of tubulin oligomers [351]. It was thus proposed that CLIP-170 localizes to the microtubule tip by co-polymerizing with tubulin, and that this property allows it to enhance microtubule rescues by delivering tubulin to the microtubule tip. However, further *in vitro* reconstitutions showed that CLIP-170 requires both EB and tyrosinated α-tubulin to track and quickly-exchange at microtubule tips [115]. Furthermore, it was shown that CLIP-170 has a negligible effect on microtubule growth speeds (arguing against the co-polymerization model), and that it is not a potent microtubule rescue factor [115, 118]. Similar observations were made for the fission-yeast CLIP-170 homologue Tip1p, although a two-fold decrease in catastrophe frequency was reported [104]. These observations suggest that CLIP-170's microtubule lattice affinity may not be high enough to trigger microtubule rescues. One likely scenario could be that through its dual association with the microtubule lattice and EB, CLIP-170 enhances the residence time of EB on the microtubule-tip, and thus reduces the catastrophe frequency. Another possible scenario is that CLIP-170's *in vivo* role as a rescue factor involves its association with CLASPs [349].

MACF (also called ACF7 in mammals [279], and Shot in *Drosophila*) has also been implicated in microtubule capture at the leading edge of motile cells and in polarized epithelial cells [339]. Besides its APC-mediated cortical targeting, MACF also contains an N-terminal F-actin-binding domain which is required for its localization at F-actin-rich regions in the cell edge and at adherens junctions [123, 352]. The C-terminus of MACF contains a microtubule binding domain (MTBD) encompassing a GAR-domain and an SXIP-containing MtLS. C-terminal fragments of MACF have been observed to bind and stabilize microtubules against depolymerization *in vivo* [123, 125, 353, 354]. *In vitro* reconstitutions with MACF are notably lacking. However, the observation that MACF-localization in actin-rich regions correlates with elongated EB1 plus-end intensity profiles [123, 125] suggests that these proteins could act in concert to stabilize microtubules, possibly by creating an extended zone of binding to the microtubule lattice.

Finally, IQGAP and APC participate in yet another microtubule-capture and stabilization complex required for polarized cell migration [313]. This complex involves both EB and the F-actin polymerase and Rho-effector formin mDia1 [355–357]. IQGAP is required for the cortical localization of Rho-activated mDia1 [358], which in turn recruits EB and APC in a microtubule-dependent manner [335]. *In vitro* work has revealed that mDia1 and mDia2 directly bind microtubules through their FH1-FH2 domains, and in doing so can slow-down both microtubule growth and shrinkage

[355, 359]. This type of stabilization mechanism is potent and long-lived, as formin-associated microtubules accumulate post-translational modifications indicative of long-term stabilization [360]. The same microtubule-capture mechanism is present in budding yeast, where homologues of APC, EB and formin anchor astral microtubules at the daughter-cell cortex to position the spindle [280, 361–363]. In this context, cortically-anchored dynein is not required for microtubule plus-end capture, but rather to reel-in the spindle to the daughter cell after astral microtubules have been captured [363].

The multiplicity of microtubule-capturing complexes at F-actin structures, many of which are to some extent orchestrated by the APC/IQGAP scaffold, suggests that perhaps not one mechanism is sufficient, but rather that cells utilize them in concert. A mechanistic understanding of the ways by which these microtubule binding +TIPs differentially participate in microtubule capture and stabilization at F-actin structures is still lacking.

1.2.3 Guidance of microtubule growth by F-actin structures

Contrary to the effects that retrogradely-flowing and contractile F-actin networks have on microtubule organization in cells, which can both translocate and induce microtubule breakage [282, 292], bundles of F-actin seem to act as positive guides for microtubule growth (Fig. 1.8 b). From a mechanical standpoint, there are three requirements for successful microtubule guidance: first, capture and stabilization of the microtubule tip, second, mechanical deflection of the stiff microtubule lattice by the F-actin bundle, and third, that the microtubule and F-actin bundle remain associated. The best studied examples of microtubule guidance occur in crawling cells and growing neurons, where microtubule growth is targeted along actin-stress fibers in the cell interior, and along actin bundles inside filopodia at the growth-cone periphery. In mammalian cells this guidance is mediated by the +TIP MACF, whose homolog in *Drosophila* is called Shot [279, 354].

As explained above, guidance of microtubule growth by stress fibers is required for microtubules to be captured in the vicinity of FAs by CLASPs, where they become tracks for the delivery of FA and ECM degradation factors to ensure cell detachment and motion [279, 342–344, 364–367]. A key aspect of this process remains unanswered: namely, what the mechanical constraints are for successful capture and redirection of microtubule growth. Studies of cells plated on adhesive micro-patterns have revealed that microtubules can undergo sharp deformations upon encounters with a stress fiber,

and that they remain attached to the fiber as they continue to grow [368]. This suggests that cross-linking proteins must be present not only at the microtubule tips, but all along the actin-microtubule interface, in order to maintain their tight association. However, MACF is not particularly enriched along stress fibers, but rather has been observed to localize at microtubule growing ends and in actin-rich regions in the cell edge and near FAs [279]. Two scenarios are thus possible: one, that the subset of microtubules that are captured is at least already partially co-aligned with the stress fiber; or two, that MACF's interaction with the stress fiber is dependent on the presence of an overlapping microtubule. The second scenario is supported by recent evidence that Shot can adopt an auto-inhibited conformation in which only its MtLS is exposed. This observation suggests that encounters with F-actin structures may release the auto-inhibition, thus exposing Shot's actin-binding and microtubule-binding domains [369].

In neuronal growth cones, guidance of microtubule growth by filopodia is required for axonal extension [124, 291, 354]. In this context, microtubules have been implicated in dictating the direction of growth, as local microtubule stabilization by taxol induces growth-cone turning in the direction of drug application, while local depolymerization with nocodazole has the converse effect [370]. However, the precise ways by which invading microtubules aid the actin protrusive machinery are not yet clear. Since growth-cone advance is inversely proportional to the rate of actin retrograde flow [213], one possibility is that invading microtubules act as mechanical *struts* against retrograde flow. Microtubules that co-align with filopodia often remain attached to, and are translocated rearwards by, the polymerizing F-actin bundle, resulting in short-wavelength microtubule buckling [291]. Similar observations of microtubule buckling in cells have revealed that the elastic environment provided by the surrounding F-actin networks can aid microtubules to withstand compressive forces in the order of tens to hundreds of picoNewtons [283, 371]. This range of forces may be sufficient to at least locally slow-down retrograde actin flow [372], and thus promote forward motion. Yet another lingering question in this context regards the ways by which microtubules selectively invade the peripheral zone of the growth cone along filopodia, since in conditions where filopodia are removed without disturbing the surrounding dendritic F-actin network, microtubules are observed to better-invade the peripheral zone [373]. Recent observations suggest that the +TIP drebrin, which localizes at the filopodial-base, may act as a gate to guide microtubules along bundles [270].

In the above-mentioned examples, microtubule guidance occurs by F-actin bundles that are anchored to their surrounding environment: in the case of stress fibers through adhesions to the ECM; and in the case of filopodia by the neighboring lamellipodial

actin meshwork. However, instances of microtubule guidance exist in which the F-actin bundle is not mechanically anchored to its surroundings. The best-studied example of this occurs in budding yeast, where microtubule growth is guided through the action of the +TIP Kar9 (the yeast homolog of APC), which binds microtubule ends via Bim1 (the yeast homolog of EB1), and which is also associated with the myosin V myo2, which guides the microtubule tip along actin cables polymerized at the cell cortex by the formin bni1 [272, 280, 361, 363, 374, 375]. Given that Bim1, like EB1, quickly exchanges at microtubule tips poses the problem of microtubules losing the connection with the actin cables. Recent *in vitro* reconstitutions of microtubule guidance by template microtubules through plus-end tracking kinesins could shed some light on this process [376, 377]. In these experiments, the locally enhanced concentration of motors at microtubule tips generated by EB1 was sufficient for microtubules to remain attached and even sustain deflections as they polymerized along template microtubules. This occurred up to a point, since at encounter angles above 90° the ability to guide microtubule growth strongly depended on the force required to bend the growing microtubule. This mechanical constraint may play a lesser role in microtubule guidance by actin cables in yeast, which are free to fluctuate, thus allowing the growing microtubule to force the F-actin bundle to move as the microtubule follows.

Finally, guidance of microtubule growth has also been observed by non-bundled F-actin structures. For example, microtubules often enter actin-rich neuronal protrusions such as dendritic spines and axonal branches [378]. The fact that in dendritic shafts and axons microtubules are tightly packed and bundled, raises the question of how they turn and enter these protrusions in the first place. In this context, septins seem to serve the role of microtubule stabilizers and guides. Septins are GTP-binding proteins, which assemble into filamentous structures that are often associated with F-actin structures near the plasma membrane [379]. Septin7, which accumulates at the base of axonal branches [380], is involved in redirecting microtubule growth into these branches [381]. Similarly, in polarizing epithelia, microtubule growing ends follow, and are captured by, septin filaments made up of the Septin2-6-7 hetero-hexameric complex [382]. To date, however, the mechanisms by which septins associate with microtubules, and how this association can result in microtubule stabilization and guidance, are not yet clear.

1.2.4 Positioning sites of F-actin polymerization by microtubules

Besides physically interacting with F-actin, microtubules are also involved in positioning sites for F-actin nucleation and polymerization. For instance, growing microtubules can trigger the formation of intrapodia, which are traveling waves of actin polymerization at the leading edge of motile cells, structurally similar to the actin *comet-tails* used by many pathogens to power their motion in the cell interior [383, 384].

The best studied examples of microtubule-mediated F-actin nucleation occur in budding and fission yeast, where microtubules that contact the cell-cortex help recruit the protein bud6, a binding-partner and activator of formin (bni1 and for3, in budding and fission yeast respectively), which results in actin-cable formation [375, 385–387]. This process is required for maintenance of cell polarity and shape, as formin-nucleated actin cables serve as tracks for the delivery of cellular growth factors [385, 388, 389]. Although bud6 directly interacts with the APC-homologues kar9 and tea1 (in budding and fission yeast, respectively) [390], recent work suggests that this interaction is not required in this context, as direct interactions between bud6/tea1 and the yeast EB1 homologues (Bim1p and Mal3 in budding and fission yeast, respectively) are sufficient to capture microtubules at the cortex [391–394].

EB1, APC and mDia1 have also been implicated in the polymerization of F-actin bundles that emanate from the cell cortex towards the cell interior [335]. Similar to their yeast counterparts, it is not clear whether their role in enabling microtubule capture at the cell cortex collaborates with, or inhibits the polymerization of F-actin by mDia1 [359]. mDia1 binds both microtubules and F-actin via the formin-homology domain, FH2 [357, 395, 396], and recent work indicates that microtubule-binding by mDia1 (and mDia2) inhibits their ability to polymerize F-actin [395]. Furthermore, *in vitro* reconstitutions of F-actin polymerization with mDia and APC revealed that APC enhances mDia-dependent actin polymerization, but that these proteins eventually detach as APC remains associated with the pointed end of the filament, while mDia moves with the polymerizing barbed end [397, 398]. Further *in vitro* studies will thus be required to elucidate how interactions between EB1, APC and the different formins are orchestrated to induce on the one hand microtubule capture and stabilization at the cell cortex, and on the other, F-actin polymerization [399].

1.2.5 Interactions through biochemical signaling

Last but not least, microtubules and F-actin profoundly affect each other's organization through biochemical signaling pathways. In this context, chief players are the RhoA, Rac1 and Cdc42 members of the Rho-family of GTPases [269, 400, 401], and the protein kinase GSK3β, all of which have been implicated in regulating actin and microtubule organization and dynamics in cells. Rho GTPases are active when bound to GTP and localized at the plasma membrane, while induction of GTP-hydrolysis through GTPase-activating proteins (GAPs) renders them inactive. Conversely, Rho GTPase re-activation occurs via guanine-nucleotide exchange factors (GEFs). Inactive Rho GTPases can be also sequestered in the cytosol by guanine nucleotide dissociation inhibitors (GDIs). The main actin-related functions of RhoA, Rac1 and Cdc42 can be generally grouped into three categories.

RhoA and acto-myosin-based contractility: RhoA achieves myosin-II activation in two ways. First, through activation of myosin light-chain kinase (MLCK), which phosphorylates the myosin light-chain (MLC), leading to myosin-II activation and contractility. Second, through activation of Rho-kinase (ROCK) which, by phosphorylating myosin light-chain phosphatase, inhibits MLC dephosporylation. RhoA-induced myosin contractility in turn triggers stress fiber and cytokinetic ring assembly. Additionally, RhoA can bind to, and activate, the formin mDia1, leading to filopodial formation [402–405].

Rac1 and lamellipodial formation: Rac1 binds to and activates the SCAR/Wave complex, which in turn activates the Arp2/3 complex, thus triggering the formation of lamellipodial F-actin networks near the plasma membrane [406].

Cdc42 and filopodial and lamellipodial formation: Cdc42 binds to, and activates, some formins (such as mDia2), resulting in the formation of filopodial extensions. In addition, Cdc42 activates both Rac1 and the Arp2/3 activator N-WASP, and is thereby also involved in the formation of lamellipodia [201, 407].

Coupled to their roles as orchestrators of F-actin architecture, RhoA, Rac1 and Cdc42 are also involved in mediating actin-microtubule coordination; for instance, in order to establish and maintain a polarized cytoskeleton during cell migration [261, 269, 401, 408].

The first evidence of Rho GTPase-mediated cytoskeletal coupling came from the observation that nocodazole-induced microtubule depolymerization leads to enhanced stress fiber networks, as a result of RhoA activation [366]. Microtubules modulate RhoA activity by sequestering RhoA GEFs along their lattice, which are released upon

microtubule depolymerization [129, 409]. Conversely, RhoA binds to, and activates, the formin mDia1, which together with APC is required to capture and stabilize microtubules that reach the cell cortex [355, 387, 410, 411]. In neuronal growth cones it has been shown that Rho kinase activation by RhoA is required to generate contractile actin bundles, which in turn create a compact bundle of microtubules that stabilizes the growth cone [293]. Yet another example of RhoA mediated cross-talk occurs during mitosis, where microtubules help determine the position of the cytokinetic ring by defining a region of locally concentrated active RhoA at the cell cortex [412].

Rac1 and Cdc42 have also been implicated in microtubule stabilization [413]. Active Rac1 and Cdc42 are required to localize IQGAP at the leading edge of motile cells, where it participates in the recruitment of several microtubule-capturing proteins such as APC, CLIP-170 and CLASP [334, 335, 338]. Conversely, microtubules at the leading-edge are required for Rac1 activation [268], and it has been further shown that APC stimulates the activity of a Rac1-specific GEF, Asef [414]. Conversely, Rac1-mediated lamellipodial activity is also involved in microtubule turnover, which stems from enhanced microtubule breakage at the contractile lamellum [413].

Finally, one emerging player in the field of actin-microtubule cross-talk, particularly during cell migration, is the protein kinase GSK3β (glycogen synthase kinase 3β) [415]. GSK3β has been shown to phosphorylate a variety of microtubule +TIPs that are normally required for cortical microtubule capture at the leading-edge of motile cells, and thus ensure cell polarity and persistent motility. Phosphorylation by GSK3β typically inhibits their ability to bind EB. However as many SXIP-motif containing +TIPs contain multiple phoshorylation sites, the effect of GSK3β is often cumulative [107]. Notable GSK3β targets are: APC [330, 416], CLASP [135, 315, 417], and MACF [339, 418]. Finally, GSK3β is inhibited at the leading edge of motile cells through Cdc42 activation of the Par6-atypical protein kinase [419].

Thus, biochemical regulation by members of the Rho-family of GTPases and GSK3β plays a defining role in the establishment and maintenance of cytoskeletal polarity during cell migration. One open question is how these different cytoskeletal regulators are spatially controlled to effect their functions at the correct cellular sites [400]. Recent work has revealed that, while RhoA is activated at the leading edge of motile cells, Rac1 and Cdc42 become active a few micrometers behind, suggesting that their activation is spatio-temporally regulated during cell migration [420].

1.3 Multiple roles for the cytoskeletal coordination toolbox

The same tools that cells use to polarize their cytoskeleton during migration are often put to use in entirely different contexts, thus revealing novel functions. For instance, during mitosis, EB, APC, CLASP and CLIP-170 are all required for the maintenance of kinetochore-microtubule attachments [102, 346, 421–426]. In polarized epithelial cells, APC, EB1 and MACF have also been implicated in the maintenance of polarized actin and microtubule cytoskeletons. In this context, APC and EB1 anchor and organize the basal microtubule network, where they do not act as +TIPs but rather localize to the microtubule lattice [427]. Similarly, EB1 and MACF are required for the formation of apico-basal composite bundles of F-actin and microtubules [428], and in the establishment of parallel arrays of microtubules anchored by APC in *Drosophila* tendon cells [310]. Moreover, cells often use a combination of interaction modules to properly organize their cytoskeleton. For instance, astral microtubule capture by cortically-anchored dynein is a requirement for proper spindle positioning [320], while acto-myosin cortical flows aid in this process by *dragging* the cortex-anchored dyneins to the sides of the cell, thus helping in centrosome separation [429].

1.4 Motivation and thesis outline

The multiplicity of actin-microtubule cross-linkers found in cells, their often overlapping localization, and the fact that they seem to behave differently depending on the cellular context is, to say the least, puzzling. Reconstituted model systems using purified proteins are ideally suited to unravel these issues, as they can separately address biochemical and mechanical interactions, and identify the minimum requirements to achieve a certain functional organization. Not surprisingly, *in vitro* reconstitutions have played a fundamental role in our current understanding of the cellular cytoskeleton [430–432].

However, despite the wealth of evidence that actin-microtubule crosstalk is vital for cellular function, to date, *in vitro* reconstitutions of actin-microtubule interactions are still rare. Notable exceptions include studies on the mechanical properties of composite actin-microtubule networks [281, 284], molecular motor motility at actin-microtubule cross-roads [433, 434], and observations of actin-microtubule co-alignment both with *Xenopus* egg-extracts [265, 266], and purified proteins [435]. However, *in vitro* studies

of the interaction between dynamic microtubules and F-actin are notably lacking. This is unfortunate, given that actin-microtubule coordination is to a very large extent mediated at the growing microtubule end, where EB acts as the organizing hub.

This thesis thus describes the development and characterization of a simplified *in vitro* model to study interactions between dynamic microtubules and F-actin. To this end, we engineered a cross-linking molecule, which we called TipAct, that can bind to F-actin directly and also localize at growing microtubule ends via EB. We subjected microtubule growth to different F-actin organizations, with and without TipAct. This was done in order to elucidate the separate contributions of steric and cross-linker-mediated interactions in dictating actin-microtubule coordination, and also to find out the ways by which the mechanical properties of pre-existing cytoskeletal architectures modulate the activity of actin-microtubule cross-linkers. The thesis is thus organized as follows:

In Chapter 2, we describe the general experimental methods applicable to all the *in vitro* assays described in this thesis. In order to work with dynamic microtubules and actin filament structures, cross-linked via fluorescently-labeled EB and TipAct molecules in solution, we developed a variety of surface assays amenable for total internal reflection fluorescence (TIRF) microscopy and quantitative image analysis.

In Chapter 3, we describe the design, purification and characterization of TipAct. To this end, we measure its actin binding affinity, and monitor its localization in cultured cells. We show that both in cells and *in vitro*, TipAct binds actin filaments, and localizes at growing microtubule ends in an EB-dependent manner. Furthermore, we show that even though TipAct has a low affinity for F-actin, when locally concentrated at microtubule tips it can efficiently link microtubules to actin filaments. Finally, we demonstrate that TipAct's actin-binding domain is insensitive to actin filament polarity.

In Chapter 4, we study the effects that actin bundle architectures can have on microtubule organization. We find that microtubule growth can be guided by F-actin bundles via two distinct mechanisms: steric deflection, when TipAct is absent, or through a capture and zippering mechanism, when TipAct is present. We show that despite its low affinity for single actin filaments, TipAct stably binds F-actin bundles and also recruits EB to the bundles. Through fluorescence recovery after photo-bleaching (FRAP) experiments, we confirm that the off-rates of TipAct and EB at actin-microtubule overlaps are reduced. These observations explain the efficiency of the capture and zippering mechanism (via TipAct), in guiding microtubule growth. Finally, we demonstrate that TipAct enables parallel arrays of F-actin bundles to globally dictate microtubule organization.

In Chapter 5, we describe the effects that growing microtubules can have on F-actin organization. To this end, we reconstitute interactions between dynamic microtubules and mobile actin filaments and bundles. We show that cross-linking via EB and TipAct can lead to both F-actin bundle and microtubule deformation as they interact. Further, we find that TipAct allows growing microtubules to transport freely-diffusing actin filaments, and to pull on actin filaments partially tethered to a glass surface. In addition, we show that when microtubules interact with two or more actin filaments, they can create F-actin bundles which subsequently recruit TipAct and act as guides for microtubule growth. Finally, we demonstrate that a radial array of microtubules (nucleated from a centrosome) can drastically reorganize an otherwise isotropic solution of actin filaments.

In Chapter 6, we study the TipAct-mediated transport of soluble actin filaments by growing microtubules. To this end, we reconstitute interactions between dynamic microtubules and single actin filaments in solution. Concomitantly, we develop a model of biased diffusion of actin filaments at microtubule tips, in order to explain the transport phenomenon. We further compare the model predictions to experimental data on actin filament transport for variable EB, TipAct and tubulin concentrations, and find a close agreement between simulations and data. Finally, we find that the biased-diffusion mechanism of actin filament transport, potentially generates forces in the picoNewton range, which are comparable to those generated by molecular motors in cells.

In Chapter 7, we give a brief conclusion and an outlook for future work.

Chapter 2

General experimental methods

2.1 Introduction

The majority of the assays in this thesis involved *in vitro* reconstitutions with dynamic microtubules and pre-polymerized actin filaments. These were typically immobilized on a glass surface and imaged by total internal reflection fluorescence (TIRF) microscopy. This chapters outlines the general methods applicable to all the *in vitro* assays described in this thesis.

2.2 Flow cell preparation and surface functionalization

To minimize non-specific binding of fluorescent proteins to the glass, hence to avoid too much background signal, we made use of thoroughly cleaned glass slides and coverslips, which were then functionalized through a variety of techniques.

2.2.1 Glass cleaning

Glass coverslips were cleaned in *base piranha* solution, a safer alternative to *acid piranha* solution that only becomes reactive when heated at or above 60°C. Storing the cleaned coverslips in a 0.1 M KOH aqueous solution activated hydroxyl (OH^-) groups on the

glass surface [436], giving the surface a net negative charge which was needed for later functionalization steps.

Base piranha was prepared under the fume hood by mixing Milli-Q water, 30% H_2O_2, and 30% NH_4OH at a 5:1:1 volume ratio in a glass beaker sufficiently large to fit a Teflon® rack holding the coverslips. The mixture was then heated to 75°C on a hot plate with continuous stirring using a magnetic bar. Meanwhile, the coverslips were rinsed twice, 5 min each, with Milli-Q water (Merck Millipore, Billerica, MA, USA) in a bath sonicator. Once the base piranha solution reached a temperature of 75°C, the Teflon® rack holding the coverslips was inserted into the beaker. After a 15 min incubation at 75°C, the coverslips were removed and rinsed in Milli-Q water in a bath sonicator for 5 minutes. The coverslips were finally stored at room temperature (RT) in a 0.1 M KOH solution until use, for up to one month.

Glass slides were cleaned in a slightly less rigorous fashion, by sequential bath-sonication steps (20 min each) in 0.1% (v/v) aqueous solution of Hellmanex™, 100% acetone, and 70% ethanol, with two 5 min rinses in Milli-Q water in between each step. Thereafter, the Teflon® rack holding the coverslips was transfered to a beaker containing a 0.1 M KOH aqueous solution for storage, and the slides were used for up to one month.

2.2.2 Flow cell preparation

Flow cells with ∼10 µl channels were assembled with strips of Parafilm® sandwiched between a cleaned glass slide and coverslip (Fig. 2.1).

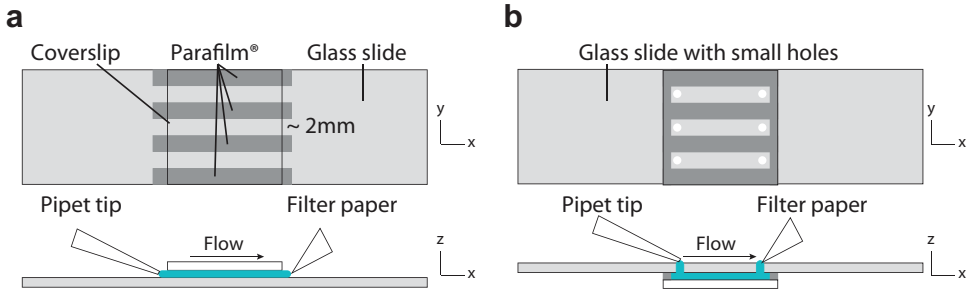

Figure 2.1: Two types of flow cells. Schematic of the two types of flow cells used. The flow cell in (b) can be used to monitor the effects of solution exchange on an inverted microscope stage.

First, a cleaned glass slide and coverslip were retrieved from the 0.1 M KOH storage solution and rinsed in a bath sonicator for 5 min in Milli-Q water. Meanwhile, using

a glass slide as a ruler, three ∼2 mm-wide and ∼2.5 cm-long channels were cut out from a piece of Parafilm®. The channels were spaced far enough so that they fit comfortably within the coverslip. Thereafter, the glass was retrieved and blow-dried with pressurized N_2 gas, and the Parafilm® placed between coverslip and glass slide. To melt the Parafilm®, the assembled flow cell was placed for ∼10 s on a 120°C hot-plate, while applying even pressure by placing a glass slide and a small metal weight on top. After this step, the surface functionalization was started right away.

For assays in which solutions had to be exchanged during the experiment, glass slides perforated with ∼ 1mm-diameter holes (spaced 20 mm apart to fit within a 2" coverslip, Fig. 2.1 b) were used. The Parafilm® channels and coverslip were mounted on these glass slides such that the holes became the entry and exit points of the channel. In this way, all solutions could be flowed in and out from the side of the glass slide, while the flow cell was already mounted on the microscope stage (Fig. 2.2).

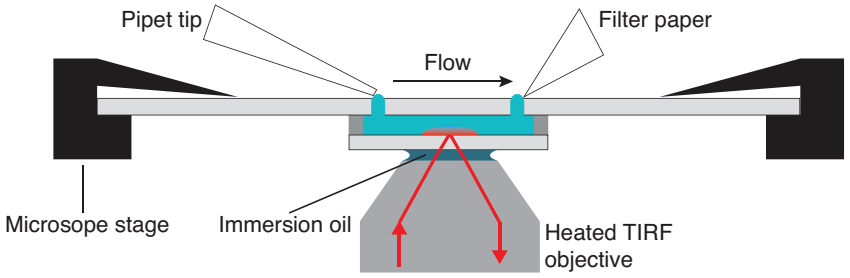

Figure 2.2: Monitoring solution exchange on the microscope stage. Schematic of solution exchange on an inverted microscope stage using the flow cell type described in Fig. 2.1 b.

2.2.3 Biotinylated and centrosome-coated surfaces

Biotin and streptavidin linkages were the main way by which we immobilized individual proteins, microtubules or actin filaments onto the coverslip surface (Fig. 2.3 a). First, the assembled flow cell channels were coated with the block co-polymer poly(L-lysine)-graft-poly(ethylene glycol) functionalized with a biotin tag (PLL-PEG-Biotin, SuSoS AG, Dübendorf, Switzerland), at a concentration of 0.2 mg/ml in MRB80 (80 mM PIPES pH 6.8 with KOH, 1 mM EGTA and 4 mM $MgCl_2$). After a 30 - 60 min incubation, the channel was rinsed with 50 - 100 µl of MRB80. Thereafter, a 50 - 100 µg/ml solution of streptavidin (or NeutrAvidin™) in MRB80 was added. After a 10 min incubation, the channel was rinsed as above. Finally, any hydrophobic patches left on the glass surface

were blocked by adding a 0.5 mg/ml solution of κ-casein in MRB80, followed by a 1% (w/v) solution of Pluronic® F-127 also in MRB80. The flow cell was incubated with each solution for 10 min, with 50 - 100 µl MRB80 rinses in between. After this step, the glass surface was ready to bind biotinylated microtubule seeds or actin filaments (Fig. 2.3 a).

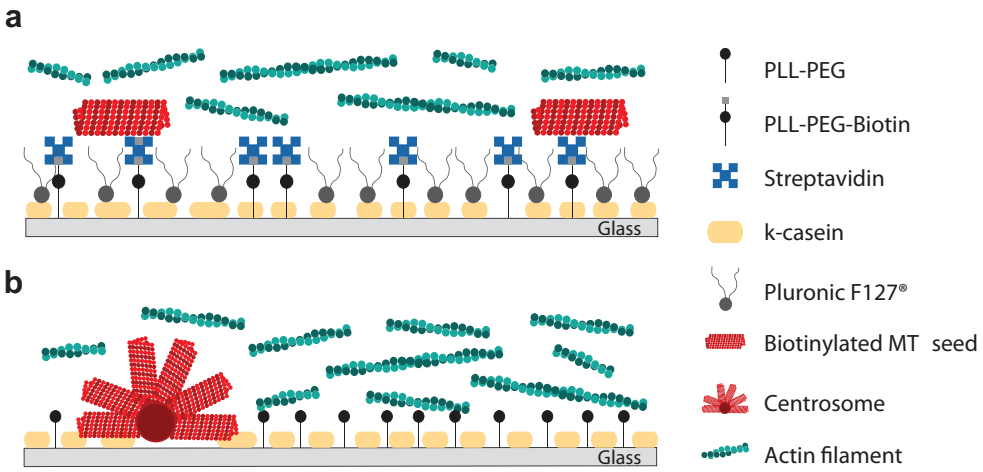

Figure 2.3: Different surfaces for microtubule nucleation. Schematic of the surface functionalization for *in vitro* assays of microtubule polymerization from GMPCPP-stabilized microtubule seeds (a), and from centrosomes (b).

For assays with centrosomes, since they can adhere non-specifically to the glass surface, the flow cell surface preparation was different (Fig. 2.3 b). First, the centrosome solution, normally stored at −80°C, was warmed to 37°C for 10 min and gently diluted in MRB80 at RT to the desired concentration. Thereafter, centrosomes were added to the flow cell, and incubated for 5 min to allow them to adhere to the surface. After a 50-100 µl rinse in MRB80, a 0.2 mg/ml PLL-PEG (SuSoS AG, Switzerland) solution in MRB80 was added, and incubated for 10 min. Finally, hydrophobic patches were blocked by flowing in 50-100 µl of a solution containing 0.1 mg/ml κ-casein and 1% (w/v) Pluronic® F-127 in MRB80. After a 15 minute incubation, the flow cell channel was rinsed one last time and used straight away.

2.3 Buffer conditions to work with actin filaments and dynamic microtubules

Traditionally, *in vitro* assays with F-actin and microtubules have been performed in radically different buffers [11, 437]. We found that MRB80 (80 mM PIPES pH 6.8 with KOH, 1 mM EGTA and 4 mM $MgCl_2$), a variant of BRB80 (otherwise known as Brinkley Reassembly Buffer) that is generally used for microtubules [8], had sufficiently high ionic strength to trigger F-actin polymerization. Conversely, we found that microtubule polymerization did not proceed in the canonical F-buffer (20 mM HEPES pH 7.4 with KOH, 1 mM EGTA, 2 mM $MgCl_2$ and 50mM KCl), which is likely due its lower ionic strength and higher pH [11]. We thus used MRB80 as the buffer for all the assays described here. For excellent guides on buffers suitable for *in vitro* biological research, we refer the reader to the following references: [438, 439].

2.3.1 Phalloidin-stabilized actin filaments

In all the *in vitro* assays presented here, we made use of pre-polymerized F-actin containing a small fraction of labeled G-actin. For the experiments with single actin filaments (Chapters 3, 5 and 6) or actin bundles (Chapters 4 and 5), phalloidin-stabilized F-actin was polymerized at a $1.0 - 1.5$ µM final G-actin concentration. For the experiments with centrosomes and single filaments (Chapter 5), G-actin was polymerized at 30 µM G-actin concentration.

To produce fluorescently labeled actin filaments, two separate solutions were prepared: First, a G-actin mix containing $\sim 12-15$ % G-actin labeled with Alexa Fluor® 488, 594 or 647 (Molecular Probes, Life Technologies, Carlsbad, CA, USA), which was kept on ice for 5 min. Second, an F-actin polymerization mix containing 5 mM DTT, phalloidin at an equimolar ratio to the final G-actin concentration, 50 mM KCl and 0.2 mM ATP in MRB80. To trigger F-actin polymerization, the F-actin polymerization mix was added to the G-actin mix, vigorously pipetted, and incubated for ∼1 hr at RT in the dark, to avoid photo-bleaching. The resulting solution of actin filaments was used up to five days after polymerization.

2.3.2 GMPCPP-stabilized microtubule seeds and centrosomes

With the exception of the experiments with centrosomes (Chapter 5), in all assays presented here we nucleated microtubules from surface-immobilized microtubule seeds. These microtubule seeds contained 12 % of fluorescently-labeled and biotinylated tubulin subunits, and were stabilized against depolymerization with the slowly-hydrolyzable GTP analog guanylyl-(α, β)-methylene-diphosphonate (GMPCPP [50]).

To obtain seeds of approximately 5 µm in length, the following steps were followed: a 20 µM tubulin mix was prepared in MRB80 which contained 70 molar percent of unlabeled tubulin (Cytoskeleton, Denver, CO, USA), 18% biotinylated tubulin (Cytoskeleton, USA) and 12% tubulin labeled with either TRITC Rhodamine, HiLyte®488 or, HiLyte®635 (Cytoskeleton, USA). To remove aggregates, the tubulin mix was centrifuged at 149,000 g for 5 min at RT with the use of an Airfuge® ultracentrifuge (Beckman Coulter, Brea, CA, USA). To trigger microtubule polymerization, GMPCPP was added to the supernatant to a final concentration of 1 mM, and the tubulin mix was incubated at 37°C for $30 - 40$ min. After this incubation step, the microtubule seeds were pelleted as above and resuspended in MRB80 to a final 20 µM tubulin concentration, assuming that 80% of the tubulin was recovered.

More stable seeds that can be frozen and stored at −80°C were produced by adding a cycle of depolymerization ($\sim$ 20 min on ice) after the second centrifugation step, followed by re-polymerization at 37°C with fresh 1 mM GMPCPP added, in order to replace more of the GDP-tubulin with GMPCPP-tubulin [436]. After the second polymerization step, these 'doubley-cycled' seeds were pelleted as before, and resuspended in MRB80 containing 15% (v/v) glycerol, to a final concentration of 5 µM tubulin (assuming 80% recovery after each centrifugation step). Thereafter, the seeds were aliquoted in $\sim$ 5 µl volumes, flash-frozen in liquid N_2 and stored at −80°C until use.

For daily use, the GMPCPP-stabilized microtubule seeds were kept in the dark at RT, and were used within two days of preparation (or thawing), since with time they tended to anneal and get longer. In a typical assay, GMPCPP-stabilized microtubule seeds were added to the flow cell at the equivalent concentration of $50 - 60$ nanomolar tubulin concentration, in a solution containing 0.1% (v/v) methyl-cellulose in MRB80, to help bring them close to the glass surface.

Centrosomes were purified by Florian Huber and Sophie Roth, with the generous help of Claude Celati (Institut Curie, Section Recherche, UMR144-CNRS, 75005 Paris, France),

from human lymphoblastic KE37 cell lines. They were stored in a 30% (w/v) sucrose solution in MRB80, in a liquid N_2 tank.

2.4 Microtubule polymerization and tip tracking assays

A minimal mixture for microtubule polymerization should contain tubulin, GTP, a surface blocking agent, an oxygen scavenging system to prevent photo-damage, and a reducing agent. When working with EB3 and other +TIPs, we used KCl to tune the ratio of their microtubule tip-to-lattice binding [82, 98]. Finally, methyl-cellulose was always included to confine out-of-plane microtubule and F-actin bundle fluctuations, as needed for TIRF microscopy. Thus, the core microtubule polymerization reaction (always made in MRB80) consisted of:

- 0.2-0.5 mg/ml κ-casein
- 0.1% (v/v) methyl-cellulose
- 1 mM GTP
- Oxygen scavenging and reducing system: 4 mM DTT, 0.2 mg/ml catalase, 0.4 mg/ml glucose oxidase and 25-50 mM D-glucose
- 50-75 mM KCl
- Tubulin (with 6 % of fluorescently-labeled subunits)

The tubulin concentration was varied depending on the experiment (Table 2.1). Typically, high tubulin concentrations were used when we needed to have long microtubules [12], such as in the actin-microtubule co-alignment experiments studied in Chapter 4.

In addition to the core microtubule polymerization reaction, additional proteins such as EBs, +TIPs, actin-binding proteins, and F-actin were typically included in the microtubule polymerization mix:

- **EB3 and TipAct**: in most experiments the concentration of EB3 (unlabeled, or GFP- and mCherry-labeled) was kept in the nanomolar range, in order to enhance the ratio of microtubule tip-to-lattice binding [104]. For most experiments the

EB3 concentration was kept at 100 nM, and the GFP-TipAct concentration at 25-50 nM. The only exceptions being in the actin-microtubule co-alignment assays in Chapter 4 in which the TipAct concentration was varied between $6.5 - 50$ nM, and in the actin-transport assays of Chapter 6, in which the EB3 and TipAct concentrations were varied between $40 - 200$ nM and $10 - 50$ nM, respectively.

- **GFP-Tip**: For the actin-microtubule co-alignment experiments in Chapter 4, where we worked with the actin-binding deficient GFP-Tip, its concentration was kept at 50 nM.
- **Fascin**: For the experiments in Chapter 4 where we worked with fascin-bundled F-actin, the microtubule polymerization reaction was supplemented with $200 - 500$ nM fascin.
- **F-actin**: For experiments with actin filaments weakly bound to the coverslip (Chapters 3 and 5), phalloidin-stabilized actin filaments were added to the flow cell along with the microtubule seeds, at the equivalent of $100 - 200$ nM G-actin concentration. Even without biotinylation, we found that the actin filaments could weakly and non-specifically bind the glass surface when streptavidin was present. For the experiments with centrosomes, phalloidin-stabilized F-actin was incorporated directly into the microtubule polymerization mix at the equivalent of 1 µM G-actin concentration. Finally, for the experiments of actin-filament transport in Chapter 6, phalloidin-stabilized actin-filaments were first sheared by vigorous pipetting, and also incorporated directly to the microtubule polymerization mix at the equivalent of 30 nM G-actin concentration.

After mixing (but before the addition of actin filaments), the microtubule polymerization reaction mix was always clarified at 149,000 g for 5 min in an Airfuge® ultracentrifuge (Beckman Coulter, USA) and immediately added to the flow cell channel. Finally, the channels were sealed either with wax or vacuum grease to avoid solvent evaporation while imaging.

Table 2.1 summarizes the key components of the microtubule polymerization reactions, as well as the imaging temperatures, for most of the assays described in this thesis.

2.5 Proteins used in this thesis

Lyophilized porcine brain tubulins (unlabeled, or labeled with TRITC Rhodamine, HiLyte®488, HiLyte®635 and biotin) were obtained from Cytoskeleton (Denver, CO,

Experiment	**Temp.** (°C)	**[Tub]** (µM)	**[EB3]** (nM)	**[TipAct]** (nM)
MT dynamics and FRAP assays on plus tips (Ch. 3)	25	16	100	50
MTs interacting with single actin filaments (Ch. 3, 5)	25	16	100	50
MT co-alignment with F-actin bundles (Ch. 4)	32-34	25-30	100	6.5-50
Centrosome-nucleated MT arrays within actin filament networks (Ch. 5)	30	20	100	100
Actin filament transport by microtubule tips (Ch. 6)	28-30	10-40	40-200	10-50

Table 2.1: Main experimental conditions for all the *in vitro* assays described in this thesis.

USA), resuspended at 50-100 µM in MRB80, snap-frozen and stored at −80°C until use.

G-Actin was purified from rabbit skeletal muscle acetone powder [437, 440] and kept at −80°C for long-term storage [440]. For daily use, G-actin was stored at 4°C in G-buffer (2 mM Tris-HCl pH 7.8, 0.2 mM Na_2ATP, 0.2 mM $CaCl_2$, 5 mM dithiothreitol (DTT)). After four weeks, the protein was clarified by centrifugation at 149,000 g for 10 min and dialysis overnight against fresh G-buffer. Alexa Fluor® 647 and 594 succinimidyl ester dyes (Molecular Probes, Life Technologies, Carlsbad, CA, USA) were used to produce labeled G-actins [440].

GST-tagged recombinant human fascin 1 (the plasmid was a generous gift from Dyche Mullins, University of California, San Francisco, U.S.A) was expressed and purified via affinity chromatography on Glutathione Sepharose 4 Fast Flow matrix (GE Healthcare Bio-Sciences AB, Uppsala, Sweden). Cleavage of the GST tag was performed with the PreScission protease system (GE Healthcare), followed by a gel-filtration step through a Superdex-200 column (GE Healthcare), [440].

6×His-tagged recombinant human EB3, GFP-EB3, mCherry-EB3 [86, 120], and GFP-Tip (elsewhere called GFP-MACF43, [107]) were kind gifts from Michel Steinmetz (Laboratory of Molecular Research, Paul Scherrer Institut, Switzerland) and Anna Akhmanova (Department of Biology, Utrecht University, the Netherlands).

The homogeneity of all recombinant proteins used in this study was confirmed by SDS-PAGE (Fig. 2.4).

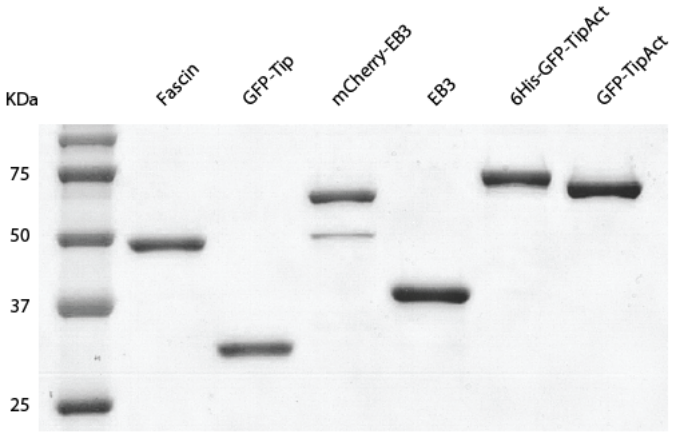

Figure 2.4: SDS-PAGE analysis of the recombinant proteins used in this study. The corresponding molecular weights are: fascin 55 kDa, GFP+TIP 30 kDa, mCherry-EB3 65 kDa, EB3 35 kDa, 6His-GFP-TipAct 76 kDa, and GFP-TipAct 74 kDa.

2.6 Buffers and stocks

We provide a list with all the key reagents and stock solutions used in this thesis in alphabetical order. Unless stated otherwise, chemicals were obtained from SIGMA Aldrich (Sigma-Aldrich Chemie B.V., the Netherlands). All stock solutions were prepared in MRB80 unless otherwise noted. For stock solutions, information is provided as follows: name (catalog number, company), concentration, storage temperature and additional details:

- ATP (disodium salt hydrate, A2383), 50mM, $-80°C$
- D-Glucose (G7528), 1M, filter, $-80°C$
- G-actin (labeled and unlabeled), for long term storage keep concentration $\geq$ 48 µM in G-buffer, $-80°C$
- Alexa Fluor® 488, Alexa Fluor® 594, and Alexa Fluor® 647succinimidyl ester dyes (A-20000, A-20004, A-20006, Molecular Probes, Life Technologies, Carlsbad, CA, USA), $-20°C$
- GMPCPP (10mM solution, NU-405, Jena Biosciences, Jena, Germany), $-80°C$

- GTP (G8877), 50mM, −80°C
- H_2O_2 (30% in water, non-stabilized, 95313), 4°C
- κ-casein (C0406), 5 mg/ml, filter, −80°C
- Methyl-cellulose (M0512), 1% (w/v), −80°C
- NeutrAvidin™ (31055, Thermo Scientific, Pierce Protein Biology Products, Rockford, IL, US), 5 mg/ml, −80°C
- NH_4OH (30% in water, 320145), RT
- Oxygen scavenging and reducing mix (50X): 200 mM DTT, 10 mg/ml catalase and 20 mg/ml glucose oxidase in MRB80, filter, −80°C
- DTT (D0632), 1M, −80°C
- Catalase (powder, C9322), −20°C
- Glucose oxidase (powder, G7016), −20°C
- Phalloidin (P2141), 1mM in methanol, −20°C
- PLL-PEG (PLL(20)-g[3.5]- PEG(2), Susos AG, Dübendorf, Switzerland), 2mg/ml, −80°C
- PLL-PEG-Biotin (PLL(20)-g[3.5]-PEG(2)/PEG(3.4)-Biotin (50%), Susos AG), 2 mg/ml, −80°C
- Pluronic® F-127 (P2443), 10% (w/v) in DMSO, RT
- Streptavidin (85878), 5 mg/ml, −80°C
- Tubulin (T240, Cytoskeleton Inc., Denver, CO, USA), 50 µM, −80°C
- Tubulin HiLyte 488-labeled, HiLyte 647-labeled, TRITC Rhodamine-labeled, and Biotin-labeled (TL488M, TL670M, TL590M, T333P, Cytoskeleton Inc), 50 µM, −80°C

2.7 Total internal reflection fluorescence (TIRF) microscopy

The best signal-to-noise ratio for *in vitro* surface assays with fluorescently-labeled proteins in solution is achieved with TIRF microscopy [441]. Since we often had to visualize two or even three proteins within one experiment, we used up to three different wavelengths: 488 nm, 561 nm and 635 nm. We found the optimal fluorophore/laser

combinations using TRITC Rhodamine-labeled tubulin, Alexa 647-labeled actin, and GFP-labeled EBs (or +TIPs). If unlabeled EBs were used, Alexa 488-labeled G-actin worked equally well.

TIRF microscopy and fluorescence recovery after photo-bleaching (FRAP) experiments were performed on an Nikon Eclipse Ti-E inverted microscope (Nikon Corporation, Tokyo, Japan) equipped with an Apo TIRF 100x1.49 N.A. oil objective, a motorized stage, Perfect Focus System (PFS), a motorized TIRF illuminator (Roper Scientific, Tucson, AZ, USA) and a QuantEM:512SC EMCCD camera (Photometrics, Roper Scientific). For excitation, we used a 561 nm (50 mW) Jive (Cobolt, Solna, Sweden) and a 488 nm (40mW) Calypso (Cobolt) diode-pumped solid state laser, and a 635 nm 28 mW Melles Griot laser (CVI Laser Optics & Melles Griot, Didam, Netherlands). For FRAP experiments the microscope was equipped with a MAG Biosystems FRAP-3D system (Photometrics, Roper Scientific) that could either be used to do FRAP-on-the-fly (point FRAP) or region of interest (ROI) FRAP experiments with diffraction-limited spots.

Most of the imaging of dynamic microtubules was performed at two seconds per frame with $100-200$ ms exposure time at 10-15% laser power (unless otherwise noted). FRAP experiments on mCherry-EB3 and GFP-TipAct at growing microtubule ends and actin bundles (Chapter 4) were performed at video rate (33 ms exposure time per frame), at 10-15% laser power for imaging, and 100% laser power for photo-bleaching.

To ensure consistent microtubule dynamics and control their growth speeds and average lengths [12], the sample temperature was regulated with the use of a home-built objective heater/cooler with a range of $15-40\pm1$°C. The temperature was set depending on the desired range of microtubule lengths. For the experiments without actin, or with single actin filaments weakly bound to the coverslip the temperature was kept at 25 ± 1°C, for the assays with linear arrays of actin bundles it was kept between $32-34\pm1$°C, for the experiments with centrosomes it was kept at 30 ± 1°C, and for the assays of actin-filament transport between $28-30\pm1$°C (Table 2.1).

2.8 Data analysis

All image processing and data analysis were performed using plugins for FIJI [442] or ImageJ [443] and custom-written programs in MATLAB (MathWorks Inc., Natick, MA,

USA). Each chapter contains a detailed explanation of the image analysis techniques developed for each specific experiment.

We thank Anna Akhmanova (Utrecht University, The Netherlands) and Michel O. Steinmetz (Paul Scherrer Institute, Switzerland) for providing us with the EB3 and GFP-Tip proteins, Dyche Mullins (UCSF, San Francisco, USA) for providing us with the fascin plasmid, and Marjolein Vinkenoog (FOM Institute AMOLF, The Netherlands) for purifying and labeling actin. We furthermore thank Henk-Jan Boluijt and the mechanical workshop at the FOM Institute AMOLF for the design and production of the glass slides we used to work directly on the microscope stage. Finally, we thank Marko Kamp (FOM Institute AMOLF, The Netherlands) and Roland Dries (TU Delft, The Netherlands) for maintaining the TIRF microscope.

Chapter 3

TipAct – An engineered actin-binding microtubule +TIP

In this chapter we outline the design, purification and characterization of TipAct, an engineered actin-microtubule cross-linking protein. We demonstrate that both in cells and in vitro, TipAct can bind to actin filaments, and localize at growing microtubule ends in an EB-dependent manner. We further demonstrate that even though TipAct has a low affinity for F-actin, when locally concentrated at microtubule tips it can link microtubules to actin filaments. During these interactions, the TipAct intensity at the microtubule tip increases, suggesting a reduced off-rate of TipAct (and possibly of EB) in regions of actin-microtubule overlap. Finally, we show that TipAct's actin-binding domain is insensitive to actin filament polarity.

3.1 Introduction

In recent years, a variety of proteins and protein complexes that mediate physical linkages between filamentous actin (F-actin), microtubules (MTs) and intermediate filaments (IFs) have been identified [260, 308, 309]. Among these, the spectraplakins (structural hybrids of spectrins and plakins [444]), stand out in that they often contain, in a single molecule, binding sites for all three cytoskeletal polymers [308, 309] (Fig. 3.1). Mammals encode two spectraplakin genes: microtubule-actin cross-linking factor (MACF, also known as ACF7) [122, 123, 279], and Dystonin (also known as BPAG1) [445]. Non-mammals typically encode only one spectraplakin gene: Short-Stop/Shot in

Drosophila melanogaster [124, 446], vab-10 in *Caenorhabditis elegans* [447, 448], and Magellan in *Danio rerio* [449, 450].

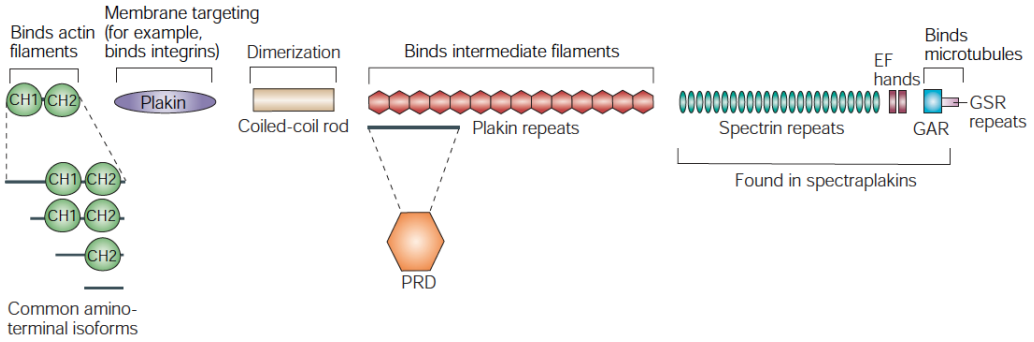

Figure 3.1: Domain organization of plakins and spectraplakins. Plakins and spectraplakins have a similar N-terminal architecture containing tandem calponin-homology (CH) actin-binding domain, a plakin domain, and a plakin repeat domain (PRD). Not all the spectraplakins have the coiled-coil dimerization domain. In addition, spectraplakins have a C-terminal spectrin-repeat rod, a pair of EF-hands, a GAR domain and a serine-rich sequence of positively-charged aminoacids (GSR), often encompassing a microtubule tip localization signal (MtLS). Figure taken from [308].

Spectraplakins are large (> 500 kDa) and long (~ 400 nm) multivalent cytoskeletal cross-linking proteins that are evolutionarily conserved among metazoans. The spectraplakin gene can encode a number of splice variants which mainly result in proteins with divergent N-terminal sequences [309, 444]. The longest spectraplakin isoforms will normally contain (Fig. 3.1):

- N-terminal actin-binding domain (ABD) consisting of tandem calponin homology (CH) domains. This type of ABD is present in other actin-binding protein families as well, such as filamin, dystrophin, utrophin, fimbrin, and α-actinin [451].
- Plakin domain, which targets plakins and some spectraplakins, such as BPAG1, to junctional complexes [308, 452, 453].
- Plakin repeat domain (PRD), which is largely used by plakins to bind intermediate filaments [307–309]. Plakins and some spectraplakin isoforms use the PRD and the plakin domain to link intermediate filaments to cell junctions. For instance, BPAG1 links keratin to β4-integrin and hemidesmosomes [452, 453]. It remains hitherto unknown whether all the members of the spectraplakin family can bind intermediate filaments.
- Sequence of spectrin repeats, which are usually involved in conferring mechanical

stability against pulling forces [454]. For instance, removing a few repeats of the spectrin repeat rod of dystrophin can result in severe muscular dystrophy [455]. In the case of the spectraplakins, the length of the rod may also be important to serve as a spacer between the microtubule- and actin-binding domains. Finally, it is unknown whether, as in the case of α-actinin, the spectrin repeats in spectraplakins also mediate dimerization, be it parallel or antiparallel [122, 456].

- A pair of EF hands, which in spectrins often transition from a closed to an open conformation upon Ca^{2+} binding [457]. In BPAG1n4, for instance, calcium-binding by the EF-hands was demonstrated to switch its localization from the tips of microtubules to the microtubule lattice by exposing the otherwise concealed microtubule-binding domain [458]. However, not all of the spectraplakins' EF-hands appear to be sensitive to calcium [309, 444].

- GAS2-related (GAR) domain, which was for a long time thought to bind and stabilize microtubules on its own [122, 124, 353], but which has been recently demonstrated to require the whole C-terminal portion (including the GSR repeats, Fig. 3.1) of the spectraplakin protein for this function [354, 459, 460].

- C-terminal tail containing one or multiple copies of the microtubule tip localization signal (MtLS [107]): a serine-rich sequence of basic and positively charged amino-acids containing the short motif SXIP, which allows them to bind end-binding (EB) proteins and localize to growing microtubule ends. Thus, spectraplakins also belong to the +TIP family of proteins [125, 354].

In short, spectraplakins contain all the functional domains necessary to cross-link F-actin and microtubules, as well as the ability to localize at growing microtubule ends. There is increasing evidence that their cross-linking activity is essential for vital cellular events [309]. For instance, in migrating cells MACF mediates the guidance of microtubule growth along actin stress fibers towards focal adhesions (FAs) [279]. This is required for the kinesin-powered delivery of FA disassembly and extra-cellular matrix degradation factors, in order to allow the cell to detach from the substrate and move [342, 364, 461]. Similarly, Shot has been shown to guide microtubule growth along F-actin bundles inside filopodia at the growth cone periphery, a requirement for the establishment and maintenance of the direction of axonal extension [291]. Neurons lacking Shot fail to extend and *stop short*, hence the protein name.

MACF and Shot are undoubtedly the best characterized spectraplakins *in vivo* [309]; however, a mechanistic understanding of their actin-microtubule cross-linking activity

is missing. For instance, it is not clear under what conditions they utilize their different modes of microtubule association (i.e. directly, by the microtubule-binding domain, or via EB). Furthermore, it is unknown whether their localization is dominated by their actin-binding or microtubule-binding domains, and whether they preferentially localize on certain F-actin architectures. Finally, an understanding of the mechanical and geometrical constraints under which spectraplakins can link and guide growing microtubules along F-actin bundles is also missing. The same can be said of other actin-microtubule cross-linking systems that also display +TIP activity, such as the GAS2-like family of proteins [459, 460], or the bim1-kar9-myo2 system of budding yeast [272, 280, 362, 374].

In order to better understand the ways by which linking growing microtubules to F-actin structures helps direct cytoskeletal coordination, as well as how the activity of cross-linkers is modulated by the mechanical properties of F-actin and microtubules, we designed a model actin-microtubule cross-linker based on the mammalian spectraplakin MACF. We decided to call it TipAct, in playful analogy to the commonly used F-actin marker LifeAct [462], but also to emphasize that it is a model system to study actin-microtubule interactions rather than a direct analog to MACF. Our GFP-TipAct construct (Figs. 3.2 b and 3.12) was designed to contain an N-terminal eGFP-tag followed by an ABD consisting of tandem calponin-homology (CH) domains [122, 124] and a C-terminal region containing an SXIP motif to bind EB proteins [107, 125, 354], and thus localize at growing microtubule ends [107]. To make the molecule amenable for expression in bacteria, we replaced the plakin domain and the long stretch of spectrin-repeats of MACF (Fig. 3.2) [309], with the short ($\sim$ 20 nm-long [463]) coiled-coil linker of cortexillin I. The coiled-coil of cortexillin served as a spacer between the actin-binding and EB-binding domains, but also induced parallel dimerization [464]. We chose to dimerize the molecule based on previous observations that multiple SXIP-motifs, be it in series or in parallel, can greatly enhance plus-end localization [107].

3.2 TipAct localization in mammalian cultured cells

To test whether TipAct's domains were functional, and also to study where it would localize, we transiently expressed it in HeLa cells. Despite its much simpler domain architecture compared to MACF (Fig. 3.2), we found that GFP-TipAct localized to the growing ends of microtubules (both at the cell interior and periphery, Fig. 3.3 a), and to

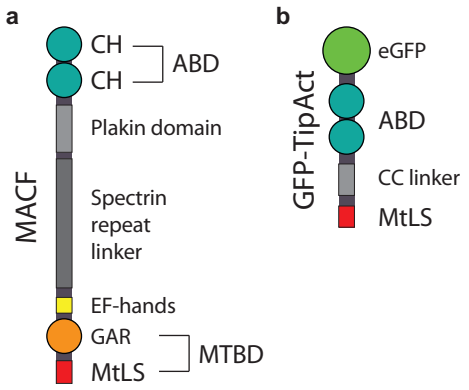

Figure 3.2: MACF and GFP-TipAct domain architecture. (a) MACF domain organization. (b) TipAct contains an N-terminal eGFP-tag, followed by the actin-binding domain (ABD), and microtubule tip localization signal (MtLS) of human MACF1. In TipAct, the ABD and MtLS are separated by the coiled-coil linker of cortexillin-I, which induces parallel dimerization.

F-actin structures near the cell edge (Fig. 3.3 b), in a remarkably similar fashion to what has been reported of full-length MACF and Shot [122, 123, 125, 352, 354, 369, 465].

In order to better visualize TipAct's actin binding ability, we depolymerized the microtubule cytoskeleton with nocodazole, which results in an increase in stress fiber number and size [366]. Figure 3.4 shows that under these conditions GFP-TipAct localized in a punctate fashion along actin stress fibers, with most intense localization at actin-rich regions near stress fiber ends, in what appeared to be focal adhesion sites.

These live-cell imaging experiments revealed that GFP-TipAct's actin-binding and EB-binding domains are functional in living cells. Moreover, that TipAct's microtubule plus-end tracking ability dominates its localization on F-actin, suggesting a higher affinity for EB than for actin filaments. Finally, the actin-binding and EB-binding domains of TipAct were sufficient for it to mimic the *in vivo* localization of full-length MACF and Shot [122, 123, 125, 352, 354, 369, 465]. Full-length MACF and Shot, however, also contain a MTBD with strong-affinity for the microtubule lattice [353], the fact that they do not localize at the microtubule lattice in cells [125] could suggest that its activity is regulated.

3.3 *In vitro* characterization of TipAct

Once the localization of GFP-TipAct was characterized in living cells, we proceeded to express and purify it using bacterial vectors. Once purified, the first step was to

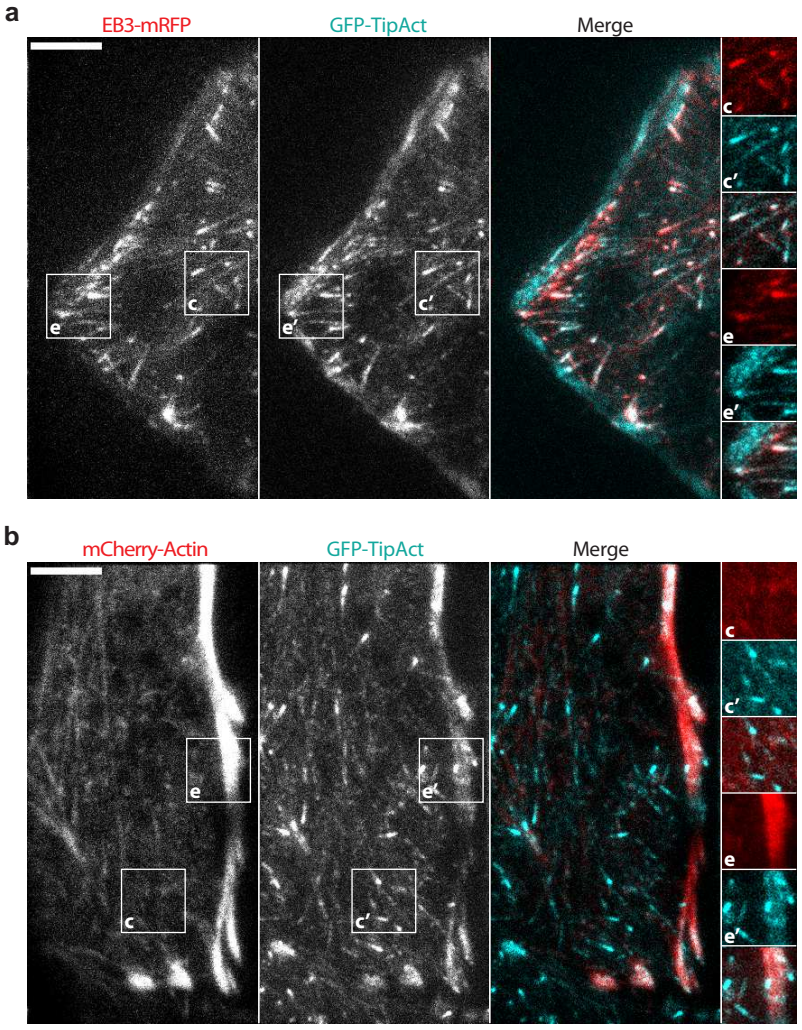

Figure 3.3: TipAct localization in cultured HeLa cells. (a) Live-cell fluorescence micrograph of a HeLa cell expressing EB3-mRFP and GFP-TipAct. TipAct localizes at growing microtubule ends both at the cell center (c, c') and at the cell edge (e, e'). (b) Live-cell fluorescence micrograph of a HeLa-R cell expressing mCherry-Actin and GFP-TipAct. TipAct localizes at actin-rich regions near the cell edge (e, e'). Scale bars: 5 µm.

characterize TipAct's actin-binding and microtubule-tip binding domains *in vitro*, through a series of biochemical and fluorescence microscopy assays.

3.3.1 Biochemical characterization of TipAct's actin-binding domain

To measure the affinity of TipAct's ABD for F-actin, we performed high-speed co-sedimentation assays with pre-polymerized actin filaments (Fig. 3.5 a). As can be

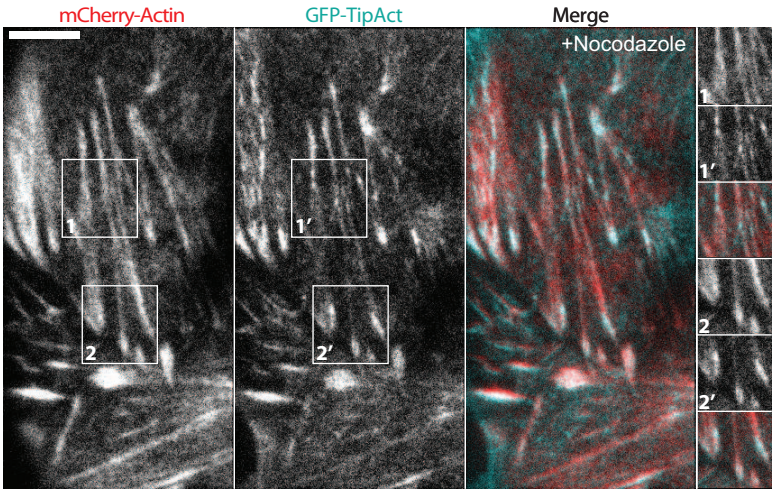

Figure 3.4: TipAct localization in cultured HeLa cells in the absence of microtubules. Live-cell fluorescence micrograph of a HeLa cell expressing mCherry-Actin and GFP-TipAct. In the absence of microtubules (depolymerized by nocodazole), TipAct localizes in a punctate fashion on stress-fibers (1,1'), and is enriched at actin-rich regions near stress fiber ends (2,2'). Scale bars: 5 µm.

observed, with increasing F-actin concentration ([F-actin]), an increasing fraction of TipAct co-sedimented. The best fit of the data shown in Figure 3.5 b to the Michaelis-Menten equation (Eq. (3.1) [466]) yielded a dissociation constant K_d of 5.2 ± 0.5 µM.

$$\frac{TipAct_{bound}}{TipAct_{total}} = \frac{[\text{F-actin}]}{[\text{F-actin}] + K_d} \tag{3.1}$$

This low affinity for F-actin is consistent with the dissociation constants of tandem-CH actin-binding domains ($K_d \sim 5 - 25$ µM) typically reported in the literature [451]. Furthermore, it explains the relatively weak localization of GFP-TipAct at F-actin structures compared to microtubule growing ends that we found through live-cell imaging (Fig. 3.3). Note, however, that a K_d of ~ 5 µM is at odds with the only two previously reported values of MACF and Shot's affinity for F-actin [124, 352], in which K_d's of 350 nM and 22 nM were measured using N-terminal fragments of MACF and Shot respectively. This discrepancy could stem from steric hindrance by the eGFP tag of TipAct, although we were careful to place spacers between all its functional domains (Fig. 3.12). Another, more likely, explanation is that in these previous studies the actin-binding affinity of MACF and Shot was measured in buffers with drastically lower ionic strengths (5 mM Tris + 50 mM KCl) than our own working buffer (80 mM Pipes + 75 mM KCl).

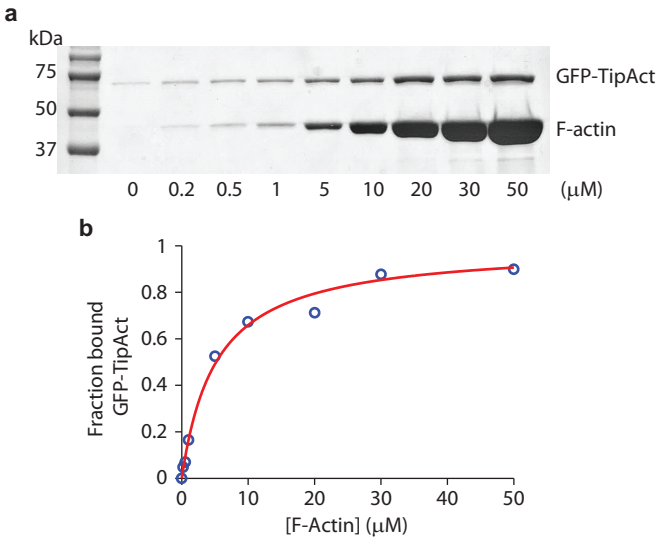

Figure 3.5: Measurement of GFP-TipAct's actin-binding affinity. (a) SDS-PAGE analysis of co-sedimentation experiments. With increasing F-actin concentration an increasing fraction of GFP-TipAct co-sedimented. The first lane of the gel shows the molecular weight marker. (b) The best fit of the data ($R^2 = 0.9916$), to Eq.(3.1) yielded a dissociation constant $K_d = 5.2 \pm 0.5$ µM.

3.3.2 TipAct relies on EB to track growing microtubule ends

Next, we tested whether TipAct's localization at microtubule ends depends on EB. To this end, we polymerized microtubules from GMPCPP-stabilized seeds immobilized on a microscope coverslip, with GFP-TipAct, in the presence or absence of EB3. A schematic of this assay is shown in Figure 3.6.

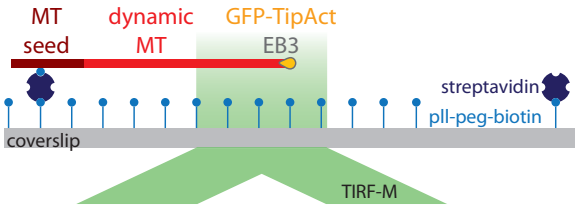

Figure 3.6: Experimental setup to study TipAct's plus-end tracking behavior. Microtubules are polymerized from GMPCPP-stabilized seeds, in the presence of EB3 and GFP-TipAct.

Kymographs of microtubule growth revealed that GFP-TipAct colocalized with mCherry-EB3 at microtubule growing ends (both plus and minus, Fig. 3.7 a). In contrast, in the absence of EB3 we found no detectable TipAct binding at any portion of the microtubules (Fig. 3.7 c). Intensity line-profiles along the TipAct and EB3 plus-end comets (dashed line in the merge panel of Fig. 3.7 a), revealed that the plus-end intensity

of TipAct did not lag behind that of EB3 (Fig. 3.7 b). This observation is in contrast to what has been reported of MACF and Shot *in vivo*, for which the peak of their intensity always localizes slightly behind that of EB [125, 354]. This suggests that other protein domains, or interactions with F-actin, may be required for this effect. Note, however, that this seems to be a common phenomenon for other microtubule +TIPs *in vivo*, which remains hitherto unexplained (Anna Akhmanova, private communication).

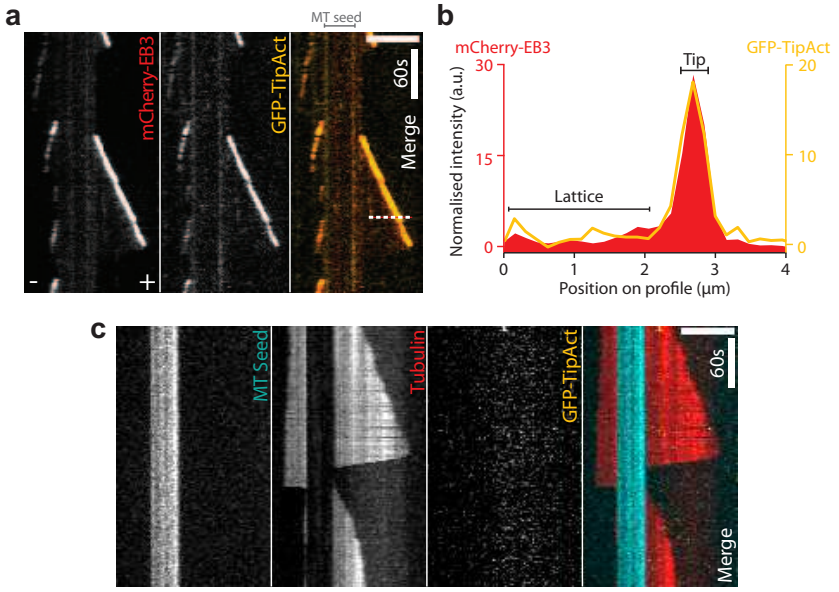

Figure 3.7: TipAct is an EB-dependent +TIP. (a) Kymograph of microtubule growth with mCherry-EB3 and GFP-TipAct. The plus (+) and minus (-) ends of the microtubule are indicated. (b) Fluorescence intensity profiles along the dashed line on the kymograph in (a) reveal that the peak comet intensity of TipAct and mCherry-EB3 co-localize. (c) Kymograph of microtubule growth with GFP-TipAct but no EB3. In this context, TipAct does not bind anywhere on the microtubule. The GFP-TipAct and mCherry-EB3 intensities were normalized by their mean values at the microtubule lattice. Scale bars, 5 µm. MT, microtubule.

3.3.3 TipAct has no effect on the polymerization dynamics of free microtubules

To test whether TipAct had any effect on microtubule growth, we measured the main parameters of microtubule dynamic instability [8]; namely, growth and shrinkage speeds, and catastrophe and rescue frequencies. Table 3.1 shows the results of this analysis. The addition of EB3 increased both the growth and shrinkage speeds, as well as the catastrophe frequency; in agreement with previous measurements [86, 100, 104]. The addition of GFP-TipAct had no further effect on microtubule polymerization dynamics.

Experiment	V_{grow} (µm/min)	T_{grow} (min)	V_{shrink} (µm/min)	T_{shrink} (min)	F_{cat} (1/min)	N_{cat}	F_{res} (1/min)	N_{res}
15 µM Tubulin	0.71±0.12	5815.03	12.55±2.28	373.93	0.15±0.07	838	0.27±0.26	76
+ 100 nM EB3	2.48±0.24	977.37	16.37±2.95	168.43	1.35±0.23	1361	0.21±0.13	36
+ 50 nM TipAct	2.46±0.47	948.6	16.29±3.37	155.67	1.21±0.19	1116	0.09±0.10	24

Table 3.1: Parameters of microtubule dynamic instability. Analysis of dynamic instability for freely growing microtubules polymerized at 25°C in the presence of 1 mM GTP and 50 mM KCl. V_{grow}, average growth speed. T_{grow}, total growth time for all experiments. V_{shrink}, average shrink speed. T_{shrink}, total shrink time for all experiments. F_{cat}, average catastrophe frequency. N_{cat}, total number of catastrophes for all experiments. F_{res}, average rescue frequency. N_{res}, total number of rescues for all experiments. For n = 4, 3 and 5 experiments, from top to bottom row. Where appropriate, values are reported as average ± standard deviation.

3.3.4 TipAct links growing microtubule ends to actin filaments

The next step was to test TipAct's plus-end tracking behavior in the vicinity of phalloidin-stabilized actin filaments bound to the coverslip (Fig. 3.8). Given the low affinity of TipAct for F-actin ($K_d \sim 5$ µM, Fig. 3.5), under the conditions of this assay (i.e. [GFP-TipAct] = 25 – 50 nM), TipAct did not detectably decorate the F-actin (Fig. 3.8, bottom panel).

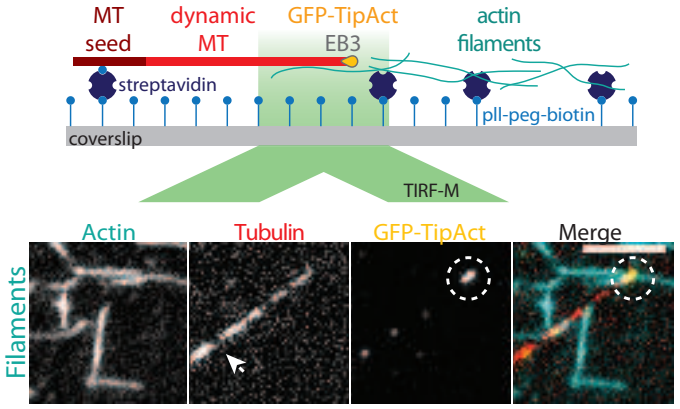

Figure 3.8: Experimental setup to study interactions between microtubules and single actin filaments. Top, microtubules were polymerized from GMPCPP-stabilized seeds, in the presence of EB3, GFP-TipAct, and surface-bound phalloidin-stabilized actin filaments. Bottom, in these experiments TipAct's localization was predominantly at microtubule tips (dashed circles). The location of the microtubule seed is indicated with an arrow in the tubulin panel. Scale bar, 5 µm.

However, microtubules with TipAct at their growing tips were still capable of transiently

capturing actin filaments (Fig. 3.9 a). This was evidenced by a cessation of actin-filament fluctuations at the point of capture, alignment of the filaments in the direction of microtubule growth, and increased filament proximity to the coverslip surface (Fig. 3.9 b). These observations indicate that the locally enhanced concentration of TipAct at microtubule tips, generated by EB3, can enhance the ability of growing microtubules to bind F-actin.

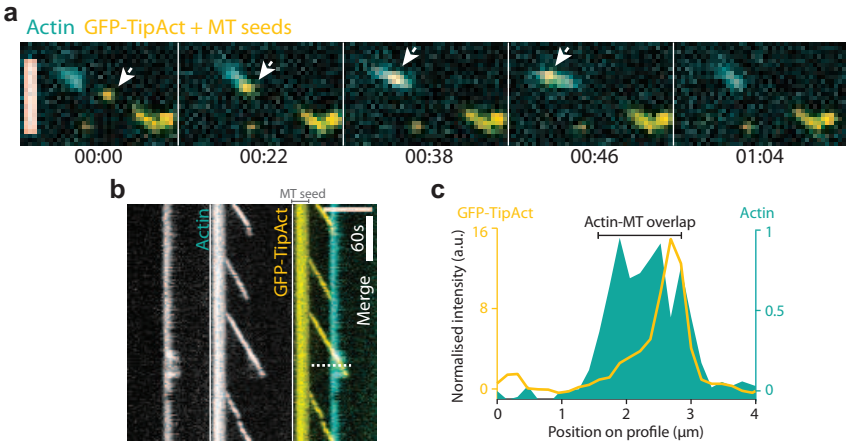

Figure 3.9: TipAct links microtubule tips to actin-filaments. (a) Time series of an experiment as in Figure 3.8. Arrows show the plus-end of a microtubule that interacts with a partially tethered actin filament as it grows. (b) Kymograph of the microtubule in (a). As actin and microtubule interact, the filament co-aligns with the microtubule and is brought closer to the surface, becoming visibe by TIRF microscopy. (c) Fluorescence intensity along the dashed line on the kymograph in (a), showing that the plus-end intensity of TipAct elongates at the actin-microtubule overlap. The GFP-TipAct intensity was normalized by its mean value at the microtubule lattice, and the actin intensity by its maximum value. Scale bars, 5 µm. Time: min:sec. MT, microtubule.

A close inspection of the TipAct plus-end comets suggested that their intensity increased upon interaction with an actin filament. In order to verify this, we aligned and averaged all the TipAct plus-end intensity profiles before and during actin-filament capture, for the interaction event shown in Fig. 3.9. Panel a in Figure 3.10 shows the regions that were averaged for the *free* and *actin-bound* TipAct comets, and panel b shows the individual and average curves. Indeed, we found that the TipAct comet became approximately 1.5 times brighter during an interaction with F-actin. Since it is unlikely that an actin-microtubule overlap enhances the on-rate of TipAct, we rather propose that the increase in intensity stems from a reduced TipAct (and possibly EB3) off-rate in this region.

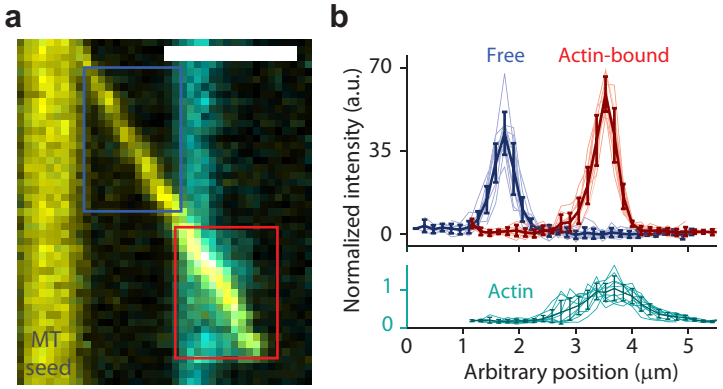

Figure 3.10: TipAct's plus-end intensity increases at actin-microtubule overlaps. (a) Zoomed-in region of the actin-microtubule interaction shown in Fig. 3.9. (b) Analysis of TipAct's plus end intensity in the regions where the microtubule was free (blue square in (a)), and actin-bound (red square in (a)). TipAct's plus-end intensity increases at actin-microtubule overlaps. The thick curves in (b) show the average profile ± standard deviation. The bottom graph shows the actin intensity profiles for the actin-bound comets (red square in (a)). The GFP-TipAct intensity was normalized by its mean value at the microtubule lattice, and the actin intensity by its maximum value. Scale bar, 5 µm. MT, microtubule.

3.3.5 TipAct's ABD is insensitive to actin-filament polarity

A final test in our characterization of TipAct's behavior *in vitro* was to verify whether its actin-binding domain is sensitive to actin-filament polarity. To this end, we looked for events in which two microtubules interacted with the same actin filament from opposite ends. As can be observed in the montage shown in Figure 3.11, microtubules could interact with actin filaments coming from both ends. This reveals that the actin-binding domain of TipAct (and hence that of MACF) is insensitive to actin filament polarity.

3.4 Discussion

In this chapter we described the design and characterization of TipAct, a model actin-microtubule cross-linker based on the spectraplakin MACF. Biochemical characterization of its actin-binding activity revealed that it has a low affinity for F-actin ($K_d \sim 5$ µM). This was confirmed through live-cell imaging experiments in which TipAct localized primarily at microtubule tips and only to a subset of F-actin structures near the cell edge. Intriguingly, similar localization patterns have been described of MACF

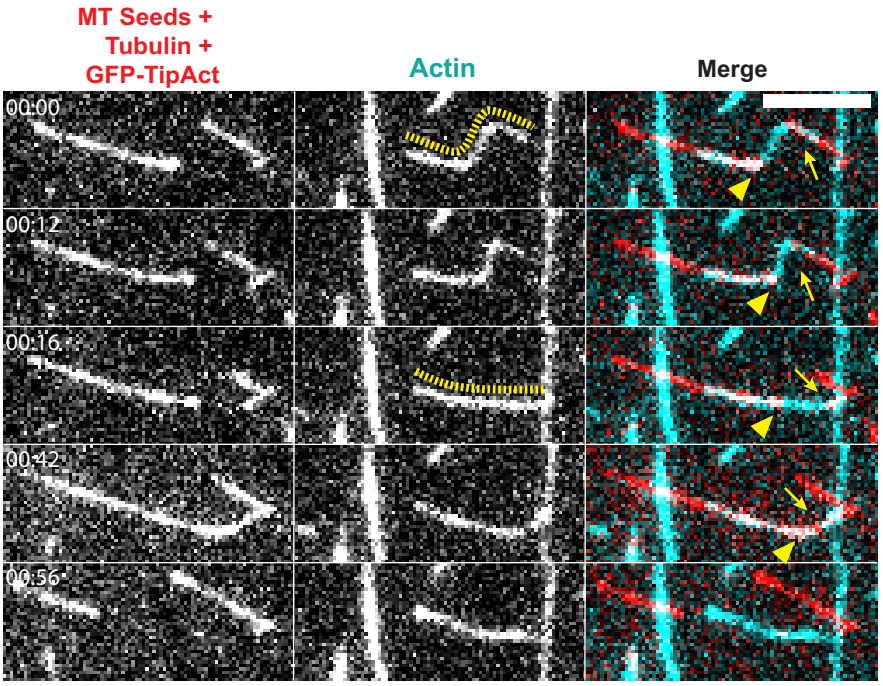

Figure 3.11: TipAct's actin-binding domain is insensitive to F-actin polarity. Time series showing two pairs of microtubules that interact with the same actin filament from opposite ends. Yellow arrowheads indicate the growing end of a microtubule that binds the actin filament from the left, and yellow arrows indicate the growing ends of two microtubules that sequentially interact with the actin filament from the right. Note the sharp deformation of the actin filament in the middle pane at $t = 0$ s, indicated by a dashed yellow line, and how it relaxes when the microtubule on the right shrinks ($t = 16$ s). Scale bar, 5 µm. Time: min:sec. MT, microtubule.

and Shot, even though they supposedly have actin-binding affinities in the nanomolar range, and also contain high-affinity microtubule-lattice binding domains [124, 352].

In vitro assays with dynamic microtubules confirmed that TipAct's plus-end localization depends on EB, and revealed that TipAct has no effect on microtubule dynamics. To our surprise, even when we added TipAct at concentrations 100-fold smaller than its K_d for F-actin, we found that its locally enhanced concentration at microtubule tips enabled microtubules to capture actin filaments. This observation suggests that collective effects help overcome the low actin-binding affinity of individual TipAct molecules. Furthermore, we found that the intensity of TipAct at actin-microtubule overlaps was higher than at free microtubule ends, indicating that the establishment of an actin-microtubule overlap locally modulates the exchange dynamics of TipAct, and possibly also of EB3. We speculate that locally concentrating a low-affinity F-actin binder at microtubule tips could be crucial for the *in vivo* activity of actin-microtubule cross-linking +TIPs, such as the spectraplakins [309], or the GAS2-like

family of proteins [459, 460]. This property could provide cells with a mechanism to control where microtubule cross-talk with single actin filaments takes place, i.e. at growing microtubule ends, while avoiding cross-linking elsewhere.

Finally, we confirmed that TipAct's actin-binding domain (and hence that of MACF) is insensitive to the polarity of actin filaments. Put together, these observations indicate that TipAct behaves as an F-actin-binding microtubule +TIP, both *in vitro* and in cultured cells.

3.5 Materials and methods

3.5.1 TipAct Cloning

GFP-TipAct was designed to contain an N-terminal enhanced-GFP (eGFP) tag followed by the actin-binding (ABD) and EB-binding domains (microtubule tip localization signal, MtLS) of full length human MACF1 (NCBI Reference Sequence: NP_036222.3), separated by the coiled-coiled linker of Cortexillin I from *Dictyostelium discoideum* [464] (Fig. 3.12). Using PCR-based strategies we obtained the five necessary fragments: eGFP, ABD (first and second CH domains, corresponding to residues Asp74 - Gly306 of full-length MACF1), Cortexillin I coiled-coiled linker (CC linker), and MtLS (corresponding to residues Glu5391 - Arg5430 of full-length MACF1), from the following cDNA clones: pEGFP-C2 (Clontech, Takara Bio Europe, Saint-Germain-en-Laye, France), IMAGE clone 30414356, LIFESEQ5427393 (Open Biosystems, Thermo Fischer, Huntsville, AL, USA), full-length Cortexillin-I in pET-15b20 (kind gift of Michel Steinmetz, Paul Scherrer Institut, Switzerland) and IMAGE clone 7476004. Each fragment was amplified using the primers indicated in Table 3.2. For protein purification, the amplified fragments were ligated into the bacterial expression vector: pET-28a (Novagen, Merck Millipore, Billerica, MA, USA), between NdeI and BamHI sites. This procedure resulted in a vector expressing the construct: eGFP - ABD - CC linker - EB-BD, with an N-terminal thrombin-cleavable 6×His tag for purification. For live-cell imaging experiments, the amplified fragments were instead ligated into the pEGFP-C2 vector (Clontech, Palo Alto, CA) between NheI and BamHI sites.

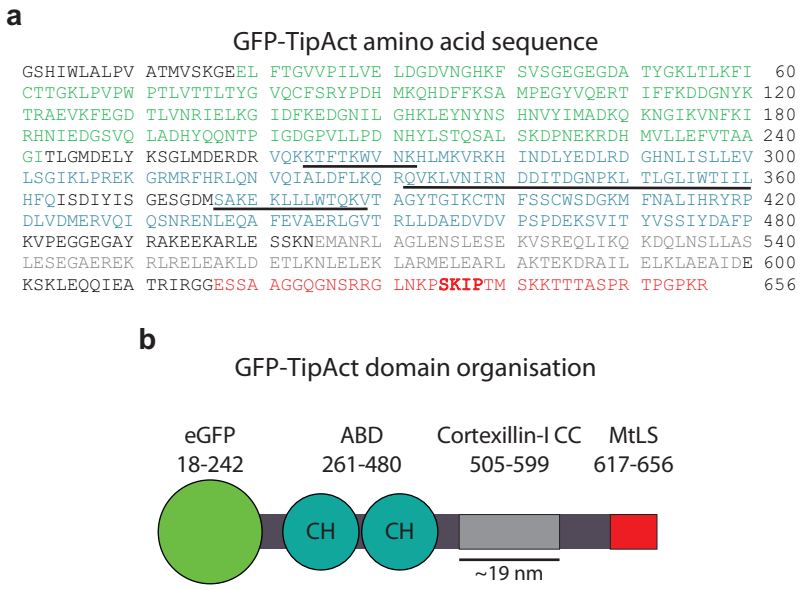

Figure 3.12: TipAct's amino-acid sequence and domain organization. (a) Amino-acid sequence of GFP-TipAct. The color-code corresponds to the domains indicated on the diagram in (b). The regions with known F-actin-binding activity are underlined. The SXIP-motif required for EB-binding is highlighted in bold red letters. The spacers between domains are indicated in black letters. (b) GFP-TipAct domain organization indicating the amino-acid numbers from the sequence in (a). ABD, actin-binding domain; CC, coiled-coil; MtLS, microtubule tip localization signal.

Regions	**Primers**
eGFP	CATATGGGGCTAGCGCTACCGGTCGCCACCATGGTGAG
eGFP:CH1	GGACGAGCTGTACAAGTCCGGACTCATGGATGAACGGG ACCGGGTTCAGAAG
CH1:CH2	CTGGACCATTATTTTGCATTTCCAGATCTCTGACATCTA CATTAGTGGAG
CH2:coiled-coil	CCTAAAGTTCCTGAGGGTGGAGAAGGGGCCTATAGAGC CAAGGAAGAGAAAGC
coiled-coil:MtLS	CAAATCGAAGCCACCAGAATCAGAGGGGGGGAAAGCAG CGCTGCAGGGGGCCAA
MtLS	GGACTCCAGGTCCCAAGCGATAAGGATCCATG

Table 3.2: DNA Primers used for GFP-TipAct construction. CH, calponin homology; MtLS, microtubule tip localization signal.

3.5.2 Cell culture, transfection and live-cell imaging

HeLa cells were maintained as previously described [87]. FuGENE (Roche Applied Science, Indianapolis, IN, USA) was used for EB3-mRFP2, mCherry-Actin3 and GFP-TipAct plasmid transfection according to manufacturer's protocols. To depolymerize the microtubule cytoskeleton, HeLa cells were incubated with 10 µM nocodazole for 2 hrs at 37°C before imaging. We verified that microtubules were fully depolymerized as TipAct no longer showed plus-end tracking behavior.

Live-cell imaging was performed on a Nikon Eclipse Ti-E inverted microscope (Nikon Corporation, Tokyo, Japan) equipped with Perfect Focus System (PFS), a CFI Apo TIRF 100x 1.49 N.A. oil objective (Nikon), a TI-TIRF-E motorized TIRF illuminator (Nikon), and a QuantEM 512SC EMCCD camera (Photometrics, Roper Scientific, Tucson, AZ, USA). The system was controlled with MetaMorph 7.5 software (Molecular Devices, Sunnyvale, CA, USA). For excitation we used 491 nm 50 mW Calypso (Cobolt, Solna, Sweden) and 561 nm 50 mW Jive (Cobolt) lasers. For simultaneous imaging of mRFP/mCherry and GFP emission we used the ET-mCherry/GFP filter set (59022, Chroma, Bellows Falls, VT, USA) together with a DV2 beam splitter (MAG Biosystems, Roper Scientific) equipped with a dichroic filter 565dcxr (Chroma) and HQ530/30m emission filter (Chroma). To maintain the cells at 37°C we used a INUG2E-ZILCS stage top incubator (Tokai Hit, Fujinomiya, Japan). 16-bit images were projected onto the CCD chip at a magnification of 0.065 µm per pixel with intermediate magnification 2.5X (C mount adapter 2.5X, Nikon). Live-cell imaging of doubly transfected cells (i.e. mCherry-EB3 and GFP-TipAct or mCherry-Actin and GFP-TipAct), was performed at an exposure time of 100 ms per frame with $10 - 15\%$ laser power.

3.5.3 TipAct purification

The *E. coli* strain T7-express (New England Biolabs, Ipswich MA) was used for expression of GFP-TipAct. Bacteria were grown at 37°C with continuous agitation, in LB (lysogeny broth [467]) containing 50 µg Kanamycin. Protein expression was induced when cultures reached an optical density of $OD_{600} = 0.8$ (for a 1 cm path length), by adding isopropyl β-D-1-thiogalactopyranoside (IPTG) to a final concentration of 0.4 mM, followed by further agitation at 20°C overnight. Cells were harvested by centrifugation at 5,000 RCF for 30 min at 4°C. Thereafter, they were resuspended in a sodium phosphate (NaPi) based working buffer (50 mM NaPi, pH 7.0, 20 mM Imidazole, 400 mM NaCl, 2mM $MgCl_2$, 5 mM β-Mercaptoethanol and 10% glycerol), supplemented with 0.1%

(w/v) Triton-X, 1 mg/ml Lysozyme (Roche Applied Science, Indianapolis, IN, USA) and 1X Complete Protease Inhibitors (EDTA-free, Roche). Cell lysis was achieved with two cycles of freeze-thawing in liquid N_2, followed by shearing of genomic DNA with a 14 gauge blunt-end needle. The cell lysate was centrifuged at 30,000 RCF for 30 min at 4°C, and the supernatant collected. Next, the supernatant was incubated at 4°C for $\sim$ 1 hr on a rotating wheel with Ni-NTA agarose (Qiagen Benelux B.V., Venlo, Netherlands) previously equilibrated in working-buffer. Before elution, the resin-bound proteins were washed twice in working buffer supplemented with 600 mM NaCl, followed by a wash in normal working buffer. Finally, the 6×His-tagged GFP-TipAct proteins were eluted using the gravity-flow method with working buffer supplemented with 280 mM Imidazole.

Cleavage of the 6×His-tag from GFP-TipAct was performed overnight at RT with 2.5 U of thrombin per mg of protein in $NaPi_{500}$ buffer (50 mM NaPi pH 7, 1 mM EDTA, 2 mM $MgCl_2$, 5 mM β-Mercaptoethanol and 10% glycerol, supplemented with 500 mM NaCl). Note that the cleavage reaction had to be optimized, the details of which are given in the following section. Uncleaved proteins were removed by running the cleavage reaction through the Ni-NTA agarose again and collecting the flow-through (cleaved proteins). The cleaved proteins were concentrated with a 30 kDa MWCO centrifugal filter unit (Merck Millipore, Billerica, MA, USA) and gel-filtered with an *Ä*kta chromatography system (GE Healthcare Bio-Sciences AB, Uppsala, Sweden) through a Superdex-200 column (GE Healthcare) equilibrated in working buffer, at a flow rate of 0.5 ml/min. The peak fractions were pooled and concentrated as before to a final concentration of 5 mg/ml, accompanied by a final buffer exchange to MRB80-KGβ (80 mM Pipes, pH 6.8 set with KOH, 4 mM $MgCl_2$ and 1 mM EDTA, supplemented with 250 mM KCl, 10% (v/v) glycerol and 5 mM β-mercaptoethanol). Thereafter, the proteins were aliquoted, snap-frozen in liquid N_2 and stored at -80°C until use. We confirmed that TipAct was stable when stored in this way, as assays performed over the course of two years were reproducible.

The homogeneity of the recombinant proteins was assessed by SDS-PAGE (Fig. 2.4), and their concentration estimated from the optical absorbance in MRB80-KGβ buffer at a wavelength of 280 nm with an extinction coefficient of 59,820 $M^{-1}cm^{-1}$ (estimated from the amino acid sequence [468]).

3.5.4 6×His tag cleavage optimization

As mentioned above, cleavage of the 6×His tag by thrombin had to be optimized. To this purpose, proteins were incubated with thrombin, at RT and 4°C, in three different buffer conditions:

- Thrombin-cleavage buffer (TCB): 20 mM Tris-HCl pH 8.4, 150 mM NaCl, 25 mM $CaCl_2$.
- NaPi-cleavage buffer + 500 mM NaCl ($NaPi_{500}$): 50 mM NaPi pH 7, 1 mM EDTA, 2 mM $MgCl_2$, 5 mM β-Mercaptoethanol and 10% glycerol, supplemented with 500 mM NaCl.
- NaPi-cleavage buffer + 250 mM NaCl ($NaPi_{250}$).

Additionally, we tested whether the addition of 1 M urea (as a mild denaturant) could aid the cleavage reaction. Thus, twelve cleavage tests were performed: three buffers (TCB, $NaPi_{500}$ and $NaPi_{250}$), with or without 1M urea, at RT or at 4°C. For cleavage, thrombin was first diluted to a 0.1 U/µl concentration in TCB, and added to a 5 mg/ml solution of 6×His-GFP-TipAct, to reach a final concentration of 2.5 U of thrombin per milligram of protein. The cleavage reactions were incubated on a rotating wheel both at RT and at 4°C, and samples were collected after 4 and 17 hrs from the start of the reaction. The success of the cleavage reaction was verified by Western Blot (WB) analysis using anti-6×His antibodies (NIH NeuroMab Facility, University of California Davis). The results of these tests are shown in Figure 3.13, only for the reactions kept at RT, since at 4°C we found nearly no cleavage of the 6×His-tag even after overnight incubation.

First, we found that the addition of urea did not aid the cleavage reaction. Second, the most efficient cleavage was obtained in TCB, since already within 4 hrs no 6×His signal was detectable by WB analysis. In contrast, for the reactions in $NaPi_{500}$ and $NaPi_{250}$ (both without urea) we had to wait overnight ($\sim$ 17 hrs) for the cleavage reaction to be complete. Given the similarity between the buffer we used to purify TipAct, and $NaPi_{500}$, we chose $NaPi_{500}$, at RT, and overnight incubation to be the optimal conditions for cleavage of the 6×His-tag. We further found that a key factor for proper 6×His removal was the ratio between 6×His-GFP-TipAct and thrombin concentrations. We found that under identical conditions, but with a 6×His-GFP-TipAct concentration above 5 mg/ml, thrombin cleaved unrestrictedly, since we often observed protein precipitation after overnight incubation (data not shown).

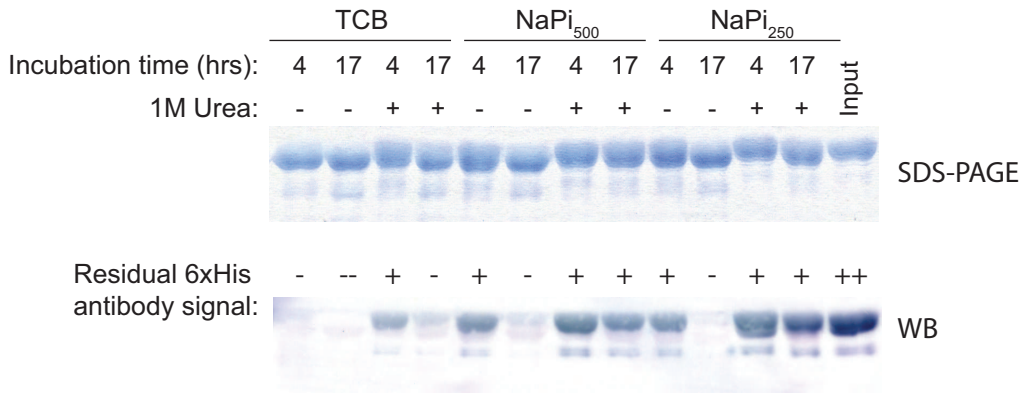

Figure 3.13: Optimization of the 6×His tag cleavage by thrombin. Top, SDS-PAGE analysis of the cleavage reactions at RT, in three different buffers (TCB, $NaPi_{500}$, and $NaPi_{250}$), ± 1 M urea, and different collection times (4 or 17 hrs). Bottom, WB analysis with anti-6×His antibody revealing residual tag after incubation with thrombin.

3.5.5 F-actin co-sedimentation assays

80 µM globular-actin (G-actin) was polymerized into F-actin for 1 hr at room temperature (RT) in MRB80 (80 mM Pipes pH 6.8, 4 mM $MgCl_2$ and 1 mM EDTA) supplemented with 5 mM Dithiothreitol (DTT), 50 mM KCl and an equimolar amount of phalloidin. Samples of increasing F-actin concentration ($0 - 50$ µM) were incubated with 1 µM GFP-TipAct at RT for 1 hr. Thereafter, free and F-actin-bound fractions were separated by high-speed centrifugation at 149,000 RCF for 30 min at RT. Pellet and supernatant samples were brought to the same final volume, and prepared for SDS-PAGE. The free and bound GFP-TipAct fractions were measured with the *Gel Analyzer* tool in FIJI [442]. The dissociation constant (K_d) of GFP-TipAct for F-actin was estimated by fitting the data in Fig. 3.5 to Eq. (3.1) using the *Curve Fitting Toolbox* in Matlab [469].

3.5.6 Plus-end tracking assays

In all the assays shown in this chapter, microtubules were polymerized with 16 µM tubulin (always at a ratio of 1:15 labeled to unlabeled subunits), 100 nM EB3 (where applicable), and 50 nM GFP-TipAct. TIRF microscopy imaging was performed at 25°C (Table 2.1). We refer the reader to Chapter 2 for the general details on how these assays were built.

3.6 Data analysis

3.6.1 Analysis of microtubule dynamic instability

The parameters of microtubule dynamic instability (Table 3.1) were determined by producing kymographs of microtubule growth (such as in Fig. 3.7 a), obtained with the *reslice* tool in FIJI [442]. These kymographs were used to manually trace the position of the seed and the microtubule tip over time, using the *segmented line* tool in FIJI. The data was analyzed with custom-built programs in Matlab to calculate the parameters of dynamic instability; namely, growth and shrinkage speed, and catastrophe and rescue frequency. The average growth and shrinkage speeds for a given experiment were obtained by weighing the individual speeds by the time that microtubules spent growing or shrinking at such speeds [104]. Catastrophe and rescue rates were obtained by dividing the total number of each event by the total time that the microtubules spent growing or shrinking. We only counted catastrophes when we could image the microtubule from the point of nucleation at the seed up until a catastrophe. The error in this case is given by the frequency divided by the square-root of the number of events [104]. All the values in Table 3.1 represent the average ± standard deviation for each parameter, from three to five experiments performed under identical conditions.

3.6.2 Analysis of TipAct plus-end intensity

The plots of GFP-TipAct and mCherry-EB3 plus-end intensity shown in Figures 3.7, 3.9 and 3.10 were obtained by tracing a two-pixel-wide line along the length of the microtubule. These values were normalized by the corresponding microtubule lattice intensity, which was obtained by averaging over a $2-5$ µm region at least 1 µm away from the peak of the comet intensity. To compare the intensity of TipAct plus-end comets at free and actin-bound microtubule tips (Fig. 3.10), the individual traces were first aligned so that the location of their peak value co-localized. Thereafter, these individual curves were averaged to obtain an estimate of the mean ± standard deviation of the TipAct intensity in both cases.

We thank Anna Akhmanova (Utrecht University, The Netherlands) and Michel O. Steinmetz (Paul Scherrer Institute, Switzerland) for advice in the design of TipAct. We thank Carol Yu, Babet van der Vaart (Eramus MC, The Netherlands), and Cristina Manatschal (Paul Scherrer Institute), for help in the cloning and purification of TipAct. We thank Florian Huber (FOM Institute AMOLF) for help with the co-sedimentation assays, and Ilya Grigoriev (Utrecht University) for help with live-cell imaging.

Chapter 4

Guidance of microtubule growth and organization by F-actin

In this chapter we study interactions between dynamic microtubules and actin filament bundles. We find that microtubule growth can be deflected by actin bundles through steric interactions in the absence of TipAct, or captured and guided via a zippering mechanism when TipAct is present. Microtubule zippering stems from TipAct's stable association with actin bundles, which recruits EB to the microtubule lattice in regions of actin-microtubule overlap. FRAP experiments reveal that both EB and TipAct's off rates are reduced in these regions, explaining the stability of the actin-microtubule connection. We further study the geometrical constraints on microtubule capture and guidance, and find that zippering via TipAct is more efficient than the deflection mechanism mediated by steric effects. Reducing the TipAct concentration shows that efficient microtubule guidance requires that the microtubule is coupled to the actin bundle all along its length. Finally, we demonstrate that TipAct allows sparse arrays of parallel F-actin bundles to globally dictate microtubule organization.

4.1 Introduction

Actin-microtubule coordination is essential for a variety of cellular processes, and in order to achieve this cells have evolved a variety of cross-talk mechanisms that are mediated by physical cross-linkers as well as signaling molecules [260]. One of the most studied instances of actin-microtubule coordination in cells consists of guidance of

microtubule growth by bundles of F-actin. This for example occurs in cell migration, where growing microtubules are targeted by the +TIP MACF along actin stress fibers towards focal adhesions (FAs) [279]. Microtubule targeting to FAs has been shown to control their disassembly [344, 364, 365], an essential requirement for cell motility [279]. FA disassembly is also regulated by the +TIP CLASP, which anchors the MACF-targeted microtubules at the cortex, in the vicinity of the FA site [87, 342]. These CLASP-anchored microtubules become tracks for the kinesin-1 dependent [343] delivery of factors involved both in endocytosis of FA components [470] and in extra-cellular matrix degradation [342].

Another important example of microtubule guidance by actin bundles occurs in extending neurons. In this situation, growing microtubules are targeted by the +TIP Shot along parallel actin bundles inside filopodia at the growth cone periphery [291, 354]. Local disruption of filopodial actin bundles or microtubules results in growth cones turning away from the site of drug application [370, 471]. It is thus widely accepted that cross-talk between filopodial actin bundles and microtubules controls the direction of growth cone extension [291, 354, 465]. However, the mechanisms by which filopodia selectively capture microtubules that invade the growth cone peripheral domain [291], and the ways by which these microtubules aid filopodia to steer a growth cone are hitherto unclear. When filopodial actin bundles are globally disrupted (without disturbing the dendritic actin meshwork that surrounds them), microtubules can indiscriminately invade the entire peripheral zone [373]. Although it has been speculated that filopodial roots acts as gates that limit the entrance into the peripheral domain [373], the mechanisms by which they would do so remain unresolved.

Even though in both examples outlined above the nature of the cross-linkers at play is known, our understanding of the ways by which they efficiently capture and guide microtubules is however incomplete. In both instances, the F-actin bundles are surrounded by a crowded environment, be it the cell interior (as in the case of stress fibers), or the lamellipodial F-actin network (as in the case of filopodial actin bundles). This raises a few questions: How do microtubules find their F-actin tracks? What is the dependency of microtubule capture and guidance on the cross-linker concentration? What are the mechanical and geometrical constraints for a microtubule to be deflected by an F-actin bundle?

Understanding the mechanisms that regulate efficient microtubule capture, as well as the geometrical and mechanical constraints that actin-microtubule cross-linkers have to offset in order to allow actin bundles to guide microtubule growth, could shed some

light onto these questions. To this end, we decided to study microtubule interactions with fascin-stabilized F-actin bundles, in the presence of EB3 and our model cross-linker TipAct. This chapter contains the results of these experiments.

4.2 TipAct and EB3 couple microtubule growth to F-actin bundles

In Chapter 3 we observed that our engineered actin-microtubule cross-linker, TipAct, can generate connections between microtubule growing ends and actin filaments (Fig. 3.9 a). This type of interactions occurred even at TipAct concentrations 100-fold lower than its dissociation constant from F-actin ($K_D \sim 5$ µM, Fig. 3.5). This observation reveals that TipAct's locally-enhanced concentration at microtubule tips (generated by EB3) can become sufficiently high to offset its low affinity for F-actin, thus allowing microtubules to bind F-actin. Furthermore, in these instances of actin-filament crosstalk with microtubule tips, we observed that the actin filament always co-aligned with the growing microtubule (Fig. 3.9 b). This can be explained by the 100-fold higher bending stiffness of microtubules ($EI_{MT} \sim 8$ pN µm^2 [89–91, 174]) compared to that of single actin filaments ($EI_{AF} \sim 0.04 - 0.07$ pN µm^2 [162, 174, 175, 472]).

Given these observations, we sought to test the hypothesis that bundled actin filaments, with an effectively higher bending stiffness [473, 474], would in turn act as guides for microtubule growth. To this end, we polymerized microtubules from GMPCPP-stabilized microtubule seeds, in the vicinity of bundles of F-actin stabilized by fascin, in the presence of 100 nM EB3 and 25-50 nM GFP-TipAct. The top panel in Figure 4.1 shows a schematic of theis assay.

In stark contrast to the microtubule-dependent interactions with single actin filaments (in otherwise identical experimental conditions), we observed that TipAct stably and independently associated with the F-actin bundles (Fig. 4.1, bottom panel). This could either be the result of the locally-increased F-actin concentration that results from bundling, or of TipAct having a different affinity for actin bundles *versus* single filaments. The latter effect has been reported of Dystrophin [475], a closely related protein to MACF (and hence TipAct), which contains a homologous tandem calponin-homology actin-binding domain [309]. In the case of TipAct an avidity effect could also be at play, since TipAct is a parallel homodimer, so that when bound to two actin filaments its

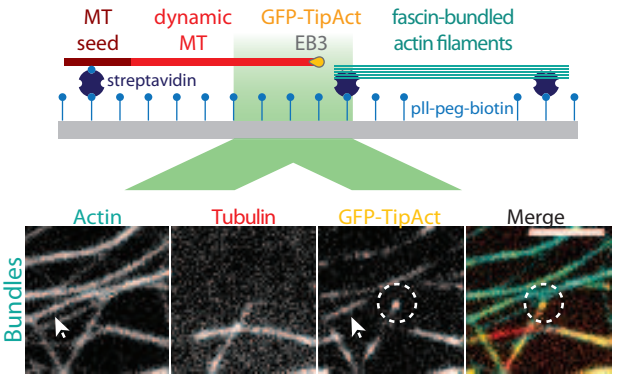

Figure 4.1: Experimental setup to study interactions between microtubules and F-actin bundles. Top, microtubules were polymerized from GMPCPP-stabilized seeds, in the presence of EB3, GFP-TipAct, and surface-bound F-actin filaments stabilized by fascin. Bottom, in these experiments TipAct localized both at microtubule tips (dashed circles) and at F-actin bundles (arrows). Scale bar, 5 µm. MT, microtubule.

effective off-rate could be reduced, and hence its affinity for actin bundles *versus* single filaments effectively increased.

We found that TipAct at F-actin bundles could also recruit mCherry-EB3 to these bundles (albeit weakly), even in the absence of microtubules (Fig. 4.2 a). In contrast, we never observed mCherry-EB3 recruitment to actin bundles when we replaced TipAct with a very similar protein construct (GFP-Tip) that lacked the actin-binding domain altogether (Fig. 4.2 b, [107]).

When we monitored microtubule growth in these assays, we observed that the enhanced TipAct (and hence EB3) localization at F-actin bundles was sufficient to force microtubule growth to proceed in tight association with the bundle (an effect we call *zippering*). Panel a in Figure 4.3 shows a montage of one such microtubule (whose plus-end is indicated by white arrowheads). Kymographs of *zippering* microtubules (Figure 4.3 b) revealed that the TipAct-dependent recruitment of mCherry-EB3 at F-actin bundles was further enhanced in regions of actin-microtubule overlap (Fig. 4.3 c). These observations suggest that actin-microtubule overlaps can have a stabilizing effect on the exchange dynamics of EB3 at microtubules and of TipAct at actin bundles. This effect is likely to enhance the strength of the actin-microtubule connection.

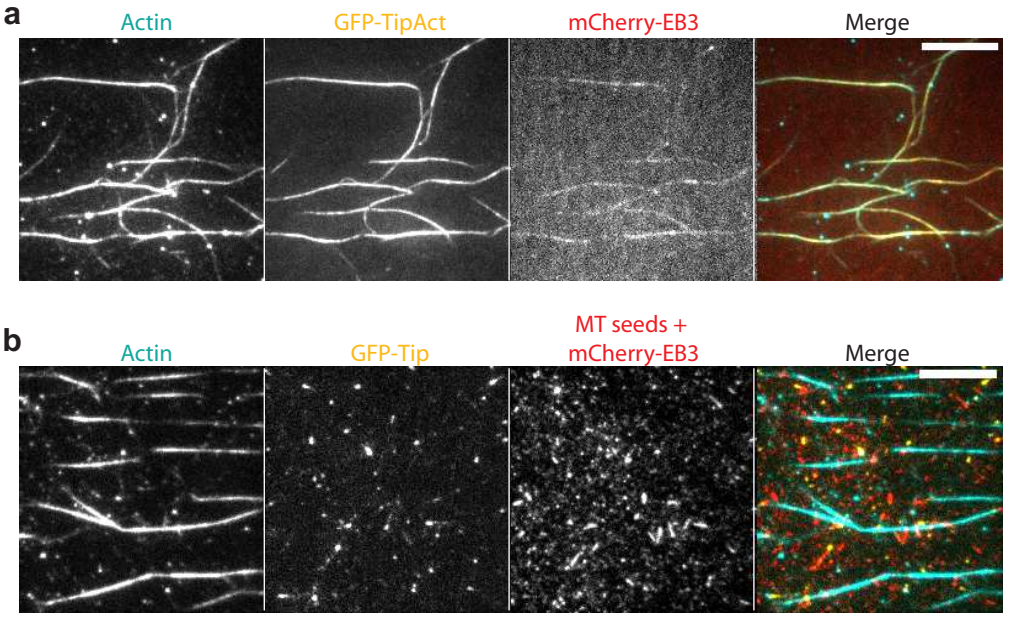

Figure 4.2: TipAct recruits EB3 to actin bundles, while a similar protein (GFP-Tip) lacking the actin-binding domain does not. (a) GFP-TipAct recruits mCherry-EB3 to fascin-stabilized F-actin bundles even in the absence of microtubules. (b) A protein construct similar to GFP-TipAct but which lacks the actin-binding domain does not localize to the F-actin bundles nor recruit mCherry-EB3 to these bundles. Scale bars, 10 µm. MT, microtubule.

4.3 EB3 and TipAct have reduced off-rates at actin-microtubule overlaps

In order to test whether the establishment of an actin-microtubule connection affects EB3 and TipAct's turnover rates, we performed high-temporal-resolution (33 ms/frame) fluorescence recovery after photobleaching (FRAP) experiments on free and actin-bound microtubule tips, as well as on free and microtubule-bound actin bundles, and tracked the fluorescence recovery of mCherry-EB3 and GFP-TipAct in all cases.

We found that both mCherry-EB3 and GPF-TipAct exchanged quickly at free microtubule growing ends (Fig. 4.4). A fit to the average fluorescence-recovery data (red curves in Fig. 4.4 b and c) to Equation (4.1) yielded an off-rate for mCherry-EB3 of $k_{off-EB:MTtip} \sim 1.8\ \mathrm{s}^{-1}$, and for GFP-TipAct of $k_{off-TA:MTtip} \sim 3.1\ \mathrm{s}^{-1}$, consistent with previously reported values of EB and +TIP exchange at microtubule growing ends [98, 100]. In the case of actin-bound microtubule tips, however, we found that fitting the fluorescence recovery data (blue curves in Fig. 4.4 b and c) with a single off-rate resulted in a poor fit to the data. We thus fit the recovery with two distinct off-rates (Eq. (4.2)),

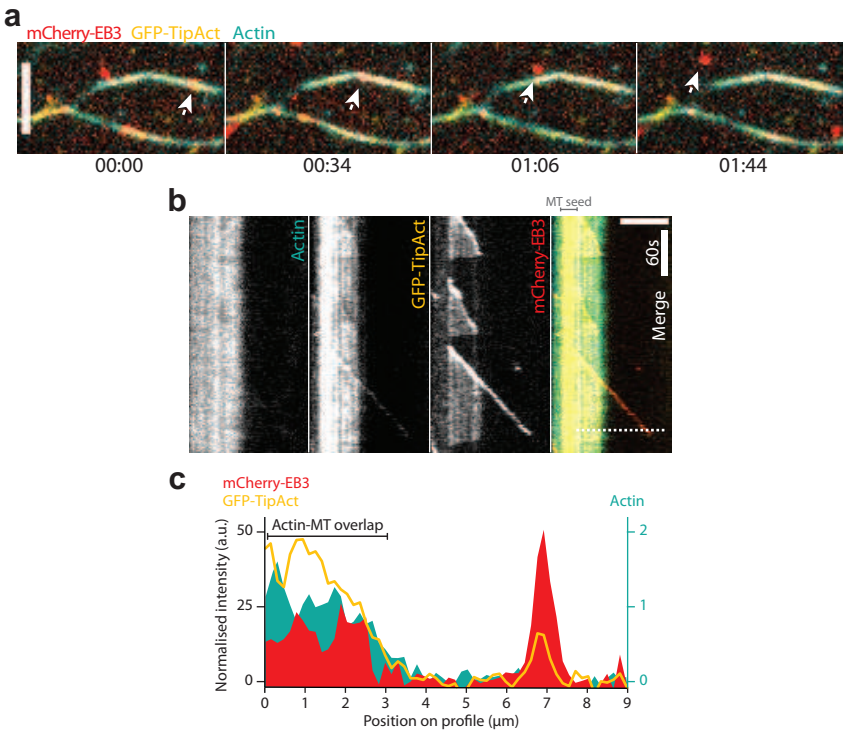

Figure 4.3: TipAct links microtubule growth to F-actin bundles. (a) Time series of an experiment as in Figure 4.1. Arrows show the plus-end of a microtubule that grows along an F-actin bundle with which it was initially co-aligned. (b) Kymograph of the microtubule indicated by arrows in (a). TipAct localizes at the F-actin bundle, and its fluorescence intensity increases in regions of actin-microtubule overlap. mCherry-EB3 localizes at microtubule tips, but also on the microtubule lattice in regions of actin-microtubule overlap. (c) Fluorescence intensity along the dashed line on the kymograph in (b), showing the accumulation of TipAct and EB3 at actin-microtubule overlaps. The GFP-TipAct and mCherry-EB3 intensities were normalized by their mean values at the free microtubule lattice, and the actin intensity by its mean value. Scale bars, 5 µm. Time: min:sec. MT, microtubule.

in order to separately account for the fraction of EB3 and TipAct not interacting with the actin bundle, and the fraction that was in contact with both microtubule tip and bundle. This revealed that the fraction of EB3 and TipAct linking the microtubule to the actin bundle exchanged three to five times slower ($k_{off-EB:MTtip-AB} = 0.8$ s^{-1}, and $k_{off-TA:MTtip-AB} = 0.7$ s^{-1}). It is worth noting that when we tried to fit the recovery data for free microtubules with two rates (Eq. (4.2)), we obtained the same value for both rates, confirming that in this situation there is only one exchanging species. As a direct consequence of the reduced off-rates of EB3 and TipAct at actin microtubule overlaps, we found that their plus-end intensity decayed to the steady-state microtubule lattice value two times slower compared to how it decayed at free microtubules. In all cases analyzed we verified that after bleaching the microtubule growth speeds remained the same (as can be observed in the example kymograph in Fig. 4.4 a). Thus, the

increased steady-state intensity of TipAct and EB3 at actin-microtubule tip overlaps can only be explained by effectively reduced off-rates. Panel d in Fig. 4.4 shows a summary of the measured rates in all cases, as obtained from fits to Equations (4.1) and (4.2).

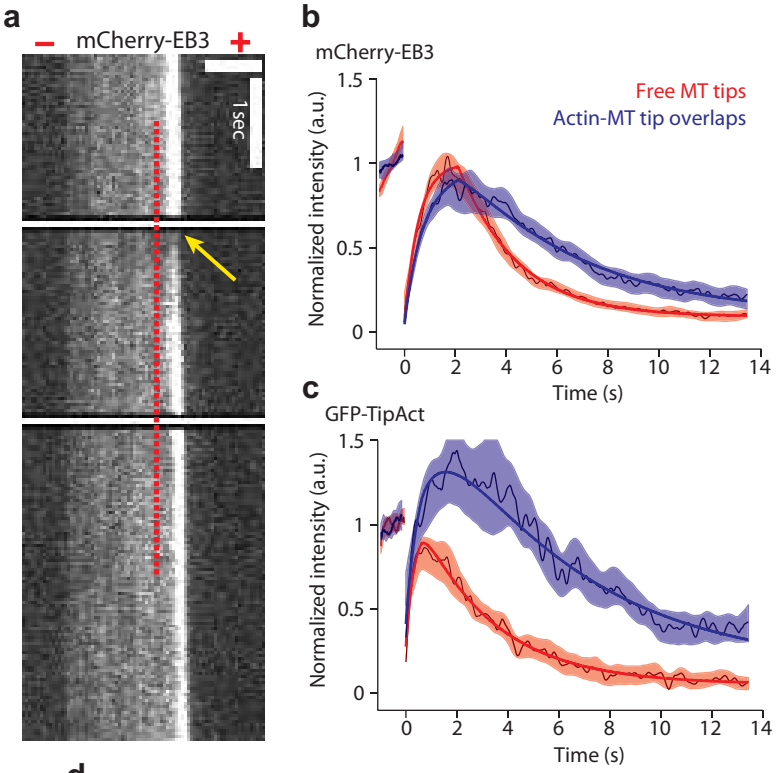

d

Protein	$k_{off\text{-}MTtip}$ (1/s)	$k_{decay\text{-}MTtip}$ (1/s)	$k_{off\text{-}MTtip}$ (1/s)	$k_{off\text{-}MTtip\text{-}AB}$ (1/s)	$k_{decay\text{-}MTtip\text{-}AB}$ (1/s)
mCherry-EB3	1.8	0.4	Fixed at 1.8	0.8	0.2
GFP-TipAct	3.1	0.3	Fixed at 3.1	0.7	0.2

Figure 4.4: FRAP experiments at microtubule plus-ends. (a) High temporal resolution (33 ms/frame) kymograph of microtubule growth showing the mCherry-EB3 intensity at the plus (+) end of a growing microtubule. The white horizontal line crossing the top of the kymograph indicates the bleaching frames, the yellow arrow the spot that was bleached, and the red-dashed line (shifted to the left of the mCherry-EB3 signal for ease of view), how the FRAP data was retrieved. Analysis of recovery curves for mCherry-EB3 (b) and GFP-TipAct (c) both at free (red) and actin-bound (blue) microtubule tips. The solid lines show the fits to Eq.(4.1) and Eq.(4.2), respectively. The thin colored lines and shaded areas show the average curves and SEM for n = 19 (free) and n = 13 (actin-bound) recovery profiles for mCherry-EB3, and n = 7 (free) and n = 6 (actin-bound) recovery profiles for GFP-TipAct respectively. Note that the maximum recovery intensity of GFP-TipAct at actin-bound microtubule tips reaches values larger than one due to the variable amount of GFP-TipAct that can localize to the F-actin bundles independently of microtubules. (d) Table showing the parameters obtained from the fits. Scale bar, 3 µm. MT, microtubule; AB, actin bundle.

Moreover, we found that GFP-TipAct stably associated with the F-actin bundles (both

free and microtubule bound), showing no recovery in either case within the timescale of observation ($k_{off-TA:AB} \leq 0.07$ s^{-1}, red and blue curves in Fig. 4.5 a and c). In contrast, mCherry-EB3 was dynamic in both cases (Fig. 4.5 b). In the case of free actin bundles (in the absence of microtubules), we fit the recovery data of EB3 (red curves in Fig. 4.5 b), with a single off-rate (Eq. (4.3)). This revealed that EB3 and TipAct do not form an irreversible complex in solution, as they dissociate in a timescale of seconds ($k_{off-EB:AB} = 0.3$ s^{-1}, Eq. (4.3)). Similar to the analysis at microtubule tips, we fit the recovery of EB3 at actin-bound microtubules (blue curves in Fig. 4.5 b), with two recovery rates (Eq. (4.4)), to separately account for the fraction of EB3 in contact with both microtubule and actin bundle, and the fraction of EB3 only in contact with the microtubule. The fraction of EB3 that only interacted with the microtubule lattice exchanged fast ($k_{off-EB:MT} = 2.2$ s^{-1}), consistent with previous reports [98]. In contrast, when bound to both microtubule lattice and actin bundle, EB3 exchanged 20 times slower ($k_{off-EB:AB-MT} \sim 0.1$ s^{-1}). Panel d in Fig. 4.5 shows a summary of the measured rates in all cases, which were obtained from fits to Equations (4.3) and (4.4).

The schematics in Figure 4.6 help us interpret these results: First, at free microtubule tips the exchange rate of EB3 and TipAct is dominated by the off-rate of EB3, which is approximately six-fold higher ($k_{off-EB:MTtip} = 1.8$ s^{-1}) than the dissociation rate of EB3 and TipAct ($k_{off-EB:AB} = 0.3$ s^{-1}). Second, TipAct's stable localization at actin bundles ($k_{off-TA:AB} < 0.07$ s^{-1}), results in the fraction of EB3s in contact with both microtubule and bundle to exchange five to twenty times slower ($k_{off-EB:MTtip-AB} = 0.8$ s^{-1}, $k_{off-EB:MT-AB} = 0.1$ s^{-1}) than they normally do on free microtubules. The FRAP experiments thus revealed two important things: first, that EB3 and TipAct do not form an irreversible complex in solution; and second, that the way by which EB3 and TipAct mediate stable linkages between actin bundles and microtubules stems from TipAct's stable localization at the actin bundles, which in turn leads to a reduced off-rate of EB3 in regions of actin-microtubule overlap.

4.4 Actin bundles capture and redirect growing microtubules

In the previous section we observed that TipAct's stable association with F-actin bundles has a stabilizing effect on EB3 in regions of actin-microtubule overlap. This helps explain how TipAct and EB3 efficiently couple microtubule growth to actin bundles (Fig. 4.3).

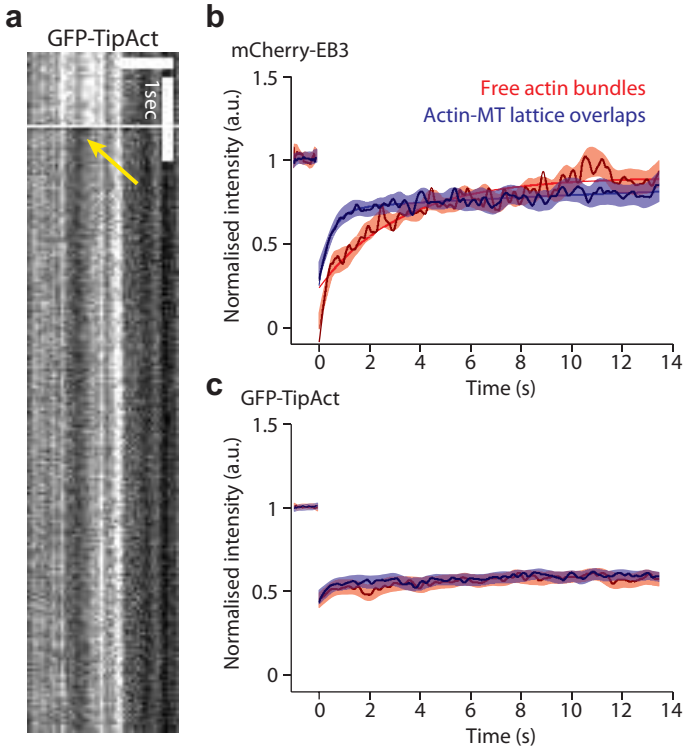

d

Protein	$k_{off\text{-}AB}$ (1/s)	$k_{off\text{-}MTlatt}$ (1/s)	$k_{off\text{-}AB\text{-}MTlatt}$ (1/s)
mCherry-EB3	0.3	2.2	0.1

Figure 4.5: FRAP experiments at F-actin bundles. (a) High temporal resolution (33 ms/frame) kymograph of GFP-TipAct on an actin bundle. The white horizontal line crossing the top of the kymograph indicates the bleaching frames and the yellow arrow the spot that was bleached. Analysis of recovery curves for mCherry-EB3 (b) and GFP-TipAct (c) both at free (red curves) and microtubule-bound (blue curves) actin bundles. The solid lines in (b) show the fits to Eq.(4.3) and Eq.(4.4), respectively. We did not fit the GFP-TipAct data since it showed no recovery in the timescale of observation. The thin colored lines and shaded areas show the average curves and SEM for n = 12 (free) and n = 17 (actin-MT overlaps) recovery profiles for mCherry-EB3, and n = 19 (free) and n = 19 (actin-MT overlaps) recovery profiles for GFP-TipAct, respectively. (d) Table showing the parameters obtained from the fits. Scale bar, 3 µm. MT, microtubule; AB, actin bundle.

However, as mentioned in the introduction, another key unanswered question in the study of actin-microtubule interactions, is what are the geometrical and mechanical constraints that cross-linkers, such as MACF and Shot, have to overcome in order to capture and redirect microtubule growth. We thus set out to test if the actin-to-microtubule linkages mediated by TipAct and EB3 could be sufficiently strong to offset the mechanical energy cost involved in deforming a microtubule that does not start-off parallel to the F-actin bundle.

To this end, we polymerized microtubules with 100 nM EB3, in the presence and absence

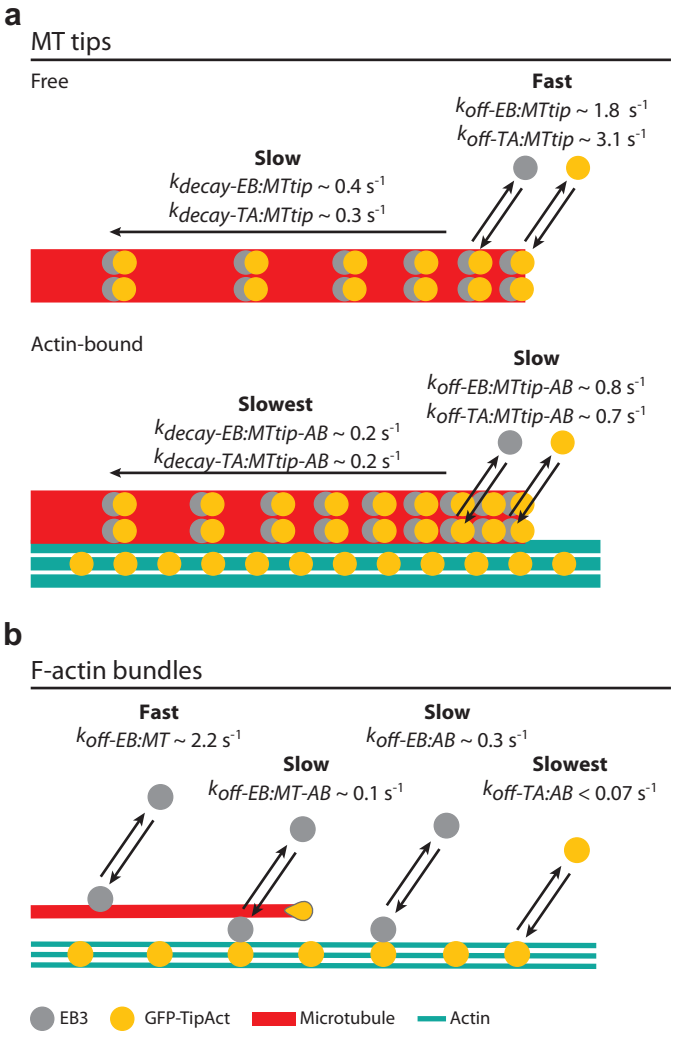

Figure 4.6: Schematics to interpret the FRAP experiments. (a) Top, at free microtubule tips, EB3 and TipAct exchange in less than 1 sec, while their intensity decays to the steady-state lattice value in $\sim 2-3$ sec. Bottom, at actin-bound microtubule tips, both EB3 and TipAct exchange more slowly, in $\sim 1-2$ sec. This results in a slower transition to the steady-state lattice intensity, in ~ 5 sec. (b) TipAct is basically *fixed* at the F-actin bundles, and recruits EB3, which exchanges in ~ 3 sec, even in the absence of microtubules. At actin-microtubule overlaps, the fraction of EB3 in contact with both the microtubule and the actin bundle exchanges even slower, in ~ 10 sec. In contrast, the fraction of EB3 only in contact with the microtubule exchanges in less than 1 sec.

of 50 nM GFP-TipAct, in the vicinity of F-actin bundles stabilized by fascin (in an assay as in Fig. 4.1). As in the previous assays, we included 0.1 % (v/v) methyl-cellulose to confine microtubule and actin-bundle out-of-plane fluctuations, allowing us to have a quasi two-dimensional system. In the presence of TipAct, microtubules were often captured by the F-actin bundles, which furthermore were able to deflect the microtubule tip so that all subsequent growth *zippered* along the bundle (Fig. 4.7 a). For microtubules that encountered the actin bundles at high angles, this resulted in sharp bends of the microtubule lattice near the point of first contact. This observation is reminiscent of recent studies of microtubule guidance by actin stress-fibers in cells cultured on adhesive micro-patterns, in which microtubules were also observed to sustain sharp deformations [368]. Likely due to the quasi two-dimensional geometry of our assays, we found that in the absence of TipAct, microtubules could also be guided by the actin bundles. However, in contrast with the sharp deformations observed in the presence of TipAct, these microtubules bent smoothly all along their length (Fig. 4.7 b). In this situation, the microtubule tip was likely *deflected* by repeated collisions with the F-actin bundle. This type of steric interactions are typically used by plant cells to organize the cortical microtubule arrays [295].

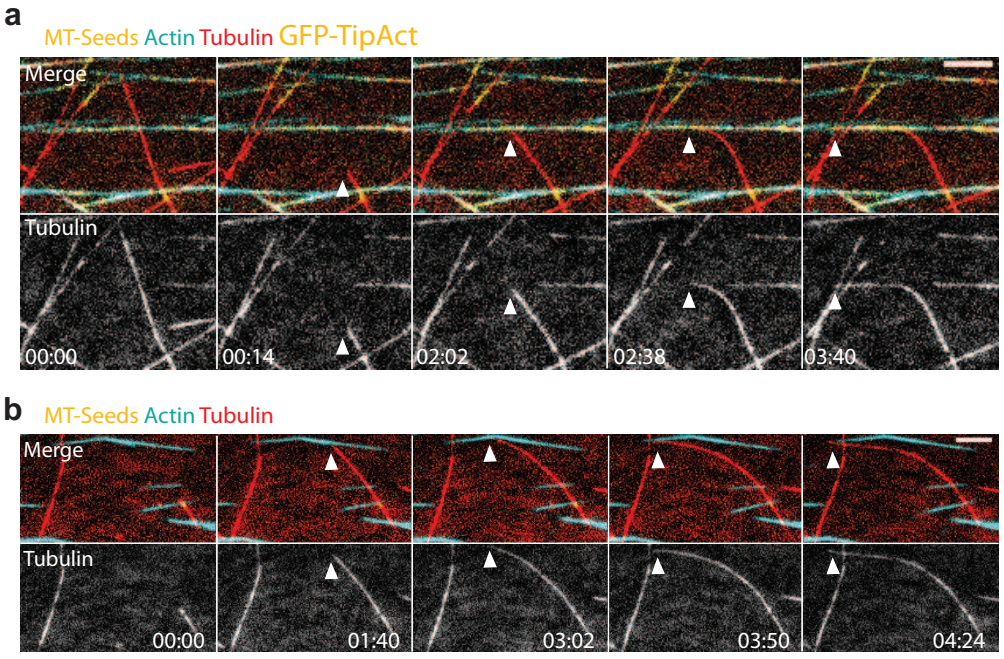

Figure 4.7: Two different mechanisms of microtubule guidance by F-actin bundles. (a) Time series of a microtubule grown with GFP-TipAct that is captured and then zippers along an F-actin bundle as it continues to grow. (b) Time series of a microtubule grown without GFP-TipAct, whose tip is mechanically deflected by an F-actin bundle as it continues to grow. In (a) and (b) the plus-ends of the microtubules are indicated by arrowheads. Scale bars, 10 µm. Time, min:sec. MT, microtubule.

Microtubules have an approximately 100-fold higher-bending stiffness ($EI_{MT} \sim 8$ pN µm^2 [89–91, 174]) compared to single actin filaments ($EI_{AF} \sim 0.04 - 0.07$ pN µm^2 [162, 174, 175, 472]), which indicates that the mechanical bending stiffness provided by actin-bundling can become comparable to that of a microtubule, so that the microtubule is deformed by the actin bundle and not the other way around. *In vitro* studies on fascin-bundled actin filaments have shown that the bending stiffness of these bundles increases both with the molar ratio of fascin to G-actin, and with the number of actin filaments in the bundle [473, 474]. In our assays, we kept the fascin to G-actin molar ratio between 1:2 and 1:5, which would correspond to an actin-bundle bending stiffness, EI_{AB}, in the range of $2 - 30$ pN µm^2 if 6-30 actin filaments were present in the bundles [473]. Although we did not measure the number of actin filaments independently, this range of values is already comparable to the bending rigidity of a microtubule. It is worth noting that in addition to the mechanical stabilization that stems from bundling F-actin, the actin bundles were also anchored to the coverslip surface, which acts to reduce their mobility and further enhance their *effective* bending rigidity.

These results show that microtubule growth can be captured and redirected by actin bundles via *zippering* with, and *deflection* without, TipAct. Furthermore, that capture and guidance can lead to mechanical deflection of the microtubule lattice (either locally with TipAct, or all along its length without it). Next, we wanted to understand under what conditions capture and guidance would occur in both cases. To this end, we monitored microtubule tip encounters with actin bundles, and characterized the outcome of these interactions into three categories, in a similar fashion as how interactions between plant cortical microtubules have been analyzed [295]: catastrophe, cross-over, and zippering or deflection, with or without TipAct respectively (Fig. 4.8 a). We studied the probability of these outcomes as a function of microtubule length L_{MT}, and intersection angle θ, between the microtubule and the F-actin bundle at the point of first contact (Fig. 4.8 a).

As discussed above, without TipAct, microtubules were deflected by collisions of their growing tip with the actin bundles. This effect was dominant at shallow angles ($< 5°$), occurred approximately 50% of the cases for intermediate angles ($5 - 25°$), and was rare at encounter angles $> 25°$ (Fig. 4.8 b). In contrast, with TipAct, the probability of zippering dominated the outcomes up to encounter angles of $\sim 25°$ (Fig. 4.8 c). Furthermore, capture of microtubule ends by TipAct reduced the probability of microtubule catastrophe induced by collisions [93] at small encounter angles (Fig. 4.8 c), and made capture insensitive to microtubule length (Fig. 4.8 d). This is in contrast to the deflection mechanism without TipAct, which was dependent (albeit weakly) on microtubule length

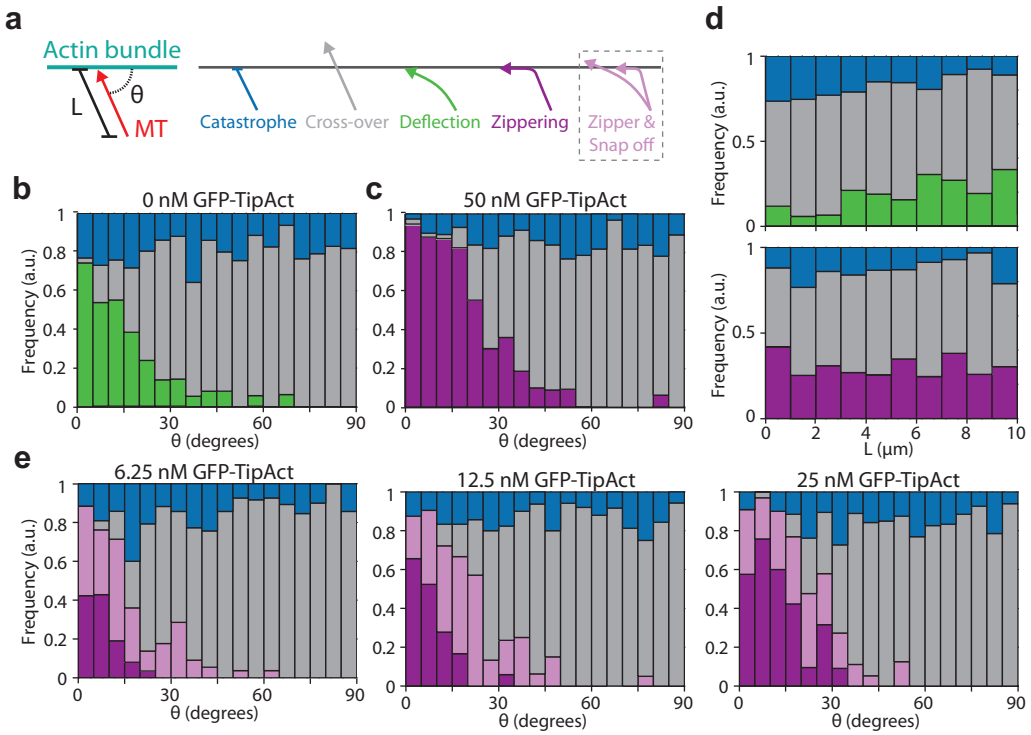

Figure 4.8: Probability of microtubule guidance by deflection *versus* zippering. (a) Classification of the interaction outcomes between growing microtubules and F-actin bundles, and how the intersection angle θ and microtubule length L were defined. Probability of each interaction outcome as a function of θ, with (c) or without (b), 50 nM GFP-TipAct. (d) Probability of each interaction outcome as a function of L, with (bottom) or without (top) 50 nM GFP-TipAct. (e) Probability of each interaction outcome as a function of θ for variable GFP-TipAct concentrations. For each of the following conditions: 0, 6.25, 12.5, 25 and 50 nM GFP-TipAct, n = 708, 459, 421, 443 and 914 interactions were analyzed respectively. The data in (b) and (c) was obtained from n = 9 and 6 experiments, respectively.

(Fig. 4.8 d), since in this case catastrophes occurred more often, especially for short microtubules. These observations highlight the mechanical component of microtubule capture and deflection, as well as the probability that during growth a microtubule is very likely to *miss* the F-actin track (especially at high angles), through spatial fluctuations of the microtubule tip in the z-direction. We anticipate that in the crowded, three-dimensional environment of the cell, capture and guidance of microtubules by actin bundles via steric effects is likely to be even less common than in the quasi two-dimensional geometry of our assays.

4.4.1 Dependency of microtubule guidance on TipAct concentration

In order to test the contributions of microtubule tip and lattice to the capture and guidance mechanism of TipAct, we performed further experiments with decreasing amounts of TipAct while keeping the EB3 concentration constant. In these situations we found that a new interaction outcome had to be added to the classification, namely *zipper & snap-off* (Fig. 4.8 a), since with decreasing TipAct concentration an increasing portion of microtubules eventually *snapped-off* the F-actin track. This occurred at both high and shallow encounter angles (Fig. 4.9 a and b), although the angular dependency of initial capture remained approximately the same (Fig. 4.8 e). Furthermore, at the lowest concentration of TipAct used (i.e. 6.25 nM), we found that a large fraction of microtubules interacted with the actin bundles solely via their growing tips (Fig. 4.9 c), resulting in a guidance mechanism nearly indistinguishable from that of mechanical deflection (Fig. 4.7 b), when TipAct was fully absent.

Put together, these observations indicate that the energy required to redirect a microtubule can be efficiently overcome when a sufficient amount of cross-linkers is present. Although guidance of microtubule growth can occur by purely steric effects (Fig. 4.7 b), in these situations the microtubule is forced to traverse the space next to the bundle. We speculate that in the crowded, three-dimensional geometry of the cell interior this mechanism of microtubule guidance is unlikely to be efficient, as microtubules will be very likely to lose their F-actin tracks. Although the microtubule tip plays a key role in the initial capture event (since we never observed a microtubule aligning with an actin bundle that it had initially crossed-over), decreasing the amount of TipAct revealed that when the density of cross-linkers is not high enough, captured microtubules are more susceptible to detach from the actin bundles. Therefore, the presence of a sufficiently-high density of cross-linkers, at the actin-microtubule overlap, is a requirement for microtubule growth to proceed in tight association with F-actin. This effect could act to protect the microtubule tip from the many obstacles ubiquitous to the crowded interior of the cell, and is likely to be one of the most efficient ways to reliably target microtubule growth to particular sites in the cell; such as focal adhesions at the end of actin stress-fibrers [279, 344, 364], or to the ends of filopodia [291, 354, 465].

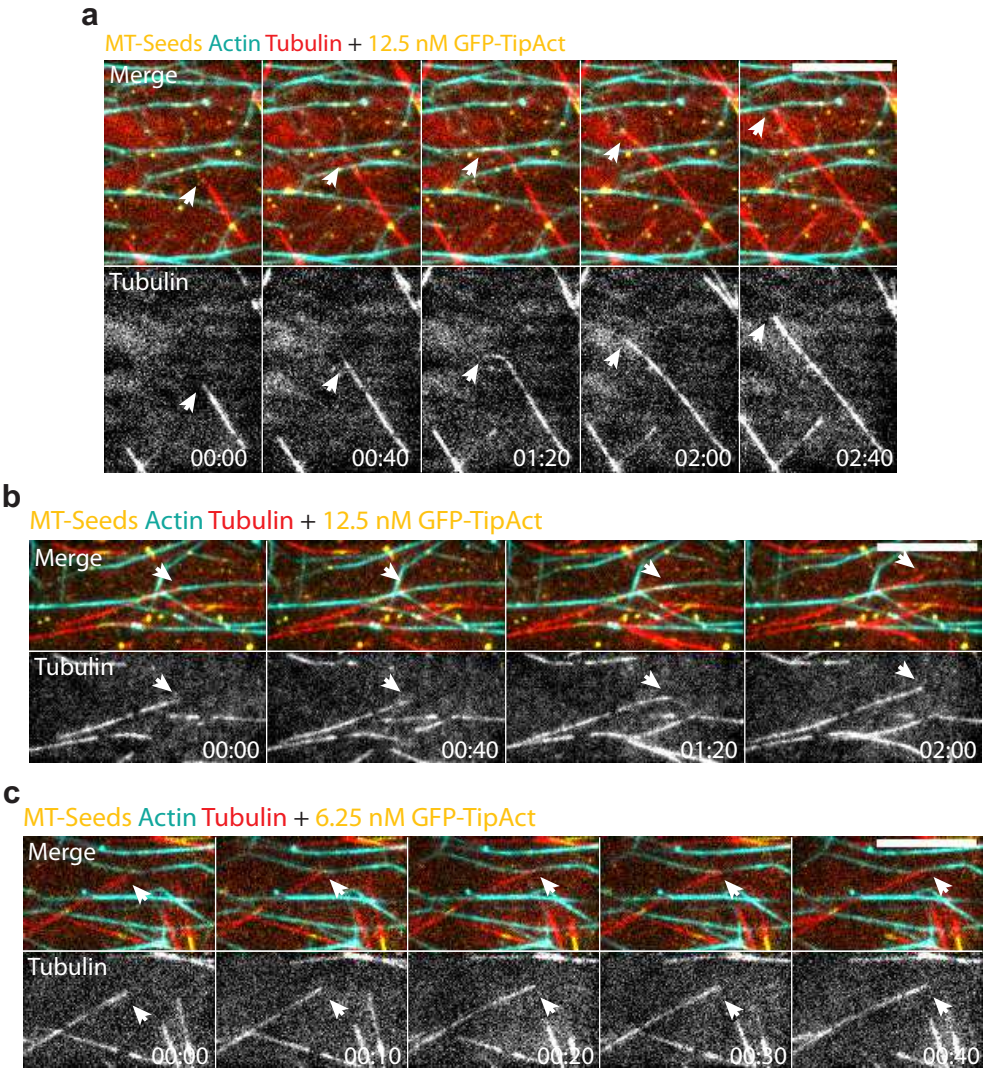

Figure 4.9: Dependency of microtubule guidance on TipAct concentration. Time series of microtubules grown with 12.5 nM GFP-TipAct, which encounter an actin bundle both at high $\sim 62°$ (a), and shallow $\sim 17°$ (b) angles, both of which begin to zipper but eventually snap-off. (c) Time series of a microtubule grown with 6.25 nM GFP-TipAct which follows the F-actin bundle only with its growing tip. In (a), (b) and (c) the plus-ends of the microtubules are indicated by arrowheads. Scale bars, 10 µm. Time, min:sec. MT, microtubule

4.5 Ordered arrays of F-actin bundles can globally dictate microtubule organization

It has been shown that actin-microtubule cross-linking +TIPs such as MACF, CLASP and APC, are necessary to establish parallel arrays of microtubules perpendicular to the cell edge [123, 279, 332, 335, 340]. Organizing microtubules in such a way facilitates the polarized transport of vesicles and proteins to the leading edge of motile cells, and to maintain directional cell migration [476]. Given that both mechanical effects and physical cross-linking by EB3 and TipAct allow F-actin bundles to guide microtubule growth (Fig. 4.7), albeit with different efficiency (Fig. 4.8), we wondered to what extent these effects would allow a well-defined F-actin bundle architecture to globally dictate microtubule organization. To this end, we generated sparse arrays of parallel F-actin bundles stabilized by fascin, interspersed with randomly oriented GMPCPP-stabilized microtubule seeds. As in the previous assays, we polymerized microtubules in quasi two-dimensional confinement by the addition of 0.1 % (v/v) methyl-cellulose, in the presence of 100 nM EB3, with or without 50 nM GFP-TipAct. Under these conditions, the average microtubule length ($\langle L_{MT} \rangle$) continuously increased (Fig. 4.16), which allowed us to monitor the temporal evolution of actin-microtubule co-alignment as a function of $\langle L_{MT} \rangle$.

The left-most panels in Figure 4.10 a show two examples of the F-actin bundle arrays we could generate, and the second and third panels the initial ($t \sim 5$ min) and final ($t \sim 1$ hr) arrays of dynamic microtubules that ensued in the presence (top), or absence (bottom), of TipAct. In both cases, at the early stages of the experiment the microtubules already adopted an average orientation angle that weakly corresponded to that of the underlying F-actin bundle array. In later stages, however, while the microtubules grown in the presence of TipAct maintained their alignment with the actin bundles, a large number of microtubules grown in the absence of TipAct were oriented at random angles relative to the mean actin bundle orientation. Plots of the distribution of microtubule orientation angle (θ_{MT}) over time, revealed that both with and without TipAct, the microtubule arrays became increasingly aligned about the mean F-actin angle ($\langle \theta_{ACTIN} \rangle$, Fig. 4.10 b). However, and in agreement with the fluorescence images shown in Figure 4.10 a, with TipAct the final peak of the distribution of θ_{MT} was narrower and more intense.

To better quantify the difference in organization efficiency that stems from physical cross-linking versus mechanical deflection, we quantified the degree of microtubule alignment

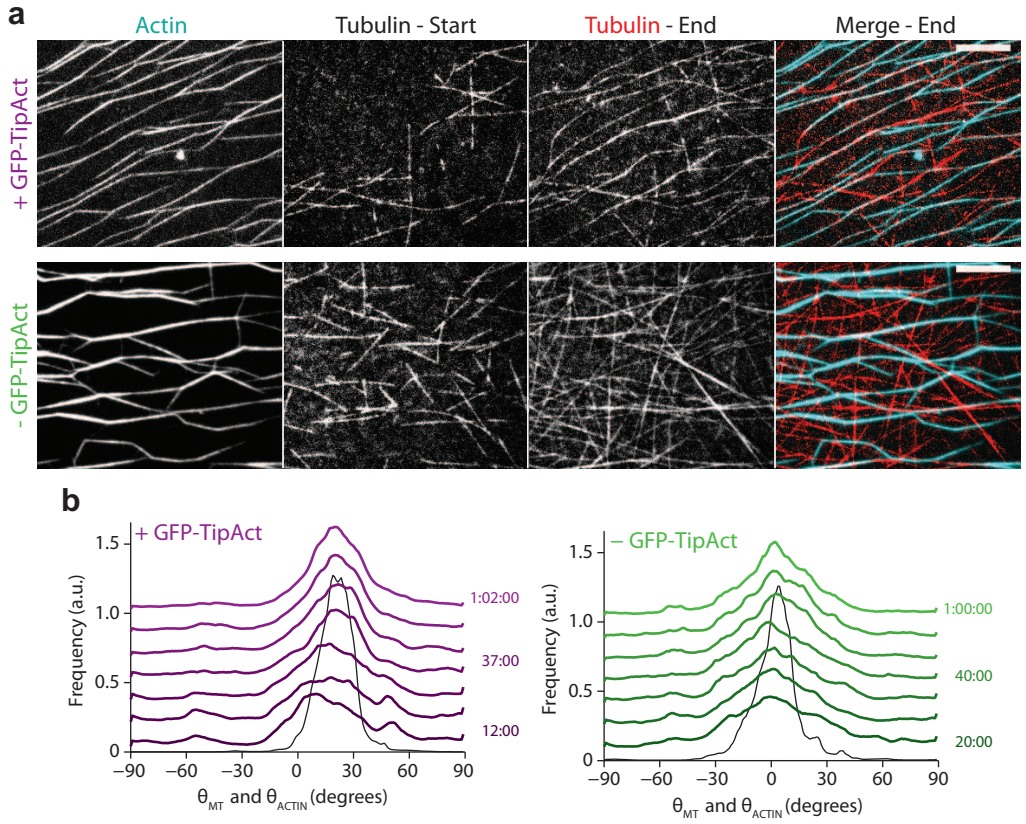

Figure 4.10: Linear arrays of F-actin bundles globally dictate microtubule organization. (a) Early ($t \sim 5$ min) and late ($t \sim 1$ hr) time points of microtubule growth within linear arrays of fascin-stabilized actin bundles with (top), and without (bottom), 50 nM GFP-TipAct. (b) Evolution of the distributions of microtubule orientation angle θ_{MT}, for the experiments in (a). Color gradients indicate the time evolution of the distribution. For ease of view, each curve is shifted 0.17 a.u. relative to the previous one. The black curves show the time-averaged distribution of F-actin bundle orientation angle $\langle\theta_{ACTIN}\rangle$.

with several such F-actin bundle arrays. To this end, we made use of an order parameter (Eq. (4.6)), a unit-less quantity typically used to estimate the strength of alignment of filamentous structures (independent of polarity), relative to a reference angle [477]. Given the dependency of microtubule capture and guidance on microtubule length (Fig. 4.8 e), we analyzed microtubule alignment as a function of $\langle L_{MT}\rangle$, which we estimated from the fraction of the field of view covered by microtubules (Fig. 4.17).

In the presence of TipAct, microtubule alignment monotonically increased with $\langle L_{MT}\rangle$ (purple data points in Fig. 4.11 a). However, in the absence of TipAct we found that, while microtubule alignment increased linearly for $\langle L_{MT}\rangle \leq 19$ µm, for higher values of $\langle L_{MT}\rangle$ the microtubule alignment showed no discernible trend (green data points in Fig. 4.11 a). In addition to this, we measured the degree of overlap between the microtubules and the F-actin bundles. As expected, through the *zippering* mechanism,

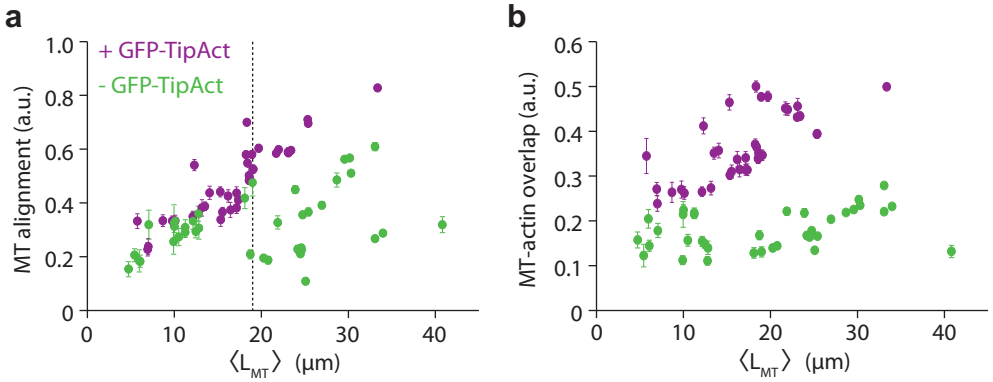

Figure 4.11: Microtubule alignment increases with $\langle L_{MT} \rangle$. Evolution of microtubule alignment (a), and actin-microtubule overlap (b), as functions of the average microtubule length, $\langle L_{MT} \rangle$. Error bars are STD. The gray-dashed line at $\langle L_{MT} \rangle = 19$ µm in (a) indicates where the trends between the zippering (with TipAct) and deflection (without TipAct) guidance mechanisms start to diverge. Data was obtained from n = 6 and 9 experiments with and without 50 nM GFP-TipAct, respectively. MT, microtubule.

microtubules grown in the presence of TipAct showed an increasing degree of overlap with the F-actin bundles with increasing $\langle L_{MT} \rangle$ (purple data points in Fig. 4.11 b). In contrast, microtubules grown without TipAct maintained an approximately constant degree of overlap with the bundles (green data points in Fig. 4.11 b), independent of $\langle L_{MT} \rangle$, which mainly consisted of random cross-overs (Fig. 4.10 a, bottom).

We then built the average distribution of microtubule orientation angles (θ_{MT}), relative to the corresponding mean actin orientation ($\langle \theta_{ACTIN} \rangle$) across experiments, and fit these average curves to a Gaussian (Eq. (4.5), Fig. 4.12). The value of μ represents the difference in mean orientation between the microtubules and the actin bundle array, i.e. $\langle \theta_{ACTIN} \rangle - \theta_{MT}$, which can be understood as the *centering efficiency*, the smaller its value, the better the actin-microtubule co-alignment. On the other hand, the value of σ can be interpreted as the *focusing efficiency*, that is, the smaller its value, the more globally the microtubule array has been aligned by the underlying actin bundle array. These plots thus reveal that microtubule *zippering* via EB3 and TipAct always results in better microtubule co-alignment with the actin-bundle arrays. This was the case both for short microtubules ($\langle L_{MT} \rangle \leq 19$ µm, Fig. 4.12 a), and even more strongly for long microtubules ($\langle L_{MT} \rangle > 19$ µm, Fig. 4.12 b). These observations confirm that even though mechanical deflection via steric interactions can under certain conditions direct microtubule growth (Fig. 4.7 b), the lack of anchors to the F-actin bundles makes microtubules susceptible to lose their tracks. Thus, in conditions where the F-actin bundles are sparse, the activity of cross-linkers is definitely required to dictate global actin-microtubule co-alignment.

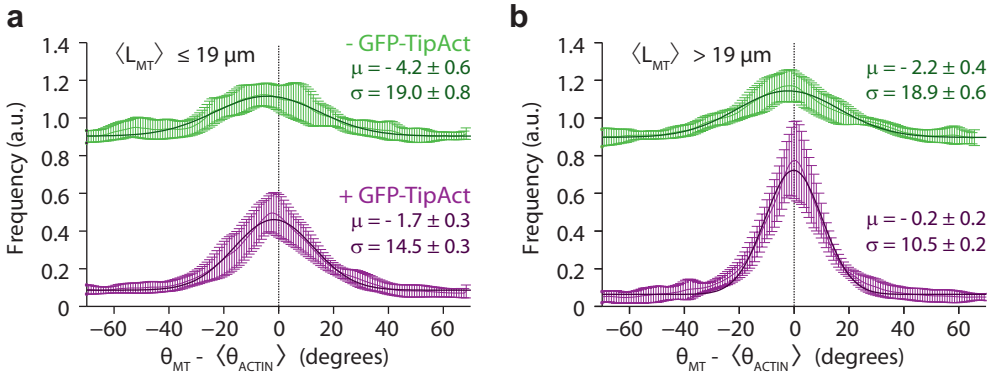

Figure 4.12: Average histograms of actin-microtubule co-alignment. Average histograms of the difference between microtubule and mean F-actin orientation angle, i.e. $\langle\theta_{ACTIN}\rangle - \theta_{MT}$, for short $\langle L_{MT}\rangle \leq 19$ (a), and long $\langle L_{MT}\rangle > 19$ (b), microtubules (as defined in Figure 4.11 a). Error bars are STD. Dark green and purple lines and insets show the fits to Eq. (4.5). Data and fits without GFP-TipAct were shifted up 0.8 a.u. for ease of view. Data is the average of n = 6 and 9 experiments, comprising 17 and 9 histograms for long microtubules, and 18 and 11 histograms for short microtubules, with and without 50 nM GFP-TipAct, respectively.

4.5.1 Actin bundle density tunes actin-microtubule coordination

In the previous section we found that actin-microtubule cross-linking via EB3 and TipAct is required to allow sparse arrays of parallel F-actin bundles to globally organize an otherwise random microtubule array. Furthermore, we found that in the absence of TipAct, microtubules are increasingly susceptible to lose track of the F-actin bundle as they grow. This observation suggests that the spatial density of F-actin bundles plays an important factor in regulating actin-microtubule organization. In fact, for all the experiments outlined above, we were careful to compare F-actin bundle arrays in which the number of bundles and their spacing was approximately the same. However, the experimental protocol to create such arrays often yielded variable F-actin bundle densities, which allowed us to study this effect.

The left panels in Figure 4.13 a show three examples of F-actin bundle arrays with different density, the middle panels show the resulting microtubule organization ∼1 hr after the start of the experiment, and the right-most panels show the merged images. With increasing F-actin bundle density, even in the absence of TipAct, the microtubules can better co-align with the underlying F-actin bundle architecture. The histograms in Fig. 4.13 b show that even though the original organization of the microtubules was approximately random, with time, the microtubules adopted the underlying F-actin

organization, with the highest degree of co-alignment with the densest F-actin bundle array.

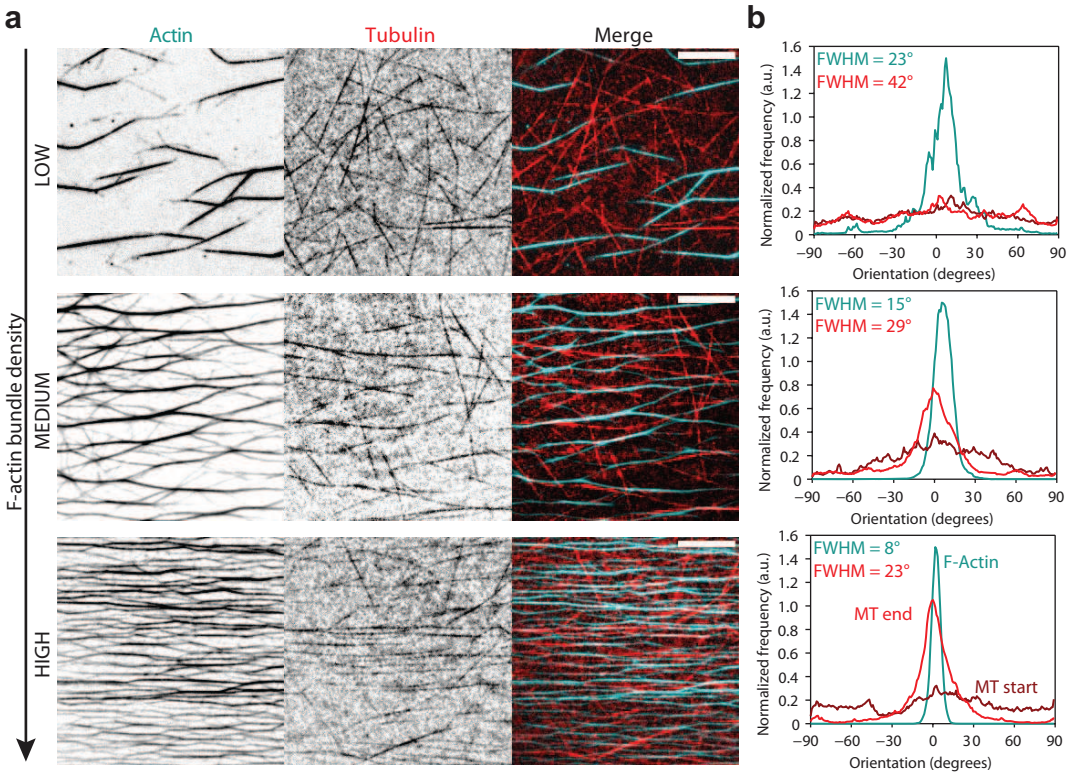

Figure 4.13: Increasing the F-actin bundle density leads to better actin-microtubule co-alignment through steric interactions. (a) Resulting microtubule organization after ∼1 hr of growth within the corresponding F-actin bundle array shown in the left panels. (b) Normalized histograms of F-actin bundle and microtubule orientation for the examples in (a), with the same color-coding. The dark- and light-red curves show the initial and final distributions of microtubule orientation. The full-width at half maximum (FWHM, obtained from fits to Eq.(4.5)), is shown in the insets, both for the actin bundles and the final microtubule arrays. Scale bars: 10 µm. MT, microtubule.

This result demonstrates that besides the action of cross-linkers, the role of steric interactions in directing actin-microtubule organization is key. And further suggests that in some contexts, cells may rely on specific F-actin architectures to direct microtubule growth, even in the absence of cross-linkers.

4.6 Discussion

In this chapter we have demonstrated the ability of F-actin bundles to capture and redirect microtubule growth. Furthermore, we have shown how microtubule capture

and guidance depends on the concentration of cross-linkers, as well as the encounter angle and length of the microtubule when it meets the actin bundle. In the presence of TipAct, guidance occurred by *zippering* of the microtubule onto the F-actin bundle, and in its absence, through steric interactions between the microtubule tip and the bundle.

Furthermore, we showed that even though TipAct is a weak actin-filament binder, with a dissociation constant for F-actin in the order of 5 µM, it nonetheless displays a strong localization at fascin-stabilized actin bundles. This could be the result of an avidity effect, given that TipAct is a parallel homodimer, which would imply that when its two actin-binding domains are bound to F-actin its effective off-rate is reduced. Similar observations have been reported of Dystrophin, a closely related protein to MACF (hence TipAct) which also contains a tandem calponin-homology (CH) actin-binding domain [475]. However, dystrophin molecules are monomeric [478], which suggests that a preference for F-actin bundles *versus* single filaments may be a property of tandem CH actin-binding domains. This could be tested, for instance, by generating monomeric versions of TipAct. Given that TipAct's actin-binding domain is identical to that of MACF, our observations could help explain MACF and Shot's predominant role as actin-microtubule cross-linkers on F-actin bundles (i.e. stress-fibers and filopodia), rather than at dendritic or cortical F-actin networks, in living cells [122, 123, 125, 352, 354, 369, 465].

TipAct's strong localization at fascin-stabilized actin bundles was sufficient to recruit EB3 to the bundles as well, even in the absence of microtubules. FRAP experiments further revealed that TipAct remains practically fixed at the bundles on the timescale of microtubule growth, as well as on the timescale of TipAct and EB3 exchange at microtubule tips. This results in enhanced steady-state concentrations of both EB3 and TipAct at actin-microtubule overlaps, which explains how they can mediate stable actin-microtubule connections. This observation could also help explain the reported enhancement of MACF, Shot and EB1 localization along microtubules in actin-rich regions in cells [123, 125]. Given that full-length MACF and Shot molecules also contain a microtubule-lattice binding domain (Fig. 3.1), we speculate that in *in vivo* this mechanism could act in synergy with (or even as a preceding step to) the establishment of actin-microtubule linkages mediated by MACF and Shot's microtubule lattice-binding domain [309, 354], which is the most heavily regulated domain of these molecules [369, 418, 458]. Finally, similar effects on EB1 localization, which result in microtubule co-alignment with stress fibers in cultured cells, have also been reported for members of the GAS2-like family of proteins [459, 460], which are structurally very similar to our TipAct construct.

Besides the enhanced localization of EB3 and TipAct at actin-microtubule overlaps, we also showed that the mechanical properties of the F-actin bundles *vis à vis* that of the microtubule play a key role in deciding who will guide who. *In vitro* experiments have revealed that fascin-stabilized actin bundles can reach bending stiffnesses in the range of $30 - 40$ pN µm^2 [473], depending on the number of actin filaments in the bundle. These values are well above the mechanical bending rigidity of a single microtubule (~ 8 pN µm^2 [89–91, 174]). This could help explain why in our assays, when a growing microtubule was being guided by an actin bundle, it was the microtubule which deformed. However, the F-actin bundles were also partially immobilized on the coverslip surface, which further prevented their deformation. In fact, mechanical stabilization of actin-bundles by the surrounding environment could also play a role in cells. For instance, in contrast to the fascin-stabilized actin bundles reconstituted *in vitro*, filopodial actin bundles in cells have been shown to be sparsely cross-linked structures, containing $\sim 10 - 20$ actin filaments [479–481], and a molar ratio of fascin to actin in the order of 1:25 [480]. *In vitro* measurements of F-actin bundle rigidity in these conditions would predict a bending rigidity for such bundles below 0.15 pN µm^2 [474]. This value is 50-fold lower than the bending rigidity of a single microtubule. However, in cells, filopodia do guide microtubule growth [291, 354], and furthermore have been shown to have bending rigidities in the order of 40 pN µm^2 [482]. Although the activity of additional F-actin bundlers may play a role in enhancing the mechanical stability of filopodial bundles, fascin is by far the dominant component [483]. This observation supports the notion that mechanical stabilization by the surrounding environment (i.e. the plasma membrane, the lamellipodial F-actin network, or anchoring at focal adhesions), could play a key role in providing F-actin bundles in cells with further mechanical stability in order to guide microtubule growth.

Finally, we showed that F-actin bundles, through their guiding effect on microtubule growth, can globally dictate microtubule organization. We found that both in the presence and absence of TipAct, an otherwise random array of dynamic microtubules could adopt the underlying organization of parallel arrays of F-actin bundles. However, without a direct actin-microtubule cross-linker, microtubules were susceptible to lose their F-actin track, unless the density of F-actin bundles was sufficiently high. In cells, both filopodia and stress fibers are sparse structures surrounded by crowded environments (i.e. the lamellipodial F-actin network, and the cell interior, respectively). It is thus likely that mechanical guidance by deflection is not the mechanism of choice for efficient guidance by either of these F-actin structures, which explains the need for direct actin-microtubule cross-linkers to carry out this function.

4.7 Materials and methods

4.7.1 Surface deposition of microtubule seeds and linear arrays of fascin-stabilized actin bundles

To generate parallel arrays of fascin-stabilized F-actin bundles, interspersed with a random collection of GMPCPP-stabilized microtubule seeds, we used flow cells which had entry and exit points on the glass slide side, which allowed us to sequentially flow in different solutions while monitoring the sample by TIRF microscopy (Fig. 2.2). Figure 4.14 shows the sequence of steps, and representative images of the flow-cell surface after each step.

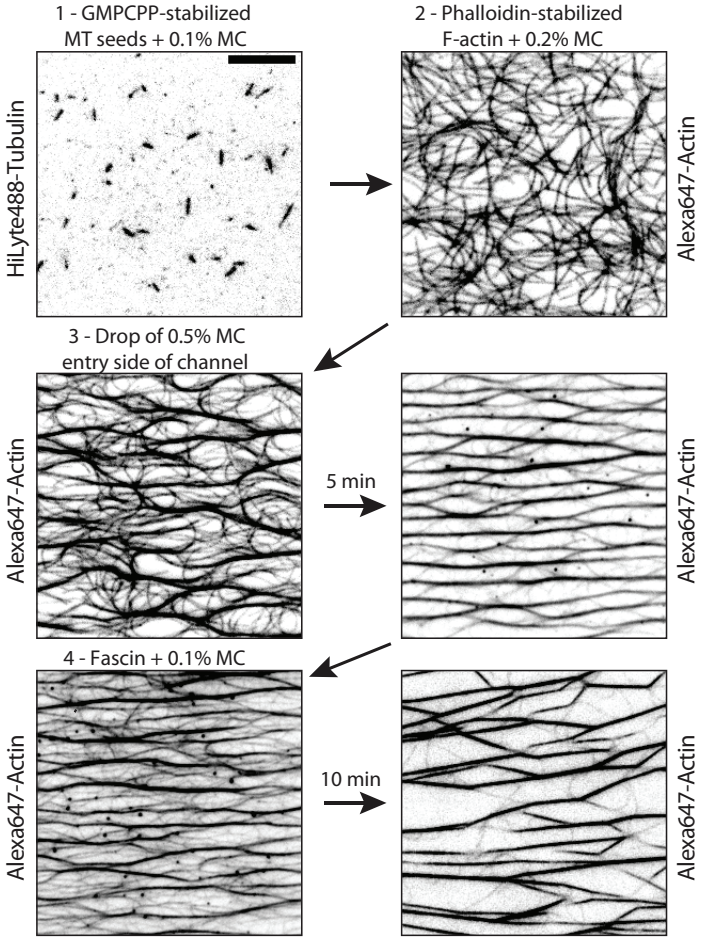

Figure 4.14: Surface deposition of microtubule seeds and linear arrays of actin bundles. TIRF images showing the sequential deposition of: (1) a random array of microtubule seeds, (2) long actin filaments, (3) a methyl-cellulose (MC) solution to align and bundle the actin filaments, and (4) a fascin solution to exchange the MC, and stabilize the F-actin bundles. Scale bar, 10 µm. MT, microtubule.

First, microtubule seeds (diluted in MRB80 with 0.1% (w/v) methyl-cellulose) were slowly added to the flow cell at what would be the equivalent of 50 - 100 nM tubulin concentration. After a 5 min incubation, the flow cell was rinsed slowly (to minimize microtubule-seed alignment) with 500 - 100 µl of MRB80. Second, pre-polymerized, phalloidin-stabilized actin filaments were added to the flow-cell at the equivalent of 1 µM G-actin concentration, in MRB80 containing 0.2% (w/v) methyl-cellulose. This was sufficient to push the filaments towards the surface without inducing bundle formation [484]. Thereafter, a drop of 0.5% (w/v) methyl-cellulose was placed at one end of the channel and allowed to diffuse in for $\sim$ 5 min to induce F-actin bundling, and cause a pressure-driven flow that aligned the bundles. After $\sim$ 5 min, the channel was rinsed with 50-100 µl of a solution containing 200-500 nM fascin, and 0.1% (w/v) methyl-cellulose. This stabilized the F-actin bundles, while removing excess methyl-cellulose. Since fascin exchanges quickly at F-actin bundles [485], its concentration in the flow-cell was kept constant for the rest of the experiment.

4.7.2 Microtubule tip-tracking assays

In all the assays shown in this chapter we aimed for long microtubules, in order to increase the chance of encounters with F-actin bundles. To this end microtubules were polymerized with 25-30 µM tubulin (always at a ratio of 1:15 labeled to unlabeled subunits), 100 nM EB3, with or without 50 nM GFP-TipAct. For experiments in which we monitored the effects of reducing TipAct concentration on the efficiency of microtubule capture by F-actin bundles, we varied the TipAct concentration between $6.5 - 50$ nM. TIRF microscopy imaging was performed between $32 - 34$°C (Table 2.1). We refer the reader to Chapter 2 for the general details on how these assays were built.

4.8 Data analysis

4.8.1 Analysis of FRAP data at growing microtubule tips and F-actin bundles

FRAP data for mCherry-EB3 and GFP-TipAct at growing microtubule plus-ends was retrieved from intensity profiles along the time-axis on kymographs of microtubule growth where either mCherry-EB3 or GFP-TipAct was bleached. Plus-ends were selected

by comparing their intensity and growth speeds to the corresponding minus-ends, and recovery was only analyzed on plus-ends that continued to grow with constant speeds after bleaching. The actual recovery data was retrieved by plotting the fluorescence intensity along a three-pixel-wide line traced vertically down the time axis on the kymograph, centered at the most intense region of the pre-FRAP plus-end intensity, to make sure that fluorescence recovery was analyzed at the same region on the microtubule lattice.

In the case of free microtubule tips (i.e. not bound to an actin bundle), and assuming that the soluble pools of mCherry-EB3 and GFP-TipAct quickly equilibrate, a reaction-limited recovery curve [486] multiplied by a decaying single-rate exponential envelope function was sufficient to describe the recovery. The decaying curve accounts for the progressive loss of affinity for EB3 at the same site on the microtubule lattice as a result of GTP hydrolysis [100]. To this curve, we added a slowly rising exponential curve shifted to $t = t_0$ in order to account for non-zero affinity of EB3 for the GDP-tubulin lattice. The equation thus used for fitting EB3 and TipAct recovery at free microtubule tips was the following:

$$\begin{aligned} I(t) = (A - B * \exp\left[-t * k_{off-free}\right]) * \\ \exp\left[-H(t-t_0) * (t-t_0) * k_{decay-free}\right] + \\ D * (1 - \exp\left[-H(t-t_0) * (t-t_0) * k_{decay-free}\right]) \end{aligned} \tag{4.1}$$

where A, B and D are constants, $k_{off-free}$ the off-rate of mCherry-EB3 (or GFP-TipAct) at microtubule tips, $k_{decay-free}$ the transition rate from a tip-like to a lattice-like binding profile (related to GTP hydrolysis), and $H(t - t_0)$ the Heaviside function to account for the fact that this transition occurs with a time delay [100]. In the case of actin-bound microtubule tips, a modified version of Eq. (4.1) was used in which two species of recovering molecules were introduced, in order to account for the fraction of mCherry-EB3 (and GFP-TipAct) molecules that were only interacting with the microtubule tip, and those linked to microtubule tip and F-actin bundle:

$$\begin{aligned} I(t) = (A - B * \exp\left[-t * k_{off-free}\right] - C * \exp\left[-t * k_{off-bound}\right]) * \\ \exp\left[-H(t-t_0) * (t-t_0) * k_{decay-bound}\right] + \\ D * (1 - \exp\left[-H(t-t_0) * (t-t_0) * k_{decay-bound}\right]) \end{aligned} \tag{4.2}$$

where A, B, C and D are constants, $k_{off-free}$ the off-rate of mCherry-EB3 (or GFP-TipAct) bound only to microtubule tips, $k_{off-bound}$ the off-rate of mCherry-EB3 (or

GFP-TipAct) bound both to the microtubule tip and actin bundle, and $k_{decay-bound}$ the transition rate from a tip-like to a lattice-like binding profile (as above). The values of $k_{off-free}$ and t_0 were fixed to the values that were obtained for free microtubule tips using Eq. (4.1). Fitting was performed on the average recovery curves (weighted by the inverse of the SEM) for n = 19 and n = 7 mCherry-EB3 and GFP-TipAct recovery profiles at free microtubule tips, and for n = 13 and n = 6 mCherry-EB3 and GFP-TipAct recovery profiles at actin-bound microtubule tips (Fig. 4.4).

FRAP data for GFP-TipAct and mCherry-EB3 on F-actin bundles and actin-microtubule lattice overlaps was similarly obtained from intensity line profiles along the time-axis on kymographs traced along the bleached F-actin bundles. Recovery data was retrieved by plotting the average fluorescence intensity along a five to ten pixel-wide line traced vertically down the time axis of the kymograph. In the case of GFP-TipAct no fitting was performed since no significant fluorescence recovery was observed (Fig. 4.5 c), at least within the same timescale of observation. On the contrary, mCherry-EB3 did exchange both on free and microtubule-bound actin bundles (Fig. 4.5 b). In the case of free actin bundles (i.e. not linked to a microtubule), and assuming that the soluble pool of mCherry-EB3 quickly equilibrates, a simple reaction-limited curve was used to describe the recovery:

$$I(t) = A - B * \exp[-t * k_{off-free}] \tag{4.3}$$

where A and B are constants, $k_{off-free1}$ the off-rate of mCherry-EB3 bound to the actin bundles via GFP-TipAct. For the case of microtubule-bound actin bundles, a modified version of Eq. (4.3) was used in which again two species of exchanging molecules were introduced, to account for the fraction of mCherry-EB3 molecules that were only interacting with the microtubule lattice, and those interacting with both microtubule lattice and TipAct at the actin bundles:

$$I(t) = A - B * \exp[-t * k_{off-free2}] - C * \exp[-t * k_{off-bound}] \tag{4.4}$$

where A, B and C are constants, $k_{off-free2}$ the off-rate of mCherry-EB3 bound only to the microtubule lattice and $k_{off-bound}$ the off-rate of mCherry-EB3 bound both to the microtubule lattice and the GFP-TipAct decorated actin bundle. Fitting was performed on the average recovery curve (weighted by the inverse of the SEM) for n = 12 curves at free actin bundles, and for n = 17 curves at microtubule-bound actin bundles (Fig. 4.5).

All fitting was performed with the *Curve Fitting Toolbox* of Matlab using the non-linear least squares method.

4.8.2 Analysis of microtubule and actin-bundle encounters

In a similar fashion to how microtubule-microtubule encounters have been classified in models of cortical microtubule arrays in plants [295], the interactions between a growing microtubule and an actin bundle were classified into three categories (Fig. 4.8 a): cross-over, catastrophe, deflection (without TipAct) and zippering (with TipAct). To quantify the probability of these outcomes, the microtubule length L_{MT} (measured from the plus end of the microtubule seed to the tip of the microtubule), and the angle θ between the orientation of the tip (defined as the end-most $\sim$2 µm-long section of microtubule) and the actin bundle, were measured at the time of intersection. Thereafter one of the outcomes defined above were assigned by monitoring the subsequent microtubule growth until the next catastrophe. This analysis was performed for n = 914, 708 interactions between growing microtubule plus-ends and F-actin bundles in the presence or absence of 50 nM GFP-TipAct, respectively, and the probability of each outcome calculated as a function of L_{MT} and θ. For the experiments with variable amounts of GFP-TipAct, the analysis was performed only for the encounter angle θ, with the exception that a new interaction outcome was included, namely *zipper & snap-off*. This analysis was performed for n = 459, 421 and 443 interactions for each of the following conditions: 6.25 nM, 12.5 nM and 25 nM GFP-TipAct, respectively.

4.8.3 Analysis of microtubule and actin bundle array orientation

To determine the orientation distributions for the linear arrays of actin bundles and the corresponding microtubule arrays, pixel-by-pixel orientation values were extracted from the fluorescence image files using the *OrientationJ* plugin [487] developed for ImageJ [443]. This plugin returns two matrices with the same size as the input image (Fig. 4.15 a), whose values at each pixel correspond to: 1) Orientation (in radians, from -$\pi/2$ to $\pi/2$), and 2) Coherency, which indicates the degree of co-alignment of a given pixel relative to its neighbors within a user-defined window (defined to range from 0 for no co-alignment, to 1 for full co-alignment). In all cases the we used the Gaussian gradient analysis method in *OrientationJ* with a window size of three pixels.

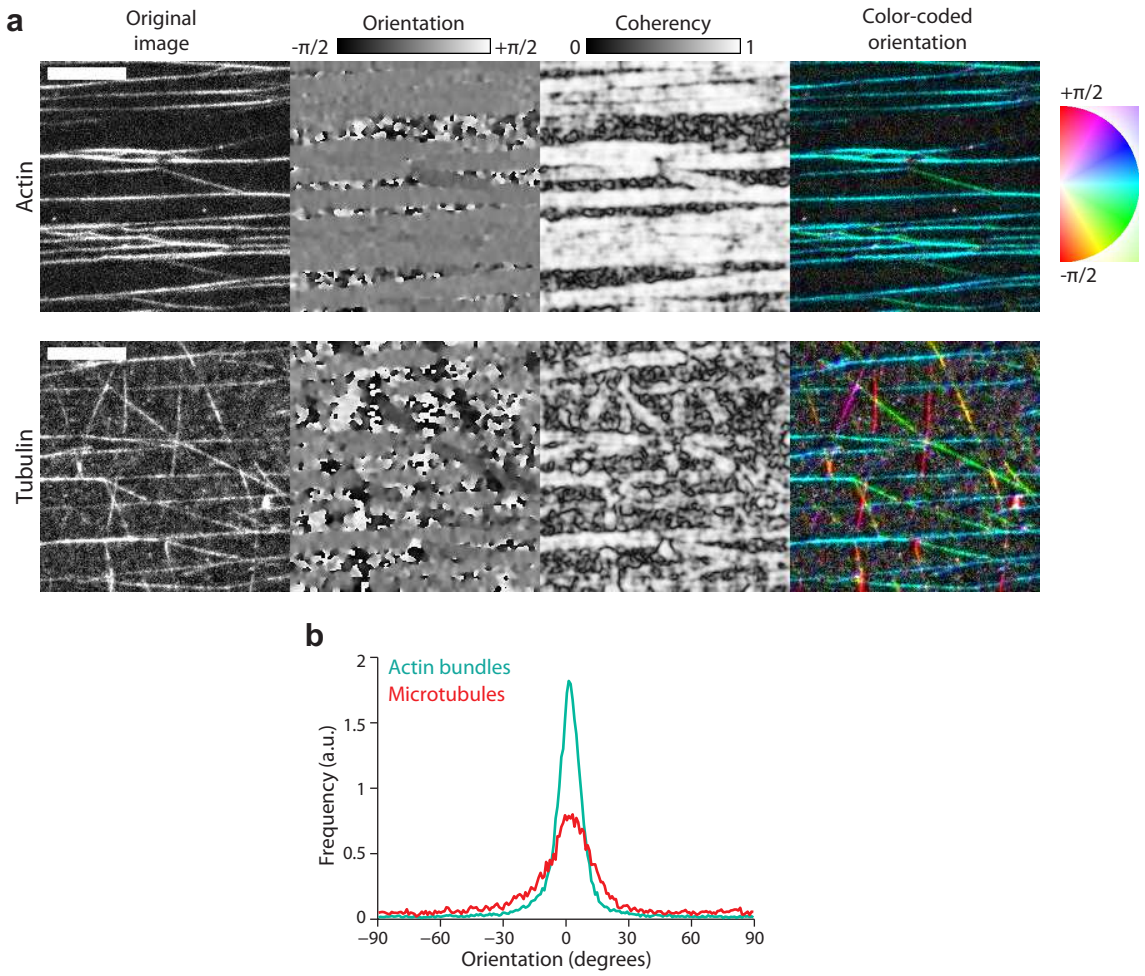

Figure 4.15: Orientation analysis. (a) Montage of the pixel-by-pixel orientation data for a sample F-actin bundle array (top), and the ensuing microtubule organization (bottom) after ~ 1 hr of growth in the presence of TipAct. The left-most panels show the fluorescence images, followed by the orientation and coherency maps. The right-most panels show the color-coded orientation maps, as indicated by the color-wheel. (b) Normalized histograms for the actin-bundle (cyan) and microtubule (red) orientations for the examples in (a). Scale bar, 10 µm.

Histograms of microtubule and actin bundle orientation angle, θ_{MT} and θ_{ACTIN} respectively (Fig. 4.15 b), were constructed using the values of the orientation matrix weighted by the coherency to minimize the contribution of pixels where no filaments were present, with a bin size of $\pi/100$. This analysis was performed for every frame in fluorescence time-lapse stacks that each corresponded to $5-10$ minutes of microtubule growth. These histograms were averaged over two minutes of microtubule growth (60 frames) and with these average curves the time-evolution of the distribution of θ_{MT} and the average distribution of θ_{ACTIN} were built (Fig. 4.10). Time zero was defined as the point when the first stack of fluorescence images was recorded; which was typically

$\sim 2-3$ min after the microtubule polymerization mix was added to the flow cell channel.

The same distributions of microtubule orientation angle (θ_{MT}), averaged over two minutes of microtubule growth, were used to build the average orientation distribution for all microtubule alignment experiments (Fig. 4.12), both with and without GFP-TipAct, for the cases where the average microtubule length was short ($\langle L_{MT} \rangle \leq 19$ µm) and long ($\langle L_{MT} \rangle > 19$ µm), as defined in Figure 4.11. To this end, all the orientation histograms corresponding to short and long microtubules were collected and shifted along the x-axis such that their corresponding mean actin orientation angle ($\langle \theta_{ACTIN} \rangle$) would fall at 0°. Thereafter, the curves were averaged and the resulting histogram was fit with the *Curve Fitting Toolbox* of Matlab using the non-linear least squares method to a Gaussian function of the form:

$$y(\theta) = A \exp\left(\frac{-(\theta - \mu)^2}{2\sigma^2}\right) + B \tag{4.5}$$

where, A is a constant, μ the mean location, σ the standard deviation, and B an offset due to noise. The value of μ represents the difference in mean orientation between the microtubules and the actin bundle array, i.e. $\langle \theta_{ACTIN} \rangle - \theta_{MT}$, which can be understood as the *centering efficiency*, the smaller its value, the better the actin-microtubule co-alignment. On the other hand, the value of σ can be interpreted as the *focusing efficiency*, that is, the smaller its value, the more globally the microtubule array has been aligned by the underlying actin bundle array. We performed this analysis for n = 6 experiments with GFP-TipAct, comprising n= 17 histograms for long microtubules and 18 histograms for short microtubules; and for n = 9 experiments without GFP-TipAct comprising 9 histograms for long microtubules and 11 histograms for short microtubules.

4.8.4 Analysis of average microtubule length

Microtubule lengths were measured manually by tracing lines along the microtubules using the *Segmented Line* function in FIJI [442]. This was performed approximately every $6-10$ min for a $\sim$50 min experiment in conditions where the average microtubule length ($\langle L_{MT} \rangle$) continuously increased, as was the case for all the experiments with linear arrays of actin bundles performed in this chapter. With these values, histograms of microtubule length were constructed with a bin size of 5 µm (Fig. 4.16 a), and fitted with a simple Exponential or Gaussian function (depending on a qualitative assessment

of the shape of the histogram), to obtain a value for the average microtubule length $\langle L_{MT} \rangle$. These values were used to construct a plot of $\langle L_{MT} \rangle$ over time (Fig. 4.16 b).

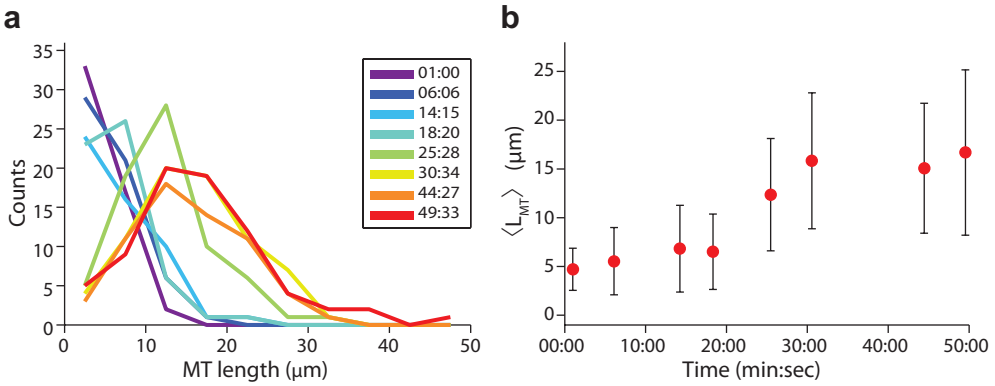

Figure 4.16: Analysis of $\langle L_{MT} \rangle$ over time. (a) Time-evolution of microtubule-length distribution for a 50 min-long dynamic microtubule experiment with the same growth conditions as the experiments with arrays of actin bundles (Fig. 4.10). The color-code indicates time as displayed in the legend (min:sec). (b), Increase in average microtubule length $\langle L_{MT} \rangle$ with time. Data points show the average of the distributions obtained by fitting an Exponential (for $t < 20$ min) or a Gaussian (for $t \geq 20$ min) distribution to the histograms in (a). Error bars indicate STD.

4.8.5 Analysis of microtubule and actin surface coverage, and actin-microtubule overlap

In order to analyze the area fraction covered by microtubules, as well as the extent of actin-microtubule overlap, binary masks were generated for both microtubule and F-actin bundle arrays using custom-written programs based on the *Image Processing Toolbox* of Matlab (Fig. 4.17 b). These masks were generated through a combination of adaptive thresholding and morphological operations.

The area coverage was defined as the ratio of the total number of white pixels in the microtubule (or F-actin) mask divided by the total number of pixels in the image (i.e. 512×512), a number which by definition ranges from zero to one. Similarly, the degree of microtubule overlap with F-actin was defined as the total number of white pixels common to the actin and microtubule masks (i.e. overlapping mask pixels, Fig. 4.17 b), divided by the total number of white pixels in the microtubule mask. By definition, this value also ranges from zero to one. The decision to use overlap instead of colocalization analysis was based on two reasons: first, because the tubulin channel was often noisy since the levels of fluorescent tubulin were kept low; and second, because we were

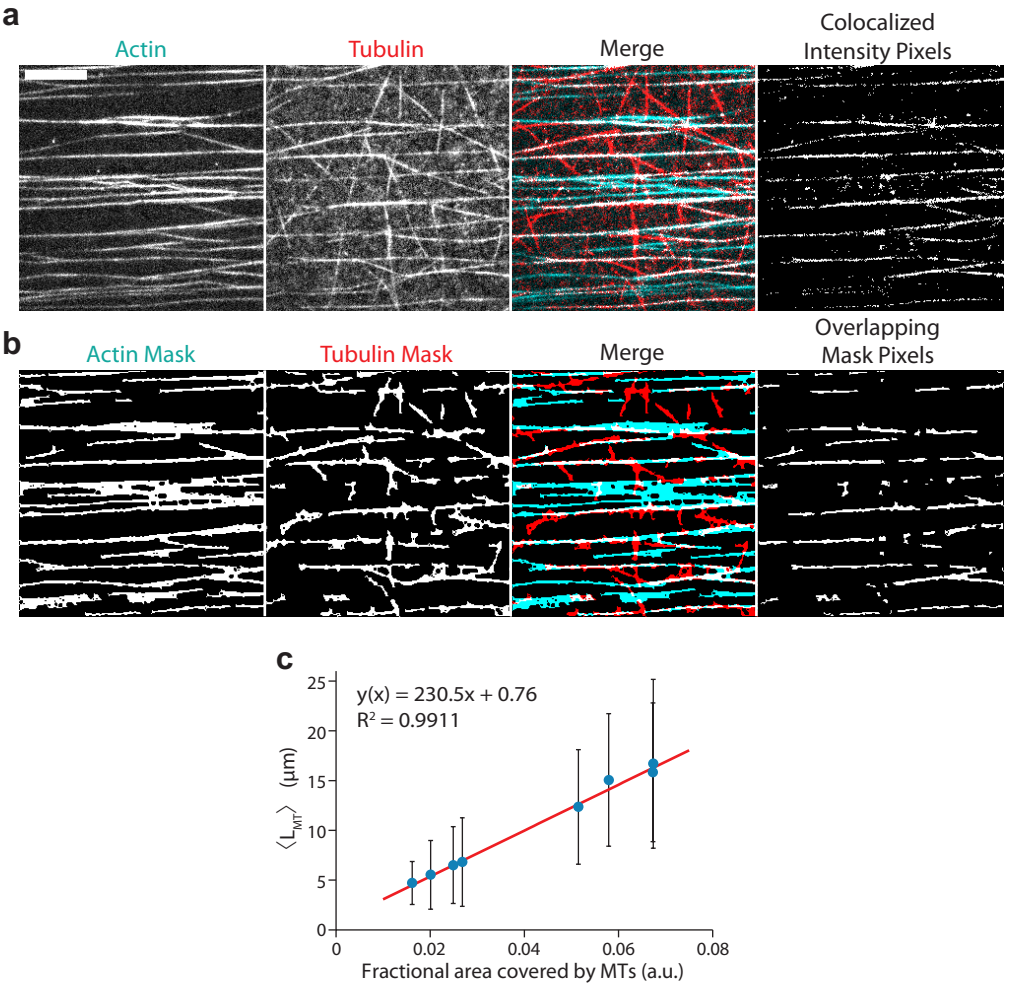

Figure 4.17: Co-localization *versus* overlap analysis, and relationship between $\langle L_{MT} \rangle$ and actin-microtubule overlap. (a) Example of co-localization analysis for the same experiment as in Figure 4.15. The two left-most panels show the actin and tubulin fluorescence intensity images, and the third panel the merged image. The right-most panel shows the co-localized intensity pixels as produced by the *Colocalization Threshold* plugin in FIJI, which estimated that 47% of the microtubule signal overlapped with that of the actin. (b) Example of area coverage and overlap analysis for the same F-actin bundle and microtubule arrays as in (a). The two left-most panels show the binary masks generated from the intensity data. The third panel shows the merged image of the binary masks, with the same color-code as in (a). The right-most panel shows the pixels that are common to both masks, i.e. the overlap between the F-actin bundles and the microtubules (48% of the pixels), which is to be compared with the co-localized intensity pixel panel in (a). (c) Linear relationship between the average microtubule length $\langle L_{MT} \rangle$, and the fraction of the image area covered by microtubules, for the same experiment as in Figure 4.16. Scale bars, 10 µm.

not interested in the correlation between the tubulin and actin intensities, but rather, within the limits of optical resolution, whether microtubules co-localized with the F-actin bundles or not. For this purpose, a binary measure was sufficient. Figure 4.17 shows a comparison between co-localization and overlap analysis that validates this approach. Panel a shows the individual intensity images, followed by the merged image and the percentage of co-localized signal as estimated using the *Colocalization Threshold* plugin in FIJI [442], which estimated that 47% of the tubulin signal colocalized with that of the actin. Conversely, panel b in Figure 4.17 shows the results of a custom-written overlap analysis program for the same images; the first two panels show the binary intensity masks generated as previously explained, the third panel the combined masks where the white pixels are those common to both masks (i.e. the overlap), which are shown alone in the last panel. In this case, 48% of the white pixels in the microtubule mask were also present in the actin mask, which is in good agreement with the estimation of the percent of colocalized signal mentioned above. Finally, as can be observed in Figure 4.17, conservative settings were used to create the binary masks so that, if anything, the actual degree of actin-microtubule overlap was underestimated. Masks were obtained for every tenth image in a stack (that is every 20 s of microtubule growth) for stacks that corresponded to five to ten minutes of microtubule growth.

4.8.6 Estimating the relationship between the area covered by microtubules and the average microtubule length

The fraction of the field of view covered by microtubules was used as a proxy for their average length $\langle L_{MT} \rangle$, since in the conditions of the co-alignment experiments microtubules grew progressively longer and the surface crowded (Fig. 4.10), making it difficult to measure microtubule lengths individually. This approach was validated by tracking the distribution of microtubule lengths over time for an experiment that evolved from short to long microtubules (Fig. 4.16) and by plotting the obtained values for $\langle L_{MT} \rangle$ against the fraction of the area covered by the microtubules at the same time-point (as obtained from the binary masks). As can be observed in panel c of Figure 4.17 these values were linearly related. The parameters of the best linear fit through the data points were thus used to get an estimate of $\langle L_{MT} \rangle$ for all experiments analyzed in Figure 4.11. It is worth noting that since this approximation only holds for fields of view with approximately equal numbers of microtubule seeds, the only experiments analyzed were those in which there were $\sim 50 \pm 10$ microtubule seeds in the field of view.

4.8.7 Determination of global F-actin bundle and microtubule alignment

The pixel-by-pixel orientation and coherency values that were used to build histograms of actin-bundle and microtubule orientation (Fig. 4.15) were also used to estimate the degree of actin bundle and microtubule alignment. This was performed with the use of an order parameter (OP), a unit-less quantity that conveys the degree of alignment of filamentous structures independent of filament polarity [477]. In two dimensions, the OP can be defined as follows:

$$OP = \left[\left(\frac{\sum_{i=1}^{n} w_i \cos(2\theta_i)}{\sum_{i=1}^{n} w_i} \right)^2 + \left(\frac{\sum_{i=1}^{n} w_i \sin(2\theta_i)}{\sum_{i=1}^{n} w_i} \right)^2 \right] \tag{4.6}$$

where θ_i and w_i correspond to the i$^{\text{th}}$ pixel's orientation and coherency values, and n to the number of pixels in the image (i.e. 512×512). By definition the OP ranges from zero (when all values of θ_i are randomly distributed) to one (in which all values of θ_i are the same).

4.8.8 Criteria for comparing experiments with linear arrays of actin bundles

A strategy had to be devised in order to fairly compare experiments of actin-microtubule co-alignment (Figures 4.11 ad 4.12), in order to make sure that the actin-bundle arrays were similarly ordered and spaced; as well as to ensure that microtubule growth started from an isotropic collection of microtubule seed orientations. To this end, experiments were compared if the microtubule seed array had an $OP \leq 0.2$, with $\sim 50 \pm 10$ microtubule seeds in the field of view. For the linear arrays of F-actin bundles, experiments were included in the analysis of Figure 4.11 if the arrays had an $OP \geq 0.80$. Since the number of bundles in the field of view could not be precisely counted, the fraction of the field of view covered by the actin bundles (as explained above) was used as a proxy for the number of bundles, and the analysis was limited to actin-bundle arrays with area coverage between 0.1-0.25.

4.8.9 Evolution of order parameter and actin-microtubule overlap as a function of the average microtubule length $\langle L_{MT} \rangle$

To build plots of microtubule alignment and actin-microtubule overlap versus $\langle L_{MT} \rangle$ (Figures 4.11 ad 4.12), these values were obtained for every tenth image in a stack (that is every 20 s of microtubule growth) and averaged over five-minutes of microtubule growth. The mean ± standard deviation of these values was then plotted for all fluorescence stacks across comparable experiments. This was performed for n = 6 experiments with GFP-TipAct comprising n = 20 different actin bundle arrays; and for n = 26 experiments without GFP-TipAct comprising n = 26 different actin bundle arrays. This means that the points in Figure 4.11 do not all represent different experiments but rather, the average of five minutes of microtubule growth within various actin bundle arrays that were collected over various experiments.

We would like to thank Florian Huber (FOM Institute AMOLF, The Netherlands) for advice on the generation of parallel arrays of actin bundles, and Feng-Ching Tsai (FOM Institute AMOLF) for help with the fascin purification. We also thank Bela Mulder and José Alvarado (FOM Institute AMOLF) for advice on the analysis of the orientation and order parameter of actin and microtubule arrays.

Chapter 5

F-actin organization by dynamic microtubules

In this chapter we study interactions between dynamic microtubules and single actin filaments, or mobile actin bundles. We find that when an actin bundle is not fully anchored to the glass surface, both the microtubule and the bundle deform as they interact. Furthermore, we show that TipAct at microtubule growing ends allows microtubules to transport freely-diffusing actin filaments, or pull on actin filaments partially tethered to the glass surface. When the density of actin filaments in solution is high, microtubules can interact with multiple actin filaments and create bundles de novo. In combination, these effects allow a radial microtubule array to globally dictate the organization of an otherwise isotropic solution of actin filaments. These observations highlight how the activity of cross-linkers can be modulated by the mechanical properties and pre-existing architecture of the cytoskeleton.

5.1 Introduction

Cytoskeletal coordination in cells is equally orchestrated by physical cross-linkers and biochemical regulators [260]. Without a doubt, the best characterized instances in which microtubules help dictate F-actin organization involve signaling via the Rho-family of GTPases [269, 401]. For instance, microtubules can control cell contractility by sequestering RhoA guanine-exchange factors (GEFs) at their lattice. Microtubule depolymerization has been shown to activate RhoA by releasing these GEFs to the

cytosol, leading to enhanced myosin-II contractility and stress-fiber formation [129, 366, 409]. A similar event occurs during mitosis, where the mitotic spindle helps define a RhoA-rich region at the cell cortex where the actin cytokinetic ring will then form [412]. Microtubules are also involved in directing lamellipodial formation, through Rac1 activation [268]. In contrast to these examples, observations in which microtubules physically re-organize the F-actin cytoskeleton through the activity of cross-linkers are conspicuously rare.

However, some of the earliest literature on actin-microtubule interactions highlighted the role that microtubules can have on actin-filament organization via cross-linkers. *In vitro* reconstitutions with *Xenopus laevis* egg extracts revealed that actin filaments co-align with microtubules nucleated from demembranated *X. laevis* sperm cells, and that with time the filaments are slowly excluded from the interior of sperm-nucleated microtubule asters [265]. Further studies, also with *Xenopus* egg-extracts, showed that actin filaments and bundles can be transported along microtubules, as well as ride as passive passengers on gliding microtubules propelled by cytoplasmic dynein [266]. Although the nature of the actin-microtubule cross-linkers at play was not clear at the time, these studies nonetheless revealed that microtubules can have a direct impact on F-actin organization. In spite of this, and with few exceptions, the best documented examples of cross-linker mediated actin-microtubule communication have focused on the effects that the actin cytoskeleton can have on microtubule organization.

Nonetheless, instances in which microtubules have been observed to direct F-actin organization *in vivo* do exist. For example, microtubules have been observed to invade filopodia located at the lateral edges of lamelliodia, which results in filopodia movement and fusion. Whether a cross-linker is involved in this interaction is not yet clear, since this effect is seemingly independent of EB being present [488]. In another example, members of the GAS2-like family of proteins, which track microtubule growing ends through associations with EB [459, 460], and also bind F-actin [489], have been shown to drastically induce alignment of actin filaments with microtubules in the presence of elevated levels of EB [113].

One of the likely reasons behind the lack of *in vivo* evidence of microtubule control over actin-filament organization, is that in animal cells F-actin structures are usually densely packed, making it difficult to image and follow single filaments individually. In plant cells, however, the bulk of the F-actin network is located at the cell interior, whereas the cortical surface is dominated by microtubules and a sparse network of actin filaments and bundles [294]. Immunofluorescence imaging of microtubules and actin filaments in

Arabidopsis thaliana cells revealed that cortical actin filaments and microtubules usually co-align [490]. Moreover, recent fluorescence live-cell imaging studies revealed that the organization of the cortical actin filament network is dependent on the organization of adjacent cortical microtubules, which act as guides for F-actin polymerization, but also are involved in transporting actin filaments, although the nature of the cross-linkers (if any) is not yet known [296].

Given these observations, we decided to experimentally test to what extent the combined activity of EB3 and TipAct allows dynamic microtubules to direct the spatial organization of actin filaments. The results of these experiments are detailed in this chapter.

5.2 Growing microtubules deform and reposition F-actin bundles

In Chapter 4 we observed that bundles of F-actin stabilized by fascin can capture and re-direct microtubule growth (Fig. 4.7). This was the result of the enhanced localization of TipAct and EB3 at actin-microtubule overlaps (Fig. 4.3), as well as the increased bending rigidity that stems from bundling the actin filaments. We moreover suggested that in cells, the mechanical environment that surrounds the actin bundle (such as the dendritic F-actin network around filopodia, or the adhesions to the substrate as in the case of stress-fibers), is likely to further ensure that the impinging microtubule is forced to co-align with the bundle.

In order to test whether microtubules can conversely deform and reorganize F-actin bundles that are not mechanically coupled to their environment, we performed experiments with fascin-stabilized actin bundles and dynamic microtubules in the presence of 100 nM EB3 and 50 nM TipAct (as schematized in Fig. 4.1). We specifically looked for instances in which microtubules interacted with bundles that were only partially anchored to the coverslip surface. As shown in Figure 5.1, in these conditions we found that when a growing microtubule was captured by an F-actin bundle, both the microtubule and the bundle deformed as the microtubule polymerized. Furthermore, after the microtubule had a catastrophe, the bundle was left in a different location. This effect is reminiscent of the above-mentioned microtubule-dependent reorganization of filopodia in cells [488], and further supports the notion that mechanical effects strongly

modulate the ability of physical cross-linkers to allow F-actin or microtubules to dictate each other's organization.

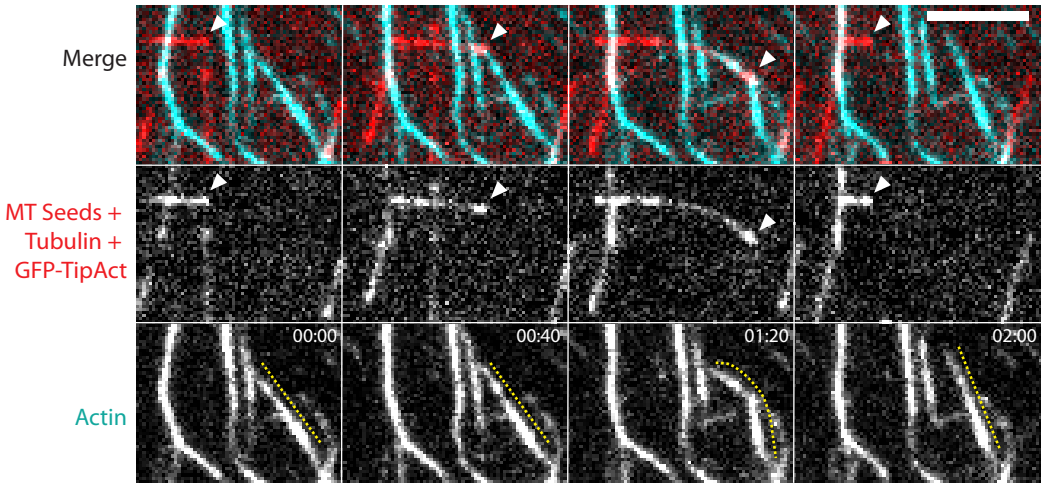

Figure 5.1: Microtubules can deform and reposition F-actin bundles. Time series showing a microtubule that interacts with a mobile F-actin bundle. As the microtubule grows, both microtubule and actin bundle deform. When the microtubule has a catastrophe and shrinks, the F-actin bundle is now displaced. The arrowheads indicate the growing microtubule plus-end, and the yellow dashed line in the actin panels shows the deformation of the actin bundle as the microtubule grows along it. Scale bar, 5 µm. Time: min:sec. MT, microtubule.

5.3 Growing microtubules exert forces on single actin filaments

The observation that mobile F-actin bundles can be deformed and reorganized by growing microtubules suggests that this effect should be even more pronounced when microtubules interact with single actin filaments. In order to test this, we polymerized microtubules in the vicinity of phalloidin-stabilized F-actin weakly anchored to the coverslip surface, in the presence of 100 nM EB3 and 50 nM TipAct (as schematized in Fig. 3.8).

We observed that transient interactions between microtubule tips and F-actin, mediated by EB3 and TipAct, were sufficient to allow microtubules to pull on partially tethered actin filaments, resulting in filament stretching in the direction of growth. Panel a in Figure 5.2 shows one example of such an event, in which the microtubule tip (indicated with a white arrowhead) captures an actin filament that is partially tethered and whose

contour (indicated by a dashed yellow line) elongates as it is pulled by the microtubule tip. The fact that in this context the actin filament is deformed by the microtubule is consistent with the much higher bending rigidity of microtubules ($EI_{MT} \sim 8$ pN µm^2 [89–91, 174]) compared to that of single actin filaments ($EI_{AF} \sim 0.04 - 0.07$ pN µm^2 [162, 174, 175, 472]).

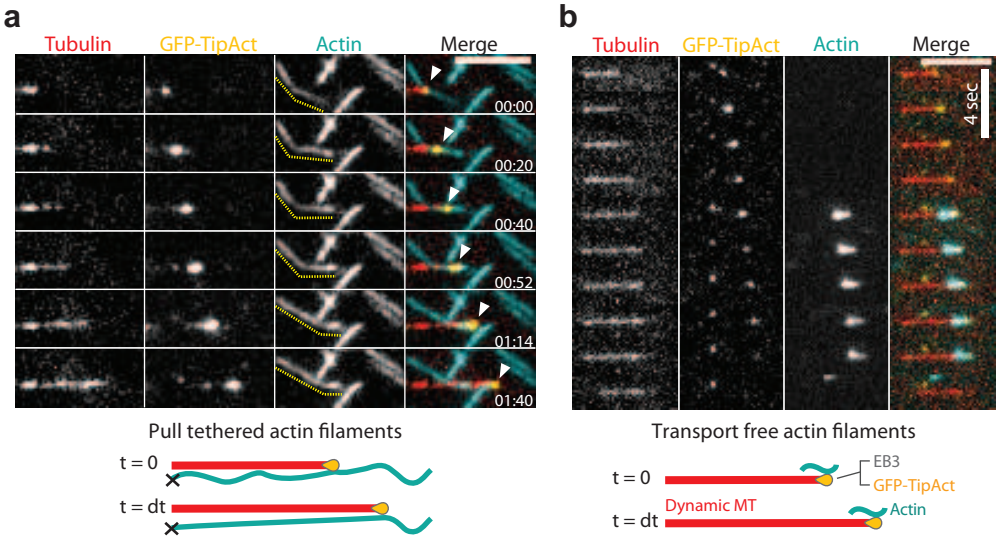

Figure 5.2: Growing microtubules transport and pull single actin filaments. (a) Top, Time series of a growing microtubule that aligns and then pulls on an actin filament that is partially tethered to the glass surface. The dashed yellow line in the actin pane shows the contour changes of the actin filament as it is pulled. The arrowheads in the merge panel show the microtubule tip. Bottom, schematic of this effect. (b) Top, time series of a growing microtubule that transports a freely-diffusing actin filament via TipAct at its growing end. Bottom, schematic of this effect. Scale bars, 5 µm. Time, min:sec. MT, microtubule.

Furthermore, in instances where the actin filament was fully mobile (Fig. 5.2 b), we observed that it could even be transported by the growing microtubule tip. Additionally, but in rare occasions, we also observed actin filaments being transported by a shrinking microtubule (data not shown). These results reveal that, even though both EB3 and TipAct exchange quickly at microtubule tips (Fig. 4.4), they can collectively generate linkages between actin filaments and microtubules that are stable enough to allow for transport and force generation. Since as the microtubule grows nothing physically moves (except the location of its tip), reveals that the shape of TipAct's binding profile at microtubule tips can apparently bias the otherwise random thermal motion of actin filaments in the direction of microtubule growth. This process is probably analogous to the way kinetochore components track depolymerizing microtubules [491]. Other observations of force-generation by microtubule +TIPs have been reported in different contexts. For instance, in cultured cells microtubules have been shown to

pull endoplasmic reticulum (ER) membrane tubes through the interaction of EBs with STIM1, a +TIP anchored at the ER [128, 492]. More recently, *in vitro* studies showed that plus-end tracking kinesins at microtubule plus-tips can collectively generate sufficient force to steer microtubule growth along template microtubules [376, 377]. We will delve deeper into this effect in Chapter 6.

5.4 Growing microtubules organize F-actin networks

Having shown that microtubules can have profound effects on actin filament shape and localization (Fig. 5.2), we wondered to what extent these effects would allow a well-defined microtubule architecture to globally dictate the organization of entangled F-actin networks. To this end, we polymerized microtubules from centrosomes in the vicinity of $\sim$ 1 µM phalloidin-stabilized actin filaments, with 100 nM EB3, in the presence or absence of 100 nM TipAct, as schematized in Figure 5.3.

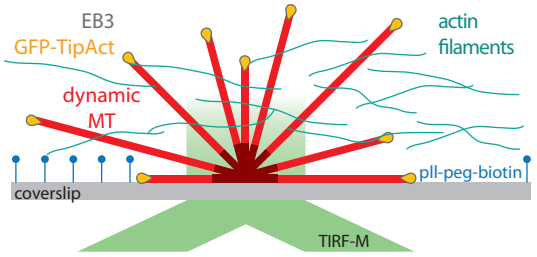

Figure 5.3: Experimental setup to study interactions between microtubules nucleated from a centrosome and single actin filaments. Microtubules were polymerized from surface-bound centrosomes, in the presence of EB3, GFP-TipAct, and phalloidin-stabilized actin-filaments in solution.

In the absence of TipAct, we found that actin filaments in the vicinity of the microtubule aster remained randomly organized (Fig. 5.4), so that their organization in no way reported the architecture of the adjacent microtubule asters. Furthermore, we did not observe that microtubules in any way inhibited the mobility of the actin filaments through steric effects. This is likely due to the low density of microtubules that nucleated from the centrosome, as well as the low concentration of actin filaments added.

In contrast, in the presence of TipAct we observed that actin filaments in the vicinity of a microtubule aster clearly adopted its radial organization (Fig. 5.5). This effect was progressive: when we followed the spatial organization of the F-actin over time (in a different experiment to the one shown in Fig. 5.5), we found that an ever-increasing

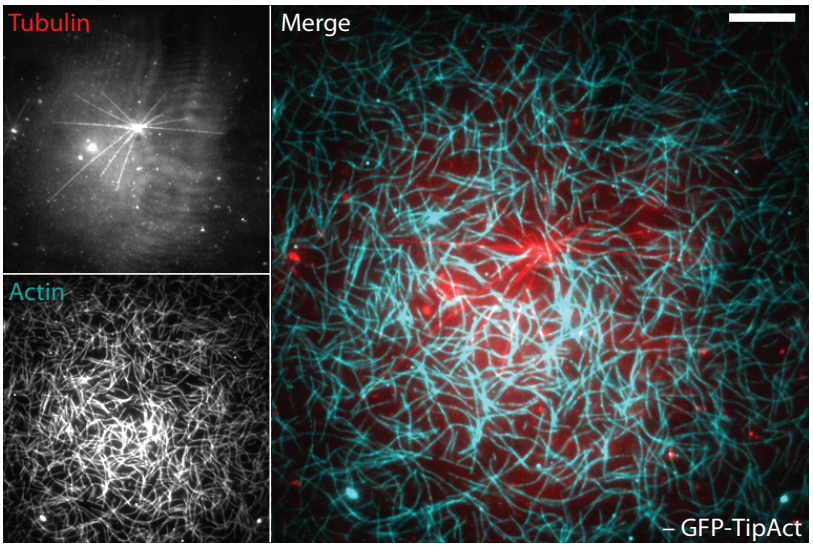

Figure 5.4: In the absence of TipAct, centrosome-nucleated microtubules have no effect on F-actin organization. Steady-state F-actin organization in the vicinity of a radial array of dynamic microtubules, polymerized in the absence of TipAct. Scale bar, 10 µm.

fraction of the actin filaments gradually co-aligned with the aster-nucleated microtubules (Fig. 5.6 a).

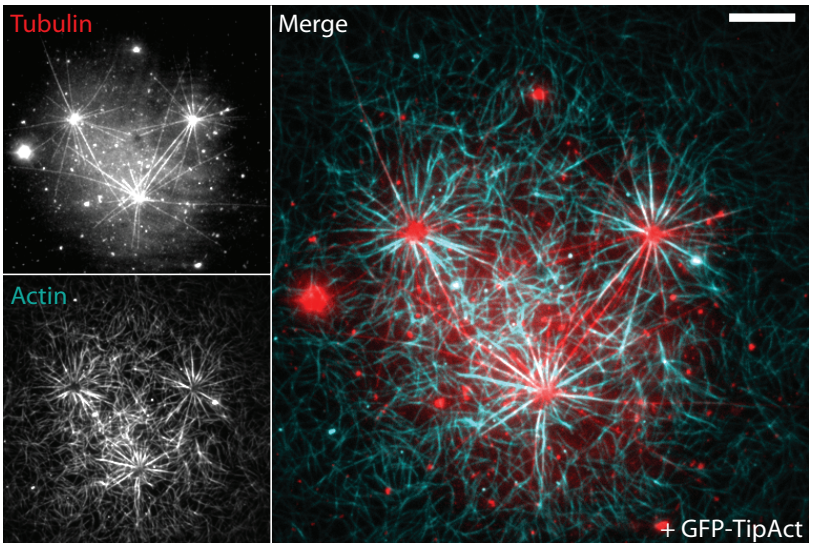

Figure 5.5: In the presence of TipAct, centrosome-nucleated microtubules can globally dictate F-actin organization. Steady-state F-actin organization in the vicinity of a radial array of dynamic microtubules, polymerized in the presence of TipAct. Scale bar, 10 µm.

In order to measure the efficiency of F-actin organization by microtubule asters in this

context, we quantified the degree of actin co-alignment with the radial microtubule architecture. To this end, we made use of an order parameter (OP), as introduced in Chapter 4 (Eq. (4.6)), which we modified to account for the radial organization of the microtubule array. The value of the *radial* OP ranges from zero to one, where zero represents a fully isotropic F-actin organization; and one, a completely radially-aligned one. As shown in Figure 5.6 b, we confirmed that with time the actin filaments increasingly adopted the radial organization of the microtubule array. The magnitude of the order parameter increased up to a maximum value of 0.4, probably limited by the number of microtubules that are polymerized by a given centrosome, as well as the fraction of F-actin not in contact with the microtubules. In contrast, without TipAct we found that the degree of radial order remained at ~ 0.1, consistent with the isotropy of the F-actin network in these situations (Fig. 5.4).

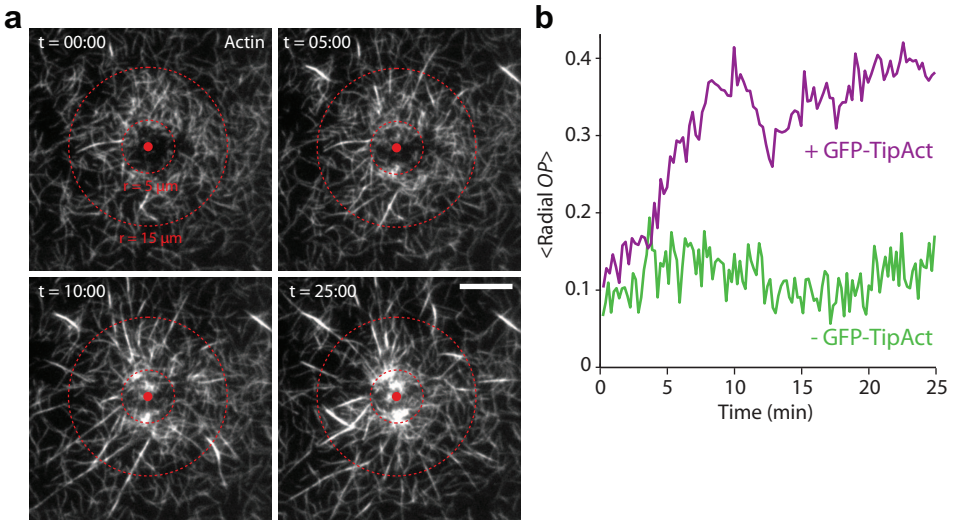

Figure 5.6: Actin filaments gradually adopt the radial organization of a microtubule aster. (a) Time evolution of actin filament organization in the vicinity of a radial array of microtubules, in the presence of TipAct. The dashed red circles show the window used to calculate the radial order parameter (OP) over time. (b) Evolution of the average radial OP over time, for the actin filament network shown in (a), and for one similar experiment but in the absence of TipAct. Scale bars, 5 µm. Time, min:sec.

5.5 Closing the loop: growing microtubules induce F-actin bundling

Besides the observation that actin filaments co-aligned with microtubules nucleated from a centrosome, we also found that these filaments appeared to be bundled (Fig.

5.5). This was striking, since in similar experimental conditions we did not find TipAct to be a strong F-actin bundler (Chapter 4). A closer inspection revealed that when microtubule tips interacted with more than one filament simultaneously, they could bring them in sufficiently close proximity to recruit TipAct, which then stabilized the newly formed bundle. An example of such an event is shown in panel a of Figure 5.7: As a microtubule (whose tip is indicated by white arrowheads) extends from left to right, it incorporates filaments into a bundle (whose contour is indicated by a dashed yellow line), which subsequently recruits TipAct. At a later stage, the newly formed bundle is followed by subsequent rounds of microtubule growth (an example of which is indicated by white arrows). The kymograph and plot in panels b and c of Figure 5.7 show that as the actin bundle forms, the intensity of TipAct along its length increases with time. This observation highlights the organizational feedback that can exist between F-actin and microtubules, even with a simple cross-linking system. Similar observations of F-actin bundling by growing microtubules have been reported in cultured plant cells, where cortical microtubules are the master regulators of cortical F-actin organization, although the nature of the putative cross-linkers is not yet known [296].

5.6 Discussion

In this chapter we reconstituted interactions between dynamic microtubules and mobile actin bundles and single filaments, in order to investigate the ways by which growing microtubules can dictate F-actin organization. First, we observed that microtubules that are captured by mobile fascin-stabilized actin bundles can simultaneously deform, and be deformed by, the actin bundles. These observations highlight the importance of the surrounding environment in mechanically stabilizing F-actin bundles (i.e. stress fibers) in order to allow them to efficiently capture and redirect microtubule growth. Furthermore, it has been speculated that one of the ways by which microtubules could also help trigger focal adhesion disassembly is through mechanical forces, which could aid in detaching the stress fibers from the adhesion sites [344]. With these experiments we show that indeed actin bundles that guide microtubule growth sustain forces that can lead to both microtubule and actin-bundle bending. In cells, these bending forces would be transmitted to the focal adhesion sites, which would have to sustain them as well.

Furthermore, we found that dynamic microtubules can regulate the spatial organization and shape of single actin filaments. Surprisingly, actin-microtubule interactions mediated

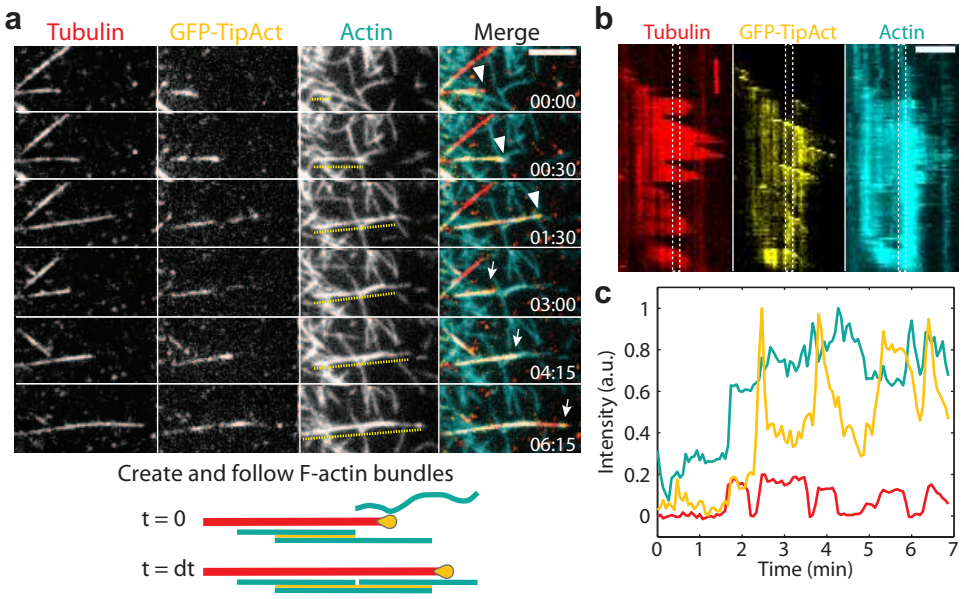

Figure 5.7: Growing microtubules can create and then follow F-actin bundles. (a) Top, time series of a growing microtubule that captures actin filaments from solution, forming a bundle that recruits TipAct, and to which the microtubule remains coupled in subsequent rounds of growth. The dashed yellow line in the actin panel indicates the location of the newly-formed actin bundle. White arrow-heads and arrows in the merge pane show two different rounds of microtubule growth. Bottom, schematic of this effect. (b) Kymograph of the microtubule shown in (a). (c) A plot of the fluorescence intensity over time, averaged over the window indicated with a white dashed square in (b). As the microtubule polymerizes and captures actin filaments from solution, TipAct is increasingly recruited to and stabilizes the newly formed bundle. Scale bars, 5 µm. Time, min:sec.

by EB3 and TipAct were sufficient not only for filaments to align in the direction of microtubule growth, but also to be pulled and transported by microtubule growing and shrinking ends. Similar observations of force generation by microtubule +TIPs have been reported, for instance with STIM1, an ER-anchored protein that through interactions with EB allows growing microtubules to pull membrane tubes [128, 492]. Although to date there is little understanding of the roles that microtubule-generated forces can have on F-actin structures in cells, indirect evidence does exist. For example, growing microtubules have been shown to spatially rearrange filopodia in cultured cells, and to mediate their fusion [488].

We argue that the lack of evidence of microtubule-dependent F-actin organization via physical cross-linkers is probably due to the high density of actin filaments in animal cells, which makes it difficult to follow the behavior of actin filaments individually. In contrast, plant cell microtubules are cortically confined, along with a sparse F-actin network composed of single filaments and bundles [294]. Work on *A. thaliana* root cells has shown that microtubules are the master orchestrators of cortical F-actin organization.

In this context, actin filaments and bundles have been observed to polymerize along, and even be transported by, growing microtubules [296].

In the experiments with radial microtubule arrays in the absence of TipAct we found that microtubules and F-actin seemingly *ignored* each other. In contrast, in the presence of TipAct the actin filaments clearly adopted the radial microtubule organization. Given that microtubule growth speed and catastrophe rate are sensitive to force [93], it would be interesting to investigate whether increasingly dense F-actin networks affect the parameters of microtubule dynamics both via steric effects, and via actin-microtubule cross-linkers. Moreover, the addition of myosin-II motors to these assays could also shed light on the effects that actively contractile F-actin networks have on microtubule polymerization dynamics and organization, in order to understand the ways by which cross-linking molecules aid microtubules to navigate lamellipodial and lamellar F-actin networks in cells [282, 292].

Finally, the addition of TipAct to the assays revealed that the activity of a simple actin-microtubule cross-linking system can already set up a feedback between F-actin and microtubule organization: First, microtubule tips can capture two or more actin filaments, and bring them in close enough proximity for TipAct to bundle them. And second, the newly formed TipAct-stabilized actin bundles can serve as guiding tracks for the growth of subsequent microtubules. It would be interesting to test whether in cells growing microtubules are involved in F-actin bundle formation as well. To this end, the development of time-resolved super-resolution techniques to look at the dynamics of single actin filaments in cells could prove very useful [493].

5.7 Materials and methods

5.7.1 Microtubule tip-tracking assays

For assays of interactions between microtubules and fascin-stabilized F-actin bundles, microtubules were polymerized from 27 µM tubulin, 100 nM EB3, 50 nM GFP-TipAct, additionally fascin was added at a concentration of $200 - 500$ nM to stabilize the F-actin bundles. For the assays of interactions between microtubules and single actin filaments, microtubules were polymerized from 16 µM tubulin, 100 nM EB3 and 50 nM GFP-TipAct. In this case, pre-polymerized phalloidin-stabilized actin filaments, at the equivalent of $100 - 200$ nM G-actin concentration, were added to the flow cell along

with the microtubule seeds. Finally, for the assays with centrosomes, microtubules were polymerized from 20 µM tubulin, 100 nM EB3, in the presence and absence of 100 nM GFP-TipAct. In this case, phalloidin-stabilized actin filaments were incorporated into the microtubule polymerization mix, at the equivalent of 1 µM G-actin concentration. TIRF microscopy imaging was performed at $25 - 30$°C (Table 2.1). We refer the reader to Chapter 2 for the general details on how these assays were built.

5.8 Data analysis

5.8.1 Analysis of F-actin radial order parameter

To quantify the extent of actin-filament network remodeling mediated by TipAct at the growing ends of microtubules nucleated from centrosomes (Fig. 5.6), the previously explained order parameter (OP, Chapter 4, Eq. (4.6)) was adapted for radial organizations. In this case, in order to account for the radial geometry of the microtubule aster, the local pixel angle (θ_i) was replaced by a relative angle measured between the locally measured value and the radial direction: $\Delta\theta_i = \theta_i - \theta_r$. For each set of data, the centrosome position was manually determined as a starting point for the automated analysis using a custom-written MATLAB program. For every distance r measured from the centre of the aster until the image border (with a step-size of one pixel), $2\pi r$ equidistant points along a circle of radius r were collected from the orientation and coherence maps derived from the *OrientationJ* plugin developed for ImageJ (Fig. 4.15) [443, 487]. Since most points along the circle did not match actual pixels, values were derived using a linear 2D interpolation (using MATLAB's *interp2* function). An arbitrary window of interest (red circles in Fig. 5.6 a) between 5 µm and 15 µm distance from the aster center (which encircled most of the microtubules), was used to get an average number for the radial OP for each frame, to ultimately plot the evolution of radial order parameter over time (Fig. 5.6 b). We found that the results of this analysis were very robust against small changes in center position, interpolation methods (i.e. linear or cubic fits), or the size of the window used to average the radial OP.

We would like to thank Sophie Roth (TU Delft, The Netherlands) and Florian Huber (FOM Institute AMOLF, The Netherlands) for purifying centrosomes. We also would like to acknowledge Florian Huber for his experiments with centrosome-nucleated microtubules and entangled F-actin networks; as well as for developing the analysis of the radial order parameter.

Chapter 6

Transport and force generation by microtubule +TIPs

In this chapter we study the transport of soluble actin filaments by TipAct proteins at growing microtubule ends. We find that filaments that are captured slightly behind the peak of TipAct's plus-end intensity are more efficiently transported than filaments that land with a portion of the length ahead of the TipAct intensity peak. We further develop a one-dimensional biased diffusion model which recapitulates the dependency of actin filament transport on the microtubule growth speed, and the length and intensity of the TipAct plus-end profile. These parameters in turn are modulated by the EB and tubulin concentration. Finally, the model predicts that through this mechanism, growing microtubules can generate picoNewton forces on actin filaments.

6.1 Introduction

Despite the low affinity of TipAct for F-actin ($K_d \sim 5$ µM, Fig. 3.5), we observed that the locally enhanced concentration of TipAct molecules at growing microtubule ends could become sufficiently high to allow microtubule tips to capture actin filaments (Fig. 3.9). Moreover, instead of simply co-aligning in the direction of microtubule growth, the captured filaments could also be transported or (if partially anchored) pulled (Fig. 5.2). These effects suggest that binding a collection of TipAct molecules, whose mean location travels with the growing microtubule tip, can result in transport and force generation. The fact that EB and TipAct establish force-generating actin-microtubule

connections is not a property of the individual molecules *per se*, but rather an emergent property that stems from collective effects, since each of these molecules exchanges quickly at microtubule growing ends (Fig. 4.4).

Similar observations of force generation by other EB-binding microtubule +TIPs have been reported in different contexts. For instance, in cells, growing microtubules have been observed to pull endoplasmic reticulum (ER) membrane tubes through the interaction of EB1 with STIM1, an SxIP-motif containing protein that is anchored at the ER [128]. More recently, guidance of microtubule growth has been reconstituted *in vitro* through the action of EB1-interacting kinesins, that can collectively steer microtubule growth along template microtubules [376, 377].

In the case of actin transport, given that when a microtubule polymerizes nothing moves (except the location of its tip), suggests a mechanism by which the TipAct binding profile at microtubule tips biases the otherwise random thermal motion of actin filaments in the direction of microtubule growth. This process is reminiscent of the *biased diffusion* transport strategy that has been proposed to explain how kinetochores remain attached to, and follow, depolymerizing microtubules [491, 494]. In this case the bias is not given by a gradient of protein concentration, but rather a loss of binding sites as the microtubule depolymerizes [491].

To better understand the transport mechanism, and how it depends on variable conditions of microtubule growth (i.e. variable EB and tubulin concentration), we optimized an experimental *in vitro* assay to enhance the number of transport events. To this end, we polymerized microtubules at different tubulin concentrations, in the presence of variable EB3 and TipAct concentrations, and a fixed amount of phalloidin-stabilized actin filaments ($\sim 30 - 50$ nM) that were previously sheared in order to obtain a large number of short filaments in solution. Panel a in Figure 6.1 shows a schematic of these assays. Panel b shows a 16×16 µm^2 area containing seven microtubules, five of which capture and transport actin filaments within a five-minute time-span. Panel c shows kymographs of such five microtubules, numbered one to five as in panel b, showing instances of actin-filament transport. With this assay we were thus able to collect a large number of transport events.

In parallel, to test whether a biased diffusion mechanism could explain our observations of actin filament transport, we developed a simulation of biased diffusion along a inhomogeneous affinity profile, given by the distribution of EB (and hence TipAct) at microtubule tips. We simulated various microtubule growth conditions corresponding to variable EB, TipAct and tubulin concentrations, in order to study how microtubule

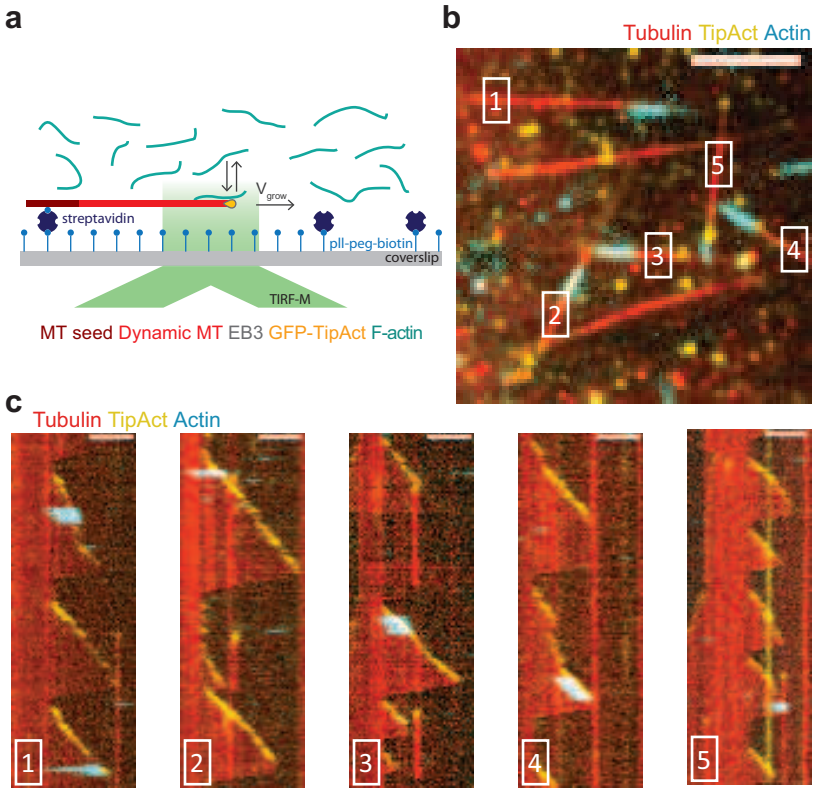

Figure 6.1: Optimized assay to study actin filament transport by microtubule growing ends. (a) Microtubules were polymerized from GMPCPP-stabilized seeds, in the presence of 27 µM tubulin, 100 nM EB3, 25 nM GFP-TipAct, and 30 nM phalloidin-stabilized actin filaments in solution. (b) Maximum intensity projection of an assay as in (a) showing five microtubules that capture and transport actin filaments. (c) Kymographs of the five microtubules, numbered as in panel (b) all of which show instances of actin filament transport. Scale bars, 5 µm. MT, microtubule.

growth velocity and the properties (i.e. length and intensity) of the TipAct comets affect the transport effect. To validate the results of our model, we compared data produced by the simulation with experimental data on actin transport under the same conditions of microtubule growth.

6.2 Model of biased actin filament diffusion at microtubule tips

We chose to model the system in one dimension as schematized in Fig. 6.2, where the microtubule tip consists of a discrete array of positions $i = 1 - N$, each of which has a distinct affinity for F-actin. The actin filament itself was modeled as a point particle

(whose position represents the edge of the filament closest to the microtubule tip), which can bind and unbind to these sites, and freely diffuse in one dimension when unbound. The rate of actin binding at position i, $k_{on}(i)$, depends directly on the affinity for the given site (a function of the local TipAct concentration), and indirectly on the probability that it reaches this site by diffusion. Conversely, the rate of detaching from site i, $k_{off}(i)$, depends on the number of TipAct molecules that the actin is bound to at the given location. We introduced motion of the microtubule tip by shifting the on and off-rate profiles at a rate defined by the microtubule growth speed, V_g, which was measured experimentally. Finally, at any moment when the actin is unbound we defined a critical time after which, if it does not re-bind, it escapes the system.

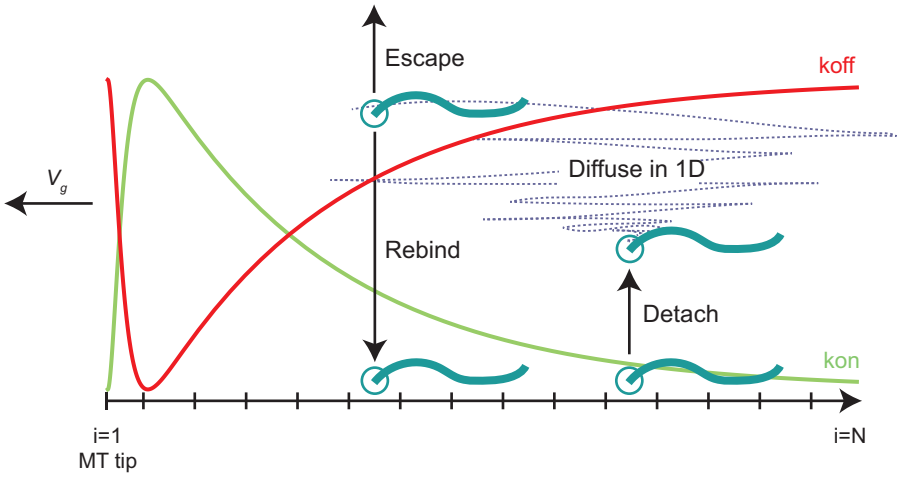

Figure 6.2: Biased diffusion model. In the model, actin filaments can bind the microtubule tips, and diffuse in one-dimension, or escape altogether, when unbound. The on- and off-rates for F-actin are determined by the distribution of TipAct molecules at the microtubule tip. The microtubule tip is modeled as a linear array of N discrete sites, each one with distinct affinity for the actin filament.

In order to fully define the model we thus had to obtain estimates for the following parameters:

- $k_{on}(i)$: The on-rate of actin filaments at microtubule tips. This depends both on the on-rate of a single TipAct molecule on F-actin ($k_{on-TipAct}$) and on the local concentration of TipAct molecules ([TipAct](i)).
- $k_{off}(i)$: The off-rate of actin filaments at microtubule tips. This depends both on the single molecule off-rate, $k_{off-TipAct}$, on F-actin, and the number of TipAct molecules, $n_{TipAct}(i)$, that an actin filament is bound to at position i.
- $D_{parallel}$: The diffusion coefficient of the actin filament. Since our experiments revealed that the actin filaments align with their longest axis parallel to the

microtubule, we calculated the diffusion coefficient along the longest axis of the actin filaments.

- V_g: The rate of microtubule growth, which was measured experimentally.

The following sections will explain in detail how we obtained estimates for all the above parameters.

6.2.1 Spatial distribution of EB binding at microtubule tips

The number of TipAct molecules that actin filaments can interact with, and hence the actin on- and off-rates at microtubule tips, are a direct outcome of the spatial distribution and concentration of EB molecules at growing microtubule ends. One key assumption of our model is that the exchange dynamics of EB and TipAct at microtubule tips are faster than those of the actin filament. Thus, as the actin filament binds or unbinds, the EB and TipAct plus-end binding profiles quickly equilibrate. In essence this allows us to study the EB and TipAct binding distributions in steady-state, and how F-actin responds to them.

The distribution of EB is modulated by varying conditions of microtubule growth (such as tubulin and EB concentration [100, 104]). To calculate the spatial distribution and local concentration of EB molecules at microtubule tips we made use of the *two-step kinetic model of microtubule maturation* recently developed by Maurer and colleagues [100]. In this scheme (Fig. 6.3), tubulin dimers incorporated to the tip of the microtubule undergo two sequential conformational (and chemical) transitions which transform them from edge-most GTP-bound tubulins to lattice-incorporated GDP-bound tubulins.

In the two-step model, the different tubulin states, and the transitions between them, are described as follows:

- State A: Edge-most GTP-bound tubulin dimers, longitudinally bound to the microtubule tip, but not fully laterally bound to their neighbors. Transitions to state B with rate k_1.
- State B: The state associated with the so called *stabilizing GTP-cap* at the microtubule tip, in which tubulin dimers are both longitudinally and laterally bound to all neighbors, and which correlates with a hitherto undefined intermediate in the GTP-hydrolysis cycle [100]. State B is the state where EB molecules bind

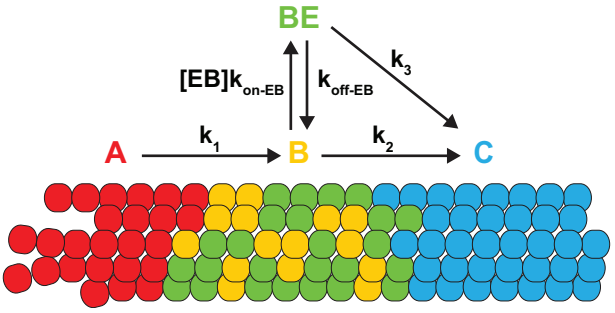

Figure 6.3: Two-state model of microtubule maturation. In this model, tubulins incorporated to the microtubule undergo two sequential conformational and biochemical transitions that transform them from GTP-bound (state A) to GDP-bound (state C). EB molecules bind the intermediate state B with high affinity, and EB-bound tubulins (state BE) transition to state C at a faster rate than empty tubulins transition from B to C. Figure modified from [100].

with high affinity. In the absence of EB, state B transitions to state C with rate k_2.

- State C: Lattice-incorporated tubulin dimers, GDP-bound.

The binding of EB molecules to state B has a two-fold effect on microtubule maturation: First, by indirectly accelerating the transition from state A to B, which possibly arises from long-range effects of EB-binding that promote lateral bonding of microtubule protofilaments [100]. And second, by offering a faster alternative path from state B to C, so that EB-bound B-sites (state BE) in the microtubule tip can transition to state C with rate k_3, where $k_3 > k_2$.

The reaction scheme shown in Figure 6.3 can be used to write down a system of master equations which govern the probability of finding a tubulin dimer in each of the four states (A, B, BE and C) as a function of time:

$$\begin{aligned}
\dot{P_A}(t) &= -k_1 P_A(t) \\
\dot{P_B}(t) &= -k_2 P_B(t) - k_{on-EB}[\mathrm{EB}] P_B(t) + k_1 P_A(t) + k_{off-EB} P_{BE}(t) \\
\dot{P_{BE}}(t) &= -k_3 P_{BE}(t) + k_{on-EB}[\mathrm{EB}] P_B(t) - k_{off-EB} P_{BE}(t) \\
\dot{P_C}(t) &= k_2 P_B(t) + k_3 P_{BE}(t) \\
P_A(0) &= 1
\end{aligned} \tag{6.1}$$

where $P_j(t)$ is the probability of finding a tubulin dimer in each of the four states ($j = A, B, BE$ and C), [EB] the concentration of EB molecules in solution (assumed

to remain constant), k_{on-EB} the on-rate of EB molecules to state B, and k_{off-EB} the off-rate of EB molecules from state BE.

If one makes the simplifying assumption that the microtubule growth speed V_g remains constant at a given EB concentration, the system of equations in Eq. (6.1) can be readily transformed so that its solutions are functions of distance x from the microtubule tip instead of time t. Note that having a time-dependent V_g would be closer to reality, since V_g tends to drop as microtubules approach a catastrophe [84]. However, kymographs of microtubule growth reveal that in the presence of EB, microtubules spend most of their time growing at an approximately constant speed (Fig. 6.1 c). Thus, letting $V_g = {}^{dx}/_{dt} =$ constant, Equation (6.1) becomes:

$$\frac{dP_j(x)}{dx} = \frac{1}{V_g}\frac{dP_j(t)}{dt} \tag{6.2}$$

where $P_j(x)$ is the probability of finding a tubulin dimer in each of the four states ($j = A, B, BE$ and C) as a function of distance x from the microtubule tip.

Through a variety of biochemical and *in vitro* assays, Maurer and colleagues were able to measure values for all the transition rates in the reaction scheme shown in Figure 6.3. The conditions of their assays (73.6 mM K-Pipes pH 6.8, 93 mM KCl and 3.06 mM $MgCl_2$, imaged at 30°C [100]) closely resembled our own (80 mM K-Pipes pH 6.8, 75 mM KCl and 4 $MgCl_2$, imaged at 28-30°C), both in terms of ionic-strength ($I \sim 0.3$ M, [495–497]) and working temperatures. Since these two parameters are the most-likely factors to impact the kinetics of the system (besides tubulin and EB concentration), we used the values they reported for all the transition rates to build a model to compare with our own experimental data.

As mentioned before, Maurer and colleagues found that the binding of EB to state B indirectly increases the transition rate k_1 from state A to B (Fig. 6.3). In their study, however, they only measured k_1 for three different EB concentrations (i.e. 1, 10 and 50 nM). In order to obtain an estimate for k_1 at any EB concentration, we used the values of k_1 they reported and fitted them to the following equation:

$$k_1 = k_0 + k_{EB-max} * \left(\frac{[\text{EB}]}{[\text{EB}] + K_{D-EB:MT}}\right) \tag{6.3}$$

where k_0 is a constant, namely the value of k_1 when no EB is present, k_{EB-max} a parameter that indicates the maximum contribution of EB in increasing the rate of this transition, [EB] is the EB concentration, and $K_{D-EB:MT}$ the dissociation constant for

EB molecules from the microtubule tip (fixed at 22 nM [100]). Figure 6.4 shows the best fit of the Maurer, *et al* data to Eq. (6.3), which we used to estimate values for k_1 at any given EB concentration.

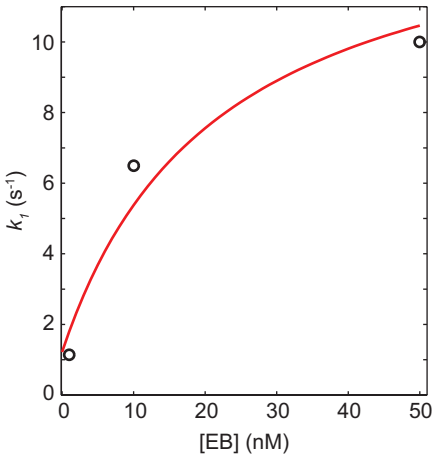

Figure 6.4: Transition rate k_1 versus [EB]. Plot of the transition rate k_1 as a function of EB concentration, [EB]. The red curve shows the fit of the data to Eq.(6.3), which was used to estimate values for k_1 for different values of [EB]. The parameters of the fit were: $k_0 = 1.2$ s^{-1} and $k_{EB-max} = 13.3$ s^{-1}, with fixed $K_{D-EB:MT} = 22$ nM. The data was obtained from [100].

Hence, the only two parameters left to fully define the system in Equation (6.2) are the EB concentration [EB], and the microtubule growth speed V_g, both of which can be varied and measured experimentally. With the aid of a custom-written program in Mathematica [498], we were able to obtain numerical solutions to all four states described by Eq. (6.2). This was performed with the input parameters described in Table 6.1.

Figure 6.5 shows an example solution for all states: $P_A(x)$, $P_B(x)$, $P_{BE}(x)$ and $P_C(x)$, obtained using the parameters in Table 6.1, letting [EB] = 100 nM and $V_g = 80$ nm/s, a typical condition in our *in vitro* assays. Of all the states described by the solutions to Eq. (6.2) we were particularly interested in the solution to state $P_{BE}(x)$ (green curve in Fig. 6.5) which represents the probability that an EB molecule will be bound at position x, which in turn modulates the binding probability of TipAct at the same location.

6.2.2 Spatial distribution of TipAct binding at microtubule tips

Having determined the spatial distribution of EB binding along the microtubule, the next step was to determine how this distribution modulates the binding of TipAct. To

Parameter	Value	Source
k_{on-EB} ($\mathrm{nM^{-1}s^{-1}}$)	0.15	[100]
k_{off-EB} ($\mathrm{s^{-1}}$)	3.4	[100]
k_2 ($\mathrm{s^{-1}}$)	0.23	[100]
k_3 ($\mathrm{s^{-1}}$)	0.73	[100]
k_1 ($\mathrm{s^{-1}}$)	Variable	[100] and Eq. (6.3)
V_g ($\mathrm{nms^{-1}}$)	Variable	Experiments
[EB] (nM)	Variable	Input

Table 6.1: Input parameters for the two-state model of microtubule-maturation. Input parameters and source from which they were obtained used to numerically estimate the solutions to Eq.(6.2).

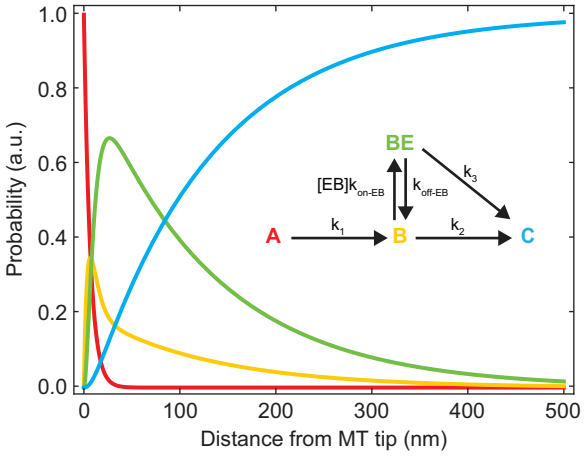

Figure 6.5: Example solutions to the two-state model of microtubule maturation. Numerical solutions obtained for Eq.(6.2), with the input parameters shown in Table 6.1, letting [EB] = 100 nM, $k_1 = 12.13\ \mathrm{s^{-1}}$, and $V_g = 80$ nm/s. $P_A(x)$ (red), $P_B(x)$ (yellow), $P_{BE}(x)$ (green) and $P_C(x)$ (blue).

this end we defined a reaction scheme which governs the kinetics of TipAct binding to EB:

$$[\mathrm{TA}] + n \times [\mathrm{EB}] \underset{k_{off-TA}}{\overset{k_{on-TA}}{\rightleftharpoons}} [\mathrm{TA}] \cdot [\mathrm{EB}]_n \tag{6.4}$$

where [TA] and [EB] represent the TipAct and EB concentrations in solution, k_{on-TA} and k_{off-TA} the on- and off-rates of TipAct to and from EB, [TA]·[EB]$_n$ the concentration of TipAct-EB complexes, and n the number of EB molecules that a single TipAct molecule

can bind. Since TipAct is a parallel homodimer and could thus potentially bind more than one EB molecule, we allowed n to vary.

The reaction scheme in Eq. (6.4) allowed us to estimate the steady-state fraction of TipAct molecules bound to EB, and thus the probability of finding TipAct molecules at microtubule tips. Given that the total number of TipAct molecules is constant (i.e. $[\mathrm{TA}]_{tot} = [\mathrm{TA}] + [\mathrm{TA}]\cdot[\mathrm{EB}]_n$), the steady state fraction of EB-bound TipAct molecules thus becomes:

$$\frac{[\mathrm{TA}]\cdot[\mathrm{EB}]_n}{\mathrm{TA}_{tot}} = \frac{[\mathrm{EB}]^n}{[\mathrm{EB}]^n + {K_{D-TA:EB}}^n} \tag{6.5}$$

where $K_{D-TA:EB} = {k_{off-TA}}/{k_{on-TA}}$ is the dissociation constant of TipAct from EB. In order to obtain values for n and $K_{D-TA:EB}$, we experimentally measured the peak intensity of TipAct at microtubule plus ends (I_{TipAct}) for various bulk EB3 concentrations ranging from 20 to 200 nM (where the EB to TipAct molar ratio was kept at 4:1). The best fit of the data shown in Figure 6.6 to Eq. (6.5) (multiplied by a constant), yielded a cooperativity index n of 2.2 ± 0.1 molecules, and a dissociation constant $K_{D-TA:EB}$ of 67.1 ± 2.2 nM. In contrast, the fit with n fixed at 1 failed to describe the data, and predicted a much lower affinity between TipAct and EB ($K_{D-TA:EB} = 179.9 \pm 88.4$ nM). Given that the fit with $n > 1$ is clearly better indicates that at microtubule tips TipAct molecules bind approximately two EB molecules; the fact that TipAct is a parallel homodimer further supports this notion. However, since the two TipAct's binding sites for EB are independent, we speculate that the cooperative effect is not necessarily a property of TipAct binding to EB in solution, but rather a consequence of the spatial distribution (i.e. surface density) of EB molecules at the microtubule tips.

Having determined the affinity, $K_{D-TA:EB}$, and cooperativity index, n, between TipAct and EB3 at microtubule tips, the next step was to translate this to a probability of finding TipAct molecules bound to microtubule-bound EBs as a function of distance x from the microtubule tip. To this end, we modified Eq. (6.5) to include the position-dependent probability of EB-localization ($P_{BE}(x)$), obtained from the solutions to Eq. (6.2). From the reaction scheme in Fig. 6.3 it follows that the steady-state probability that position x on the microtubule will be occupied by EB is given by:

$$P_{BE}(x) = \frac{[\mathrm{EB}]P_B(x)}{K_{D-EB:MT}} \tag{6.6}$$

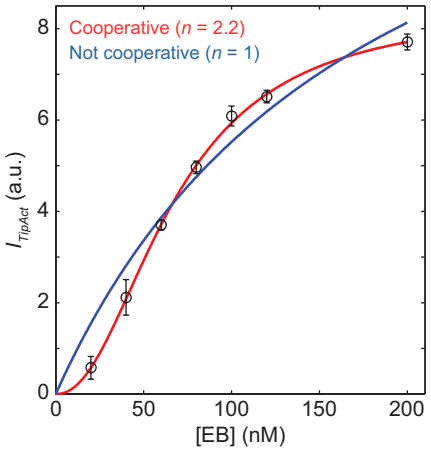

Figure 6.6: TipAct microtubule tip intensity versus EB concentration. Plot of the experimentally-measured peak TipAct plus-end intensity as a function of variable EB concentration, [EB]. The red curve shows the fit of the data to Eq.(6.5), letting n vary. The parameters of the fit obtained were: $I_{TipAct} = 8.4 \pm 0.2$, $K_{D-TA:EB} = 67.1 \pm 2.2$ nM and $n = 2.2 \pm 0.1$. In contrast, the blue curve shows the fit to Eq.(6.5) fixing $n = 1$, which predicts a lower affinity between EB and TipAct: $K_{D-TA:EB} = 179.9.1 \pm 88.4$ nM. Data are the average of n = 84,106,93,212,123,201 and 213 TipAct comets, corresponding to EB concentrations: 20, 40, 60, 80, 100, 120 and 200 nM respectively.

Hence, solving Eq. (6.6) for [EB] and inserting in Eq. (6.5) we obtain an expression for the position-dependent probability of finding a TipAct molecule bound to microtubule-bound EBs, $P_{TA}(x)$:

$$P_{TA}(x) = \frac{\left(\frac{P_{BE}(x)}{P_B(x)} \times K_{D-EB:MT}\right)^n}{\left(\frac{P_{BE}(x)}{P_B(x)} \times K_{D-EB:MT}\right)^n + {K_{D-TA:EB}}^n} \tag{6.7}$$

Panels a and b in Figure 6.7 show the position-dependent probability of EB-binding ($P_{BE}(x)$), and panels c and d the corresponding position-dependent probability of finding a TipAct molecule bound at the same location ($P_{TA}(x)$), calculated for a variety of EB (red) and tubulin (blue) concentrations.

As can be observed, in comparison to their EB counterparts, the TipAct plus-end intensity profiles will always be less intense and more narrow. This is both due to the cooperative nature of binding between TipAct and EB at microtubule tips, as well as the lower affinity between TipAct and EB ($\sim$ 67 nM, Fig. 6.6) compared to the affinity between EB and microtubule tip ($\sim$ 22 nM, [100]). Finally, with increasing EB concentration, the TipAct plus-end profiles get longer and more intense; whereas with increasing tubulin concentration the TipAct plus-end profiles get longer, but their maximum intensity remains constant.

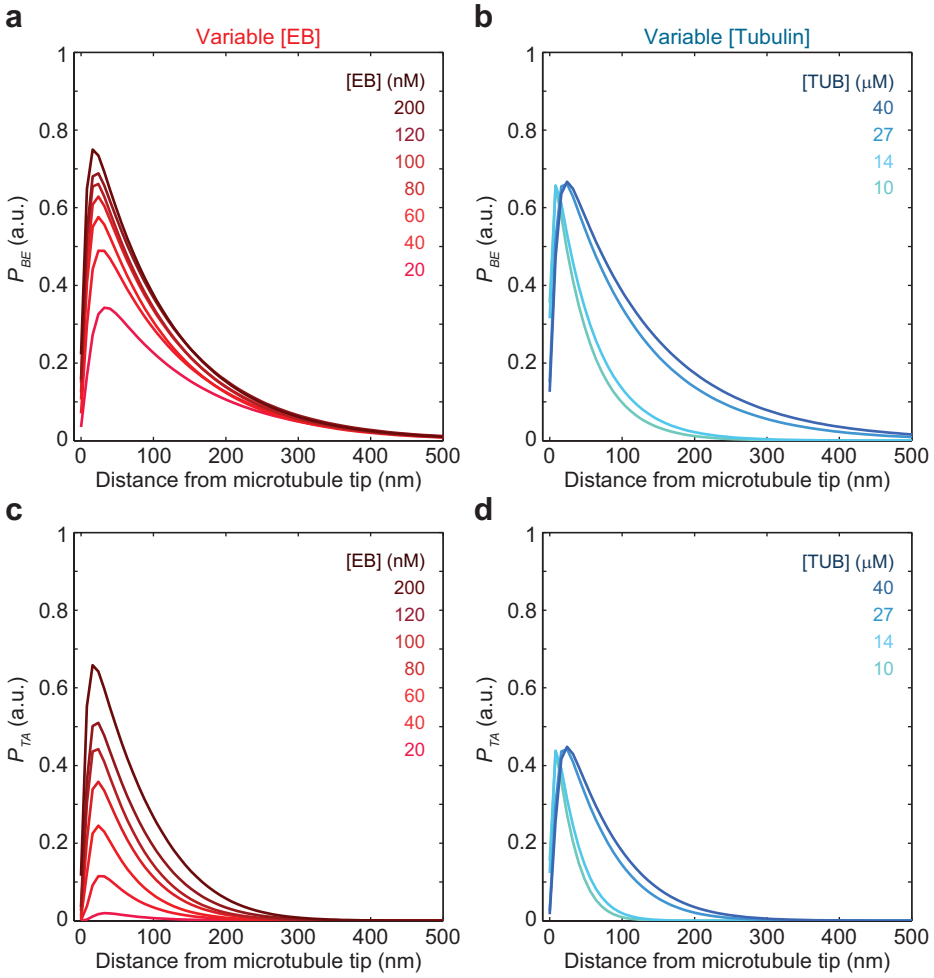

Figure 6.7: Probability of EB and TipAct binding as a function of distance from the microtubule tip. Probability of EB-binding ($P_{BE}(x)$, Eq.(6.2)), calculated for variable EB (a) and tubulin (b) concentrations. Corresponding probability of TipAct-binding ($P_{TA}(x)$, Eq.(6.7)), calculated for the same EB (c) and tubulin (d) concentrations as in (a) and (b).

6.2.3 Local concentration and number of TipAct molecules

Having obtained a solution for the probability of finding microtubule-bound TipAct molecules as a function of distance x from the tip (Fig. 6.7, c and d), the next step was to use this information to define the TipAct local concentration. In other words, the locally enhanced concentration (relative to the bulk value) which allows microtubule growing ends to capture actin filaments, even though TipAct is itself a low-affinity F-actin binder (Fig. 3.5).

To estimate the number of TipAct molecules bound as a function of position x along the microtubule, we multiplied the probability of a site being occupied by TipAct ($P_{TA}(x)$,

Eq. (6.7)), with the maximum number of binding sites possible. EB molecules bind to the microtubule between protofilaments (except at the seam), at the interface between four tubulin dimers [84]. This means that for each circumferential layer of tubulin dimers added, there will be maximally 12 new EB-binding sites created (Fig. 6.8 a); hence, maximally $n_{TipAct-max} = 12$ TipAct binding-sites as well. Hence, the maximum number of TipAct molecules bound at position x is given by:

$$n_{TipAct}(x) = n_{TipAct-max} \times P_{TA}(x) \tag{6.8}$$

However, since actin filaments have a diameter in the order of $\sim$ 4 nm [183], it is very unlikely that they will interact with TipAct molecules located around the whole circumference of the microtubule (Fig. 6.8 b). This means that in reality the maximum number of TipAct molecules that an actin filament will be bound to at a given position will not be $n_{TipAct-max} = 12$ (Eq. (6.8)), but lower. Since we cannot easily predict (or measure) the exact number of protofilaments available to capture a filament, we decided to perform simulations allowing F-actin to interact with TipAct molecules located at one, two and three consecutive protofilaments. In this case, the maximum number of molecules available for an actin filament to bind are $n_{TipAct-max} = 1$, 2 and 3.

In order to estimate TipAct's local concentration, besides the local number of molecules we also had to define an effective interaction volume around the microtubule, V_{eff}, within which actin filaments can be captured. Panel b in Figure 6.8 shows the scheme we used for this purpose: V_{eff} was defined as a cylindrical shell whose inner radius is the outer radius of the microtubule ($R_{MT} \sim 12.5$ nm), whose outer radius is defined by the sum of R_{MT} and the approximate lengths of the EB ($L_{EB} = 8$ nm [98]) and TipAct ($L_{TipAct} \sim 20$ nm [463]) molecules, and whose length is given by the length of one tubulin dimer (~ 8 nm [56]). In practice, this assumption means that an actin filament outside this cylindrical shell will not be captured. This is likely to be the case given the high ionic strength $I = 0.270$ M [495–497] of our working buffer (80 mM PIPES, pH 6.8, 4 mM Mg_2Cl, 1 mM EGTA and 75 mM KCl), which corresponds to a Debye screening length for electrostatic interactions below one nanometer [495].

Having defined the effective interaction volume V_{eff}, and the number of TipAct molecules $n_{TipAct}(x)$ at position x, the local concentration of TipAct molecules (defined in units of nm^{-3}), simply becomes:

$$[\text{TipAct}](x) = \frac{n_{TipAct}(x)}{V_{eff}} \tag{6.9}$$

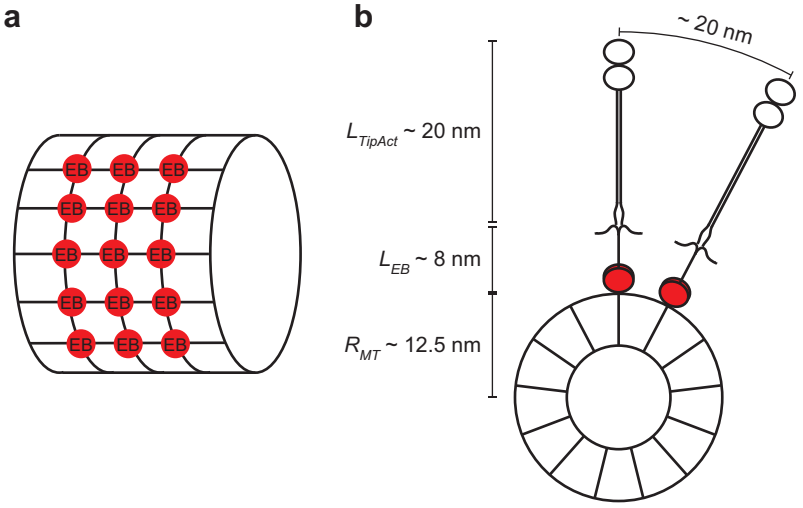

Figure 6.8: Maximum number of EB binding sites, and estimation of V_{eff}. (a) Schematic showing EB-binding sites at the microtubule. (b) Procedure to estimate the effective interaction volume, V_{eff}, based on the approximate dimensions of the microtubule (MT), EB and TipAct molecules.

Figure 6.9 shows the curves for $n_{TipAct}(x)$ and [TipAct](x) calculated for the same TipAct binding-probability profiles ($P_{TA}(x)$) shown in Fig. 6.7. Note that at certain values of x the average number of molecules can at times be less than one, since this value depends on the probability that a TipAct will be bound at this location.

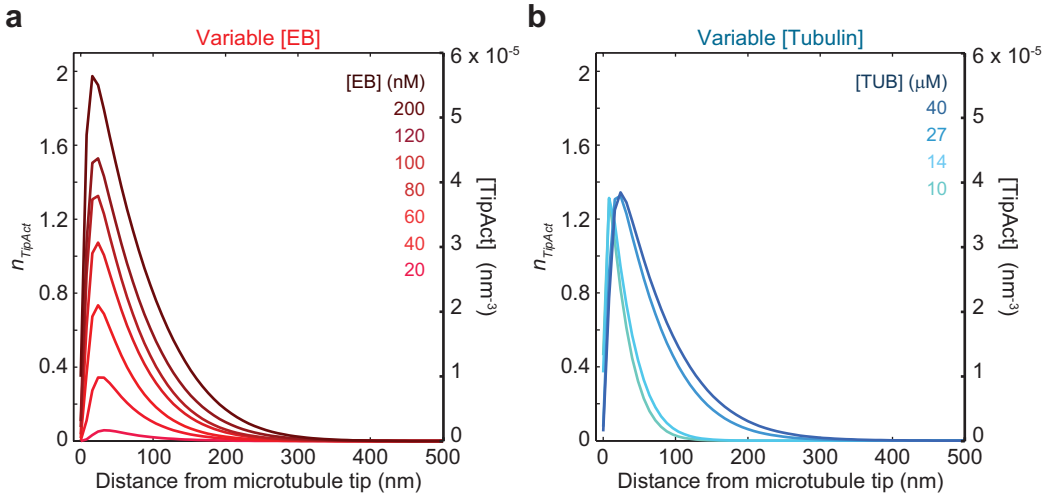

Figure 6.9: Number and concentration of microtubule-bound TipAct molecules as a function of position. Number ($n_{TipAct}(x)$, Eq.(6.8)), and concentration ([TipAct](x), Eq.(6.9)) of TipAct molecules calculated for variable EB (a) and tubulin (b) concentrations. Assuming that TipAct molecules at three protofilaments can bind to the actin filament.

6.2.4 Effective on- and off-rates of actin filaments at microtubule tips

In order to obtain the effective on- and off-rates of actin filaments at microtubule tips, in addition to the local concentration [TipAct](x) and number $n_{TipAct}(x)$ of TipAct molecules, we also required the on- an off-rates of a single TipAct molecule on actin filaments. To obtain these numbers, we performed high-temporal resolution (33 ms/frame) TIRF-imaging of TipAct molecules in solution, in the vicinity of phalloidin-stabilized actin filaments bound to a glass surface. Kymographs traced along the length of the actin filaments (Fig. 6.10 a) revealed multiple binding and unbinding events. To obtain an estimate for the off-rate for a single molecule ($k_{off-TipAct}$), we recorded the dwell time of 301 such events, and plot their distribution (Fig. 6.10 b). A single-exponential fit to these single-molecule dwell times (red line) yielded an average dwell time $\langle \tau_{TipAct} \rangle = 111 \pm 6$ ms, which corresponds to a single-molecule off-rate $k_{off-TipAct} = 0.009 \pm 0.001$ s^{-1}.

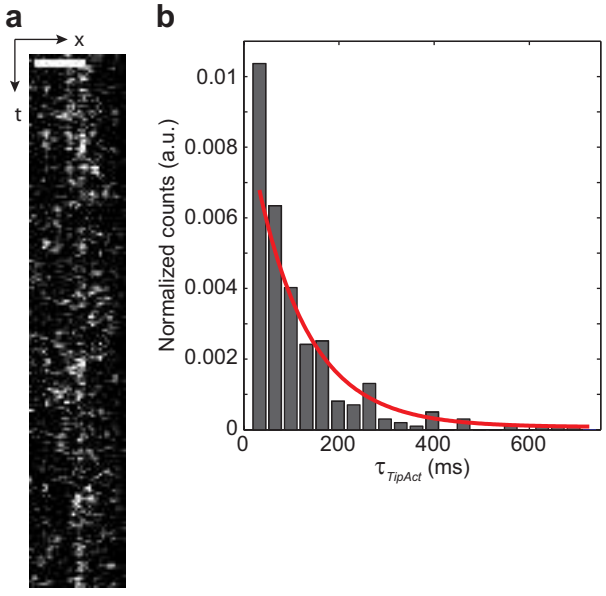

Figure 6.10: TipAct single-molecule dwell times on actin filaments. (a) High temporal resolution kymograph (33 ms/frame) of TipAct molecules showing multiple binding and unbinding events at a surface-bound actin filament. (b) Normalized distribution of TipAct dwell times (τ_{TipAct}), and single-exponential fit (red curve) which yielded an average dwell time $\langle \tau_{TipAct} \rangle = 111 \pm 6$ ms. n = 301.

To estimate the single molecule on-rate ($k_{on-TipAct}$), we made use of our measurement of the dissociation constant of TipAct from F-actin, $K_{D-TA:FA} = 5.2$ µM (Fig. 3.5),

and with the use of the following relationship:

$$K_{D-TA:FA} = \frac{k_{off-TipAct}}{k_{on-TipAct}},$$

thus determined the single molecule on-rate to be $k_{on-TipAct} = 0.0018$ µM^{-1}s^{-1}.

Given our estimates for [TipAct](x) (Eq.(6.9)), and $n_{TipAct}(x)$ (Eq.(6.8)), as well as for $k_{off-TipAct}$ and $k_{on-TipAct}$, we could thus calculate the on- and off-rates of actin filaments as functions of distance x from the microtubule tip. For a point particle, the on-rate at position x, $k_{on}(x)$, is defined as the product of the concentration of TipAct molecules at the same location times the on-rate to bind a single TipAct molecule, namely:

$$k_{on}(x) = k_{on-TipAct} \times [\text{TipAct}](x) \tag{6.10}$$

However, to account for the fact that actin filaments are not point particles but elongated objects, the on-rate $k_{on}(x)$ was modified. We assumed that if an actin filament were captured by a single TipAct molecule at the microtubule tip, immediately after, the remainder of the filament would zipper and be captured as well. This assumption means that the effective probability of actin filament capture is given by the sum of the probability of all the ways by which it can be captured. Hence, the effective on-rate, $k_{on-eff}(x)$, can be defined as the sum of all the on-rates for all sites along that microtubule tip that a single filament of length L can span, namely:

$$k_{on-eff}(x) = \sum_{i=x-L}^{i=x} k_{on}(i) \tag{6.11}$$

Figure 6.11 shows curves both for $k_{on}(x)$ and $k_{on-eff}(x)$ calculated for the same [TipAct](x) curves shown in Figure 6.9, assuming a filament length $L \geq 500$ nm, so that it would span the whole length of the TipAct comet.

In contrast to the on-rate, we reasoned that the actin filament off-rate, $k_{off}(x)$, does not depend on the local TipAct concentration, but rather on the number of TipAct molecules that the filament is bound to at position x ($n_{TipAct}(x)$). We assumed that if an actin filament were linked to $n_{TipAct} > 1$ molecules, to fully detach, all these molecules would have to let go of the filament at the same time. If the rate of re-binding is fast (which is likely, given that the rest of the filament will be kept in close proximity to the microtubule by the other linkages), this means that the likelihood of a filament fully detaching

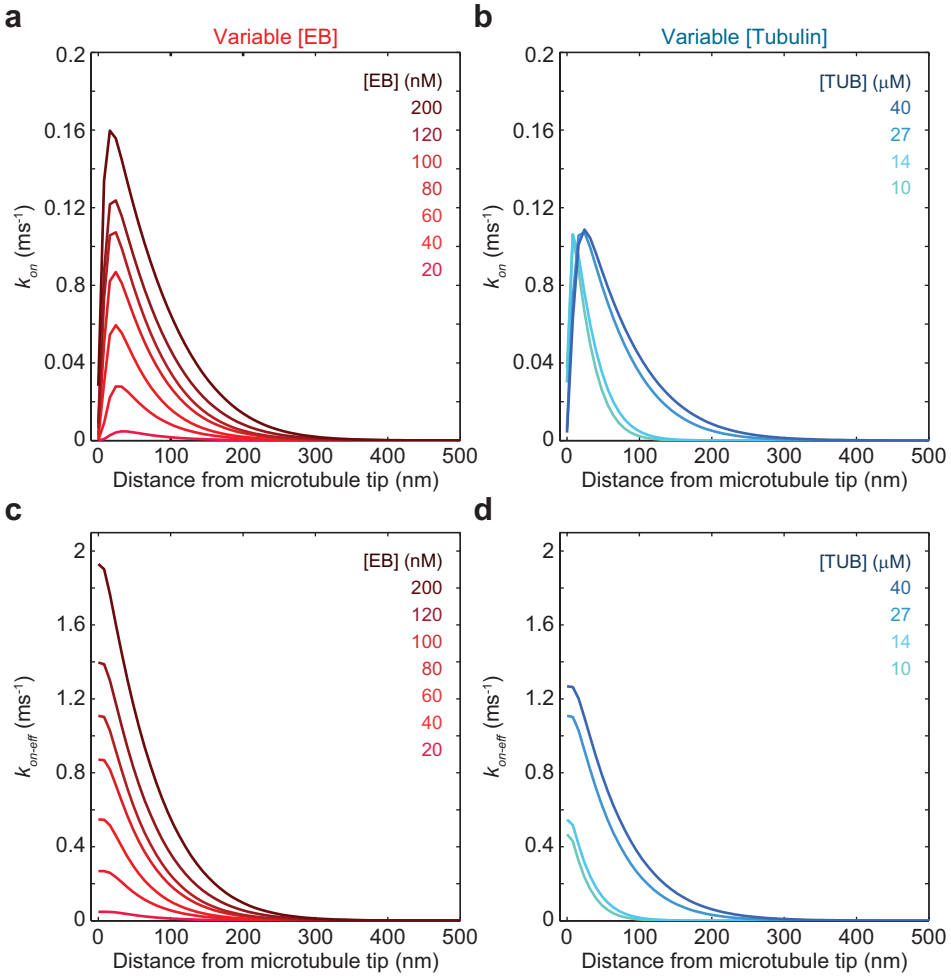

Figure 6.11: On-rates for point-particles and actin filaments as a function of position. On-rate for point particles ($k_{on}(x)$, Eq.(6.10)) calculated for variable EB (a) and tubulin (b) concentrations. Corresponding effective on-rate ($k_{on-eff}(x)$, Eq.(6.11)) for actin filaments of length $L \geq 500$ nm, calculated for the same EB (c) and tubulin (d) concentrations as in (a) and (b). Assuming that TipAct molecules at three protofilaments can bind to the actin filament.

will drop rapidly with increasing n_{TipAct}. This cooperative effect was first proposed to model kinetochore attachment to depolymerizing microtubules [494], and could help understand why, even though TipAct is a low-affinity actin binder ($K_{D-TA:FA} \sim 5$ μM), when locally concentrated at microtubule tips it can still collectively generate stable actin-microtubule connections. For a point particle bound to $n_{TipAct}(x)$ molecules, the off-rate is given by:

$$k_{off}(x) = (k_{off-TipAct})^{n_{TipAct}(x)} \tag{6.12}$$

Where the single-molecule off-rate $k_{off-TipAct}$ must be defined in units of time that make its magnitude less than one. Mathematically this ensures that the off-rate will

decrease with increasing n_{TipAct} [494]. Here, to account for the fact that actin filaments are not point particles but elongated objects, the number of molecules at position x was modified again to account for all the sites on the microtubule tip that a filament of length L can span, namely:

$$n_{TipAct-eff}(x) = \sum_{i=x-L}^{i=x} n_{TipAct}(i) \tag{6.13}$$

Consequently, the effective off-rate, $k_{off-eff}(x)$, of actin filaments at microtubule tips becomes:

$$k_{off-eff}(x) = (k_{off-TipAct})^{n_{TipAct-eff}(x)} \tag{6.14}$$

Figure 6.12 shows curves for $n_{TipAct-eff}(x)$ and $k_{off-eff}(x)$, for actin filaments of length $L \geq 500$ nm (i.e. longer than the TipAct comet). As can be seen, the higher the EB and tubulin concentration, the wider the region where $n_{TipAct-eff}(x)$ is greater than one, and hence the longer the region where $k_{off-eff}(x)$ is approximately zero.

6.2.5 Actin filament diffusion coefficient $D_{\parallel}$, and microtubule growth speed V_g

As explained in the introduction, we chose to model the transport of actin filaments through a biased diffusion mechanism (Fig. 6.2), where the actin filament binds and unbinds an inhomogeneously distributed concentration of TipAct molecules at microtubule tips, and is freely diffusible when unbound. Hence, the only two parameters left to fully define the model are the diffusion coefficient of the actin filaments $D_{\parallel}$, and the microtubule growth speed V_g.

To account for the diffusive motion of the filament when it is free, and given that we are modeling the system in one dimension, we had to estimate the diffusion coefficient of the filaments in the direction of microtubule growth, since with very few exceptions, and most certainly due to the elongated nature of the TipAct comet, the actin filaments were transported with their longest axis parallel to that of the microtubule (Fig. 6.1). In a regime where the actin filaments are dilute, such as in our assays ([F-actin] $\sim$ 30 nM), their diffusive motion can be described with the diffusion equations developed for the thermal motion of non-interacting thin rigid rods [499]. The diffusion coefficient in the direction of the longest axis of such a thin rigid rod is described by the following

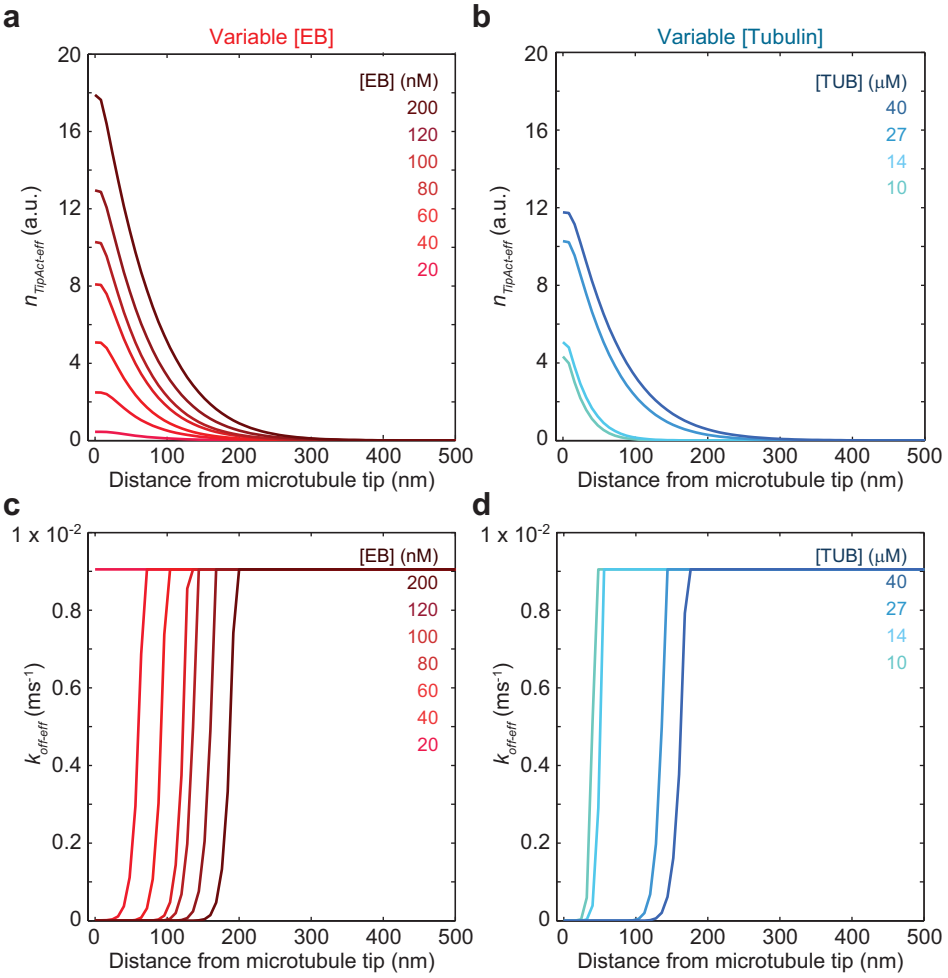

Figure 6.12: Effective number of TipAct molecules and effective off-rate for actin filaments as a function of position. Effective number of TipAct molecules that actin filaments of length $L \geq 500$ nm can bind ($n_{TipAct-eff}(x)$, Eq.(6.13)) calculated for variable EB (a) and tubulin (b) concentrations. Corresponding effective off-rate ($k_{off-eff}(x)$, Eq.(6.14)) calculated for the same EB (c) and tubulin (d) concentrations as in (a) and (b). Assuming that TipAct molecules at three protofilaments can bind to the actin filament.

expression [499]:

$$D_{\parallel} = \frac{k_b T ln(L/b)}{2\pi\eta L}, \tag{6.15}$$

where $k_b = 1.381 \times 10^{-23}$ JK^{-1} is Boltzmann's constant, T the absolute temperature (which in our experiments was kept between 28-30°C = 301.15 − 303.15 K), η the viscosity of the solution (which we estimated to be 1.3 mPa·s, since we always add 0.1 % w/v methyl-cellulose to the buffer to keep the microtubules close to the surface [500]), L the actin filament length, and $b = 4$ nm the filament diameter. With these

parameters we were thus able to obtain an estimate for $D_{\parallel}$ as a function of filament length L, as shown in Fig. 6.13.

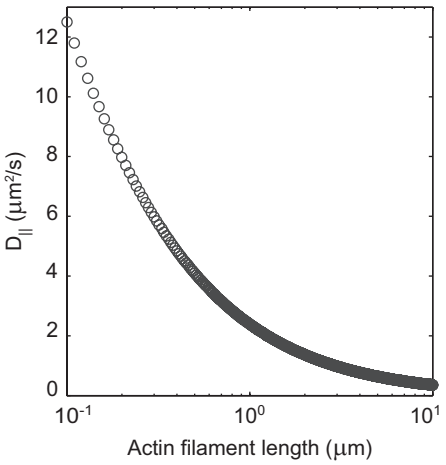

Figure 6.13: Actin filament diffusion coefficient in the direction of its longest axis. Solution to Eq.(6.15) as a function of actin filament length, L. Letting: $k_b = 1.381 \times 10^{-23}$ JK^{-1}, $T = 301.15$ K, $\eta = 1.3$ mPa·s and $b = 4$ nm.

The final parameter needed to complete the model was the microtubule growth speed V_g, which determines how fast the TipAct plus-end profile will travel, and hence how fast the actin filament has to diffuse to keep up with it. To this end, we measured the growth speeds of microtubules polymerized at different conditions: variable EB (while keeping Tubulin constant at 27 µM, as well as the molar ratio between EB and TipAct at 4:1); and variable tubulin (while keeping EB at 100 nM and TipAct at 25 nM). Figure 6.14 shows the results from these experiments: the red and blue data points in panels b and c show the results from the global measurement of V_g. These averages are broad given that they span from the moment the microtubule nucleates up until it has a catastrophe (Fig. 6.14 a). In contrast, the black data points are the average growth speeds measured only in portions of microtubule growth in which the actin filaments were transported. This shows that the filaments tend to be captured and transported by microtubule tips in the periods of faster (and more stable) microtubule growth. To fairly compare simulation with experiment, instead of using the global average value of V_g (red and blue data points in Fig. 6.14 b and c), for the simulations we chose to use the values of V_g corresponding to the periods during which actin filaments were mostly captured (black data points in Fig. 6.14 b and c).

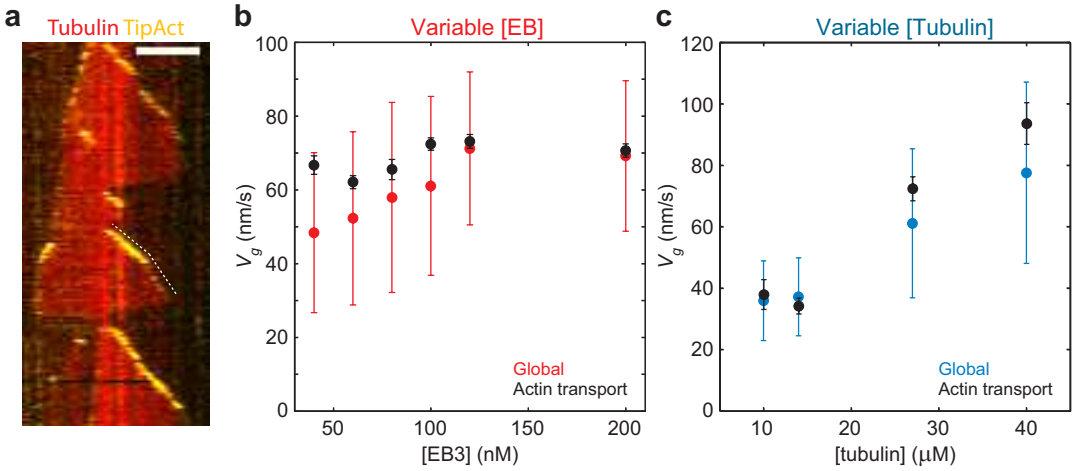

Figure 6.14: Microtubule growth speeds at variable EB and tubulin concentrations. (a) Example kymograph of microtubule growth with 27 μM tubulin, 100 nM EB3, and 25 nM TipAct, showing that microtubules often transition between different growth-speeds, V_g. Experimentally-measured average values of V_g for variable EB3 (b) and tubulin (c) concentrations. The red and blue data points in (b) and (c) show the global averages (from nucleation up until catastrophe), and the black data points the averages only gathered during instances of actin filament transport.

6.3 Gillespie-based simulations of actin filament transport by growing microtubules

As explained in the introduction, we chose to model the transport of actin filaments with a one-dimensional biased diffusion scheme. The simulation itself was implemented using a Doob-Gillespie stochastic algorithm [501] in which the microtubule was modeled as a discrete array of $i = 1...N$ reaction volumes each with distinct on-rate ($k_{on-eff}(i)$, Fig. 6.11) and off-rate ($k_{off-eff}(i)$, Fig. 6.12) for F-actin. The actin filament was modeled as a point particle (which represents the location of the edge of the filament closest to the microtubule tip) that can bind and unbind at each location i, and freely diffuse in one dimension when unbound.

To simulate actin filament diffusion, we defined a diffusion rate k_{diff} between adjacent reaction volumes. It has been previously shown that the Gillespie algorithm correctly approximates diffusion provided that the rate is chosen to be $k_{diff} = D_{\|}/h^2$, where $D_{\|}$ is the diffusion coefficient of the moving species (i.e. the actin filament, in the direction of its longest axis) and h the width of the reaction volume [502]. In our case $h = 8$ nm, given by the size of the tubulin dimer [56], which also corresponds to the spacing of EB molecules at microtubule tips [84]. Finally, to simulate microtubule growth, both

the on- and off-rates were shifted laterally at a rate corresponding to the microtubule growth speed V_g.

Figure 6.15 shows a schematic of the algorithm's implementation. When the filament is bound, the only thing that can occur is detachment. Conversely, when it is free, the filament can either re-bind, diffuse one unit ($h = 8$ nm) to the left or to the right. We arbitrarily defined an actin filament to have escaped if it spent at least 500 ms in free diffusion, since in preliminary tests we found that after such a time the motion of the filaments was often uncorrelated from that of the moving microtubule tip (data not shown). Concomitantly with each reaction step, we monitored the total time elapsed and shifted the rates to the left (the arbitrarily chosen direction of microtubule growth) when the elapsed time reached the minimum time required for the microtubule to grow one unit ($h = 8$ nm), as defined by the experimentally determined growth speed V_g (Fig. 6.14).

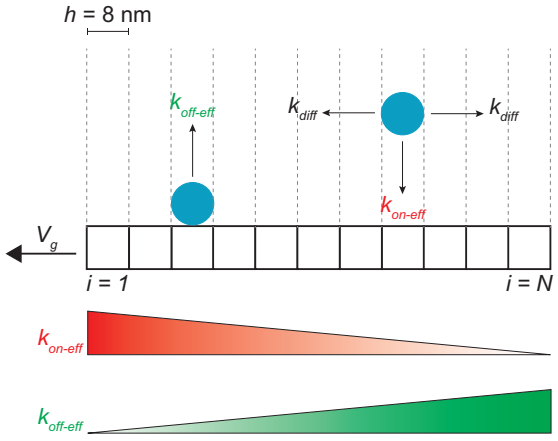

Figure 6.15: Scheme for Gillespie-based simulation of actin filament transport by microtubule tips. The microtubule tip was modeled as a discrete array of N bins of width $h = 8$ nm, each with different on and off rates for F-actin. The actin filament was modeled as a point-particle, which tracked the edge of the filament closest to the edge of the microtubule tip. To account for the filament length, the point-particle on and off rates were modified (k_{on-eff}Eq.(6.11), and $k_{off-eff}$ Eq.(6.14)). When bound, the only possible event is to detach. When unbound, the filament can either diffuse left or right (with rate $k_{diff} = D_{\parallel}/h^2$) or rebind. The rates were shifted to the left at the experimentally-measured microtubule speed, and filament escape was defined when the filament spent ≥ 500 ms in free diffusion.

We performed simulations for six EB and four tubulin concentrations, respectively, corresponding to the conditions for which we also had experimental data (Fig. 6.14). For each condition, we simulated the transport for nine different actin-filament lengths ranging from 0.5 to 20 µm, and for each filament length we ran the simulation 300

times. At each start of the simulation, the actin filament initial position was fixed to be exactly one unit ($h = 8$ nm) behind the microtubule tip. We found that this initial location did not matter much since the filaments, through diffusive excursions, quickly lost memory of their initial location.

6.4 Simulation results: effects of variable actin filament length, EB and tubulin concentrations

6.4.1 Single filament behavior is highly stochastic

The first result to come out of the simulation was that at the single-filament level the actin-transport effect is stochastic. Figure 6.16 a and b show all 300 hundred trajectories simulated both for a 1 µm and a 20 µm-long actin filament at the microtubule growth conditions indicated in panel a. The trajectories are colored from dark to light blue according to their duration, with the longest trajectory overlaid in black. As can be seen, the transport is dominated by short events, with few long excursions. Moreover, a comparison between panels a and b in Figure 6.16 suggests that shorter filaments tend to localize closer to (or right on top of) the microtubule tip, whereas longer filaments tend to follow microtubule growth at some distance from the tip.

To better understand the transport effect, we focused our analysis on the three parameters most amenable for comparison with experimental data: the duration of the transport event (*following time*), the difference in speed between microtubule growth and actin transport, and finally the average distance between the microtubule tip and the nearest edge of the actin filament. Panel c in Fig. 6.16 shows the distributions for these three parameters, for the 300 simulated trajectories corresponding to actin filament lengths of 1, 5 and 20 µm, at the microtubule growth conditions indicated in panel a. As can be seen, all three parameters depend on the filament length. The shorter filaments were transported at speeds closer to the microtubule growth speed, which resulted in increased duration of the transport events (Fig. 6.16 a and c). This is most likely due to their higher diffusion coefficient (Fig. 6.13), which allows them to explore a larger area in less time, giving them an increased chance of catching up with the moving tip and re-binding.

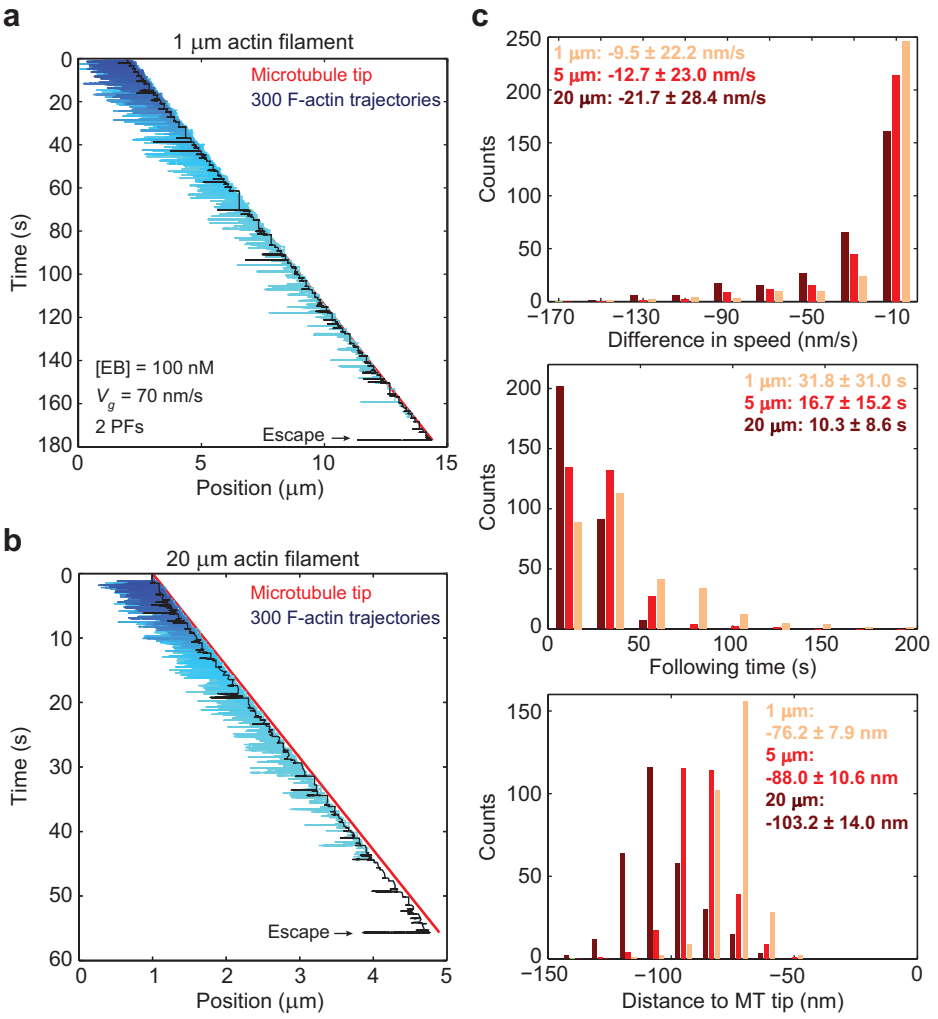

Figure 6.16: Single actin filament transport behavior. Overlaid transport trajectories for 300 simulated 1 µm (a), and 20 µm (b) actin filaments, for the microtubule growth conditions indicated in panel (a). The position of the microtubule tip is indicated in red. The dark-to-light blue gradient indicates the duration of the trajectories. The longest trajectory is overlaid in black. The point of actin filament escape is indicated with a black arrow. (c) Distributions of difference in speed (top), following time (middle) and distance to the tip (bottom) for actin filaments of length 1, 5 and 20 1 µm respectively, at the simulated microtubule growth conditions indicated in panel (a). The insets show the average ± standard deviation of these parameters, for all the trajectories simulated. In all cases shown, we assumed that two protofilaments (PFs) could bind the actin filament.

6.4.2 Actin filament transport for variable EB and tubulin concentrations

Given that all three quantities of interest (following time, difference in speed, and distance to microtubule tip) are not deterministic but rather distributed (Fig. 6.16), we chose to compare the mean of their distributions (plus-minus standard error) for all simulated filament lengths, across all experimental conditions.

A detailed inspection of kymographs of experimentally observed actin transport events, revealed that actin filaments which are captured behind or at the very peak of the TipAct profile (*trailers*, Fig. 6.17 a), tend to follow the microtubule tip more efficiently compared to those that are initially captured with a portion of the actin filament ahead of the tip (*leaders*, Fig. 6.17 b), which tend to lag behind. We reasoned that this is due to the number of TipAct molecules available to the two types of filaments. On the one hand, *trailing* filaments bind an approximately constant number of TipAct molecules (Fig. 6.17 c), and they thus tend to follow with almost no lag, often remaining at some distance behind the peak of the TipAct intensity (Fig. 6.17 a). On the other hand, *leading* filaments can bind an increasing number of TipAct molecules as the microtubule continues to grow (Fig. 6.17 d). Hence, they tend to follow the microtubule tip with a higher lag in speed (Fig. 6.17 b). Given these two distinct actin-transport behaviors, we decided to separate the simulated data in a similar fashion: *trailing* actin filaments were defined as filaments which never diffused further than 100 nm ahead of the microtubule tip. Conversely, actin filaments were classified as *leaders* if they diffused $\geq$ 100 nm beyond the microtubule tip at some point during their trajectories.

With this classification in mind we first analyzed the probability that filaments of different lengths remain as *trailers*, given that in our simulations all filaments were initialized one unit ($h = 8$ nm) behind the microtubule tip. As can be seen in Figure 6.18 a, the probability of actin-filament *trailing* increased with filament length as well as EB concentration. This is likely due to two things: first, longer filaments have lower diffusion coefficients (Fig. 6.13), which makes it harder for them to diffuse to the peak of the TipAct plus-end profile before being captured; and second, higher EB concentrations result in higher microtubule growth speeds (Fig. 6.14), as well as more elongated and concentrated TipAct plus-end profiles (Fig. 6.7). In combination, these two effects make it *harder* for the actin filaments to diffuse all the way (or beyond) the most intense region of the TipAct comet before being captured, and thus they remain *trailers*.

Given that the portion of actin filaments remaining as *trailers* dominated the number of

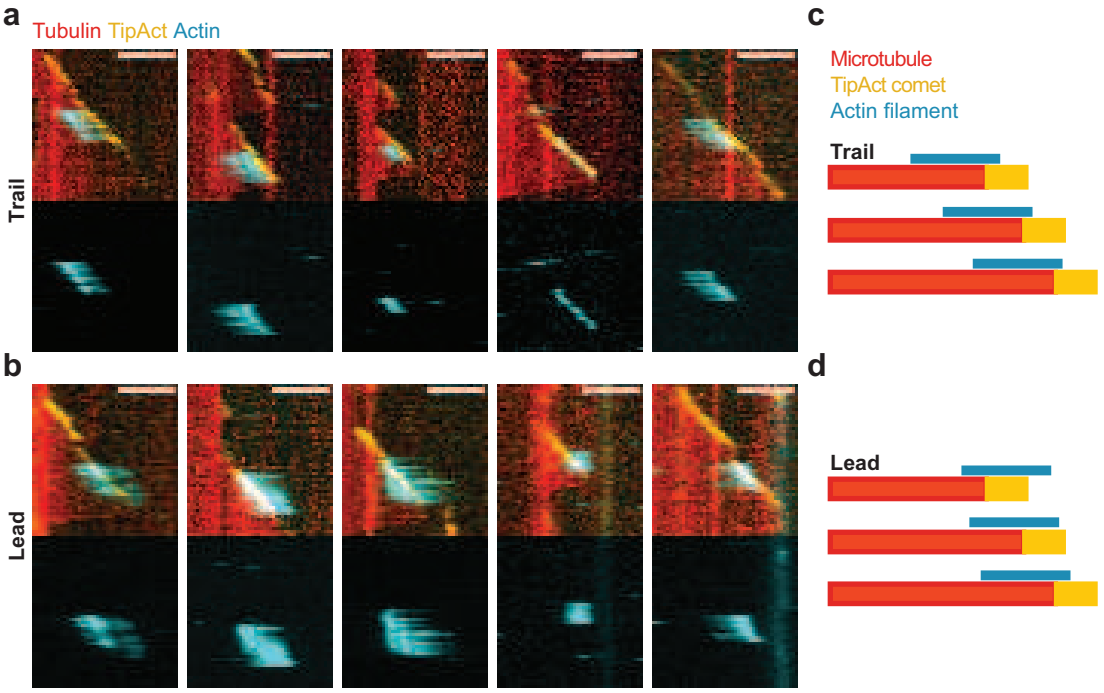

Figure 6.17: Gallery of example kymographs of *trailing* and *leading* actin filaments. (a) Examples of *trailing* actin filaments which follow the growing microtubule plus-end with almost no difference in speed, and remain at non-zero distance behind the peak of the TipAct plus-end intensity. (b) Examples of *leading* actin filaments which land ahead of the microtubule plus-end, and follow the growing microtubule tip with a lag in speed. Schematics of *trailing* (c) and *leading* (d) actin-filament behavior, showing the different length of the TipAct plus-end region available to each type of filament. In (a) and (b) microtubules were polymerized in the presence of 27 µM tubulin, 100 nM EB3 and 25 nM GFP-TipAct. Scale bars, 5 µm.

transport events across all filament lengths simulated, we decided to focus the analysis on this type of transport. To be able to fully capture the *leading* filament behavior we would have to modify the simulation to allow the actin filaments to start at a range of positions ahead of the microtubule tip. This, however, was beyond the time-scope of this study.

Thus, panels b, c and d in Figure 6.18 show the results for the distance to the microtubule tip, following time and difference in speed, for the portion of the simulated trajectories which behaved as *trailers*, for a range of EB concentrations of 40 to 200 nM. First, due to EB's effect on the microtubule growth speed and the length and intensity of the TipAct plus-end comet, we found that the average distance from the microtubule tip increased with increasing EB concentration (Fig. 6.18 b). We also observed a weak increase in average distance to the tip for increasing filament lengths due to their lower diffusion coefficients.

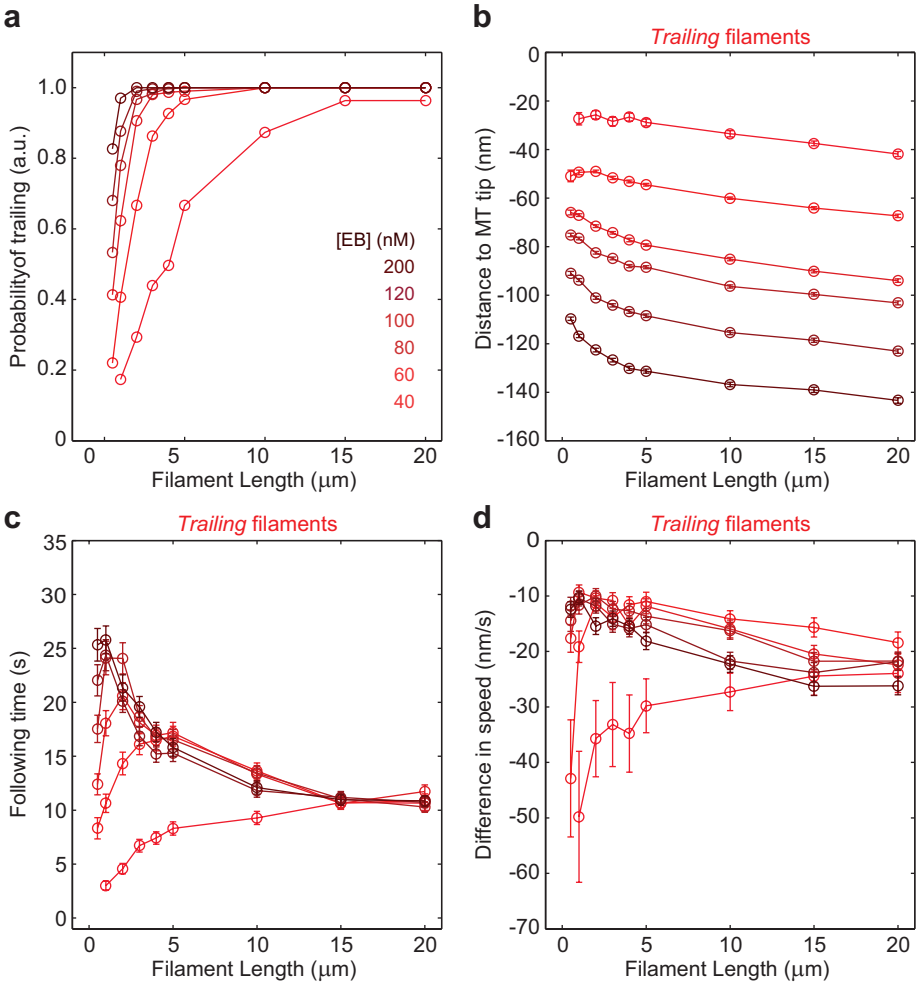

Figure 6.18: Actin transport efficiency depends on the filament length and EB concentration. (a) Probability of actin-filaments remaining as *trailers* as a function of variable EB concentration and filament length. Average distance to the microtubule tip (b), following time (c) and difference in speed (c), for the fraction of simulated trajectories that behaved as *trailers* as a function of filament length, for the same variable EB concentrations indicated in (a). Assuming that two protofilaments are available to capture the actin filament.

The following time increased with EB concentration for short filaments, but was approximately constant for longer filaments ($\geq$ 10 μm). Furthermore, there appeared to be an optimal filament length for most successful transport at a given EB concentration. This optimal length shifted to smaller values with increasing EB concentration, up until 200 nM where the maximum following time occurred at the shortest filament simulated (i.e. 0.5 μm). Finally, with the exception of the lowest EB concentrations tested (40 and 60 nM), the difference in speed between microtubule growth and actin transport weakly increased with EB concentration. The higher variability in the 40 and 60 nM data (particularly for short filaments, $\leq$ 5 μm), is due to the lower number of trajectories

that went into the averages, since at these EB concentrations, a significant fraction of the simulated trajectories behaved as *leaders* (Fig. 6.18 a).

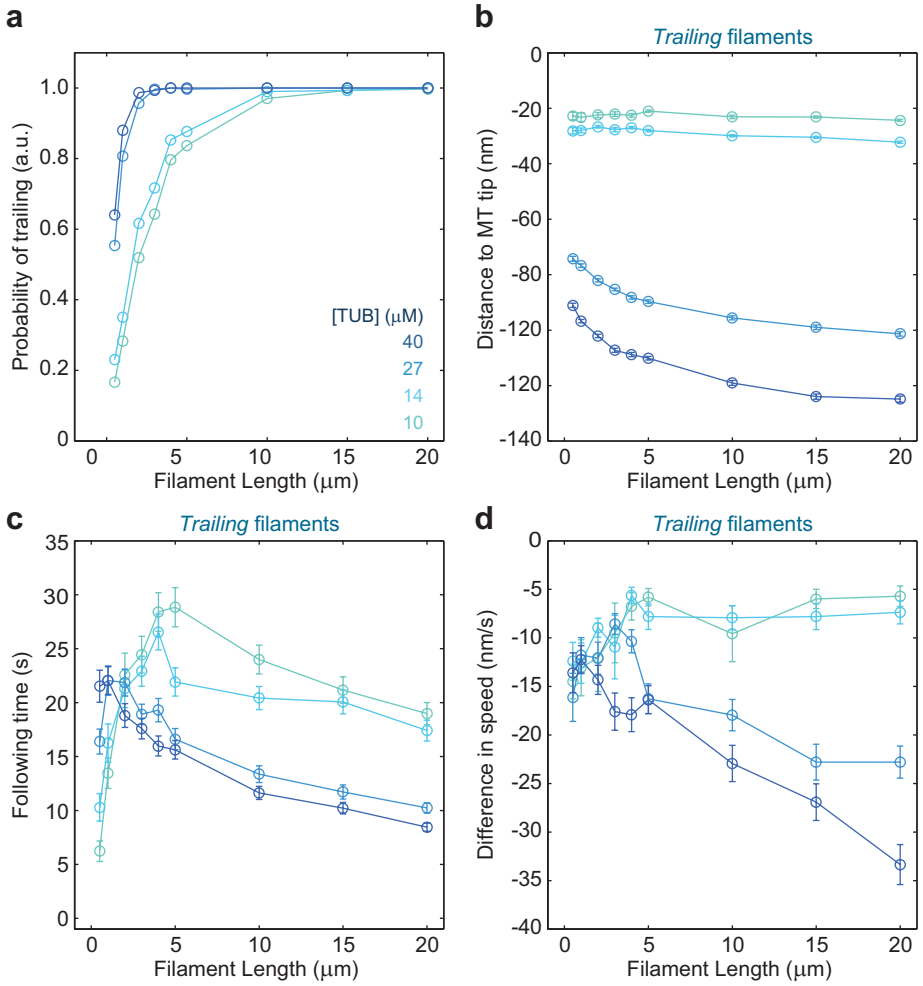

Figure 6.19: Actin transport efficiency depends on the filament length and tubulin concentration. (a) Probability of actin-filaments remaining as *trailers* as a function of variable tubulin concentration and filament length. Average distance to the microtubule tip (b), following time (c) and difference in speed (c), for the fraction of simulated trajectories that behaved as *trailers* as a function of filament length, for the same variable tubulin concentrations indicated in (a). Assuming that two protofilaments are available to capture the actin filament.

Figure 6.19 shows a similar analysis across tubulin concentrations ranging from 10 to 40 µM. The probability that an actin filament remained a *trailer* increased with filament length and tubulin concentration. Similarly to the varying EB situation, this is due to a couple of things: first, the lower diffusion coefficient of longer filaments; and second, the marked increase in microtubule growth speed (Fig. 6.13 b), and length of TipAct's plus-end profiles (Fig. 6.7 d) that result from increasing tubulin concentration.

For the fraction of trajectories that behaved as *trailers*, the average distance between the actin filament and the microtubule tip increased with increasing tubulin concentration (Fig. 6.19 b). This is most likely due to the increasing length of the TipAct plus-end profile (Fig. 6.7 d), which allows for actin filament capture at a wider range of distances from the microtubule tip. The following time also showed a dependence on filament length consistent with the EB simulations. We observed an optimal filament length to follow a growing microtubule tip at a given tubulin concentration, which became smaller with increasing tubulin. In contrast to the variable EB simulations, we found that the following time decreased with increasing tubulin concentration (Fig. 6.19 c). Finally, the difference in speed between microtubule growth and actin-filament transport was more strongly dependent on tubulin concentration than in the varying EB simulations.

These observations indicate that there are three main regulators of actin-filament transport by microtubule growing ends: First, the length of the actin filament, since simulations for a variety of filament lengths showed that longer filaments (with lower diffusion coefficients) have a harder time keeping up with the moving tip. Second, the microtubule growth speed, since simulations showed that with increasing EB and tubulin concentration (both of which increase the growth speed), actin filaments had a harder time keeping up by diffusion with the growing tip. And finally, the length and concentration of the TipAct profile at microtubule tips. The length regulates how far behind the microtubule tip the actin filament can still be captured; and the concentration regulates the probability of recapture and release.

6.5 Comparison between simulation and experimental data

Having studied through simulations how, in our biased-diffusion model, actin filament transport depends on the filament length, the microtubule growth speed, and the length and intensity of the TipAct plus-end profiles, the next step was to compare the simulation results with the experimental data. The simulations revealed that the efficiency of actin transport depends on filament length (Fig. 6.18 and Fig. 6.19). However, it was difficult to experimentally collect sufficient transport events to distinguish across actin-filament lengths. Thus, we decided to compare simulation and experiment across all actin filament lengths simulated with the global averages obtained experimentally. In other words, the data points in Figure 6.20 show the mean and standard deviation for

all the experimentally measured data (irrespective of filament length, but separated between *trailers* and *leaders*), and the colored areas the ranges that the simulations covered for all *trailing* filaments (which as mentioned above, dominated the simulations), with all filament-lengths pooled together. Three colored ranges are shown to differentiate simulations that allowed TipAct molecules at one, two and three adjacent protofilaments to bind to actin filaments. The experimental data for variable EB concentration was obtained from actin-transport assays at 27 µM tubulin, with a fixed ratio between EB3 and TipAct concentration of 4:1; and in the assays at variable tubulin concentration, the concentrations of EB3 and TipAct were kept constant at 100 nM and 25 nM respectively. All imaging was performed between 28 and 30°C.

Panels a and b in Figure 6.20 show the following time across a range of EB and tubulin concentrations. The simulations for one, two and three protofilaments did not vary much between each other for this parameter. Both in simulation and experiment the average following time increased with increasing EB concentration. As mentioned before, this is likely the combined result of the weak increase in growth speeds and marked increase in TipAct concentration at microtubule tips. Conversely, with increasing tubulin concentration the average following time tended to decrease, albeit more markedly in experiment than in simulation. As discussed above, this decrease is likely the result of the marked increase in growth speeds and length of the TipAct plus-end profiles.

Panels c and d in Fig. 6.20 show the difference in speed across the same EB and tubulin concentrations as in a and b. With increasing EB concentration the average difference in speed for *trailing* filaments remained nearly constant both in simulation and experiment. Moreover, the simulations successfully captured the magnitude of the speed. With the exception of the one-protofilament simulation,in which the predicted values were more broadly distributed at low EB and tubulin concentrations. In contrast, and as mentioned above, the *leading* filaments tended to follow the microtubule tip with a higher, but EB-independent lag in speed. This likely stems from the elongated nature of the contact zone between actin and microtubule (Fig. 6.17 d), as well as the very weak increase in growth speeds with increasing EB concentration (Fig. 6.14 a).

With increasing tubulin concentration (Fig. 6.20 d), we observed a marked increase in lag in speed in experiments, and a somewhat weaker increase in simulation. Both *trailing* and *leading* filaments tended to lag behind the microtubule tip more strongly with increasing tubulin. This lag most likely stems from the lengthening of the TipAct plus-end profiles (Fig. 6.7) and the marked increase in growth speeds (Fig. 6.14) with increasing tubulin concentration. Similarly to the EB case, the simulations for two

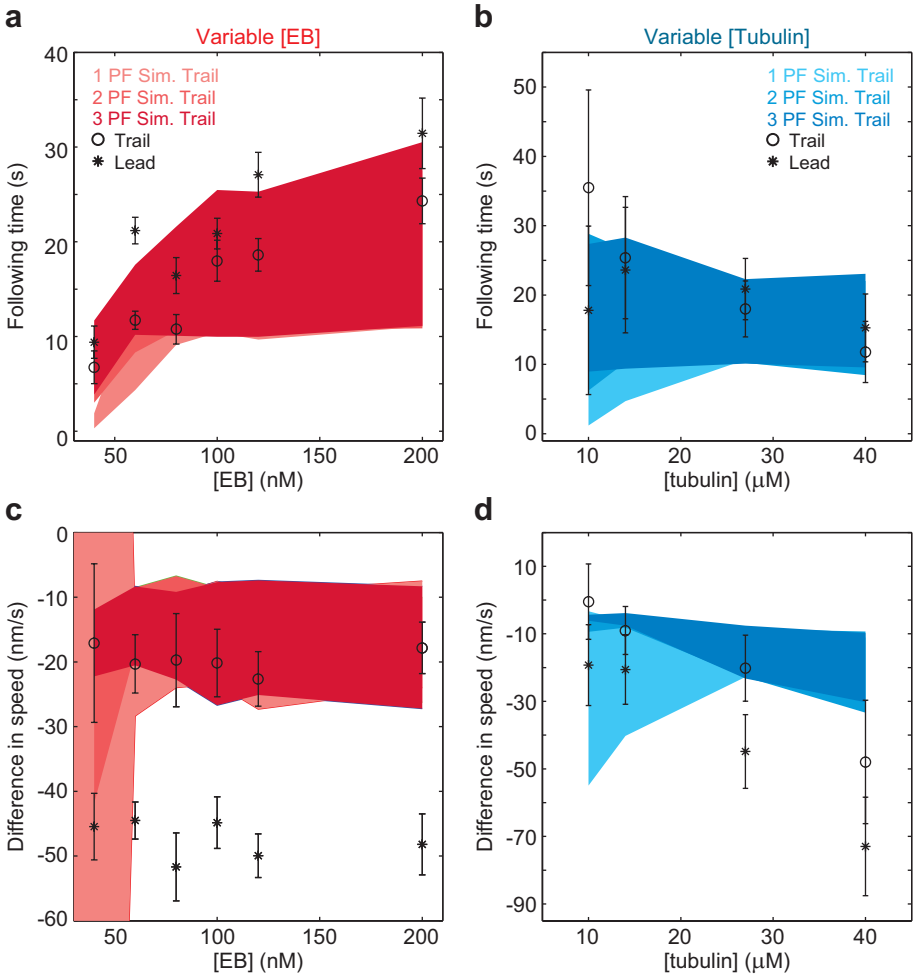

Figure 6.20: Comparison between data and simulation: following time and difference in speed. Experimental average following-time for *trailing* (circles) and *leading* (stars) actin filaments (averaged over all filament lengths), as a function of variable EB (a) and tubulin (b) concentration. Experimental average difference in speed for *trailing* (circles) and *leading* (stars) actin filaments (averaged over all filament lengths), as a function of variable EB (a) and tubulin (b) concentration. The colored areas in (a), (b), (c) and (d) show the minimum and maximum ranges predicted by the simulation allowing TipAct at one, two and three adjacent protofilaments to bind to the actin filament, as indicated in (a) and (b).

and three protofilaments were nearly indistinguishable from each other, whereas the values predicted by the one protofilament simulation were more broadly distributed, particularly at the low tubulin concentrations.

6.6 Further predictions of the model

Given that our model of actin transport through a biased-diffusion mechanism closely resembled the experimental data both in trends and absolute magnitudes, we turned to the predictions made by the simulation which would be more challenging to measure experimentally: first, the average distance between the actin filament and microtubule tip, and second, an estimation of the range of forces that the biased-diffusion mechanism can generate.

6.6.1 Average distance from the microtubule tip

One prediction of the simulation is that both with increasing EB and tubulin concentration the average distance between *trailing* filaments and the microtubule tip should increase. Figure 6.21 shows the distance from the microtubule tip predicted by the one, two and three protofilament simulations, for variable EB and tubulin concentration respectively. The data points show the average ± standard deviation (irrespective of actin-filament length), and the colored areas the maximum ranges covered by the simulations. The range of distances predicted (0 - 160 nm) lies well below the diffraction limit of our microscope ($\sim$ 270 nm, for the emission wavelength of Alexa-647-labeled F-actin which we used in all experiments [503]). A precise measurement of the distance between actin and microtubule tip could be obtained with higher-resolution imaging techniques, which are unfortunately hampered by acquisition times that are incompatible with the timescales of microtubule growth in these assays (30 - 100 $\mathrm{nm\,s^{-1}}$, Fig. 6.14). Alternatively, fitting the F-actin edge-intensity with a step-function, and Tip-Act plus-end intensity with a Gaussian function, could help refine the position measurements. At the point of completion of this thesis, however, we can only assert, as the actin-transport kymographs in Figure 6.17 reveal, that *trailing* filaments do follow the microtubule tip at some non-zero distance from the peak intensity of the TipAct comet, consistent with this prediction.

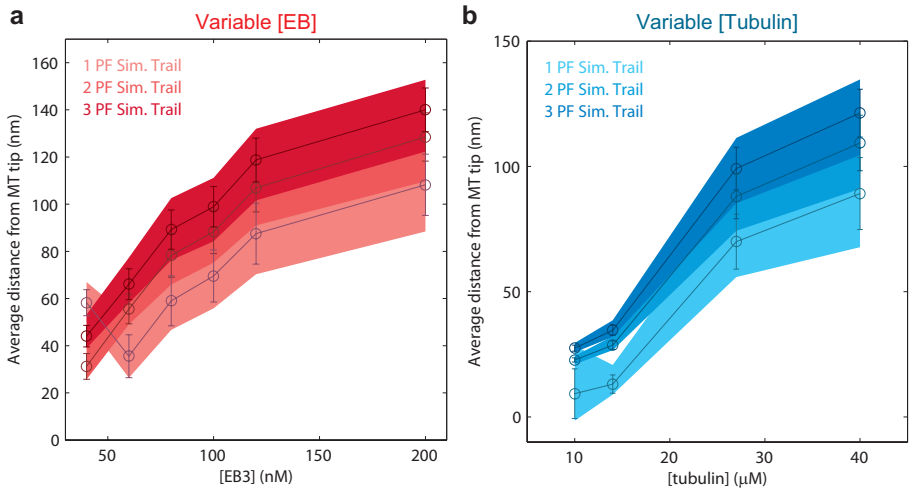

Figure 6.21: Average distance between actin filaments and microtubule tips increases with EB and tubulin concentration. Predicted average distance between actin filaments and microtubule tip (independent of actin filament length) for variable EB (a) and tubulin (c) concentrations. The data points and lines show the average ± standard deviation, and the colored areas the minimum and maximum ranges predicted by the simulation allowing TipAct at one, two and three adjacent protofilaments to bind to the actin filament, as indicated.

6.6.2 Force generation by the biased-diffusion mechanism of actin-filament transport

To compute the force that microtubules can exert on actin filaments via TipAct molecules at their growing ends, we turned back to our discretized model of the microtubule tip (Fig. 6.15). In the model, the microtubule tip consists of $i = 1...N$ sites, each one with a different affinity for F-actin. Given that each site can be in one of two states, free or occupied by F-actin, allowed us to study the system from a thermodynamic standpoint. Letting ΔG_i be the free energy difference between the free and occupied states at site i, and setting the energy of the free state to be zero, the partition function at site i is simply defined as:

$$Z_i = e^{-\Delta G_i / k_b T} + 1 \tag{6.16}$$

where k_b is Boltzmann's constant and T the absolute temperature. ΔG_i represents the Gibb's free energy change resulting from binding an actin filament at position i, which depends on the local on-rate ($k_{on-eff}(i)$, Eq.(6.11)) and off-rate ($k_{off-eff}(i)$, Eq.(6.14)) for F-actin:

$$\Delta G_i = k_b T \ln \left(\frac{k_{off-eff}(i)}{k_{on-eff}(i)} \right) \tag{6.17}$$

Combining Eq.(6.16) and Eq.(6.17), the partition function at position i thus becomes:

$$Z_i = \left(\frac{k_{on-eff}(i)}{k_{off-eff}(i)} \right) + 1 \tag{6.18}$$

Having defined the partition function of the system in terms of the effective on- and off-rates at position i, it is straightforward to calculate the Helmholtz' free energy F_i, and hence the force at the same location, that is:

$$F_i = -k_b T \ln Z_i = U_i - TS \tag{6.19}$$

where U and S are the internal energy and entropy. Assuming that S is independent of position, the force f_i that the local concentration of TipAct molecules at growing microtubule ends can exert on an actin filament thus becomes:

$$f_i = -\frac{dF_i}{dx} = -\frac{dU_i}{dx} \tag{6.20}$$

Figure 6.22 shows the expected values for f_i (Eq. (6.20)) as a function of distance from the microtubule tip over the ranges of EB and tubulin concentrations studied in the simulation, using the values for $k_{on-eff}(i)$ and $k_{off-eff}(i)$ shown in Figures 6.11 and 6.12.

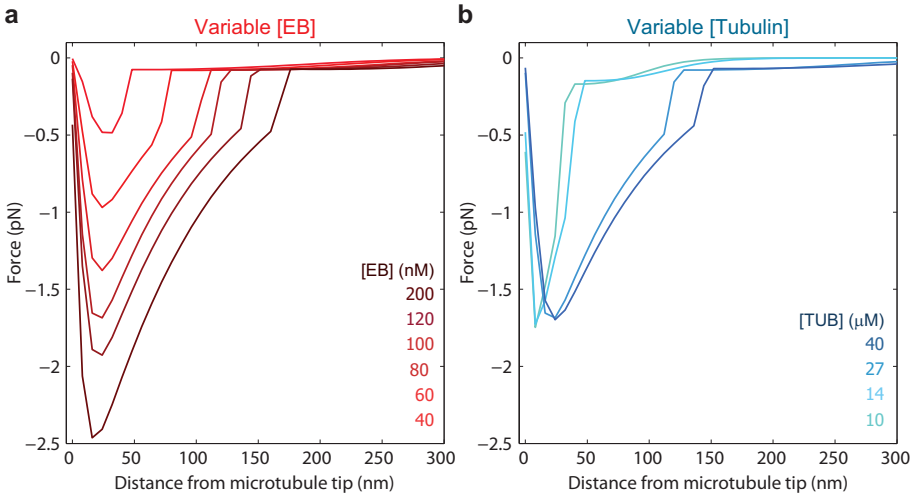

Figure 6.22: Forces generated by the biased-diffusion mechanism of actin-transport. Estimated forces using Eq. (6.20) for variable EB (a) and tubulin (b) concentrations. Assuming that TipAct molecules at two protofilaments can bind to the actin filament.

As can be observed, the maximum pulling force increases with increasing EB concentration, as does the range of distances at which forces can still be sensed by the actin filament. In contrast, the maximum force is independent of tubulin concentration, although the range of distances from the microtubule tip at which significant forces can be exerted increases with tubulin concentration. Interestingly, the predicted ranges of forces lies within the picoNewton range, which is comparable to the forces generated by molecular motors ($\sim 1-6$ pN [504]). This suggests that this force-generating mechanism could play a significant role in cells, potentially allowing microtubules to exert forces on weakly cross-linked actin-filament structures, leading to their reorganization.

6.7 Discussion

In this chapter we have studied how the non-homogeneous distribution of EB (and hence TipAct) molecules at growing microtubule ends can result in transport and force generation on actin filaments. We demonstrated the ways by which the shape of the TipAct profile (both its concentration and length) as well as the microtubule growth velocity can affect the transport effect. Both from simulation and experiment we found that increasing microtubule growth velocities negatively affect the transport of actin filaments, since the filaments rely on diffusive motion to catch up with the moving microtubule tip. Similarly, we found that the length of the TipAct plus-end profile negatively regulates the transport, by allowing microtubule tips to capture actin filaments at a wider range of distances, hence disallowing them to diffuse and catch up with the most intense region of TipAct concentration. In contrast, the peak concentration of TipAct molecules at microtubule tips positively regulated the transport behavior, which resulted in actin filaments to follow the microtubule tip for longer periods of time.

Experimental data revealed that filaments that land with a portion of their length ahead of the microtubule tip (i.e. *leaders*) behave significantly different from filaments that land right on top of or even behind the tip (i.e. *trailers*). Our simulations managed to successfully capture the main experimental parameters measured for the *trailing* filaments, namely following time and difference in speed. However, we did not have time to run the simulations for *leading* filament transport, which would entail allowing the filaments to land at a range of distances ahead of the microtubule tip. Completing the simulation to account for both types of actin-filament behavior will be the subject of future work.

Finally, using a simple thermodynamic model for a two-state system we were able to estimate the range of forces that the biased-diffusion actin-transport mechanism can produce. These forces lie within the picoNewton range, which is comparable to the forces exerted by molecular motors [504]; and is also consistent with measurements of the detachment force of endoplasmic-reticulum tubules from microtubule tips [492]. Hence, this mechanism is a likely candidate to play a role in cytoskeletal coordination between F-actin and microtubules. Although beyond the scope of this study, it would be interesting to experimentally validate the model predictions, for instance with an optical tweezers assay.

Despite the close agreement between simulation and data, there are some caveats to the model we wish to discuss: first, the assumption that to move at all the actin filaments must first fully detach from the microtubule tip; and second, the assumption that, once free, the actin filaments only diffuse in one-dimension. The first assumption implies that microtubule-bound actin filaments will remain immobile for a given amount of time before the microtubule tip travels and the effective off-rate increases. To get a sense of the relevant time scales, we returned to the data produced by the simulations and calculated the average time that actin filaments spent bound (i.e. immobile) between diffusion events. Figure 6.23 shows the average bound times predicted by the one, two and three protofilament simulations, for variable EB and tubulin concentration respectively. The data points show the average $\pm$ standard deviation (averaged over all actin filament lengths), and the colored areas the maximum ranges covered by the simulations. As can be observed, the simulations predicted that actin filaments would remain immobile in the order of one second between diffusion events.

In order to test this, and given that in our experiments most of the imaging was performed at 2 sec/frame, we performed additional high-temporal resolution imaging ($\sim$ 33 ms/frame) of actin-transport events. Panel a in Fig. 6.24 shows three such kymographs of actin-filament transport. Although even at this time resolution it was not possible to fully assert whether the filaments had immobile stretches in the order of a second, we found that the filaments moved rather smoothly and continuously even at these timescales. To get a sense of the range of distances that an actin filament could travel between frames, we monitored the location of the actin filament in the middle kymograph in Figure 6.24 a, by fitting its intensity profile with a Gaussian function at each frame. A histogram of the step sizes revealed that on average the actin filament only traveled $\pm$ 5 nm between 33 ms frames (Fig. 6.24 b). These small displacements are somewhat at odds with the lengths covered by actin-filament diffusion as predicted by the simulation (Fig. 6.16 a and b). In fact, a histogram of the maximum distance covered

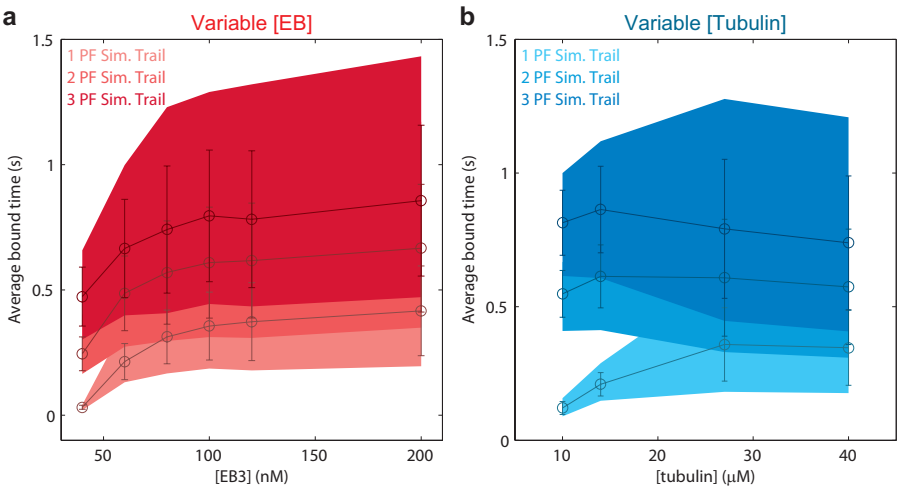

Figure 6.23: Predicted actin-filament bound times between diffusive events. Predicted actin-filament average bound times (independent of actin filament length) for variable EB (a) and tubulin (c) concentrations. The data points and lines show the average ± standard deviation, and the colored areas the minimum and maximum ranges predicted by the simulation allowing TipAct at one, two and three adjacent protofilaments to bind to the actin filament, as indicated.

by diffusive excursions for a 1 µm actin filament, revealed that the average diffusion distance predicted by the simulation would be in the order of ∼ 100 nm, with longer excursions reaching up to 2 - 3 µm (Fig. 6.24 c). The fact that in the experiments the actin filaments moved rather smoothly could suggest that we are underestimating both the effective on- and off- rates (Eq. (6.11) and Eq. (6.14), respectively); or alternatively, that in the proximity of the TipAct comet their diffusion coefficient is somehow reduced.

The second simplifying assumption of the model was that actin filaments diffuse purely in one dimension when detached. This is unlikely, given that there is no physical constraint to allow diffusion only in one dimension when the actin is released from the microtubule tip. One reason behind this assumption was that in simulations in which we allowed the actin filaments to diffuse in three-dimensions, once detached these filaments rarely found the microtubule tip again (data not shown).

Given the observation that in experiments the actin filaments followed the microtubule tip in a smooth fashion, together with the observation that simulations in three-dimensions failed to account for the transport of actin filaments by microtubule tips could mean two things: one, that we are underestimating the effective on and off rates; or two, that actin filaments are instead capable of diffusing even when bound to the TipAct comet. We envision that the second scenario could happen in two different ways: one,

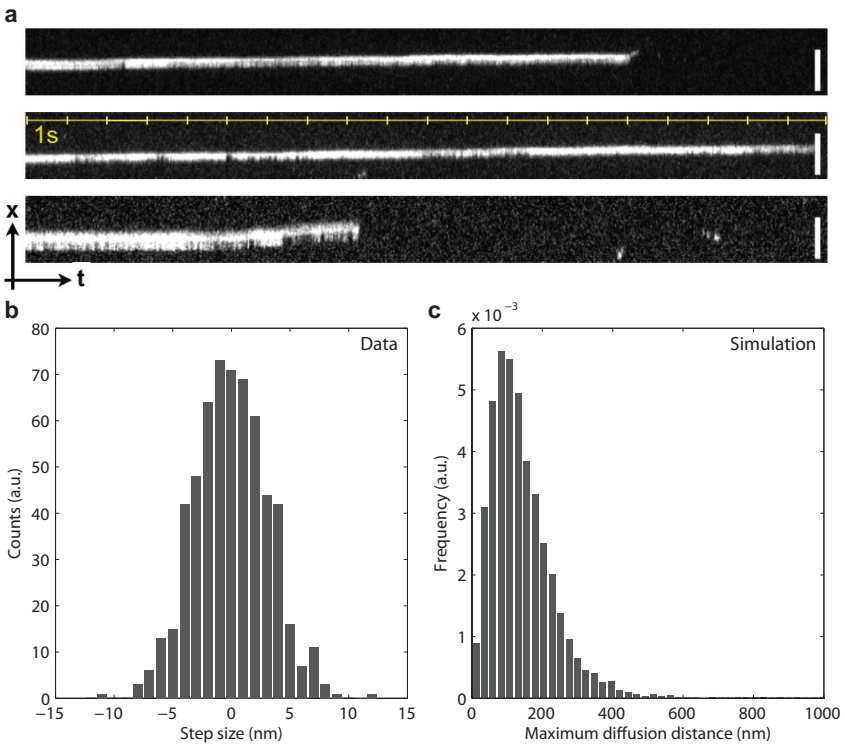

Figure 6.24: In experiments actin-filaments follow the microtubule tip smoothly. (a) Examples of high temporal-resolution kymographs showing three actin filaments that are smoothly being transported by microtubule tips (TipAct signal not shown). In all cases, the actin-filament is anchored at the top, while the portion of the filament not anchored can be seen to fluctuate in and out of the TIRF field of view. (b) Experimental distribution of actin filament steps in between 33 ms frames. (c) Simulated distribution of the distances covered during actin filament diffusive trajectories. Scale bars, 5 µm.

if the actin-binding domain of TipAct had a weakly-bound state on actin filaments (as some molecular motors do [504]); or two, if as a result of spatial fluctuations and random detachments the TipAct molecules could effectively *relay* the actin filament towards regions of higher TipAct concentration. In both cases we expect that the actin-filament mobility would strongly depend on the number of TipAct molecules they would be bound to. We think that either modification to the model would not drastically change the actin-transport dependencies on EB and tubulin concentration, since for instance we expect the actin-bound effective diffusion coefficient to scale with the number of TipAct molecules that the filament is attached to, in a similar fashion as the way we currently estimate the effective off-rate (Eq. 6.11, Fig. 6.12).

Finally, two pieces of evidence further support a modification to the current model: first, we found that *leading* actin filaments did not have to wait for the microtubule tip to grow beyond their leading edge to be able to move, as would be predicted by the current model (Fig. 6.17 b). And second, when we polymerized microtubules in the

presence of GTPγS (a slowly-hydrolyzable analog of GTP), which relocalizes EB3 (and hence TipAct) to the whole microtubule lattice [83], we observed that actin filaments could follow depolymerizing microtubules (Fig. 6.24 b), as well as diffuse along the microtubule lattice until their entire length was in contact with the microtubule (Fig. 6.24 a). In this case, even though there is no loss of binding sites (as the intensity of EB and hence of TipAct remains constant), the actin filaments are still able to move. It will be subject of future work to modify the simulation to account for these new observations.

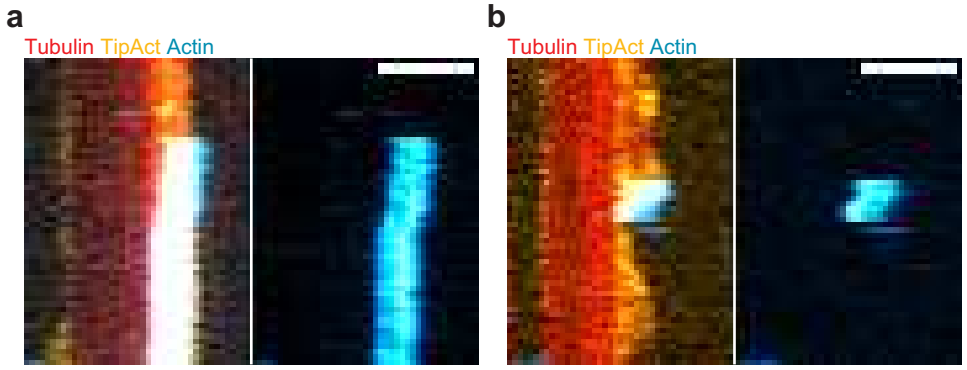

Figure 6.25: Actin filament transport on GTPγS-microtubules (a) Kymograph showing an actin filament that diffuses on a GTPγS microtubule lattice. (b) Kymograph showing an actin filament that follows a depolymerizing GTPγS microtubule. In (a) and (b) microtubules were polymerized in the presence of 16 µM tubulin, 100 nM EB3, 5 nM GFP-TipAct and 1 mM GTPγS. Scale bars, 5 µm.

In conclusion, we found that TipAct at growing microtubule tips can transport actin filaments. The efficiency of actin filament transport strongly depends on whether the filament lands behind the peak of the TipAct plus-end intensity (i.e. *trailing*) or ahead (i.e. *leading*). A model of biased diffusion at microtubule tips recapitulates the dependency of actin filament transport on EB and tubulin concentration, which modulate both the microtubule growth speeds, as well as the length and intensity of the TipAct profiles at microtubule tips. The model further predicted that actin-filament transport will be most efficient for short filaments. Finally, the model predicts that through this mechanism, growing microtubules can exert picoNewton forces on single actin filaments.

Other observations of transport and force generation by microtubule +TIPs have been made, for instance STIM1, an ER anchored protein which allows microtubules to pull membrane tubes from ER [128]. And also by plus-end tracking kinesins that can sustain sufficient force to steer microtubule growth along template microtubules [376, 377]. It

would be interesting to verify whether our model also helps explain these observations. And to investigate whether in cells, this mechanism is employed by growing microtubules to spatially reorganize actin-filament structures.

6.8 Materials and methods

6.8.1 Assays of actin-filament transport by microtubule tips

For the assays with variable EB concentration ($20 - 200$ nM), microtubules were polymerized with 27 µM tubulin (always at a ratio of 1:15 labeled to unlabeled subunits), while the ratio of EB to TipAct concentration was kept at 4:1. For the assays with variable tubulin concentration ($10 - 40$ µM), microtubules were polymerized with 100 nM EB and 25 nM TipAct. Phalloidin-stabilized actin filaments were added directly to the tubulin polymerization mix, at a concentration of $30 - 50$ nM. Before adding, the filaments were sheared 20 times with vigorous pipetting, to break them into smaller pieces (average length ~ 1 µm). TIRF microscopy imaging was performed at $28 - 30$°C (Table 2.1). We refer the reader to Chapter 2 for the general details on how these assays were built.

6.8.2 TipAct binding on surface-bound actin filaments

To find the single-molecule dwell time of TipAct on F-actin, phalloidin-stabilized actin filaments were bound to the coverslip surface via biotin-streptavidin links. Thereafter, TipAct was added to the flow cell at a concentration of 25 nM, in the presence of an oxygen scavenging system (Chapter 2), 0.2 mg/ml κ-casein and 50 mM KCl, in MRB80. TIRF microscopy imaging was performed at 33 ms/frame and 25°C.

6.9 Data analysis

6.9.1 Analysis of TipAct plus-end intensity

To obtain an average value for TipAct's peak plus-end intensity for variable EB concentrations (Fig. 6.6), the entire TipAct plus-end intensity profile was first obtained

from a two-pixel-wide line along the length of the microtubule. These profiles were each normalized by their corresponding microtubule lattice intensity, which was obtained by averaging over a $2 - 5$ µm region at least 1 µm away from the TipAct plus-end comet. After normalization, the TipAct intensity profiles were fit with a simple Gaussian function to find their peak value, and these values were finally averaged to find I_{TipAct} at the given EB concentration. The data in Fig. 6.6 shows the average ± SEM for n = 84,106,93,212,123,201 and 213 TipAct comets, corresponding to the following EB concentrations: 20, 40, 60, 80, 100, 120 and 200 nM respectively.

6.9.2 Analysis of TipAct single molecule dwell time on actin filaments

Single molecule dwell-times of TipAct on actin filaments were retrieved from kymographs traced along surface-bound actin filaments (Fig. 6.10) using a custom-built program in Matlab. Briefly, two-pixel wide intensity line profiles, spaced one-pixel apart, were traced down the time-axis of the kymograph. A binding event was defined when the intensity crossed-over a threshold, defined by the single-molecule intensity at the given illumination conditions. The corresponding unbinding event was defined when the intensity went again below the single-molecule intensity. With this method, 301 individual dwell times (τ_{TipAct}) were recorded and used to build the histogram shown in Figure 6.10.

6.9.3 Analysis of microtubule dynamic instability

Microtubule growth speeds V_g were determined by producing kymographs of microtubule growth (such as in Fig. 6.1), obtained with the *reslice* tool in FIJI [442]. These kymographs were used to manually trace the position of the seed and the microtubule tip over time, using the *segmented line* tool in FIJI. The data was analyzed with custom-built programs in Matlab. The average growth speed was obtained by weighing the individual speed by the time that microtubules spent growing or shrinking at such speed [104]. The data in Fig. 6.14 represent the average ± standard deviation from one to two experiments.

6.9.4 Automated analysis of actin-filament transport

The experimental parameters of actin-filament transport (i.e. difference in speed and following time) for variable EB and tubulin concentrations were obtained via semi-automated analysis in both FIJI and Matlab. First, regions of actin-filament transport (as shown in Fig. 6.26 a) were obtained by manually cropping the selected region from kymographs of microtubule growth that displayed instances of F-actin transport (as in Fig. 6.1). The cropped kymographs were then used to create binary masks for both TipAct and actin-filament channels through a combination of morphological operations using the *Image Analysis Toolbox* of Matlab (Fig. 6.26 b). The binary masks were used to narrow down the region where a Gaussian curve was fit to the TipAct and F-actin intensity at each frame. The Gaussian fit provided the location of the peak TipAct and F-actin intensity, as well as their edges, which were defined as the full-width at half maximum.

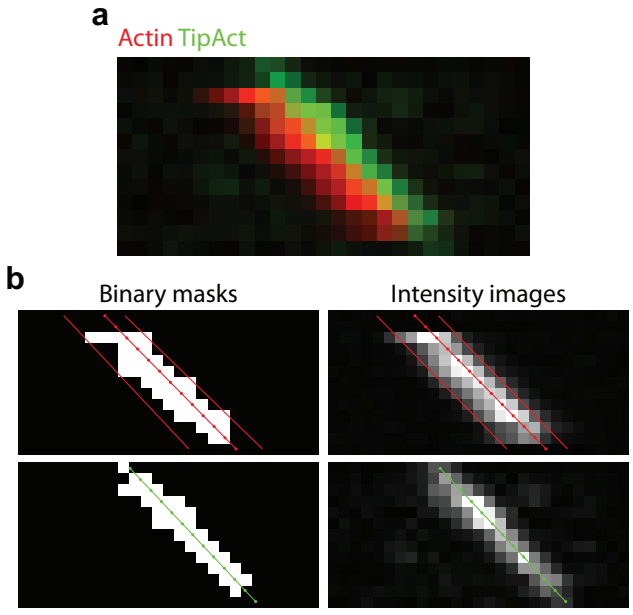

Figure 6.26: Automated analysis of actin filament transport. (a) Selected region of a kymograph showing the TipAct plus end intensity (green) and the F-actin intensity (red) for a *trailing* filament. The microtubule growth conditions were 27 µM tubulin, 60 nM EB3 and 15 nM GFP-TipAct. (b) Left, binary masks used to estimate the F-actin (top) and TipAct speeds (bottom). Right, Intensity images overlaid with the estimated contours obtained by fitting a Gaussian function to the F-actin (top) and TipAct (bottom) intensity at each frame. The F-actin channel shows both the mean location, and full-width at half maximum, and the TipAct channel only the mean location.

The TipAct and actin filament speeds were obtained by plotting the location of the mean of the Gaussian fits over time, and fitting this data with a line, whose slope represented

the speed. Furthermore, the edges of the actin filament were used to automatically define whether the filament was a *leader* or a *trailer* as follows: a filament was classified as a *trailer* if at the moment of landing, its right-most edge did not exceed the TipAct plus-end comet localization by more than two pixels, which in our microscope (with a resolution of 158 nm/pixel) approximately corresponded to the diffraction limit ($\sim$ 334 nm) of the spectral emission of Alexa-647-labeled actin filaments. In contrast, *leading* filaments were classified as such if they landed more than two pixels ahead of the peak of the TipAct plus-end intensity. Finally, the following time was measured using the binary masks, taking the difference between the time of detaching and the time of landing. In experiments, where the TipAct intensity was low (i.e. at EB concentrations of 40 and 60 nM, corresponding to TipAct concentrations of 10 and 15 nM), we visually verified that the measured TipAct speeds were correct, and manually corrected those that were not. We performed this analysis for n = 8, 63, 21, 14, 48 and 38 *trailing*, and n = 30, 86, 41, 30, 39 and 22f *leading* actin filaments for the experiments with variable EB concentration (i.e. [EB] = 40, 60, 80, 100, 120 and 200 nM, respectively), and for n = 19, 23, 14 and 25 *trailing* and n= 20, 25, 30 and 35 *leading* actin filaments for the experiments with variable tubulin concentration (i.e. [tubulin] = 10, 14, 27 and 40 µM, respectively). The data was collected from one to two experiments for each experimental condition.

We would like to acknowledge the important contribution of Michele Monti (FOM Institute AMOLF, The Netherlands) to the development of the biased-diffusion model of actin filament transport, and its implementation in the simulations. We also thank Pieter Rein ten Wolde (FOM Institute AMOLF) for his advice on the model design and implementation.

Chapter 7

Conclusions and outlook

Cells, the basic unit of life, have the fantastic ability to change shape, divide and move. These vital processes are powered by a dynamic supramolecular assembly collectively called the cytoskeleton. The eukaryotic cytoskeleton consists of three networks of protein polymers: filamentous actin (F-actin), microtubules, and, in metazoans, intermediate filaments. These polymeric systems display distinct dynamical and mechanical properties, which cells put to use in a variety of processes, such as: migration, division, polarization, and intracellular transport. In addition, the growing list of proteins that mediate cytoskeletal communication; either directly, via physical cross-links, or indirectly, through biochemical regulation, strongly indicates that in cells, the activity of the three cytoskeletal systems is tightly coordinated.

Despite our wealth of knowledge on actin, microtubules and intermediate filaments, a detailed picture of how their functions are coordinated in cells is still lacking. *In vitro* reconstitutions, with purified proteins, have played a fundamental role in our understanding of how these different cytoskeletal systems individually shape the cell interior. Notwithstanding, reconstitutions of composite cytoskeletal systems are still rare.

In this thesis, through a series of *in vitro* experiments, we made a first attempt at understanding how dynamic microtubules and actin filaments affect each other's organization. To this end, we engineered an actin-binding microtubule plus-end tracking protein, which we call TipAct. Even though TipAct is not a physiologically relevant cross-linker *per se*, with this simple system we could nonetheless reproduce physiologically relevant behaviors, and even predict hitherto unexpected ones. For instance, we were able to recapitulate the *in vivo* observation of microtubule capture and guidance by bundles of

F-actin. Moreover, we could show that a well-defined array of parallel actin bundles can globally organize microtubule growth. Conversely, we found that microtubules can also globally dictate actin filament organization, as TipAct molecules at their growing ends allow them to transport, pull, and induce the bundling of individual actin filaments.

Thus, with the use of a minimal model system, reconstituted from purified proteins, we managed to shed light on the ways by which linking growing microtubule ends to F-actin structures can help direct cytoskeletal organization. Our results suggest that cells can put cross-linkers to use in different contexts, and that this can lead to distinct organizational outcomes. Furthermore, that independently of biochemical regulation, a variety of cytoskeletal organizations can arise from the interplay between physical crosslinks and the mechanical properties of F-actin and microtubule structures.

Despite the many new insights on actin-microtubule coordination acquired with the TipAct system, it has also opened many new questions.

First, in Chapter 3 we observed that TipAct has a low affinity for actin filaments ($K_d \sim 5$ µM); meaning that in the conditions of our assays (in the 25 to 100 nM range) it is only capable of binding actin filaments when locally concentrated at microtubule tips. In stark contrast, in Chapter 4 we observed that at the same concentrations, TipAct stably binds to fascin-stabilized actin bundles, showing no exchange in a time scale of several seconds. This difference in binding properties is puzzling, and we do not have a good explanation for it yet. One possibility is that the actin filament spacing within the fascin-stabilized bundles makes it possible for TipAct's two ABDs to bind to two actin filaments at the same time, effectively reducing its off-rate through an avidity effect. Another possibility is that tandem CH domains are sensitive to twisting and stretching of the actin filaments, such as occurs in fascin-stabilized bundles [505]. These alternative scenarios could be tested, on the one hand, by generating bundles of F-actin with other well-established F-actin bundling proteins such as α-actinin, which generate bundles with different actin filament spacing [506]. On the other hand, by engineering a monomeric version of TipAct. These new experiments could also shed light on the localization and cross-linking behavior of MACF (the human spectraplakin protein on which TipAct was based [309]), which appears to preferentially cross-link microtubules to actin bundles (i.e. stress fibers and filopodia), in cells.

Second, in Chapter 4 we studied the geometrical constraints under which sparse arrays of F-actin bundles can capture and guide growing microtubules, in a quasi two-dimensional geometry. However, even the thin lamellipodium at the periphery of migrating cells is not sufficiently thin to be considered two-dimensional. Nor are the bundles of F-actin

known to guide microtubules in cells (i.e. filopodia and stress fibers) free standing, but are rather surrounded by dense and actively-remodeling environments (i.e. lamellipodial and lamellar F-actin networks, and the cytosolic microtubule and intermediate filament networks). It thus remains an open question how microtubules navigate their crowded surroundings to eventually find an F-actin track. This type of question could be approached from different angles. First, by more advanced *in vitro* reconstitutions that make use of micro-patterning techniques to locally generate dense F-actin networks with mixed architectures (i.e. bundles within an F-actin mesh) [507]. And second, by the addition of myosin II motors to induce F-actin network contractility, in order to monitor how microtubule dynamics respond to F-actin network activity, both in the presence and absence of cross-linkers. These experiments could also reveal the ways by which actin-microtubule cross-linkers promote, or inhibit, microtubule breakage by contractile F-actin networks, as has been observed in cells [282].

Third, in all the assays described in this thesis we used EB and TipAct concentrations in the $10 - 100$ nM range. However, in cells, the EB concentration ($\sim 100 - 1000$ nM) is approximately $100 - 10,000$ times higher than that of other +TIPs, such as MACF [113]. For an average eukaryotic cell, with a volume of $\sim 2,000 - 4000$ µm^3 [508], this means that while there are $\sim 0.5 - 1.5$ million EB molecules, there are only $\sim 100 - 5,000$ copies of any given +TIP. This difference in protein numbers thus raises a couple of questions: First, how do the many +TIPs present at growing microtubule ends exert their different (and often opposing) activities at the same location? And second, given our observations that actin-microtubule interactions mediated by TipAct strongly depend on the protein concentration at actin-microtubule overlaps (Chapters 4 and 6), how do cells spatially and temporally regulate the activity of the many physiologically relevant actin-microtubule cross-linking +TIPs so they can effectively exert their activity? These questions could be tested first, via *in vitro* assays in which a combination of different +TIPs is present, while monitoring how they affect microtubule dynamics in combination. And second, with assays in which the physiologically-relevant +TIP protein concentrations and ratios are used.

Fourth, in Chapter 6 we studied the effect of actin filament transport by microtubule growing ends. A model of biased diffusion along the TipAct profile at microtubule tips was sufficient to explain the dependency of transport on the microtubule growth speed, and the EB and TipAct concentrations in solution. This model also predicted that, through this mechanism, microtubules potentially generate picoNewton forces on actin filament structures. Although this observation is novel, other reports of force generation via microtubule +TIPS have been reported in different contexts. For instance by STIM1,

a +TIP anchored at the endoplasmic reticulum (ER), which allows microtubules to pull ER membrane tubes. The force ranges predicted by our model could be tested by a simple *in vitro* reconstitution in which TipAct is anchored at a vesicular membrane, in the vicinity of microtubules growing in the presence of EB. Similar to experiments done with membrane tether pulling by motors walking along microtubule tracks [509].

There are still many more questions than answers in the field of cytoskeletal coordination. One key question is how cells make use of the multiplicity of actin-microtubule cross-linkers (and their spatiotemporal regulation by biochemical signaling networks), to efficiently coordinate their cytoskeletal systems. The TipAct system is just a starting point. In the future, we hope that more complex reconstitutions of composite cytoskeletal networks, involving dynamic microtubules, actively remodeling actin filament networks, and perhaps even intermediate filaments, will follow.

Bibliography

[1] Davidson, M. W. Molecular Expressions - Fluorescence Digital Image Gallery (1995). URL `http://micro.magnet.fsu.edu/primer/techniques/fluorescence/gallery/cells/index.html`.

[2] Murphy, D. B. Functions of tubulin isoforms. *Curr. Opin. Cell Biol.* **3**, 43–51 (1991).

[3] Oakley, B. R. An abundance of tubulins. *Trends Cell Biol.* **10**, 537–542 (2000).

[4] Zheng, Y., Wong, M. L., Alberts, B. & Mitchison, T. Nucleation of microtubule assembly by a gamma-tubulin-containing ring complex. *Nature* **378**, 578–583 (1995).

[5] Oegema, K. *et al.* Characterization of two related Drosophila γ-tubulin complexes that differ in their ability to nucleate microtubules. *J. Cell Biol.* **144**, 721–733 (1999).

[6] Leguy, R., Melki, R., Pantaloni, D. & Carlier, M. F. Monomeric γ-tubulin nucleates microtubules. *J. Biol. Chem.* **275**, 21975–21980 (2000).

[7] Kollman, J. M., Merdes, A., Mourey, L. & Agard, D. A. Microtubule nucleation by γ-tubulin complexes. *Nat. Rev. Mol. Cell Biol.* **12**, 709–721 (2011).

[8] Mitchison, T. & Kirschner, M. Dynamic instability of microtubule growth. *Nature* **312**, 237–242 (1984).

[9] Akhmanova, A. & Steinmetz, M. O. Tracking the ends: a dynamic protein network controls the fate of microtubule tips. *Nat. Rev. Mol. Cell Biol.* **9**, 309–322 (2008).

[10] Karecla, P., Hirst, E. & Bayley, P. Polymorphism of tubulin assembly in vitro. *J. Cell Sci.* **94**, 479–488 (1989).

[11] Olmsted, J. B. & Borisy, G. G. Ionic and nucleotide requirements for microtubule polymerization in vitro. *Biochemistry* **14**, 2996–3005 (1975).

[12] Fygenson, D. K., Braun, E. & Libchaber, A. Phase diagram of microtubules. *Phys. Rev. E* **50**, 1579–1588 (1994).

[13] Tilney, L. G. *et al.* Microtubules: evidence for 13 protofilaments. *J. Cell Biol.* **59**, 267–275 (1973).

[14] Amos, L. & Klug, A. Arrangement of subunits in flagellar microtubules. *J. Cell Sci.* **14**, 523–549 (1974).

[15] Nogales, E., Whittaker, M., Milligan, R. A. & Downing, K. H. High-resolution model of the microtubule. *Cell* **96**, 79–88 (1999).

[16] Nogales, E. Structural insights into microtubule function. *Annu. Rev. Biochem.* **69**, 277–302 (2000).

[17] Sept, D., Baker, N. A. & McCammon, J. A. The physical basis of microtubule structure and stability. *Protein Sci.* **12**, 2257–2261 (2003).

[18] Katsuki, M., Drummond, D. R. & Cross, R. A. Ectopic A-lattice seams destabilize microtubules. *Nat. Commun.* **5**, 3094 (2014).

[19] Mitchison, T. J. Localization of an exchangeable GTP binding site at the plus end of microtubules. *Science* **261**, 1044–1047 (1993).

[20] Johnson, K. A. & Borisy, G. G. Kinetic analysis of microtubule self-assembly in vitro. *J. Mol. Biol.* **117**, 1–31 (1977).

[21] Voter, W. A. & Erickson, H. P. The kinetics of microtubule assembly. Evidence for a two-stage nucleation mechanism. *J. Biol. Chem.* **259**, 10430–10438 (1984).

[22] Flyvbjerg, H., Jobs, E. & Leibler, S. Kinetics of self-assembling microtubules: an "inverse problem" in biochemistry. *Proc. Natl. Acad. Sci. U. S. A.* **93**, 5975–5979 (1996).

[23] Caudron, N., Valiron, O., Usson, Y., Valiron, P. & Job, D. A reassessment of the factors affecting microtubule assembly and disassembly in vitro. *J. Mol. Biol.* **297**, 211–220 (2000).

[24] Job, D., Valiron, O. & Oakley, B. Microtubule nucleation. *Curr. Opin. Cell Biol.* **15**, 111–117 (2002).

[25] Bré, M. H. & Karsenti, E. Effects of brain microtubule-associated proteins on microtubule dynamics and the nucleating activity of centrosomes. *Cell Motil. Cytoskeleton* **15**, 88–98 (1990).

[26] Fygenson, D. K., Flyvbjerg, H., Sneppen, K., Libchaber, A. & Leibler, S. Spontaneous nucleation of microtubules. *Phys. Rev. E* **51**, 5058–5063 (1995).

[27] Hyman, A. & Karsenti, E. The role of nucleation in patterning microtubule networks. *J. Cell Sci.* **111**, 2077–2083 (1998).

[28] Zhai, Y., Kronebusch, P. J., Simon, P. M. & Borisy, G. G. Microtubule dynamics at the G2/M transition: Abrupt breakdown of cytoplasmic microtubules at nuclear envelope breakdown and implications for spindle morphogenesis. *J. Cell Biol.* **135**, 201–214 (1996).

[29] Raynaud-Messina, B. & Merdes, A. Gamma-tubulin complexes and microtubule organization. *Curr. Opin. Cell Biol.* **19**, 24–30 (2007).

[30] Moritz, M., Braunfeld, M. B., Guénebaut, V., Heuser, J. & Agard, D. A. Structure of the gamma-tubulin ring complex: a template for microtubule nucleation. *Nat. Cell Biol.* **2**, 365–370 (2000).

[31] Bartolini, F. & Gundersen, G. G. Generation of noncentrosomal microtubule arrays. *J. Cell Sci.* **119**, 4155–4163 (2006).

[32] Petry, S., Groen, A. C., Ishihara, K., Mitchison, T. J. & Vale, R. D. Branching microtubule nucleation in xenopus egg extracts mediated by augmin and TPX2. *Cell* **152**, 768–777 (2013).

[33] Kamasaki, T. *et al.* Augmin-dependent microtubule nucleation at microtubule walls in the spindle. *J. Cell Biol.* **202**, 25–32 (2013).

[34] Hotta, T. *et al.* Characterization of the Arabidopsis Augmin Complex Uncovers Its Critical Function in the Assembly of the Acentrosomal Spindle and Phragmoplast Microtubule Arrays. *Plant Cell* **24**, 1494–1509 (2012).

[35] Hashimoto, T. A ring for all: γ-tubulin-containing nucleation complexes in acentrosomal plant microtubule arrays. *Curr. Opin. Plant Biol.* **16**, 698–703 (2013).

[36] Chabin-Brion, K. *et al.* The Golgi complex is a microtubule-organizing organelle. *Mol. Biol. Cell* **12**, 2047–2060 (2001).

[37] Ríos, R. M., Sanchís, A., Tassin, A. M., Fedriani, C. & Bornens, M. GMAP-210 recruits γ-tubulin complexes to cis-Golgi membranes and is required for Golgi ribbon formation. *Cell* **118**, 323–335 (2004).

[38] Efimov, A. *et al.* Asymmetric CLASP-Dependent Nucleation of Noncentrosomal Microtubules at the trans-Golgi Network. *Dev. Cell* **12**, 917–930 (2007).

[39] Zhu, X. & Kaverina, I. Golgi as an MTOC: Making microtubules for its own good. *Histochem. Cell Biol.* **140**, 361–367 (2013).

[40] Meads, T. & Schroer, T. A. Polarity and nucleation of microtubules in polarized epithelial cells. *Cell Motil. Cytoskeleton* **32**, 273–288 (1995).

[41] Mogensen, M. Microtubule release and capture in epithelial cells. *Biol. Cell* **91**, 331–341 (1999).

[42] Mogensen, M. M., Malik, A., Piel, M., Bouckson-Castaing, V. & Bornens, M. Microtubule minus-end anchorage at centrosomal and non-centrosomal sites: the role of ninein. *J. Cell Sci.* **113**, 3013–3023 (2000).

[43] Moss, D. K. *et al.* Ninein is released from the centrosome and moves bi-directionally along microtubules. *J. Cell Sci.* **120**, 3064–3074 (2007).

[44] Goodwin, S. S. & Vale, R. D. Patronin Regulates the Microtubule Network by Protecting Microtubule Minus Ends. *Cell* **143**, 263–274 (2010).

[45] Jiang, K. *et al.* Microtubule Minus-End Stabilization by Polymerization-Driven CAMSAP Deposition. *Dev. Cell* **28**, 295–309 (2014).

[46] Carlier, M. F. & Pantaloni, D. Kinetic analysis of guanosine 5'-triphosphate hydrolysis associated with tubulin polymerization. *Biochemistry* **20**, 1918–1924 (1981).

[47] Carlier, M. F. & Pantaloni, D. Assembly of microtubule protein: role of guanosine di- and triphosphate nucleotides. *Biochemistry* **21**, 1215–1224 (1982).

[48] Carlier, M. F., Didry, D. & Pantaloni, D. Microtubule elongation and guanosine 5'-triphosphate hydrolysis. Role of guanine nucleotides in microtubule dynamics. *Biochemistry* **26**, 4428–4437 (1987).

[49] Arai, T. & Kaziro, Y. Effect of guanine nucleotides on the assembly of brain microtubules: Ability of 5-guanylyl imidodiphosphate to replace GTP in promoting the polymerization of microtubules. *Biochem. Biophys. Res. Commun.* **69**, 369–376 (1976).

[50] Hyman, A. A., Salser, S., Drechsel, D. N., Unwin, N. & Mitchison, T. J. Role of GTP hydrolysis in microtubule dynamics: information from a slowly hydrolyzable analogue, GMPCPP. *Mol. Biol. Cell* **3**, 1155–1167 (1992).

[51] Weisenberg, R. C., Deery, W. J. & Dickinson, P. J. Tubulin-nucleotide interactions during the polymerization and depolymerization of microtubules. *Biochemistry* **15**, 4248–4254 (1976).

[52] Mejillano, M. R., Shivanna, B. D. & Himes, R. H. Studies on the nocodazole-induced GTPase activity of tubulin. *Arch. Biochem. Biophys.* **336**, 130–138 (1996).

[53] Brouhard, G. J. & Rice, L. M. The contribution of -tubulin curvature to microtubule dynamics. *J. Cell Biol.* **207**, 323–334 (2014).

[54] Kirschner, M. W., Williams, R. C., Weingarten, M. & Gerhart, J. C. Microtubules from mammalian brain: some properties of their depolymerization products and a proposed mechanism of assembly and disassembly. *Proc. Natl. Acad. Sci. U. S. A.* **71**, 1159–1163 (1974).

[55] Steinmetz, M. O. *et al.* Op18/stathmin caps a kinked protofilament-like tubulin tetramer. *EMBO J.* **19**, 572–580 (2000).

[56] Nogales, E., Wolf, S. G. & Downing, K. H. Structure of the alpha beta tubulin dimer by electron crystallography. *Nature* **391**, 199–203 (1998).

[57] Gigant, B. *et al.* The 4 A X-ray structure of a tubulin:stathmin-like domain complex. *Cell* **102**, 809–816 (2000).

[58] Nawrotek, A., Knossow, M. & Gigant, B. The determinants that Govern microtubule assembly from the atomic structure of GTP-tubulin. *J. Mol. Biol.* **412**, 35–42 (2011).

[59] Ayaz, P., Ye, X., Huddleston, P., Brautigam, C. A. & Rice, L. M. A TOG: ab-tubulin complex structure reveals conformation-based mechanisms for a microtubule polymerase. *Science* **337**, 857–60 (2012).

[60] Buey, R. M., Fernando Díaz, J. & Andreu, J. M. The nucleotide switch of tubulin and microtubule assembly: A polymerization-driven structural change. *Biochemistry* **45**, 5933–5938 (2006).

[61] Rice, L. M., Montabana, E. A. & Agard, D. A. The lattice as allosteric effector: structural studies of alphabeta- and gamma-tubulin clarify the role of GTP in microtubule assembly. *Proc. Natl. Acad. Sci. U. S. A.* **105**, 5378–5383 (2008).

[62] Mandelkow, E. M., Mandelkow, E. & Milligan, R. A. Microtubule dynamics and microtubule caps: A time-resolved cryo-electron microscopy study. *J. Cell Biol.* **114**, 977–991 (1991).

[63] Chrétien, D., Fuller, S. D. & Karsenti, E. Structure of growing microtubule ends: Two-dimensional sheets close into tubes at variable rates. *J. Cell Biol.* **129**, 1311–1328 (1995).

[64] VanBuren, V., Odde, D. J. & Cassimeris, L. Estimates of lateral and longitudinal bond energies within the microtubule lattice. *Proc. Natl. Acad. Sci. U. S. A.* **99**, 6035–6040 (2002).

[65] Alushin, G. M. *et al.* High-Resolution microtubule structures reveal the structural transitions in $\alpha\beta$-tubulin upon GTP hydrolysis. *Cell* **157**, 1117–1129 (2014).

[66] Wadsworth, P. & McGrail, M. Interphase microtubule dynamics are cell type-specific. *J. Cell Sci.* **95**, 23–32 (1990).

[67] Salmon, E. D., Leslie, R. J., Saxton, W. M., Karow, M. L. & McIntosh, J. R. Spindle microtubule dynamics in sea urchin embryos: Analysis using a fluorescein-labeled tubulin and measurements of fluorescence redistribution after laser photobleaching. *J. Cell Biol.* **99**, 2165–2174 (1984).

[68] Vorobjev, I. A., Rodionov, V. I., Maly, I. V. & Borisy, G. G. Contribution of plus and minus end pathways to microtubule turnover. *J. Cell Sci.* **112**, 2277–2289 (1999).

[69] Needleman, D. J. *et al.* Fast microtubule dynamics in meiotic spindles measured by single molecule imaging: evidence that the spindle environment does not stabilize microtubules. *Mol. Biol. Cell* **21**, 323–333 (2010).

[70] Saxton, W. M. Tubulin dynamics in cultured mammalian cells. *J. Cell Biol.* **99**, 2175–2186 (1984).

[71] Holmfeldt, P., Stenmark, S. & Gullberg, M. Interphase-specific phosphorylation-mediated regulation of tubulin dimer partitioning in human cells. *Mol. Biol. Cell* **18**, 1909–1917 (2007).

[72] Ringhoff, D. N. & Cassimeris, L. Stathmin regulates centrosomal nucleation of microtubules and tubulin dimer/polymer partitioning. *Mol. Biol. Cell* **20**, 3451–3458 (2009).

[73] Goshima, G., Wollman, R., Stuurman, N., Scholey, J. M. & Vale, R. D. Length control of the metaphase spindle. *Curr. Biol.* **15**, 1979–1988 (2005).

[74] Reber, S. B. *et al.* XMAP215 activity sets spindle length by controlling the total mass

of spindle microtubules. *Nat. Cell Biol.* **15**, 1116–22 (2013).

[75] Loughlin, R., Wilbur, J. D., McNally, F. J., Nédélec, F. J. & Heald, R. Katanin contributes to interspecies spindle length scaling in xenopus. *Cell* **147**, 1397–1407 (2011).

[76] Rankin, K. E. & Wordeman, L. Long astral microtubules uncouple mitotic spindles from the cytokinetic furrow. *J. Cell Biol.* **190**, 35–43 (2010).

[77] Wordeman, L. & Stumpff, J. Microtubule Length Control, a Team Sport? *Dev. Cell* **17**, 437–438 (2009).

[78] Carlier, M. F., Didry, D., Simon, C. & Pantaloni, D. Mechanism of GTP hydrolysis in tubulin polymerization: characterization of the kinetic intermediate microtubule-GDP-Pi using phosphate analogues. *Biochemistry* **28**, 1783–1791 (1989).

[79] Walker, R. A., Pryer, N. K. & Salmon, E. D. Dilution of individual microtubules observed in real time in vitro: Evidence that cap size is small and independent of elongation rate. *J. Cell Biol.* **114**, 73–81 (1991).

[80] Caplow, M. & Shanks, J. Evidence that a single monolayer tubulin-GTP cap is both necessary and sufficient to stabilize microtubules. *Mol. Biol. Cell* **7**, 663–675 (1996).

[81] Gardner, M. K. *et al.* Rapid microtubule self-assembly kinetics. *Cell* **146**, 582–592 (2011).

[82] Zanic, M., Stear, J. H., Hyman, A. A. & Howard, J. EB1 recognizes the nucleotide state of tubulin in the microtubule lattice. *PLoS One* **4** (2009).

[83] Maurer, S. P., Bieling, P., Cope, J., Hoenger, A. & Surrey, T. GTPgammaS microtubules mimic the growing microtubule end structure recognized by end-binding proteins (EBs). *Proc. Natl. Acad. Sci. U. S. A.* **108**, 3988–3993 (2011).

[84] Maurer, S. P., Fourniol, F. J., Bohner, G., Moores, C. A. & Surrey, T. EBs recognize a nucleotide-dependent structural cap at growing microtubule ends. *Cell* **149**, 371–82 (2012).

[85] Akhmanova, A. & Steinmetz, M. O. Microtubule end binding: EBs sense the guanine nucleotide state. *Curr. Biol.* **21**, R283–R285 (2011).

[86] Komarova, Y. *et al.* Mammalian end binding proteins control persistent microtubule growth. *J. Cell Biol.* **184**, 691–706 (2009).

[87] Lansbergen, G. & Akhmanova, A. Microtubule plus end: A hub of cellular activities. *Traffic* **7**, 499–507 (2006).

[88] Seetapun, D., Castle, B. T., McIntyre, A. J., Tran, P. T. & Odde, D. J. Estimating the microtubule GTP cap size in vivo. *Curr. Biol.* **22**, 1681–7 (2012).

[89] Venier, P., Maggs, A. C., Carlier, M. F. & Pantaloni, D. Analysis of microtubule rigidity using hydrodynamic flow and thermal fluctuations. *J. Biol. Chem.* **269**, 13353–13360 (1994).

[90] Kikumoto, M., Kurachi, M., Tosa, V. & Tashiro, H. Flexural rigidity of individual microtubules measured by a buckling force with optical traps. *Biophys. J.* **90**, 1687–1696 (2006).

[91] Hawkins, T. L., Sept, D., Mogessie, B., Straube, A. & Ross, J. L. Mechanical properties of doubly stabilized microtubule filaments. *Biophys. J.* **104**, 1517–28 (2013).

[92] Dogterom, M. & Yurke, B. Measurement of the force-velocity relation for growing microtubules. *Science* **278**, 856–860 (1997).

[93] Janson, M. E., de Dood, M. E. & Dogterom, M. Dynamic instability of microtubules is regulated by force. *J. Cell Biol.* **161**, 1029–1034 (2003).

[94] Moran, U., Phillips, R. & Milo, R. SnapShot: Key numbers in biology. *Cell* **141**, 1262–1262.e1 (2010).

[95] Su, L. K. *et al.* APC binds to the novel protein EB1. *Cancer Res.* **55**, 2972–2977 (1995).

[96] Sen, I., Veprintsev, D., Akhmanova, A. & Steinmetz, M. O. End Binding Proteins Are Obligatory Dimers. *PLoS One* **8** (2013).

[97] Slep, K. C. *et al.* Structural determinants for EB1-mediated recruitment of APC and spectraplakins to the microtubule plus end. *J. Cell Biol.* **168**, 587–598 (2005).

[98] Buey, R. M. *et al.* Insights into EB1 structure and the role of its C-terminal domain for discriminating microtubule tips from the lattice. *Mol. Biol. Cell* **22**, 2912–2923 (2011).

[99] Kanaba, T. *et al.* Microtubule-binding sites of the CH domain of EB1 and its autoinhibition revealed by NMR. *Biochim. Biophys. Acta - Proteins Proteomics* **1834**, 499–507 (2013).

[100] Maurer, S. P. *et al.* EB1 accelerates two conformational transitions important for microtubule maturation and dynamics. *Curr. Biol.* **24**, 372–384 (2014).

[101] Tirnauer, J. S., O'Toole, E., Berrueta, L., Bierer, B. E. & Pellman, D. Yeast Bim1p promotes the G1-specific dynamics of microtubules. *J. Cell Biol.* **145**, 993–1007 (1999).

[102] Rogers, S. L., Rogers, G. C., Sharp, D. J. & Vale, R. D. Drosophila EB1 is important for proper assembly, dynamics, and positioning of the mitotic spindle. *J. Cell Biol.* **158**, 873–884 (2002).

[103] Tirnauer, J. S., Grego, S., Salmon, E. D. & Mitchison, T. J. EB1-microtubule interactions in Xenopus egg extracts: role of EB1 in microtubule stabilization and mechanisms of targeting to microtubules. *Mol. Biol. Cell* **13**, 3614–3626 (2002).

[104] Bieling, P. *et al.* Reconstitution of a microtubule plus-end tracking system in vitro. *Nature* **450**, 1100–1105 (2007).

[105] Wang, H.-W. & Nogales, E. Nucleotide-dependent bending flexibility of tubulin regulates microtubule assembly. *Nature* **435**, 911–915 (2005).

[106] Nakamura, S. *et al.* Dissecting the Nanoscale Distributions and Functions of Microtubule-End-Binding Proteins EB1 and ch-TOG in Interphase HeLa Cells. *PLoS One* **7** (2012).

[107] Honnappa, S. *et al.* An EB1-Binding Motif Acts as a Microtubule Tip Localization Signal. *Cell* **138**, 366–376 (2009).

[108] Zeiss. Zeiss Online Campus -Fluorescent Protein Fusions Image Gallery. URL `http://zeiss-campus.magnet.fsu.edu/galleries/fpfusions/index.html`.

[109] Bu, W. & Su, L.-K. Characterization of functional domains of human EB1 family proteins. *J. Biol. Chem.* **278**, 49721–49731 (2003).

[110] Akhmanova, A. & Hoogenraad, C. C. Microtubule plus-end-tracking proteins: Mechanisms and functions. *Curr. Opin. Cell Biol.* **17**, 47–54 (2005).

[111] Jaworski, J., Hoogenraad, C. C. & Akhmanova, A. Microtubule plus-end tracking proteins in differentiated mammalian cells. *Int. J. Biochem. Cell Biol.* **40**, 619–637 (2008).

[112] Gouveia, S. M. & Akhmanova, A. Cell and molecular biology of microtubule plus end tracking proteins: end binding proteins and their partners. *Int. Rev. Cell Mol. Biol.* **285**, 1–74 (2010).

[113] Jiang, K. *et al.* A proteome-wide screen for mammalian SxIP motif-containing microtubule plus-end tracking proteins. *Curr. Biol.* **22**, 1800–1807 (2012).

[114] Perez, F., Diamantopoulos, G. S., Stalder, R. & Kreis, T. E. CLIP-170 highlights growing microtubule ends in vivo. *Cell* **96**, 517–527 (1999).

[115] Bieling, P. *et al.* CLIP-170 tracks growing microtubule ends by dynamically recognizing composite EB1/tubulinbinding sites. *J. Cell Biol.* **183**, 1223–1233 (2008).

[116] Dragestein, K. A. *et al.* Dynamic behavior of GFP-CLIP-170 reveals fast protein turnover on microtubule plus ends. *J. Cell Biol.* **180**, 729–737 (2008).

[117] Komarova, Y. *et al.* EB1 and EB3 control CLIP dissociation from the ends of growing microtubules. *Mol. Biol. Cell* **16**, 5334–5345 (2005).

[118] Dixit, R. *et al.* Microtubule plus-end tracking by CLIP-170 requires EB1. *Proc. Natl. Acad. Sci. U. S. A.* **106**, 492–497 (2009).

[119] Li, W. *et al.* EB1 promotes microtubule dynamics by recruiting Sentin in Drosophila cells. *J. Cell Biol.* **193**, 973–983 (2011).

[120] Montenegro Gouveia, S. *et al.* In vitro reconstitution of the functional interplay between MCAK and EB3 at microtubule plus ends. *Curr. Biol.* **20**, 1717–1722 (2010).

[121] Tsvetkov, A. S., Samsonov, A., Akhmanova, A., Galjart, N. & Popov, S. V. Microtubule-binding proteins CLASP1 and CLASP2 interact with actin filaments. *Cell Motil. Cytoskeleton* **64**, 519–530 (2007).

[122] Leung, C. L., Sun, D., Zheng, M., Knowles, D. R. & Liem, R. K. H. Microtubule actin cross-linking factor (MACF): a hybrid of dystonin and dystrophin that can interact with the actin and microtubule cytoskeletons. *J. Cell Biol.* **147**, 1275–1285 (1999).

[123] Kodama, A., Karakesisoglou, I., Wong, E., Vaezi, A. & Fuchs, E. ACF7: An essential integrator of microtubule dynamics. *Cell* **115**, 343–354 (2003).

[124] Lee, S. & Kolodziej, P. A. Short Stop provides an essential link between F-actin and microtubules during axon extension. *Development* **129**, 1195–1204 (2002).

[125] Applewhite, D. A. *et al.* The spectraplakin Short stop is an actin-microtubule cross-linker that contributes to organization of the microtubule network. *Mol. Biol. Cell* **21**, 1714–1724 (2010).

[126] Mimori-Kiyosue, Y., Shiina, N. & Tsukita, S. The dynamic behavior of the APC-binding protein EB1 on the distal ends of microtubules. *Curr. Biol.* **10**, 865–868 (2000).

[127] Nakamura, M., Zhou, X. Z. & Lu, K. P. Critical role for the EB1 and APC interaction in the regulation of microtubule polymerization. *Curr. Biol.* **11**, 1062–1067 (2001).

[128] Grigoriev, I. *et al.* STIM1 Is a MT-Plus-End-Tracking Protein Involved in Remodeling of the ER. *Curr. Biol.* **18**, 177–182 (2008).

[129] Rogers, S. L., Wiedemann, U., Häcker, U., Turck, C. & Vale, R. D. Drosophila RhoGEF2 associates with microtubule plus ends in an EB1-dependent manner. *Curr. Biol.* **14**, 1827–1833 (2004).

[130] Bjelić, S. *et al.* Interaction of mammalian end binding proteins with CAP-Gly domains of CLIP-170 and p150glued. *J. Struct. Biol.* **177**, 160–167 (2012).

[131] Wu, X., Xiang, X. & Hammer, J. A. Motor proteins at the microtubule plus-end. *Trends Cell Biol.* **16**, 135–143 (2006).

[132] Slep, K. C. & Vale, R. D. Structural Basis of Microtubule Plus End Tracking by XMAP215, CLIP-170, and EB1. *Mol. Cell* **27**, 976–991 (2007).

[133] Honnappa, S., John, C. M., Kostrewa, D., Winkler, F. K. & Steinmetz, M. O. Structural insights into the EB1-APC interaction. *EMBO J.* **24**, 261–269 (2005).

[134] Buey, R. M. *et al.* Sequence determinants of a microtubule tip localization signal (MtLS). *J. Biol. Chem.* **287**, 28227–28242 (2012).

[135] Watanabe, T. *et al.* Phosphorylation of CLASP2 by GSK-3beta regulates its interaction

with IQGAP1, EB1 and microtubules. *J. Cell Sci.* **122**, 2969–2979 (2009).

[136] Weisbrich, A. *et al.* Structure-function relationship of CAP-Gly domains. *Nat. Struct. Mol. Biol.* **14**, 959–967 (2007).

[137] Slep, K. C. The role of TOG domains in microtubule plus end dynamics. *Biochem. Soc. Trans.* **37**, 1002–1006 (2009).

[138] Brouhard, G. J. *et al.* XMAP215 Is a Processive Microtubule Polymerase. *Cell* **132**, 79–88 (2008).

[139] Trushko, A., Schäffer, E. & Howard, J. The growth speed of microtubules with XMAP215-coated beads coupled to their ends is increased by tensile force. *Proc. Natl. Acad. Sci. U. S. A.* **110**, 14670–5 (2013).

[140] Zanic, M., Widlund, P. O., Hyman, A. a. & Howard, J. Synergy between XMAP215 and EB1 increases microtubule growth rates to physiological levels. *Nat. Cell Biol.* **15**, 1–8 (2013).

[141] van der Vaart, B. *et al.* SLAIN2 links microtubule plus end-tracking proteins and controls microtubule growth in interphase. *J. Cell Biol.* **193**, 1083–1099 (2011).

[142] Al-Bassam, J. & Chang, F. Regulation of microtubule dynamics by TOG-domain proteins XMAP215/Dis1 and CLASP. *Trends Cell Biol.* **21**, 604–614 (2011).

[143] Asakura, S. & Oosawa, F. Dephosphorylation of adenosine triphosphate in actin solutions at low concentrations of magnesium. *Arch. Biochem. Biophys.* **87**, 273–280 (1960).

[144] Pfaendtner, J., Branduardi, D., Parrinello, M., Pollard, T. D. & Voth, G. A. Nucleotide-dependent conformational states of actin. *Proc. Natl. Acad. Sci. U. S. A.* **106**, 12723–12728 (2009).

[145] Begg, D. A., Rodewald, R. & Rebhun, L. I. The visualization of actin filament polarity in thin sections. Evidence for the uniform polarity of membrane-associated filaments. *J. Cell Biol.* **79**, 846–852 (1978).

[146] Nürnberg, A., Kitzing, T. & Grosse, R. Nucleating actin for invasion. *Nat. Rev. Cancer* **11**, 177–187 (2011).

[147] Kasai, M., Asakura, S. & Oosawa, F. The cooperative nature of G-F transformation of actin. *Biochim. Biophys. Acta* **57**, 22–31 (1962).

[148] Pollard, T. D. & Craig, S. W. Mechanism of actin polymerization. *Trends Biochem. Sci.* **7**, 55–58 (1982).

[149] Steinmetz, M. O., Goldie, K. N. & Aebi, U. A correlative analysis of actin filament assembly, structure, and dynamics. *J. Cell Biol.* **138**, 559–574 (1997).

[150] Carlier, M. F., Pantaloni, D. & Korn, E. D. The effects of Mg2+ at the high-affinity and low-affinity sites on the polymerization of actin and associated ATP hydrolysis. *J. Biol. Chem.* **261**, 10785–10792 (1986).

[151] Blanchoin, L. & Pollard, T. D. Hydrolysis of ATP by polymerized actin depends on the bound divalent cation but not profilin. *Biochemistry* **41**, 597–602 (2002).

[152] Pollard, T. D. & Weeds, A. G. The rate constant for ATP hydrolysis by polymerized actin. *FEBS Lett.* **170**, 94–98 (1984).

[153] Pollard, T. D. Rate constants for the reactions of ATP- and ADP-actin with the ends of actin filaments. *J. Cell Biol.* **103**, 2747–2754 (1986).

[154] Neuhaus, J. M., Wanger, M., Keiser, T. & Wegner, A. Treadmilling of actin. *J. Muscle Res. Cell Motil.* **4**, 507–527 (1983).

[155] Fujiwara, I., Takahashi, S., Tadakuma, H., Funatsu, T. & Ishiwata, S. Microscopic

analysis of polymerization dynamics with individual actin filaments. *Nat. Cell Biol.* **4**, 666–673 (2002).

[156] Lappalainen, P. & Drubin, D. G. Cofilin promotes rapid actin filament turnover in vivo. *Nature* **388**, 78–82 (1997).

[157] Bindschadler, M., Osborn, E. A., Dewey, C. F. & McGrath, J. L. A mechanistic model of the actin cycle. *Biophys. J.* **86**, 2720–2739 (2004).

[158] Carlier, M. F. & Pantaloni, D. Control of actin dynamics in cell motility. *J. Mol. Biol.* **269**, 459–467 (1997).

[159] Korn, E. D., Carlier, M. F. & Pantaloni, D. Actin polymerization and ATP hydrolysis. *Science* **238**, 638–644 (1987).

[160] Carlier, M. F. & Pantaloni, D. Direct evidence for ADP-Pi-F-actin as the major intermediate in ATP-actin polymerization. Rate of dissociation of Pi from actin filaments. *Biochemistry* **25**, 7789–7792 (1986).

[161] Rickard, J. E. & Sheterline, P. Effect of ATP removal and inorganic phosphate on length redistribution of sheared actin filament populations. Evidence for a mechanism of end-to-end annealing. *J. Mol. Biol.* **201**, 675–681 (1988).

[162] Isambert, H. *et al.* Flexibility of actin filaments derived from thermal fluctuations. Effect of bound nucleotide, phalloidin, and muscle regulatory proteins. *J. Biol. Chem.* **270**, 11437–11444 (1995).

[163] Jégou, A. *et al.* Individual actin filaments in a microfluidic flow reveal the mechanism of ATP hydrolysis and give insight into the properties of profilin. *PLoS Biol.* **9** (2011).

[164] Mullins, R. D., Kelleher, J. F., Xu, J. & Pollard, T. D. Arp2/3 complex from Acanthamoeba binds profilin and cross-links actin filaments. *Mol. Biol. Cell* **9**, 841–852 (1998).

[165] Ichetovkin, I., Grant, W. & Condeelis, J. Cofilin produces newly polymerized actin filaments that are preferred for dendritic nucleation by the Arp2/3 complex. *Curr. Biol.* **12**, 79–84 (2002).

[166] Suarez, C. *et al.* Cofilin tunes the nucleotide state of actin filaments and severs at bare and decorated segment boundaries. *Curr. Biol.* **21**, 862–868 (2011).

[167] Pollard, T. D., Blanchoin, L. & Mullins, R. D. Molecular mechanisms controlling actin filament dynamics in nonmuscle cells. *Annu. Rev. Biophys. Biomol. Struct.* **29**, 545–576 (2000).

[168] Safer, D., Elzinga, M. & Nachmias, V. T. Thymosin ??4 and Fx, an actin-sequestering peptide, are indistinguishable. *J. Biol. Chem.* **266**, 4029–4032 (1991).

[169] Pantaloni, D. & Carlier, M. F. How profilin promotes actin filament assembly in the presence of thymosin $\beta 4$. *Cell* **75**, 1007–1014 (1993).

[170] Selden, L. A., Kinosian, H. J., Estes, J. E. & Gershman, L. C. Impact of profilin on actin-bound nucleotide exchange and actin polymerization dynamics. *Biochemistry* **38**, 2769–2778 (1999).

[171] Yarmola, E. G. & Bubb, M. R. Profilin: emerging concepts and lingering misconceptions. *Trends Biochem. Sci.* **31**, 197–205 (2006).

[172] Yarmola, E. G. & Bubb, M. R. How depolymerization can promote polymerization: The case of actin and profilin. *BioEssays* **31**, 1150–1160 (2009).

[173] Dickinson, R. B., Southwick, F. S. & Purich, D. L. A direct-transfer polymerization model explains how the multiple profilin-binding sites in the actoclampin motor promote rapid actin-based motility. *Arch. Biochem. Biophys.* **406**, 296–301 (2002).

[174] Gittes, F., Mickey, B., Nettleton, J. & Howard, J. Flexural rigidity of microtubules and actin filaments measured from thermal fluctuations in shape. *J. Cell Biol.* **120**, 923–934 (1993).

[175] Yasuda, R., Miyata, H. & Kinosita, K. Direct measurement of the torsional rigidity of single actin filaments. *J. Mol. Biol.* **263**, 227–236 (1996).

[176] Dupuis, D. E., Guilford, W. H., Wu, J. & Warshaw, D. M. Actin filament mechanics in the laser trap. *J. Muscle Res. Cell Motil.* **18**, 17–30 (1997).

[177] Kawamura, M. & Maruyama, K. Electron microscopic particle length of F-actin polymerized in vitro. *J. Biochem.* **67**, 437–457 (1970).

[178] Sept, D., Xu, J., Pollard, T. D. & McCammon, J. A. Annealing accounts for the length of actin filaments formed by spontaneous polymerization. *Biophys. J.* **77**, 2911–2919 (1999).

[179] Young, M. E., Cooper, J. A. & Bridgman, P. C. Yeast actin patches are networks of branched actin filaments. *J. Cell Biol.* **166**, 629–635 (2004).

[180] Rodal, A. A., Kozubowski, L., Goode, B. L., Drubin, D. G. & Hartwig, J. H. Actin and septin ultrastructures at the budding yeast cell cortex. *Mol. Biol. Cell* **16**, 372–384 (2005).

[181] McGrath, J. L., Osborn, E. A., Tardy, Y. S., Dewey, C. F. & Hartwig, J. H. Regulation of the actin cycle in vivo by actin filament severing. *Proc. Natl. Acad. Sci. U. S. A.* **97**, 6532–6537 (2000).

[182] Kasza, K. E. *et al.* Actin filament length tunes elasticity of flexibly cross-linked actin networks. *Biophys. J.* **99**, 1091–1100 (2010).

[183] Pollard, T. D. Regulation of actin filament assembly by Arp2/3 complex and formins. *Annu. Rev. Biophys. Biomol. Struct.* **36**, 451–477 (2007).

[184] Chhabra, E. S. & Higgs, H. N. The many faces of actin: matching assembly factors with cellular structures. *Nat. Cell Biol.* **9**, 1110–1121 (2007).

[185] Blanchoin, L., Boujemaa-Paterski, R., Sykes, C. & Plastino, J. Actin dynamics, architecture, and mechanics in cell motility. *Physiol. Rev.* **94**, 235–63 (2014).

[186] dos Remedios, C. G. *et al.* Actin binding proteins: regulation of cytoskeletal microfilaments. *Physiol. Rev.* **83**, 433–473 (2003).

[187] Clark, A. G., Dierkes, K. & Paluch, E. K. Monitoring actin cortex thickness in live cells. *Biophys. J.* **105**, 570–580 (2013).

[188] Bray, D. & White, J. G. Cortical flow in animal cells. *Science* **239**, 883–888 (1988).

[189] Stewart, M. P. *et al.* Hydrostatic pressure and the actomyosin cortex drive mitotic cell rounding. *Nature* **469**, 226–230 (2011).

[190] Salbreux, G., Charras, G. & Paluch, E. Actin cortex mechanics and cellular morphogenesis. *Trends Cell Biol.* **22**, 536–545 (2012).

[191] Hird, S. N. & White, J. G. Cortical and cytoplasmic flow polarity in early embryonic cells of Caenorhabditis elegans. *J. Cell Biol.* **121**, 1343–1355 (1993).

[192] Mayer, M., Depken, M., Bois, J. S., Jülicher, F. & Grill, S. W. Anisotropies in cortical tension reveal the physical basis of polarizing cortical flows. *Nature* **467**, 617–621 (2010).

[193] Biro, M. *et al.* Cell cortex composition and homeostasis resolved by integrating proteomics and quantitative imaging. *Cytoskeleton* **70**, 741–754 (2013).

[194] Abercrombie, M., Heaysman, J. E. & Pegrum, S. M. The locomotion of fibroblasts in culture. IV. Electron microscopy of the leading lamella. *Exp. Cell Res.* **67**, 359–367

(1971).

[195] Ponti, A., Machacek, M., Gupton, S. L., Waterman-Storer, C. M. & Danuser, G. Two distinct actin networks drive the protrusion of migrating cells. *Science* **305**, 1782–1786 (2004).

[196] Small, J. V., Isenberg, G. & Celis, J. E. Polarity of actin at the leading edge of cultured cells. *Nature* **272**, 638–639 (1978).

[197] Cramer, L. P. Identification of Novel Graded Polarity Actin Filament Bundles in Locomoting Heart Fibroblasts: Implications for the Generation of Motile Force. *J. Cell Biol.* **136**, 1287–1305 (1997).

[198] Svitkina, T. M. & Borisy, G. G. Arp2/3 complex and actin depolymerizing factor/cofilin in dendritic organization and treadmilling of actin filament array in lamellipodia. *J. Cell Biol.* **145**, 1009–1026 (1999).

[199] Bailly, M. *et al.* The F-actin side binding activity of the Arp2/3 complex is essential for actin nucleation and lamellipod extension. *Curr. Biol.* **11**, 620–625 (2001).

[200] Machesky, L. M. *et al.* Scar, a WASp-related protein, activates nucleation of actin filaments by the Arp2/3 complex. *Proc. Natl. Acad. Sci. U. S. A.* **96**, 3739–3744 (1999).

[201] Rohatgi, R. *et al.* The interaction between N-WASP and the Arp2/3 complex links Cdc42-dependent signals to actin assembly. *Cell* **97**, 221–231 (1999).

[202] Breitsprecher, D. *et al.* Molecular mechanism of Ena/VASP-mediated actin-filament elongation. *EMBO J.* **30**, 456–467 (2011).

[203] Footer, M. J., Kerssemakers, J. W. J., Theriot, J. A. & Dogterom, M. Direct measurement of force generation by actin filament polymerization using an optical trap. *Proc. Natl. Acad. Sci. U. S. A.* **104**, 2181–2186 (2007).

[204] Parekh, S. H., Chaudhuri, O., Theriot, J. A. & Fletcher, D. A. Loading history determines the velocity of actin-network growth. *Nat. Cell Biol.* **7**, 1219–1223 (2005).

[205] Heath, J. P. Behaviour and structure of the leading lamella in moving fibroblasts. I. Occurrence and centripetal movement of arc-shaped microfilament bundles beneath the dorsal cell surface. *J. Cell Sci.* **60**, 331–354 (1983).

[206] Flanagan, L. A. *et al.* Filamin A, the Arp2/3 complex, and the morphology and function of cortical actin filaments in human melanoma cells. *J. Cell Biol.* **155**, 511–517 (2001).

[207] Esue, O., Tseng, Y. & Wirtz, D. α-actinin and filamin cooperatively enhance the stiffness of actin filament networks. *PLoS One* **4** (2009).

[208] Medeiros, N. A., Burnette, D. T. & Forscher, P. Myosin II functions in actin-bundle turnover in neuronal growth cones. *Nat. Cell Biol.* **8**, 215–226 (2006).

[209] Haviv, L., Gillo, D., Backouche, F. & Bernheim-Groswasser, A. A Cytoskeletal Demolition Worker: Myosin II Acts as an Actin Depolymerization Agent. *J. Mol. Biol.* **375**, 325–330 (2008).

[210] Wilson, C. A. *et al.* Myosin II contributes to cell-scale actin network treadmilling through network disassembly. *Nature* **465**, 373–377 (2010).

[211] Murrell, M. P. & Gardel, M. L. F-actin buckling coordinates contractility and severing in a biomimetic actomyosin cortex. *Proc. Natl. Acad. Sci.* **109**, 20820–20825 (2012).

[212] Yang, Q., Zhang, X.-F., Pollard, T. D. & Forscher, P. Arp2/3 complex-dependent actin networks constrain myosin II function in driving retrograde actin flow. *J. Cell Biol.* **197**, 939–56 (2012).

[213] Lin, C. H. & Forscher, P. Growth cone advance is inversely proportional to retrograde F-actin flow. *Neuron* **14**, 763–771 (1995).

[214] Hu, K., Ji, L., Applegate, K. T., Danuser, G. & Waterman-Storer, C. M. Differential transmission of actin motion within focal adhesions. *Science* **315**, 111–115 (2007).

[215] Gupton, S. L. *et al.* Cell migration without a lamellipodium. *J. Cell Biol.* **168**, 619–631 (2005).

[216] Hotulainen, P. & Lappalainen, P. Stress fibers are generated by two distinct actin assembly mechanisms in motile cells. *J. Cell Biol.* **173**, 383–394 (2006).

[217] Oakes, P. W., Beckham, Y., Stricker, J. & Gardel, M. L. Tension is required but not sufficient for focal adhesion maturation without a stress fiber template. *J. Cell Biol.* **196**, 363–374 (2012).

[218] Burridge, K. & Wittchen, E. S. The tension mounts: Stress fibers as force-generating mechanotransducers. *J. Cell Biol.* **200**, 9–19 (2013).

[219] Heath, J. P. & Holifield, B. F. On the mechanisms of cortical actin flow and its role in cytoskeletal organisation of fibroblasts. *Symp. Soc. Exp. Biol.* **47**, 35–56 (1993).

[220] Burnette, D. T. *et al.* A contractile and counterbalancing adhesion system controls the 3D shape of crawling cells. *J. Cell Biol.* **205**, 83–96 (2014).

[221] Millán, J. *et al.* Adherens junctions connect stress fibres between adjacent endothelial cells. *BMC Biol.* **8**, 11 (2010).

[222] Huveneers, S. *et al.* Vinculin associates with endothelial VE-cadherin junctions to control force-dependent remodeling. *J. Cell Biol.* **196**, 641–652 (2012).

[223] Fededa, J. P. & Gerlich, D. W. Molecular control of animal cell cytokinesis. *Nat. Cell Biol.* **14**, 440–447 (2012).

[224] Mishra, M. *et al.* In vitro contraction of cytokinetic ring depends on myosin II but not on actin dynamics. *Nat. Cell Biol.* **15**, 853–9 (2013).

[225] Mendes Pinto, I., Rubinstein, B., Kucharavy, A., Unruh, J. R. & Li, R. Actin Depolymerization Drives Actomyosin Ring Contraction during Budding Yeast Cytokinesis. *Dev. Cell* **22**, 1247–1260 (2012).

[226] Theriot, J. A. & Mitchison, T. J. Actin microfilament dynamics in locomoting cells. *Nature* **352**, 126–131 (1991).

[227] Theriot, J. A. & Mitchison, T. J. Comparison of actin and cell surface dynamics in motile fibroblasts. *J. Cell Biol.* **119**, 367–377 (1992).

[228] Pelham, R. J. & Chang, F. Actin dynamics in the contractile ring during cytokinesis in fission yeast. *Nature* **419**, 82–86 (2002).

[229] Herrmann, H., Bär, H., Kreplak, L., Strelkov, S. V. & Aebi, U. Intermediate filaments: from cell architecture to nanomechanics. *Nat. Rev. Mol. Cell Biol.* **8**, 562–573 (2007).

[230] Kim, S. & Coulombe, P. A. Intermediate filament scaffolds fulfill mechanical, organizational, and signaling functions in the cytoplasm. *Genes Dev.* **21**, 1581–1597 (2007).

[231] Szeverenyi, I. *et al.* The human intermediate filament database: Comprehensive information on a gene family involved in many human diseases. *Hum. Mutat.* **29**, 351–360 (2008).

[232] Huber, F., Boire, A., López, M. P. & Koenderink, G. H. Cytoskeletal crosstalk: when three different personalities team up. *Curr. Opin. Cell Biol.* **32**, 39–47 (2015).

[233] Mencarelli, C., Ciolfi, S., Caroti, D., Lupetti, P. & Dallai, R. Isomin: a novel cytoplasmic intermediate filament protein from an arthropod species. *BMC Biol.* **9**, 17 (2011).

[234] Strelkov, S. V., Herrmann, H. & Aebi, U. Molecular architecture of intermediate filaments.

Bioessays **25**, 243–51 (2003).

[235] Sokolova, A. V. *et al.* Monitoring intermediate filament assembly by small-angle x-ray scattering reveals the molecular architecture of assembly intermediates. *Proc. Natl. Acad. Sci. U. S. A.* **103**, 16206–16211 (2006).

[236] Ip, W., Hartzer, M. K., Pang, Y. Y. & Robson, R. M. Assembly of vimentin in vitro and its implications concerning the structure of intermediate filaments. *J. Mol. Biol.* **183**, 365–375 (1985).

[237] Geisler, N., Schünemann, J., Weber, K., Häner, M. & Aebi, U. Assembly and architecture of invertebrate cytoplasmic intermediate filaments reconcile features of vertebrate cytoplasmic and nuclear lamin-type intermediate filaments. *J. Mol. Biol.* **282**, 601–617 (1998).

[238] Herrmann, H., Häner, M., Brettel, M., Ku, N. O. & Aebi, U. Characterization of distinct early assembly units of different intermediate filament proteins. *J. Mol. Biol.* **286**, 1403–1420 (1999).

[239] Chou, Y. H., Bischoff, J. R., Beach, D. & Goldman, R. D. Intermediate filament reorganization during mitosis is mediated by p34cdc2 phosphorylation of vimentin. *Cell* **62**, 1063–1071 (1990).

[240] Ku, N. O. & Omary, M. B. Keratins turn over by ubiquitination in a phosphorylation-modulated fashion. *J. Cell Biol.* **149**, 547–552 (2000).

[241] Omary, M. B., Ku, N. O., Tao, G. Z., Toivola, D. M. & Liao, J. 'Heads and tails' of intermediate filament phosphorylation: multiple sites and functional insights. *Trends Biochem. Sci.* **31**, 383–394 (2006).

[242] Sihag, R. K., Inagaki, M., Yamaguchi, T., Shea, T. B. & Pant, H. C. Role of phosphorylation on the structural dynamics and function of types III and IV intermediate filaments. *Exp. Cell Res.* **313**, 2098–2109 (2007).

[243] Izawa, I. & Inagaki, M. Regulatory mechanisms and functions of intermediate filaments: A study using site- and phosphorylation state-specific antibodies. *Cancer Sci.* **97**, 167–174 (2006).

[244] Yoon, K. H. *et al.* Insights into the dynamic properties of keratin intermediate filaments in living epithelial cells. *J. Cell Biol.* **152**, 503–516 (2001).

[245] Moch, M., Herberich, G., Aach, T., Leube, R. E. & Windoffer, R. Measuring the regulation of keratin filament network dynamics. *Proc. Natl. Acad. Sci. U. S. A.* **110**, 10664–9 (2013).

[246] Murray, M. E., Mendez, M. G. & Janmey, P. a. Substrate stiffness regulates solubility of cellular vimentin. *Mol. Biol. Cell* **25**, 87–94 (2014).

[247] Hohenadl, M., Storz, T., Kirpal, H., Kroy, K. & Merkel, R. Desmin filaments studied by quasi-elastic light scattering. *Biophys. J.* **77**, 2199–2209 (1999).

[248] Mücke, N. *et al.* Assessing the Flexibility of Intermediate Filaments by Atomic Force Microscopy. *J. Mol. Biol.* **335**, 1241–1250 (2004).

[249] Herrmann, H., Strelkov, S. V., Burkhard, P. & Aebi, U. Intermediate filaments: Primary determinants of cell architecture and plasticity. *J. Clin. Invest.* **119**, 1772–1783 (2009).

[250] Kreplak, L., Bär, H., Leterrier, J. F., Herrmann, H. & Aebi, U. Exploring the mechanical behavior of single intermediate filaments. *J. Mol. Biol.* **354**, 569–77 (2005).

[251] Janmey, P. A., Euteneuer, U., Traub, P. & Schliwa, M. Viscoelastic properties of vimentin compared with other filamentous biopolymer networks. *J. Cell Biol.* **113**, 155–160 (1991).

[252] Janmey, P. A., Shah, J. V., Janssen, K. P. & Schliwa, M. Viscoelasticity of intermediate filament networks. *Subcell. Biochem.* **31**, 381–97 (1998).

[253] Ma, L., Xu, J., Coulombe, P. A. & Wirtz, D. Keratin filament suspensions show unique micromechanical properties. *J. Biol. Chem.* **274**, 19145–19151 (1999).

[254] Qin, Z., Kreplak, L. & Buehler, M. J. Hierarchical structure controls nanomechanical properties of vimentin intermediate filaments. *PLoS One* **4** (2009).

[255] Sivaramakrishnan, S., DeGiulio, J. V., Lorand, L., Goldman, R. D. & Ridge, K. M. Micromechanical properties of keratin intermediate filament networks. *Proc. Natl. Acad. Sci. U. S. A.* **105**, 889–894 (2008).

[256] Lee, C. H. & Coulombe, P. A. Self-organization of keratin intermediate filaments into cross-linked networks. *J. Cell Biol.* **186**, 409–421 (2009).

[257] Nolting, J.-F. & Köster, S. Influence of microfluidic shear on keratin networks in living cells. *New J. Phys.* **15**, 045025 (2013).

[258] Coulombe, P. A. & Wong, P. Cytoplasmic intermediate filaments revealed as dynamic and multipurpose scaffolds. *Nat. Cell Biol.* **6**, 699–706 (2004).

[259] Yarm, F., Sagot, I. & Pellman, D. The social life of actin and microtubules: Interaction versus cooperation (2001).

[260] Rodriguez, O. C. *et al.* Conserved microtubule-actin interactions in cell movement and morphogenesis. *Nat. Cell Biol.* **5**, 599–609 (2003).

[261] Siegrist, S. E. & Doe, C. Q. Microtubule-induced cortical cell polarity. *Genes Dev.* **21**, 483–496 (2007).

[262] Chang, L. & Goldman, R. D. Intermediate filaments mediate cytoskeletal crosstalk. *Nat. Rev. Mol. Cell Biol.* **5**, 601–613 (2004).

[263] Abercrombie, M. The bases of the locomotory behaviour of fibroblasts. *Exp. Cell Res.* **Suppl 8**, 188–198 (1961).

[264] Vasiliev, J. M. *et al.* Effect of colcemid on the locomotory behaviour of fibroblasts. *J. Embryol. Exp. Morphol.* **24**, 625–640 (1970).

[265] Sider, J. R. *et al.* Direct observation of microtubule-f-actin interaction in cell free lysates. *J. Cell Sci.* **112**, 1947–1956 (1999).

[266] Waterman-Storer, C. *et al.* Microtubules remodel actomyosin networks in Xenopus egg extracts via two mechanisms of F-actin transport. *J. Cell Biol.* **150**, 361–376 (2000).

[267] Canman, J. C. & Bement, W. M. Microtubules suppress actomyosin-based cortical flow in Xenopus oocytes. *J. Cell Sci.* **110**, 1907–1917 (1997).

[268] Waterman-Storer, C. M., Worthylake, R. A., Liu, B. P., Burridge, K. & Salmon, E. D. Microtubule growth activates Rac1 to promote lamellipodial protrusion in fibroblasts. *Nat. Cell Biol.* **1**, 45–50 (1999).

[269] Etienne-Manneville, S. & Hall, A. Rho GTPases in cell biology. *Nature* **420**, 629–635 (2002).

[270] Geraldo, S., Khanzada, U. K., Parsons, M., Chilton, J. K. & Gordon-Weeks, P. R. Targeting of the F-actin-binding protein drebrin by the microtubule plus-tip protein EB3 is required for neuritogenesis. *Nat. Cell Biol.* **10**, 1181–1189 (2008).

[271] Solinet, S. *et al.* The actin-binding ERM protein Moesin binds to and stabilizes microtubules at the cell cortex. *J. Cell Biol.* **202**, 251–260 (2013).

[272] Yin, H., Pruyne, D., Huffaker, T. C. & Bretscher, A. Myosin V orientates the mitotic spindle in yeast. *Nature* **406**, 1013–1015 (2000).

[273] Frey, N., Klotz, J. & Nick, P. Dynamic bridges a calponin-domain kinesin from rice links actin filaments and microtubules in both cycling and non-cycling cells. *Plant Cell Physiol.* **50**, 1493–1506 (2009).

[274] Nadar, V. C., Lin, S. & Baas, P. W. Microtubule Redistribution in Growth Cones Elicited by Focal Inactivation of Kinesin-5. *J. Neurosci.* **32**, 5783–5794 (2012).

[275] Leung, C. L., Zheng, M., Prater, S. M. & Liem, R. K. H. The BPAG1 locus: Alternative splicing produces multiple isoforms with distinct cytoskeletal linker domains, including predominant isoforms in neurons and muscles. *J. Cell Biol.* **154**, 691–697 (2001).

[276] Mao, Y. FORMIN a link between kinetochores and microtubule ends. *Trends Cell Biol.* **21**, 625–629 (2011).

[277] Shen, Q. T. *et al.* Structural insights into WHAMM-mediated cytoskeletal coordination during membrane remodeling. *J. Cell Biol.* **199**, 111–124 (2012).

[278] Moseley, J. B. *et al.* Regulated binding of adenomatous polyposis coli protein to actin. *J. Biol. Chem.* **282**, 12661–12668 (2007).

[279] Wu, X., Kodama, A. & Fuchs, E. ACF7 Regulates Cytoskeletal-Focal Adhesion Dynamics and Migration and Has ATPase Activity. *Cell* **135**, 137–148 (2008).

[280] Lee, L. *et al.* Positioning of the mitotic spindle by a cortical-microtubule capture mechanism. *Science* **287**, 2260–2262 (2000).

[281] Lin, Y.-C., Koenderink, G. H., MacKintosh, F. C. & Weitz, D. A. Control of non-linear elasticity in F-actin networks with microtubules. *Soft Matter* **7**, 902 (2011).

[282] Gupton, S. L., Salmon, W. C. & Waterman-Storer, C. M. Converging populations of f-actin promote breakage of associated microtubules to spatially regulate microtubule turnover in migrating cells. *Curr. Biol.* **12**, 1891–1899 (2002).

[283] Brangwynne, C. P. *et al.* Microtubules can bear enhanced compressive loads in living cells because of lateral reinforcement. *J. Cell Biol.* **173**, 733–741 (2006).

[284] Brangwynne, C. P., Koenderink, G. H., MacKintosh, F. C. & Weitz, D. A. Nonequilibrium microtubule fluctuations in a model cytoskeleton. *Phys. Rev. Lett.* **100** (2008).

[285] Esue, O., Carson, A. A., Tseng, Y. & Wirtz, D. A direct interaction between actin and vimentin filaments mediated by the tail domain of vimentin. *J. Biol. Chem.* **281**, 30393–30399 (2006).

[286] Flitney, E. W., Kuczmarski, E. R., Adam, S. A. & Goldman, R. D. Insights into the mechanical properties of epithelial cells: the effects of shear stress on the assembly and remodeling of keratin intermediate filaments. *FASEB J.* **23**, 2110–2119 (2009).

[287] Salmon, W. C., Adams, M. C. & Waterman-Storer, C. M. Dual-wavelength fluorescent speckle microscopy reveals coupling of microtubule and actin movements in migrating cells. *J. Cell Biol.* **158**, 31–37 (2002).

[288] Windoffer, R., Wöll, S., Strnad, P. & Leube, R. E. Identification of novel principles of keratin filament network turnover in living cells. *Mol. Biol. Cell* **15**, 2436–2448 (2004).

[289] Mandato, C. A. & Bement, W. M. Actomyosin transports microtubules and microtubules control actomyosin recruitment during Xenopus oocyte wound healing. *Curr. Biol.* **13**, 1096–1105 (2003).

[290] Forscher, P. & Smith, S. J. Actions of cytochalasins on the organization of actin filaments and microtubules in a neuronal growth cone. *J. Cell Biol.* **107**, 1505–1516 (1988).

[291] Schaefer, A. W., Kabir, N. & Forscher, P. Filopodia and actin arcs guide the assembly and transport of two populations of microtubules with unique dynamic parameters in neuronal growth cones. *J. Cell Biol.* **158**, 139–152 (2002).

[292] Waterman-Storer, C. M. & Salmon, E. D. Actomyosin-based retrograde flow of microtubules in the lamella of migrating epithelial cells influences microtubule dynamic instability and turnover and is associated with microtubule breakage and treadmilling. *J. Cell Biol.* **139**, 417–434 (1997).

[293] Schaefer, A. W. *et al.* Coordination of Actin Filament and Microtubule Dynamics during Neurite Outgrowth. *Dev. Cell* **15**, 146–162 (2008).

[294] Dixit, R. & Cyr, R. The cortical microtubule array: from dynamics to organization. *Plant Cell* **16**, 2546–2552 (2004).

[295] Dixit, R. & Cyr, R. Encounters between dynamic cortical microtubules promote ordering of the cortical array through angle-dependent modifications of microtubule behavior. *Plant Cell* **16**, 3274–3284 (2004).

[296] Sampathkumar, A. *et al.* Live cell imaging reveals structural associations between the actin and microtubule cytoskeleton in arabidopsis. *Plant Cell* **23**, 2302–2313 (2011).

[297] Quinlan, M. E., Heuser, J. E., Kerkhoff, E. & Mullins, R. D. Drosophila Spire is an actin nucleation factor. *Nature* **433**, 382–388 (2005).

[298] Rosales-Nieves, A. E. *et al.* Coordination of microtubule and microfilament dynamics by Drosophila Rho1, Spire and Cappuccino. *Nat. Cell Biol.* **8**, 367–376 (2006).

[299] Quinlan, M. E., Hilgert, S., Bedrossian, A., Mullins, R. D. & Kerkhoff, E. Regulatory interactions between two actin nucleators, Spire and Cappuccino. *J. Cell Biol.* **179**, 117–128 (2007).

[300] Dahlgaard, K., Raposo, A. A. S. F., Niccoli, T. & St Johnston, D. Capu and Spire assemble a cytoplasmic actin mesh that maintains microtubule organization in the Drosophila oocyte. *Dev. Cell* **13**, 539–53 (2007).

[301] Mori, M. *et al.* Intracellular transport by an anchored homogeneously contracting F-actin meshwork. *Curr. Biol.* **21**, 606–611 (2011).

[302] Almonacid, M., Terret, M.-E. & Verlhac, M.-H. Actin-based spindle positioning: new insights from female gametes. *J. Cell Sci.* **127**, 477–83 (2014).

[303] Azoury, J. *et al.* Spindle Positioning in Mouse Oocytes Relies on a Dynamic Meshwork of Actin Filaments. *Curr. Biol.* **18**, 1514–1519 (2008).

[304] Schuh, M. & Ellenberg, J. A New Model for Asymmetric Spindle Positioning in Mouse Oocytes. *Curr. Biol.* **18**, 1986–1992 (2008).

[305] Holubcová, Z., Howard, G. & Schuh, M. Vesicles modulate an actin network for asymmetric spindle positioning. *Nat. Cell Biol.* **15**, 937–47 (2013).

[306] Jo, Y.-J., Jang, W.-I., Namgoong, S. & Kim, N.-H. Actin-capping proteins play essential roles in asymmetric division of maturing mouse oocytes. *J. Cell Sci.* **128**, 160–170 (2015).

[307] Leung, C. L., Green, K. J. & Liem, R. K. H. Plakins: A family of versatile cytolinker proteins. *Trends Cell Biol.* **12**, 37–45 (2002).

[308] Jefferson, J. J., Leung, C. L. & Liem, R. K. H. Plakins: goliaths that link cell junctions and the cytoskeleton. *Nat. Rev. Mol. Cell Biol.* **5**, 542–553 (2004).

[309] Suozzi, K. C., Wu, X. & Fuchs, E. Spectraplakins: Master orchestrators of cytoskeletal dynamics. *J. Cell Biol.* **197**, 465–475 (2012).

[310] Subramanian, A. *et al.* Shortstop recruits EB1/APC1 and promotes microtubule assembly at the muscle-tendon junction. *Curr. Biol.* **13**, 1086–1095 (2003).

[311] Roger, B., Al-Bassam, J., Dehmelt, L., Milligan, R. A. & Halpain, S. MAP2c, but not

tau, binds and bundles F-actin via its microtubule binding domain. *Curr. Biol.* **14**, 363–371 (2004).

[312] Näthke, I. S., Adams, C. L., Polakis, P., Sellin, J. H. & Nelson, W. J. The adenomatous polyposis coli tumor suppressor protein localizes to plasma membrane sites involved in active cell migration. *J. Cell Biol.* **134**, 165–179 (1996).

[313] Gundersen, G. G. & Bulinski, J. C. Selective stabilization of microtubules oriented toward the direction of cell migration. *Proc. Natl. Acad. Sci. U. S. A.* **85**, 5946–5950 (1988).

[314] Akhmanova, A. *et al.* CLASPs Are CLIP-115 and -170 Associating Proteins Involved in the Regional Regulation of Microtubule Dynamics in Motile Fibroblasts. *Cell* **104**, 923–935 (2001).

[315] Wittmann, T. & Waterman-Storer, C. M. Spatial regulation of CLASP affinity for microtubules by Rac1 and GSK3beta in migrating epithelial cells. *J. Cell Biol.* **169**, 929–939 (2005).

[316] Tahirovic, S. & Bradke, F. Neuronal polarity. *Cold Spring Harb. Perspect. Biol.* **1** (2009).

[317] Bellett, G. *et al.* Microtubule plus-end and minus-end capture at adherens junctions is involved in the assembly of apico-basal arrays in polarised epithelial cells. *Cell Motil. Cytoskeleton* **66**, 893–908 (2009).

[318] Kaverina, I. & Straube, A. Regulation of cell migration by dynamic microtubules. *Semin. Cell Dev. Biol.* **22**, 968–974 (2011).

[319] Etienne-Manneville, S. Microtubules in cell migration. *Annu. Rev. Cell Dev. Biol.* **29**, 471–99 (2013).

[320] Kotak, S., Busso, C. & Gönczy, P. NuMA phosphorylation by CDK1 couples mitotic progression with cortical dynein function. *EMBO J.* **32**, 2517–29 (2013).

[321] Kotak, S., Busso, C. & Gönczy, P. Cortical dynein is critical for proper spindle positioning in human cells. *J. Cell Biol.* **199**, 97–110 (2012).

[322] Laan, L. *et al.* Cortical dynein controls microtubule dynamics to generate pulling forces that position microtubule asters. *Cell* **148**, 502–514 (2012).

[323] Hendricks, A. G. *et al.* Dynein tethers and stabilizes dynamic microtubule plus ends. *Curr. Biol.* **22**, 632–637 (2012).

[324] Kiyomitsu, T. & Cheeseman, I. M. Chromosome- and spindle-pole-derived signals generate an intrinsic code for spindle position and orientation. *Nat. Cell Biol.* **14**, 311–7 (2012).

[325] Kiyomitsu, T. & Cheeseman, I. M. Cortical dynein and asymmetric membrane elongation coordinately position the spindle in anaphase. *Cell* **154**, 391–402 (2013).

[326] Zheng, Z. *et al.* Evidence for dynein and astral microtubule-mediated cortical release and transport of Gαi/LGN/NuMA complex in mitotic cells. *Mol. Biol. Cell* **24**, 901–13 (2013).

[327] Grill, S. W., Howard, J., Schäffer, E., Stelzer, E. H. K. & Hyman, A. A. The distribution of active force generators controls mitotic spindle position. *Science* **301**, 518–521 (2003).

[328] Munemitsu, S. *et al.* The APC gene product associates with microtubules in vivo and promotes their assembly in vitro. *Cancer Res.* **54**, 3676–3681 (1994).

[329] Mimori-Kiyosue, Y., Shiina, N. & Tsukita, S. Adenomatous polyposis coli (APC) protein moves along microtubules and concentrates at their growing ends in epithelial cells. *J. Cell Biol.* **148**, 505–517 (2000).

[330] Zumbrunn, J., Kinoshita, K., Hyman, A. A. & Näthke, I. S. Binding of the adenomatous

polyposis coli protein to microtubules increases microtubule stability and is regulated by GSK3β phosphorylation. *Curr. Biol.* **11**, 44–49 (2001).

[331] Kita, K., Wittmann, T., Näthke, I. S. & Waterman-Storer, C. M. Adenomatous polyposis coli on microtubule plus ends in cell extensions can promote microtubule net growth with or without EB1. *Mol. Biol. Cell* **17**, 2331–2345 (2006).

[332] Barth, A. I. M., Siemers, K. A. & Nelson, W. J. Dissecting interactions between EB1, microtubules and APC in cortical clusters at the plasma membrane. *J. Cell Sci.* **115**, 1583–1590 (2002).

[333] Townsley, F. M. & Bienz, M. Actin-dependent membrane association of a Drosophila epithelial APC protein and its effect on junctional Armadillo. *Curr. Biol.* **10**, 1339–1348 (2000).

[334] Watanabe, T. *et al.* Interaction with IQGAP1 links APC to Rac1, Cdc42, and actin filaments during cell polarization and migration. *Dev. Cell* **7**, 871–883 (2004).

[335] Wen, Y. *et al.* EB1 and APC bind to mDia to stabilize microtubules downstream of Rho and promote cell migration. *Nat. Cell Biol.* **6**, 820–830 (2004).

[336] Grohmann, A., Tanneberger, K., Alzner, A., Schneikert, J. & Behrens, J. AMER1 regulates the distribution of the tumor suppressor APC between microtubules and the plasma membrane. *J. Cell Sci.* **120**, 3738–3747 (2007).

[337] Pfister, A. S., Hadjihannas, M. V., Röhrig, W., Schambony, A. & Behrens, J. Amer2 protein interacts with EB1 protein and adenomatous polyposis coli (APC) and controls microtubule stability and cell migration. *J. Biol. Chem.* **287**, 35333–35340 (2012).

[338] Fukata, M. *et al.* Rac1 and Cdc42 capture microtubules through IQGAP1 and CLIP-170. *Cell* **109**, 873–885 (2002).

[339] Zaoui, K., Benseddik, K., Daou, P., Salaün, D. & Badache, A. ErbB2 receptor controls microtubule capture by recruiting ACF7 to the plasma membrane of migrating cells. *Proc. Natl. Acad. Sci. U. S. A.* **107**, 18517–18522 (2010).

[340] Mimori-Kiyosue, Y. *et al.* CLASP1 and CLASP2 bind to EB1 and regulate microtubule plus-end dynamics at the cell cortex. *J. Cell Biol.* **168**, 141–153 (2005).

[341] Lansbergen, G. *et al.* CLASPs Attach Microtubule Plus Ends to the Cell Cortex through a Complex with LL5β. *Dev. Cell* **11**, 21–32 (2006).

[342] Stehbens, S. J. *et al.* CLASPs link focal-adhesion-associated microtubule capture to localized exocytosis and adhesion site turnover. *Nat. Cell Biol.* **16**, 561–73 (2014).

[343] Krylyshkina, O. *et al.* Modulation of substrate adhesion dynamics via microtubule targeting requires kinesin-1. *J. Cell Biol.* **156**, 349–359 (2002).

[344] Stehbens, S. & Wittmann, T. Targeting and transport: How microtubules control focal adhesion dynamics. *J. Cell Biol.* **198**, 481–489 (2012).

[345] Al-Bassam, J. *et al.* CLASP promotes microtubule rescue by recruiting tubulin dimers to the microtubule. *Dev. Cell* **19**, 245–258 (2010).

[346] Maiato, H., Khodjakov, A. & Rieder, C. L. Drosophila CLASP is required for the incorporation of microtubule subunits into fluxing kinetochore fibres. *Nat. Cell Biol.* **7**, 42–47 (2005).

[347] Patel, K., Nogales, E. & Heald, R. Multiple domains of human CLASP contribute to microtubule dynamics and organization in vitro and in Xenopus egg extracts. *Cytoskeleton* **69**, 155–165 (2012).

[348] Bratman, S. V. & Chang, F. Stabilization of Overlapping Microtubules by Fission Yeast CLASP. *Dev. Cell* **13**, 812–827 (2007).

[349] Komarova, Y. A., Akhmanova, A. S., Kojima, S. I., Galjart, N. & Borisy, G. G. Cytoplasmic linker proteins promote microtubule rescue in vivo. *J. Cell Biol.* **159**, 589–599 (2002).

[350] Brunner, D. & Nurse, P. CLIP170-like tip1p spatially organizes microtubular dynamics in fission yeast. *Cell* **102**, 695–704 (2000).

[351] Arnal, I., Heichette, C., Diamantopoulos, G. S. & Chrétien, D. CLIP-170/tubulin-curved oligomers coassemble at microtubule ends and promote rescues. *Curr. Biol.* **14**, 2086–2095 (2004).

[352] Karakesisoglou, I., Yang, Y. & Fuchs, E. An epidermal plakin that integrates actin and microtubule networks at cellular junctions. *J. Cell Biol.* **149**, 195–208 (2000).

[353] Sun, D., Leung, C. L. & Liem, R. K. Characterization of the microtubule binding domain of microtubule actin crosslinking factor (MACF): identification of a novel group of microtubule associated proteins. *J. Cell Sci.* **114**, 161–172 (2001).

[354] Alves-Silva, J. *et al.* Spectraplakins Promote Microtubule-Mediated Axonal Growth by Functioning As Structural Microtubule-Associated Proteins and EB1-Dependent +TIPs (Tip Interacting Proteins). *J. Neurosci.* **32**, 9143–9158 (2012).

[355] Palazzo, A. F., Cook, T. A., Alberts, A. S. & Gundersen, G. G. mDia mediates Rho-regulated formation and orientation of stable microtubules. *Nat. Cell Biol.* **3**, 723–729 (2001).

[356] Brandt, D. T. & Grosse, R. Get to grips: steering local actin dynamics with IQGAPs. *EMBO Rep.* **8**, 1019–1023 (2007).

[357] Bartolini, F. & Gundersen, G. G. Formins and microtubules. *Biochim. Biophys. Acta - Mol. Cell Res.* **1803**, 164–173 (2010).

[358] Brandt, D. T. *et al.* Dia1 and IQGAP1 interact in cell migration and phagocytic cup formation. *J. Cell Biol.* **178**, 193–200 (2007).

[359] Bartolini, F. *et al.* The formin mDia2 stabilizes microtubules independently of its actin nucleation activity. *J. Cell Biol.* **181**, 523–536 (2008).

[360] Thurston, S. F., Kulacz, W. A., Shaikh, S., Lee, J. M. & Copeland, J. W. The Ability to Induce Microtubule Acetylation Is a General Feature of Formin Proteins. *PLoS One* **7** (2012).

[361] Korinek, W. S., Copeland, M. J., Chaudhuri, A. & Chant, J. Molecular linkage underlying microtubule orientation toward cortical sites in yeast. *Science* **287**, 2257–2259 (2000).

[362] Miller, R. K., Cheng, S. C. & Rose, M. D. Bim1p/Yeb1p mediates the Kar9p-dependent cortical attachment of cytoplasmic microtubules. *Mol. Biol. Cell* **11**, 2949–2959 (2000).

[363] Huisman, S. M. & Segal, M. Cortical capture of microtubules and spindle polarity in budding yeast - where's the catch? *J. Cell Sci.* **118**, 463–471 (2005).

[364] Kaverina, I., Rottner, K. & Small, J. V. Targeting, capture, and stabilization of microtubules at early focal adhesions. *J. Cell Biol.* **142**, 181–190 (1998).

[365] Kaverina, I., Krylyshkina, O. & Small, J. V. Microtubule targeting of substrate contacts promotes their relaxation and dissociation. *J. Cell Biol.* **146**, 1033–1043 (1999).

[366] Liu, B. P., Chrzanowska-Wodnicka, M. & Burridge, K. Microtubule depolymerization induces stress fibers, focal adhesions, and DNA synthesis via the GTP-binding protein Rho. *Cell Adhes. Commun.* **5**, 249–255 (1998).

[367] Palazzo, A. F. & Gundersen, G. G. Microtubule-actin cross-talk at focal adhesions. *Sci. STKE* **2002**, pe31 (2002).

[368] Huda, S. *et al.* Microtubule guidance tested through controlled cell geometry. *J. Cell Sci.* **125**, 5790–5799 (2012).

[369] Applewhite, D. A., Grode, K. D., Duncan, M. C. & Rogers, S. L. The actin-microtubule cross-linking activity of Drosophila Short stop is regulated by intramolecular inhibition. *Mol. Biol. Cell* **24**, 2885–93 (2013).

[370] Buck, K. B. & Zheng, J. Q. Growth cone turning induced by direct local modification of microtubule dynamics. *J. Neurosci.* **22**, 9358–9367 (2002).

[371] Wang, N. *et al.* Mechanical behavior in living cells consistent with the tensegrity model. *Proc. Natl. Acad. Sci. U. S. A.* **98**, 7765–7770 (2001).

[372] Zimmermann, J. *et al.* Actin filament elasticity and retrograde flow shape the force-velocity relation of motile cells. *Biophys. J.* **102**, 287–295 (2012).

[373] Burnette, D. T., Schaefer, A. W., Ji, L., Danuser, G. & Forscher, P. Filopodial actin bundles are not necessary for microtubule advance into the peripheral domain of Aplysia neuronal growth cones. *Nat. Cell Biol.* **9**, 1360–1369 (2007).

[374] Hwang, E., Kusch, J., Barral, Y. & Huffaker, T. C. Spindle orientation in Saccharomyces cerevisiae depends on the transport of microtubule ends along polarized actin cables. *J. Cell Biol.* **161**, 483–488 (2003).

[375] Graziano, B. R. *et al.* Mechanism and cellular function of Bud6 as an actin nucleation-promoting factor. *Mol. Biol. Cell* **22**, 4016–4028 (2011).

[376] Doodhi, H., Katrukha, E. A., Kapitein, L. C. & Akhmanova, A. Mechanical and geometrical constraints control kinesin-based microtubule guidance. *Curr. Biol.* **24**, 322–8 (2014).

[377] Chen, Y., Rolls, M. M. & Hancock, W. O. An EB1-kinesin complex is sufficient to steer microtubule growth in vitro. *Curr. Biol.* **24**, 316–21 (2014).

[378] Jaworski, J. *et al.* Dynamic Microtubules Regulate Dendritic Spine Morphology and Synaptic Plasticity. *Neuron* **61**, 85–100 (2009).

[379] Mostowy, S. & Cossart, P. Septins: the fourth component of the cytoskeleton. *Nat. Rev. Mol. Cell Biol.* (2012).

[380] Tada, T. *et al.* Role of Septin Cytoskeleton in Spine Morphogenesis and Dendrite Development in Neurons. *Curr. Biol.* **17**, 1752–1758 (2007).

[381] Hu, J. *et al.* Septin-driven coordination of actin and microtubule remodeling regulates the collateral branching of axons. *Curr. Biol.* **22**, 1109–15 (2012).

[382] Bowen, J. R., Hwang, D., Bai, X., Roy, D. & Spiliotis, E. T. Septin GTPases spatially guide microtubule organization and plus end dynamics in polarizing epithelia. *J. Cell Biol.* **194**, 187–97 (2011).

[383] Rochlin, M. W., Dailey, M. E. & Bridgman, P. C. Polymerizing microtubules activate site-directed F-actin assembly in nerve growth cones. *Mol. Biol. Cell* **10**, 2309–2327 (1999).

[384] Ray, K., Marteyn, B., Sansonetti, P. J. & Tang, C. M. Life on the inside: the intracellular lifestyle of cytosolic bacteria. *Nat. Rev. Microbiol.* **7**, 333–340 (2009).

[385] Feierbach, B., Verde, F. & Chang, F. Regulation of a formin complex by the microtubule plus end protein tea1p. *J. Cell Biol.* **165**, 697–707 (2004).

[386] Martin, S. G., Rincón, S. A., Basu, R., Pérez, P. & Chang, F. Regulation of the formin for3p by cdc42p and bud6p. *Mol. Biol. Cell* **18**, 4155–4167 (2007).

[387] Minc, N., Bratman, S. V., Basu, R. & Chang, F. Establishing New Sites of Polarization by Microtubules. *Curr. Biol.* **19**, 83–94 (2009).

[388] Behrens, R. & Nurse, P. Roles of fission yeast tea1p in the localization of polarity factors and in organizing the microtubular cytoskeleton. *J. Cell Biol.* **157**, 783–793 (2002).

[389] Chesarone, M. A., DuPage, A. G. & Goode, B. L. Unleashing formins to remodel the actin and microtubule cytoskeletons. *Nat. Rev. Mol. Cell Biol.* **11**, 62–74 (2010).

[390] Miller, R. K., Matheos, D. & Rose, M. D. The cortical localization of the microtubule orientation protein, Kar9p, is dependent upon actin and proteins required for polarization. *J. Cell Biol.* **144**, 963–975 (1999).

[391] Segal, M., Bloom, K. & Reed, S. I. Bud6 directs sequential microtubule interactions with the bud tip and bud neck during spindle morphogenesis in Saccharomyces cerevisiae. *Mol. Biol. Cell* **11**, 3689–3702 (2000).

[392] Huisman, S. M. *et al.* Differential contribution of Bud6p and Kar9p to microtubule capture and spindle orientation in S. cerevisiae. *J. Cell Biol.* **167**, 231–244 (2004).

[393] Delgehyr, N., Lopes, C. S. J., Moir, C. A., Huisman, S. M. & Segal, M. Dissecting the involvement of formins in Bud6p-mediated cortical capture of microtubules in S. cerevisiae. *J. Cell Sci.* **121**, 3803–3814 (2008).

[394] Ten Hoopen, R. *et al.* Mechanism for astral microtubule capture by cortical Bud6p priming spindle Polarity in S. cerevisiae. *Curr. Biol.* **22**, 1075–1083 (2012).

[395] Gaillard, J. *et al.* Differential interactions of the formins INF2, mDia1, and mDia2 with microtubules. *Mol. Biol. Cell* **22**, 4575–4587 (2011).

[396] Breitsprecher, D. & Goode, B. L. Formins at a glance. *J. Cell Sci.* **126**, 1–7 (2013).

[397] Okada, K. *et al.* Adenomatous polyposis coli protein nucleates actin assembly and synergizes with the formin mDia1. *J. Cell Biol.* **189**, 1087–1096 (2010).

[398] Breitsprecher, D. *et al.* Rocket launcher mechanism of collaborative actin assembly defined by single-molecule imaging. *Science* **336**, 1164–8 (2012).

[399] Daou, P. *et al.* Essential and nonredundant roles for Diaphanous formins in cortical microtubule capture and directed cell migration. *Mol. Biol. Cell* **25**, 658–68 (2014).

[400] Pertz, O. Spatio-temporal Rho GTPase signaling - where are we now? *J. Cell Sci.* **123**, 1841–1850 (2010).

[401] Hall, A. Rho family GTPases. *Biochem. Soc. Trans.* **40**, 1378–82 (2012).

[402] Ridley, A. J. & Hall, A. The small GTP-binding protein rho regulates the assembly of focal adhesions and actin stress fibers in response to growth factors. *Cell* **70**, 389–399 (1992).

[403] Chrzanowska-Wodnicka, M. & Burridge, K. Rho-stimulated contractility drives the formation of stress fibers and focal adhesions. *J. Cell Biol.* **133**, 1403–1415 (1996).

[404] Watanabe, N. *et al.* p140mDia, a mammalian homolog of Drosophila diaphanous, is a target protein for Rho small GTPase and is a ligand for profilin. *EMBO J.* **16**, 3044–3056 (1997).

[405] Amano, M. *et al.* Formation of actin stress fibers and focal adhesions enhanced by Rho-kinase. *Science* **275**, 1308–1311 (1997).

[406] Ridley, A. J., Paterson, H. F., Johnston, C. L., Diekmann, D. & Hall, A. The small GTP-binding protein rac regulates growth factor-induced membrane ruffling. *Cell* **70**, 401–410 (1992).

[407] Nobes, C. D. & Hall, A. Rho, rac, and cdc42 GTPases regulate the assembly of multimolecular focal complexes associated with actin stress fibers, lamellipodia, and filopodia. *Cell* **81**, 53–62 (1995).

[408] Wittmann, T. & Waterman-Storer, C. M. Cell motility: can Rho GTPases and microtubules point the way? *J. Cell Sci.* **114**, 3795–3803 (2001).

[409] Krendel, M., Zenke, F. T. & Bokoch, G. M. Nucleotide exchange factor GEF-H1 mediates cross-talk between microtubules and the actin cytoskeleton. *Nat. Cell Biol.* **4**, 294–301 (2002).

[410] Cook, T. A., Nagasaki, T. & Gundersen, G. G. Rho guanosine triphosphatase mediates the selective stabilization of microtubules induced by lysophosphatidic acid. *J. Cell Biol.* **141**, 175–185 (1998).

[411] Zaoui, K., Honoré, S., Isnardon, D., Braguer, D. & Badache, A. Memo - RhoA - mDia1 signaling controls microtubules, the actin network, and adhesion site formation in migrating cells. *J. Cell Biol.* **183**, 401–408 (2008).

[412] Bement, W. M., Benink, H. A. & Von Dassow, G. A microtubule-dependent zone of active RhoA during cleavage plane specification. *J. Cell Biol.* **170**, 91–101 (2005).

[413] Wittmann, T., Bokoch, G. M. & Waterman-Storer, C. M. Regulation of leading edge microtubule and actin dynamics downstream of Rac1. *J. Cell Biol.* **161**, 845–851 (2003).

[414] Akiyama, T. & Kawasaki, Y. Wnt signalling and the actin cytoskeleton. *Oncogene* **25**, 7538–7544 (2006).

[415] Sun, T., Rodriguez, M. & Kim, L. Glycogen synthase kinase 3 in the world of cell migration. *Dev. Growth Differ.* **51**, 735–742 (2009).

[416] Barth, A. I. M., Caro-Gonzalez, H. Y. & Nelson, W. J. Role of adenomatous polyposis coli (APC) and microtubules in directional cell migration and neuronal polarization. *Semin. Cell Dev. Biol.* **19**, 245–251 (2008).

[417] Kumar, P. *et al.* GSK3beta phosphorylation modulates CLASP-microtubule association and lamella microtubule attachment. *J. Cell Biol.* **184**, 895–908 (2009).

[418] Wu, X. *et al.* Skin stem cells orchestrate directional migration by regulating microtubule-ACF7 connections through GSK3β. *Cell* **144**, 341–52 (2011).

[419] Etienne-Manneville, S. & Hall, A. Cdc42 regulates GSK-3beta and adenomatous polyposis coli to control cell polarity. *Nature* **421**, 753–756 (2003).

[420] Machacek, M. *et al.* Coordination of Rho GTPase activities during cell protrusion. *Nature* **461**, 99–103 (2009).

[421] Dujardin, D. *et al.* Evidence for a role of CLIP-170 in the establishment of metaphase chromosome alignment. *J. Cell Biol.* **141**, 849–862 (1998).

[422] Lin, H. *et al.* Polyploids require Bik1 for kinetochore-microtubule attachment. *J. Cell Biol.* **155**, 1173–1184 (2001).

[423] Kaplan, K. B. *et al.* A role for the Adenomatous Polyposis Coli protein in chromosome segregation. *Nat. Cell Biol.* **3**, 429–432 (2001).

[424] Tirnauer, J. S., Canman, J. C., Salmon, E. D. & Mitchison, T. J. EB1 targets to kinetochores with attached, polymerizing microtubules. *Mol. Biol. Cell* **13**, 4308–4316 (2002).

[425] Maiato, H. *et al.* Human CLASP1 is an outer kinetochore component that regulates spindle microtubule dynamics. *Cell* **113**, 891–904 (2003).

[426] Green, R. A. & Kaplan, K. B. Chromosome instability in colorectal tumor cells is associated with defects in microtubule plus-end attachments caused by a dominant mutation in APC. *J. Cell Biol.* **163**, 949–961 (2003).

[427] Reilein, A. & Nelson, W. J. APC is a component of an organizing template for cortical microtubule networks. *Nat. Cell Biol.* **7**, 463–473 (2005).

[428] Goldspink, D. a. *et al.* The microtubule end-binding protein EB2 is a central regulator of microtubule reorganisation in apico-basal epithelial differentiation. *J. Cell Sci.* **126**, 4000–14 (2013).

[429] Rosenblatt, J., Cramer, L. P., Baum, B. & McGee, K. M. Myosin II-dependent cortical movement is required for centrosome separation and positioning during mitotic spindle assembly. *Cell* **117**, 361–372 (2004).

[430] Dogterom, M. & Surrey, T. Microtubule organization in vitro. *Curr. Opin. Cell Biol.* **25**, 23–9 (2013).

[431] Mullins, R. D. & Hansen, S. D. In vitro studies of actin filament and network dynamics. *Curr. Opin. Cell Biol.* **25**, 6–13 (2013).

[432] Huber, F. *et al.* Emergent complexity of the cytoskeleton: from single filaments to tissue. *Adv. Phys.* **62**, 1–112 (2013).

[433] Ali, M. Y. *et al.* Myosin Va maneuvers through actin intersections and diffuses along microtubules. *Proc. Natl. Acad. Sci. U. S. A.* **104**, 4332–4336 (2007).

[434] Schroeder, H. W., Mitchell, C., Shuman, H., Holzbaur, E. L. F. & Goldman, Y. E. Motor Number Controls Cargo Switching at Actin-Microtubule Intersections In Vitro. *Curr. Biol.* **20**, 687–696 (2010).

[435] Selden, S. C. & Pollard, T. D. Interaction of actin filaments with microtubules is mediated by microtubule-associated proteins and regulated by phosphorylation. *Ann. N. Y. Acad. Sci.* **466**, 803–812 (1986).

[436] Gell, C. *et al.* Microtubule dynamics reconstituted in vitro and imaged by single-molecule fluorescence microscopy. *Methods Cell Biol.* **95**, 221–45 (2010).

[437] Pardee, J. D. & Spudich, J. A. Mechanism of K+-induced actin assembly. *J. Cell Biol.* **93**, 648–654 (1982).

[438] Good, N. E. *et al.* Hydrogen ion buffers for bifological Research. *Biochemistry* **5**, 467–477 (1966).

[439] Ferguson, W. J. *et al.* Hydrogen ion buffers for biological research. *Anal. Biochem.* **104**, 300–310 (1980).

[440] Gentry, B. S. *et al.* Multiple actin binding domains of Ena/VASP proteins determine actin network stiffening. *Eur. Biophys. J.* **41**, 979–990 (2012).

[441] Preciado López, M. *et al.* In vitro reconstitution of dynamic microtubules interacting with actin filament networks. In Vale, R. D. (ed.) *Methods Enzymol.*, vol. 540, chap. 17, 301–320 (Elsevier Inc., Amsterdam, 2014).

[442] Schindelin, J. *et al.* Fiji: an open-source platform for biological-image analysis. *Nat. Methods* **9**, 676–682 (2012).

[443] Schneider, C. A., Rasband, W. S. & Eliceiri, K. W. NIH Image to ImageJ: 25 years of image analysis. *Nat. Methods* **9**, 671–675 (2012).

[444] Röper, K., Gregory, S. L. & Brown, N. H. The 'spectraplakins': cytoskeletal giants with characteristics of both spectrin and plakin families. *J. Cell Sci.* **115**, 4215–4225 (2002).

[445] Young, K. G. & Kothary, R. Dystonin/Bpag1–a link to what? *Cell Motil. Cytoskeleton* **64**, 897–905 (2007).

[446] Lee, S., Harris, K. L., Whitington, P. M. & Kolodziej, P. A. short stop is allelic to kakapo, and encodes rod-like cytoskeletal-associated proteins required for axon extension. *J. Neurosci.* **20**, 1096–1108 (2000).

[447] Bosher, J. M. *et al.* The Caenorhabditis elegans vab-10 spectraplakin isoforms protect the epidermis against internal and external forces. *J. Cell Biol.* **161**, 757–768 (2003).

[448] Kim, H.-S. *et al.* VAB-10 spectraplakin acts in cell and nuclear migration in Caenorhabditis elegans. *Development* **138**, 4013–4023 (2011).

[449] Dosch, R. *et al.* Maternal control of vertebrate development before the midblastula transition: Mutants from the zebrafish I. *Dev. Cell* **6**, 771–780 (2004).

[450] Gupta, T. *et al.* Microtubule actin crosslinking factor 1 regulates the balbiani body and animal-vegetal polarity of the zebrafish oocyte. *PLoS Genet.* **6** (2010).

[451] Gimona, M., Djinovic-Carugo, K., Kranewitter, W. J. & Winder, S. J. Functional plasticity of CH domains. *FEBS Lett.* **513**, 98–106 (2002).

[452] Guo, L. *et al.* Gene targeting of BPAG1: abnormalities in mechanical strength and cell migration in stratified epithelia and neurologic degeneration. *Cell* **81**, 233–243 (1995).

[453] Yang, Y. *et al.* An essential cytoskeletal linker protein connecting actin microfilaments to intermediate filaments. *Cell* **86**, 655–665 (1996).

[454] Bhasin, N. *et al.* Molecular extensibility of mini-dystrophins and a dystrophin rod construct. *J. Mol. Biol.* **352**, 795–806 (2005).

[455] Durbeej, M. & Campbell, K. P. Muscular dystrophies involving the dystrophin-glycoprotein complex: An overview of current mouse models. *Curr. Opin. Genet. Dev.* **12**, 349–361 (2002).

[456] Broderick, M. J. F. & Winder, S. J. Spectrin, alpha-actinin, and dystrophin. *Adv. Protein Chem.* **70**, 203–246 (2005).

[457] Travé, G., Lacombe, P. J., Pfuhl, M., Saraste, M. & Pastore, A. Molecular mechanism of the calcium-induced conformational change in the spectrin EF-hands. *EMBO J.* **14**, 4922–4931 (1995).

[458] Kapur, M. *et al.* Calcium tips the balance: a microtubule plus end to lattice binding switch operates in the carboxyl terminus of BPAG1n4. *EMBO Rep.* **13**, 1021–9 (2012).

[459] Stroud, M. J., Kammerer, R. A. & Ballestrem, C. Characterization of G2L3 (GAS2-like 3), a new microtubule- and actin-binding protein related to spectraplakins. *J. Biol. Chem.* **286**, 24987–24995 (2011).

[460] Stroud, M. J. *et al.* GAS2-like proteins mediate communication between microtubules and actin through interactions with end-binding proteins. *J. Cell Sci.* **127**, 2672–82 (2014).

[461] Krylyshkina, O. *et al.* Nanometer targeting of microtubules to focal adhesions. *J. Cell Biol.* **161**, 853–859 (2003).

[462] Riedl, J. *et al.* Lifeact: a versatile marker to visualize F-actin. *Nat. Methods* **5**, 605–607 (2008).

[463] Faix, J. *et al.* Cortexillins, major determinants of cell shape and size, are actin- bundling proteins with a parallel coiled-coil tail. *Cell* **86**, 631–642 (1996).

[464] Steinmetz, M. O. *et al.* A distinct 14 residue site triggers coiled-coil formation in cortexillin I. *EMBO J.* **17**, 1883–1891 (1998).

[465] Sanchez-Soriano, N. *et al.* Mouse ACF7 and drosophila short stop modulate filopodia formation and microtubule organisation during neuronal growth. *J. Cell Sci.* **122**, 2534–2542 (2009).

[466] Johnson, K. A. & Goody, R. S. The original Michaelis constant: Translation of the 1913 Michaelis-Menten Paper. *Biochemistry* **50**, 8264–8269 (2011).

[467] Bertani, G. Studies on lysogenesis. I. The mode of phage liberation by lysogenic Escherichia coli. *J. Bacteriol.* **62**, 293–300 (1951).

[468] Gasteiger, E. *et al.* *The Proteomics Protocols Handbook - Chapter 52: Protein Identification and Analysis Tools on the ExPASy Server* (Humana Press, Totowa, NJ, 2005).

[469] The Mathworks, I. MATLAB and Curve Fitting Toolbox Release 2012b (2012).

[470] Conner, S. D. & Schmid, S. L. Regulated portals of entry into the cell. *Nature* **422**, 37–44 (2003).

[471] Zhou, F.-Q. Q., Waterman-Storer, C. M. & Cohan, C. S. Focal loss of actin bundles causes microtubule redistribution and growth cone turning. *J. Cell Biol.* **157**, 839–849 (2002).

[472] McCullough, B. R., Blanchoin, L., Martiel, J. L. & De La Cruz, E. M. Cofilin Increases the Bending Flexibility of Actin Filaments: Implications for Severing and Cell Mechanics. *J. Mol. Biol.* **381**, 550–558 (2008).

[473] Claessens, M. M. A. E., Bathe, M., Frey, E. & Bausch, A. R. Actin-binding proteins sensitively mediate F-actin bundle stiffness. *Nat. Mater.* **5**, 748–753 (2006).

[474] Takatsuki, H., Bengtsson, E. & Må nsson, A. Persistence length of fascin-cross-linked actin filament bundles in solution and the in vitro motility assay. *Biochim. Biophys. Acta - Gen. Subj.* **1840**, 1933–1942 (2014).

[475] Orlova, A. *et al.* Binding of dystrophin's tandem calponin homology domain to F-actin is modulated by actin's structure. *Biophys. J.* **80**, 1926–1931 (2001).

[476] Gundersen, G. G., Gomes, E. R. & Wen, Y. Cortical control of microtubule stability and polarization. *Curr. Opin. Cell Biol.* **16**, 106–112 (2004).

[477] Alvarado, J., Mulder, B. M. & Koenderink, G. H. Alignment of nematic and bundled semiflexible polymers in cell-sized confinement. *Soft Matter* **10**, 2354–64 (2014).

[478] Rybakova, I. N. & Ervasti, J. M. Dystrophin-glycoprotein complex is monomeric and stabilizes actin filaments in vitro through a lateral association. *J. Biol. Chem.* **272**, 28771–28778 (1997).

[479] Mogilner, A. & Rubinstein, B. The physics of filopodial protrusion. *Biophys. J.* **89**, 782–795 (2005).

[480] Aratyn, Y. S., Schaus, T. E., Taylor, E. W. & Borisy, G. G. Intrinsic dynamic behavior of fascin in filopodia. *Mol. Biol. Cell* **18**, 3928–3940 (2007).

[481] Mattila, P. K. & Lappalainen, P. Filopodia: molecular architecture and cellular functions. *Nat. Rev. Mol. Cell Biol.* **9**, 446–454 (2008).

[482] Zidovska, A. & Sackmann, E. On the mechanical stabilization of filopodia. *Biophys. J.* **100**, 1428–1437 (2011).

[483] Vignjevic, D. *et al.* Role of fascin in filopodial protrusion. *J. Cell Biol.* **174**, 863–875 (2006).

[484] Popp, D., Yamamoto, A., Iwasa, M. & Maéda, Y. Direct visualization of actin nematic network formation and dynamics. *Biochem. Biophys. Res. Commun.* **351**, 348–353 (2006).

[485] Courson, D. S. & Rock, R. S. Actin cross-link assembly and disassembly mechanics for α-actinin and fascin. *J. Biol. Chem.* **285**, 26350–26357 (2010).

[486] Sprague, B. L., Pego, R. L., Stavreva, D. A. & McNally, J. G. Analysis of binding reactions by fluorescence recovery after photobleaching. *Biophys. J.* **86**, 3473–3495 (2004).

[487] Rezakhaniha, R. *et al.* Experimental investigation of collagen waviness and orientation

in the arterial adventitia using confocal laser scanning microscopy. *Biomech. Model. Mechanobiol.* **11**, 461–473 (2012).

[488] Schober, J. M., Komarova, Y. A., Chaga, O. Y., Akhmanova, A. & Borisy, G. G. Microtubule-targeting-dependent reorganization of filopodia. *J. Cell Sci.* **120**, 1235–1244 (2007).

[489] Goriounov, D., Leung, C. & Ronald K. H. Liem. Protein products of human Gas2-related genes on chromosomes 17 and 22 (hGAR17 and hGAR22) associate with both microfilaments and microtubules. *J. Cell Sci.* **116**, 1045–1058 (2003).

[490] Collings, D. A. & Wasteneys, G. O. Actin microfilament and microtubule distribution patterns in the expanding root of Arabidopsis thaliana. *Can. J. Bot.* **83**, 579–590 (2005).

[491] Powers, A. F. *et al.* The Ndc80 Kinetochore Complex Forms Load-Bearing Attachments to Dynamic Microtubule Tips via Biased Diffusion. *Cell* **136**, 865–875 (2009).

[492] Waterman-Storer, C. M., Gregory, J., Parsons, S. F. & Salmon, E. D. Membrane/microtubule tip attachment complexes (TACs) allow the assembly dynamics of plus ends to push and pull membranes into tubulovesicular networks in interphase Xenopus egg extracts. *J. Cell Biol.* **130**, 1161–1169 (1995).

[493] Fernández-Suárez, M. & Ting, A. Y. Fluorescent probes for super-resolution imaging in living cells. *Nat. Rev. Mol. Cell Biol.* **9**, 929–943 (2008).

[494] Hill, T. L. Theoretical problems related to the attachment of microtubules to kinetochores. *Proc. Natl. Acad. Sci. U. S. A.* **82**, 4404–4408 (1985).

[495] Debye, P. & Hückel, E. Zur Theorie der Elektrolyte. I. Gefrierpunktserniedrigung und verwandte Erscheinungen. *Phys. Zeitschrift* **24**, 185–206 (1923).

[496] Hatae, J., Fujishiro, N. & Kawata, H. Determination of the Appropriate Valences of 1,4-Piperazinediethanesulfonic Acids (PIPES) in Physiological pH. *Biol. Pharm. Bull.* **17**, 437–439 (1994).

[497] R. N. Roy, J. J. Gibbons, J. L. Padron, J. M. Second-Stage Dissociation Constants of Piperazine-N, N'-bis(2-ethanesulfonic acid) Monosodium Monohydrate and Related Thermodynamic Functions in Water from 5 to 55 C. *Anal. Chem.* **52**, 2409–2412 (1980).

[498] Wolfram Research, I. Mathematica (2014).

[499] Doi, M. & Edwards, S. *The Theory of Polymer Dynamics* (Clarendon Press, Oxford, 1986).

[500] Methylcellulose, Cat No. 9004-67-5. Sigma-Aldrich Chemie. URL `https://www.sigmaaldrich.com/content/dam/sigma-aldrich/docs/Sigma-Aldrich/Product_Information_Sheet/m0262pis.pdf`.

[501] Gillespie, D. T. Exact stochastic simulation of coupled chemical reactions. *J. Phys. Chem.* **81**, 2340–2361 (1977).

[502] Erban, R., Chapman, J. & Maini, P. A practical guide to stochastic simulations of reaction-diffusion processes (2007). arXiv:`0704.1908`.

[503] Rayleigh, L. XXXI. Investigations in optics, with special reference to the spectroscope. *Philos. Mag. Ser. 5* **8**, 261–274 (1879).

[504] Mallik, R. & Gross, S. P. Molecular motors: Strategies to get along. *Curr. Biol.* **14** (2004).

[505] Claessens, M. M. A. E., Semmrich, C., Ramos, L. & Bausch, A. R. Helical twist controls the thickness of F-actin bundles. *Proc. Natl. Acad. Sci. U. S. A.* **105**, 8819–8822 (2008).

[506] Taylor, K. A. & Taylor, D. W. Formation of two-dimensional complexes of F-actin and

crosslinking proteins on lipid monolayers: demonstration of unipolar alpha-actinin-F-actin crosslinking. *Biophys. J.* **67**, 1976–1983 (1994).

[507] Vignaud, T., Blanchoin, L. & Théry, M. Directed cytoskeleton self-organization. *Trends Cell Biol.* **22**, 671–681 (2012).

[508] Milo, R., Jorgensen, P., Moran, U., Weber, G. & Springer, M. BioNumbers The database of key numbers in molecular and cell biology. *Nucleic Acids Res.* **38** (2009).

[509] Koster, G., VanDuijn, M., Hofs, B. & Dogterom, M. Membrane tube formation from giant vesicles by dynamic association of motor proteins. *Proc. Natl. Acad. Sci. U. S. A.* **100**, 15583–15588 (2003).

Samenvatting

Cellen, de bouwstenen van het leven, hebben het fascinerend vermogen om van vorm te veranderen, te delen en te bewegen. Deze vitale processen worden aangedreven door een dynamisch supramoleculair network dat het cytoskelet genoemd wordt. Het cytoskelet van eukaryote cellen bestaat uit drie netwerken van eiwit polymeren: filamenteus actine (F-actine), microtubuli, en, in metazoa, intermediaire filamenten. Deze polymeren hebben unieke dynamische en mechanische eigenschappen, die cellen in staat stellen een breed scala aan functies te vervullen. Bijvoorbeeld om de morfologische veranderingen aan te drijven die noodzakelijk zijn bij celdeling, om cellen van mechanische stabiliteit te voorzien, en als wegennetwerk voor intracellulair transport van vesikels en organellen.

In het verleden zijn actine filamenten, microtubuli en intermediaire filamenten meest-al los van elkaar bestudeerd. Enerzijds geeft deze aanpak een gedetailleerd beeld van hun biochemische, dynamische, mechanische en structurele eigenschappen. Aan de andere kant, echter, heeft dit ons belemmerd een beeld te vormen van het cytoskelet als een zeer complex en nauw verweven geheel. Er is inmiddels een groeiende lijst van eiwitten geidentificeerd die communicatie tussen de drie cytoskelet systemen verzorgen, fysiek of via signalering, hetgeen suggereert dat in cellen de activiteit van de drie onderdelen van het cytoskelet onderling strikt gekkoördineerd is. Het is echter moeilijk een duidelijk beeld te krijgen van de invloed van deze eiwitten op de coördinatie. Dit omdat de eiwitconcentratie in de cel bijzonder hoog is, en onderzoek verder wordt bemoeilijkt door de dichtheid en diversiteit van het cytoskelet netwerk en de aanwezigheid van een veelvoud aan *cross-linkers* en biochemische regulatoren.

Modelsystemen, met slechts een beperkt aantal cellulaire eiwitten, zijn zeer geschikt om deze complexiteit te ontrafelen. Ze geven een duidelijk beeld van de biochemische en mechanische interacties tussen de eiwitten en tonen de minimale benodigdheden van het systeem om een bepaalde functie te kunnen vervullen. Hoewel de bestudering van modelsystemen onze kennis van elk van de drie onderdelen van het cytoskelet vergroot heeft, zijn tot op heden *in vitro* studies van de interacties tussen deze onderdelen van het cytoskelet zeer zeldzaam.

Daarom is het doel van dit proefschrift een vereenvoudigd *in vitro* model systeem te ontwikkelen zodat we de interacties tussen microtubuli en actine filamenten kunnen bestuderen: de twee meest dynamische onderdelen van het eukaryote cytoskelet. Hiertoe hebben we een *cross-linking* molecuul ontwikkeld (deze noemen we TipAct), dat direct aan F-actine bindt en zich concentreert aan de groeiende uiteindes van microtubuli. Dit laatste gebeurt doordat TipAct bindt aan EB (end-binding) eiwitten, die specifiek het groeiende uiteinde van de microtubulus herkennen. Vervolgens observeerden we de groei van microtubuli in aanwezigheid van F-actine filamenten met fluorescentie microscopie. Om de afzonderlijke invloed van sterische interacties en door cross-linkers begeleide actine-microtubulus-interacties bestuderen voerden we de experimenten uit in aan- en afwezigheid van TipAct. Verder bestudeerden we de invloed van verschillende typen actine netwerken, die typische situaties in de cel representeren.

In Hoofdstuk 1, beschrijven we de eigenschappen van de drie eukaryote cytoskelet systemen: actine, microtubuli en intermediaire filamenten, en hoe elk afzonderlijk de binnenkant van de cel vormgeven. Vervolgens verleggen we het focus naar de *cross-talk* binnen het cytoskelet, met de nadruk op actine-microtubulus interacties. We bespreken het mechanisme dat cross-linking proteïnen en biochemische regulatoren in staat stelt de architectuur van het cytoskelet efficiënt op te bouwen, en hoe de activiteit van cross-linkers beïnvloed wordt door de mechanische en dynamische eigenschappen van microtubuli, actine filamenten en intermediaire filamenten.

In Hoofdstuk 2 beschrijven we de experimentele methoden die van toepassing zijn op alle *in vitro* analyses die in dit proefschrift beschreven worden. We werken met dynamische (aktief groeiende en krimpende) microtubuli en actine filamenten, welke zijn *gecross-linked* via fluorescent gelabelde EB en TipAct moleculen in de oplossing. Hiervoor hebben we een aantal oppervlakte analyses, geschikt voor *total internal reflection fluoresence* (TIRF) microscopie, ontwikkeld alsmede kwantitatieve beeldanalyse algoritmes.

In hoofdstuk 3 beschrijven we de ontwikkeling, opzuivering, en biochemische karakterisatie van TipAct. Eerst laten we zien dat zowel in cellen als *in vitro* TipAct bindt aan actine filamenten, en dat het zich door interactie met EB-eiwitten bevindt aan de groeiende uiteindes van microtubuli. Daarnaast tonen we aan dat hoewel TipAct geen hoge affiniteit heeft voor F-actine, het toch efficiënt F-actine kan binden aan microtubuli door lokaal verhoogde concentraties aan de microtubuli uiteindes. Deze lokaal verhoogde concentraties aan de uiteindes van microtubuli zijn te verklaren door een lokaal verlaagde snelheid waarmee TipAct en EB dissociëren in de overlapzones van

actine met en microtubulus. Ten slotte laten we zien dat het actine-bindende domein van TipAct niet gevoelig is voor de actine filament polariteit.

In hoofdstuk 4 beschrijven we de effecten van F-actine structuren op microtubuli organisatie. Om dit te bereiken reconstrueren we interacties tussen dynamische microtubuli en bundels van actine filamenten. We zien dat microtubuli groei langs actine bundels geleid kan worden door twee verschillende mechanismes: sterische afbuiging als TipAct afwezig is, of door vang- en ritsmechanismen als TipAct aanwezig is. We laten zien dat ondanks de lage affiniteit voor enkele actine filamenten, TipAct toch stabiel bindt aan F-actine bundels, en ook dat het EB rekruteert naar deze bundels. Met behulp van *fluorescence recovery after photo-bleaching* (FRAP) experimenten tonen we aan dat dissociatie snelheden van TipAct en EB inderdaad lager zijn in zones waar actine en microtubuli overlappen. Deze observaties verklaren de hoge efficiëntie van het invang- en ritsmechanismen (van TipAct) bij het leiden van microtubuli groei. Ten slotte laten we zien dat TipAct ervoor zorgt dat parallelle bundels van F-actine bundels op grotere schaal de organisatie van microtubuli dicteren.

In hoofdstuk 5 beschrijven we de effecten die groeiende microtubuli kunnen hebben op F-actine organisatie. Om dit te bereiken, reconstrueren we interacties tussen dynamische microtubuli en mobiele actine filamenten en bundels. We laten zien dat *cross-linking* via EB en TipAct kan leiden tot zowel vervorming van de F-actine bundels als van de microtubuli. Daarnaast tonen we aan dat TipAct groeiende microtubuli in staat stelt vrij diffunderende actine filamenten te transporteren, en aan actine filamenten te trekken die deels aan het glas bevestigd zijn. We zien dat microtubuli ook tijdens hun groei actine filamenten kunnen bundelen, waarbij de actine bundels vervolgens TipAct kunnen rekruteren. Ten slotte laten we zien dat dankzij deze mechanismen een radiale structuur (die ontstaat vanuit het centrosoom) een initieel isotrope oplossing van actine filamenten drastisch kan reorganiseren.

In hoofdstuk 6 bestuderen we hoe groeiende microtubuli actine filamenten kunnen transporteren via interacties gemedieerd door TipAct. Hiertoe combineren we experiementen met dynamische microtubuli en actine filamenten met het opstellen van een model voor asymmetrische diffusie van de actine filamenten door wisselwerkingen met de uiteindes van de microtubuli. Als we voorspellingen uit dit model vergelijken met experimentele data (filament transport voor verschillende EB, TipAct, en tubuli concentraties) zien we een goede overeenkomst tussen simulaties en experimenten. Ten slotte tonen we aan dat de krachten die gemoeid zijn met dit transport van de orde van enkele picoNewtons zijn, vergelijkbaar met krachten die worden opgewekt door moleculaire motoren in cellen.

Al met al hebben we door een minimaal model systeem te gebruiken van gezuiverde eiwitten inzicht verkregen in de manier waarop interacties tussen microtubuli uiteindes en F-actine structuren tot structurering van het cytoskelet leidden. De TipAct crosslinker zorgt ervoor dat actine bundels microtubuli kunnen leiden, en dus organiseren, in hun groei. Een verrassende ontdekking is dat hetzelfde systeem ook groeiende microtubuli in staat stelt om actine filamenten te reorganiseren. Dit toont aan dat *cross-linker* activiteit gemoduleerd wordt door de mechanische eigenschappen van de al bestaande architectuur van het cytoskelet. Wij concluderen dus dat – onafhankelijk van biochemische regulatie – een scala aan cytoskelet structuren kan ontstaan door de interactie tussen fysische *cross-links* en de mechanische eigenschappen van F-actine en microtubuli structuren.

We thank Joris Paijmans and Martijn Wehrens (FOM Institute AMOLF, The Netherlands) for carefully translating this section into Dutch.

List of Publications

Laan, L., Pavin, N., Husson, J., Romet-Lemonne, G., van Duijn, M., Preciado López, M., Vale, R.D., Jülicher, F., Reck-Peterson, S.L. & Dogterom, M. Cortical dynein controls microtubule dynamics to generate pulling forces that position microtubule asters. *Cell* **148**, 502-14 (2012).

Preciado López, M., Huber, F., Grigoriev, I., Steinmetz, M.O., Akhmanova, A., Dogterom, M. & Koenderink, G.H. In vitro reconstitution of dynamic microtubules interacting with actin filament networks. In Vale, R. D. (ed.) *Methods Enzymol.*, vol. 540, chap. 17, 301-320 (Elsevier Inc., Amsterdam, 2014).

Preciado López, M., Huber, F., Grigoriev, I., Steinmetz, M.O., Akhmanova, A., Koenderink, G.H. & Dogterom, M. Actin-microtubule coordination at growing microtubule ends. *Nat. Commun.* **5**, 4778 (2014).

Huber, F., Boire, A., Preciado López, M. & Koenderink, G.H. Cytoskeletal crosstalk: when three different personalities team up. *Curr. Opin. Cell Biol.* **32**, 39-47 (2015).

Preciado López, M., Monti, M., ten Wolde, P.R., Koenderink, G.H. & Dogterom, M. Transport and force generation by microtubule +TIPs. (*in preparation*)

Preciado López, M., Dogterom, M. & Koenderink, G.H. Physical principles of actin-microtubule coordination. (*in preparation*)

Acknowledgements

My PhD has been a period full of emotion. I started full of excitement and expectation, transitioned to despair and exhaustion, and ended with a newfound love and respect for research and science. Through these zigzagging years in Amsterdam, I have been accompanied by many people without whom everything would have been, to say the least, much harder.

First, I would like to thank Gijsje and Marileen. From the start you gave me all the freedom to let my imagination and efforts fly in any direction I wanted. You have been a source of inspiration, knowledge and patience, and it has been a real pleasure to work with you. I want to thank you for your support during difficult times, and for helping me put life and work in perspective.

Being a veteran at AMOLF, I have had the chance to meet a lot of wonderful people that I also want to mention, in no particular order. Bergin, Svenja, Marina, José, Brian, Nicola, Marian, Milena, Georges, Bela, Tomek, Marjon, Jochen, Tom, Björn, Filipe, Niels, Chris, Alexandra, Katja, Andrew, Pieter Rein, Yuval, Leffert, Nicholas, Faranaaz, Aditya, Adi, David, Ronald, Arif, Stephen, Eva, Florian, Bart, Keita, Gesa, Maurits, Sarah, Iza, Stef, Wouter, Guizela, Shayla, Stijn, Corianne, Sander, Stephan, Clare, Dmitry, Lars, Matthias, Bob, Simone, Ilya, Hinco, Marko, Roland... And many more I am missing. You have each colored my days (and nights) in Amsterdam in your own special ways, and I will always think of you with a smile.

I want to extend a warm thank you to Jan, Wiebe, Ed, Juliette, Marjolein, Arnelli, Willem, Vanda and Marjo. Not only have you made my time at AMOLF manageable, but you have also made it cozy and familiar. I love coming to AMOLF and seeing your smiles, hearing about your holidays, your families, your lives outside of work. I appreciate all these moments and will sorely miss them when I leave.

I want to thank Anna and Michel, without your advice and support this work would not have been possible. Also, I extend the biggest thank you to Carol, Babet, Cristina

and Ilya who helped me to learn molecular biology and to look at cells. I also thank Clare, Marcel, Erwin, Lukas and Kees for carefully reading the thesis manuscript.

Fe, we started this Amsterdam adventure together. Thank you for the many years we shared, and for all the wonderful memories.

Jean, you were my first friend in Amsterdam. But you left too soon, and I have since missed our nights out exploring this beautiful city, our long conversations, and the shared bottles of wine. I have yet to find another friend with whom I can fight so well.

Steven, we have been friends almost from the start! I am happy for every lunch we enjoyed in our own secretly kept havens. I am thankful for all the conversations, concerts, parties, movies, and for all the time we have spent together.

Adriana, you were a ray of sunshine in the middle of the winter. I am so happy we got to share a house, even if just for a short time. You were an instantaneous friend, and I thank you for that.

Laurens, what can I say? You have been such a supportive and helpful friend. Perhaps without knowing, you helped me through some of the most difficult times with your nonjudgemental way of being. I am thankful for everything I have learned from you.

Jul, your arrival to my life was a gift. I am so happy we got to spend the last year together. All the conversations we had, the openness of our friendship, the easiness of it all, it was truly great. I will miss you horribly, but I am sure we will meet again and again. Thank you for supporting my thesis-writing madness, for feeding me, and for keeping the house out of chaos during this time.

Hobbes and Peppe, you are my connection to the not so distant past. You have given me so much love and friendship, and I am thankful for that.

Hans, Elkan, Celita and Leonor. You were my family away from home. Thank you for hosting me all these years, for making me feel at home, and for letting me peek into your family life.

Pietro, we have been friends for so long. Arriving to the Netherlands knowing that I would find a familiar face made everything easier. Thank you for all the delicious meals, and for sharing with me your amazing way of thinking.

Peter, thank you for all the conversations and discussions. I have learned a lot from life this last year, and I owe it in great part to your calm objectivity.

Nyx, thank you for being an integral part of my life. You have been a source of strength in innumerable occasions.

Nùr, Sophie, Noreen, Fatemeh, Martijn, Felipe, Sebastian, Feng, Joris, Jeanette, Ioana, Baldo and Pierre. I spent a long part of my AMOLF time with you. You are truly wonderful, helpful, and easy-going people, and I am thankful for having met you.

Mic, Agatina, Simone, Jaco, Ade and Cristina. Your arrival to AMOLF was simply refreshing. Time with you is always full of fun and laughter. I am very happy for having stayed a little longer in Amsterdam and getting to know you.

Lutz, I am so happy to have finally get to know you, years after we actually met! Thank you for your sweetness, your smile, and for laughing at my silly jokes.

Brotchen, Rita, Elito, Wes, Agus, Mar, Mayriux, Pabli, Anni, Gero, Enas, Rodrigo, Sonia, Carlota, Saran, Jess, Leo, Vin, Daniel, Danush, Natty, Jenna, Momo, Natsuko, Alexia, Emi, Gov, Wilo, Kasper, Marce, and Adriano. Friends and anchors to the many places I have stepped on. You are sources of inspiration and diversity in my life. I love you and miss you always.

And finally, I want to thank my family, which is just so big and makes every second a happy one. Especially, I extend my biggest *gracias* to my mother, my father and my sisters. Mapá, pamá, Pollo and Shim, you are the sunshine of my life. Thank you for the support and love through these crazy years. I love you with all my heart, and could not be more thankful for having you in my life.

Sincerely yours,

Maga